Universiteit Gent
Faculteit Wetenschappen
Vakgroep Fysica en
Sterrenkunde

Advanced analytical methods in stellar dynamical modelling

Emmanuel Van Hese

Promotors: Prof. Dr. Maarten Baes
Prof. Dr. Herwig Dejonghe

Proefschrift tot het bekomen van de graad van
Doctor in de Wetenschappen: Sterrenkunde
Academiejaar 2013-2014

Promotors:

Prof. Dr. Maarten Baes
Vakgroep Fysica en Sterrenkunde
Universiteit Gent

Prof. Dr. Herwig Dejonghe
Vakgroep Fysica en Sterrenkunde
Universiteit Gent

Other members of the examination board:

Prof. Dr. Dirk Poelman
Voorzitter Examenjury
Vakgroep Vastestofwetenschappen
Universiteit Gent

Prof. Dr. Luca Ciotti
Dipartimento di Fisica e Astronomia
Università di Bologna

Prof. Dr. Steen Hansen
Dark Cosmology Centre
Københavns Universitet

Prof. Dr. Sven De Rijcke
Vakgroep Fysica en Sterrenkunde
Universiteit Gent

Prof. Dr. Henri Verschelde
Vakgroep Fysica en Sterrenkunde
Universiteit Gent

Prof. Dr. Hans Vernaeve
Vakgroep Wiskunde
Universiteit Gent

Dankwoord

Het einde van een tijdperk. Dat is wel het minste dat ik kan zeggen over de periode die ik nu afsluit, en die het merendeel van mijn volwassen leven in beslag heeft genomen. Het is een tijd geweest van transpiratie, desperatie, en – gelukkig – af en toe ook wat inspiratie. Maar bovenal is een leerperiode geweest, waarin ik mezelf heb leren kennen.

Mijn bijzondere dank gaat uit naar mijn promotoren; ik dank Herwig Dejonghe voor de kans die ik heb gekregen om dit onderzoek te doen, de expertise die hij heeft gedeeld, en mijn tijd als tijdelijk assistent bij de oefeningen Algemene Sterrenkunde. Ik dank Maarten Baes van harte voor de zeer aangename en vruchtbare samenwerking, en zijn belangrijke rol als mentor. Zijn enthousiasme en blijvende steun, professioneel en moreel, waren cruciaal om dit doctoraat tot een goed einde te brengen. Mijn dank gaat ook uit naar Sven De Rijcke; met hem heb ik eveneens heel goed samengewerkt, en ik kon steeds bij hem terecht als ik vragen had.

Ik heb in de ganse periode zoveel collega's zien komen en gaan dat ik geen poging durf te ondernemen om ze allemaal op te noemen, maar ik wil ze stuk voor stuk bedanken voor de talloze fijne momenten die we hebben gedeeld. Om toch één iemand op te noemen, wil ik graag Veronique De Bruyne vermelden, die me altijd een hart onder de riem heeft gestoken.

Dank natuurlijk aan mijn vrienden, die mij zo'n duizend keer de gordijnen hebben ingejaagd met die vreselijke vraag "En hoe is 't met het doctoraat?" Godzijdank zal ik die rotvraag nooit meer krijgen... Merci dat jullie in mij zijn blijven geloven, en dat jullie op tijd en stond mijn zorgen konden doen vergeten.

Maar bovenal gaat mijn speciale dank uit naar de twee meest geweldige mensen op deze wereld: mijn ouders. Zij zijn altijd onvoorwaardelijk achter mij blijven staan, en zonder hen had ik dit nooit kunnen doen. Dit proefschrift wil ik dan ook van harte aan hen opdragen.

Emmanuel Van Hese
Juni 2014

Samenvatting

Algemene situering

Alle stellaire structuren in het heelal, van zonnestelsels, bolhopen en galaxieën, tot groepen, clusters en superclusters van galaxieën, en de donkere materie-halo's die hen omgeven, worden vormgegeven door een enkele dominerende kracht: zwaartekracht. De vraag hoe deze systemen zich gedragen is dan ook een fundamenteel vraagstuk in de theoretische astrofysica.

In wezen zijn er twee complementaire technieken ontwikkeld om de dynamische structuur van grote gravitationele systemen te analyseren. De eerste methode behelst numerieke N-deeltjessimulaties, die ons helpen om de evolutie van structuurvorming in het heelal te doorgronden. De tweede methode, die de focus zal zijn van deze dissertatie, is stellaire dynamica, dit wil zeggen de constructie van theoretische modellen door technieken uit de statistische fysica toe te passen en aldus discrete systemen te beschrijven in termen van continue grootheden. In het bijzonder wenst men zogenaamde *distributiefuncties in de faseruimte* te construeren, en hun eigenschappen te bestuderen.

Hoewel zulke dynamische modellen noodzakelijkerwijs geïdealiseerde beschrijvingen zijn van stellaire structuren – men moet systemen beschouwen die geëvolueerd zijn naar een quasi-evenwichtstoestand, met weinig substructuur en met een hoge graad van symmetrie (sferisch, axiaal symmetrisch, etc) – is ondanks deze beperkingen stellaire dynamica een essentieel instrument om inzicht te verkrijgen in de dynamische structuur van stellaire systemen, bijvoorbeeld door hun baanconfiguratie of hun snelheidsverdeling te tonen. Bovendien kunnen dynamische modellen dienst doen om begincondities te genereren voor bijkomende N-deeltjessimulaties. Beide technieken vullen elkaar dus aan in de studie van gravitationele systemen.

Dynamisch modelleren: algemeen

Een distributiefunctie in de faseruimte beschrijft in essentie de waarschijnlijkheid dat men een object vindt in het systeem op een bepaalde plaats en met een bepaalde snelheid. Als ook de totale gravitationele potentiaal gegeven is, dan is de baan van dit object volledig gedetermineerd; met andere woorden, een distributiefunctie beschrijft de volledige dynamische structuur van een stellair systeem, en alle observationele grootheden kunnen hiervan afgeleid worden. De belangrijkste hiervan zijn de dichtheid en de snelheidsdisper-

sies (die de gemiddelde kwadratische snelheden op een bepaalde plaats en in een bepaalde richting weergeven).

Het centrale vraagstuk in stellaire dynamica betreft aldus het zoeken naar geschikte distributiefuncties die consistent zijn met een gegeven verzameling datapunten. Dit kunnen ruimtelijke grootheden zijn, bijvoorbeeld data gedistilleerd uit simulaties van donkere materie-halo's, maar het kunnen ook geprojecteerde observationele grootheden zijn, zoals de posities aan de hemel en de Dopplersnelheden van galaxieën in een cluster.

Een belangrijke stelling zegt dat voor een brede klasse van evenwichtssystemen de distributiefunctie enkel afhankelijk is van hoogstens drie integralen van de beweging. Maar desondanks blijft het algemene geval te gecompliceerd om op te lossen. We zijn daarom genoodzaakt om systemen te beschouwen met extra symmetrieën. In het bijzonder beperken we ons tot sferische systemen zonder rotatie. Voor deze klasse van systemen is de distributiefunctie enkel afhankelijk van twee integralen, de baanenergie en het draaimoment.

Natuurlijk is sferische symmetrie een aanzienlijke vereenvoudiging, maar dit laat ons toe om op een elegante en geavanceerde manier distributiefuncties te construeren, en hun eigenschappen op een gedetailleerde manier te analyseren. Bovendien zijn dergelijke modellen een betekenisvolle benadering voor de systemen die we zullen beschouwen, namelijk clusters van galaxieën en donkere materie-halo's. De technieken die we in deze dissertatie zullen behandelen zijn dan ook een eerste aanzet, die in later werk kunnen uitgebreid worden naar algemenere (axiaal-symmetrische) structuren.

Dynamisch modelleren: probleemstelling

De meest gebruikte techniek in dynamisch modelleren is de zogenaamde *Schwarzschild methode*. Deze houdt in dat men een distributiefunctie opbouwt door individuele banen toe te voegen die een gegeven dataset fitten. Hoewel deze methode zeer algemeen is, heeft ze ook nadelen: zo creëert een collectie van discrete banen een ietwat onfysische dynamische structuur, die moeilijk te interpreteren is. Bovendien is het numeriek lastig om uit een dergelijke distributiefunctie alle relevante observationele grootheden te berekenen.

In onze onderzoeksgroep is er daarom een meer geavanceerde variant van deze methode ontwikkeld. In dit algoritme wordt een distributiefunctie niet opgebouwd uit aparte banen, maar gecreëerd als een lineaire combinatie van meer elementaire analytische basisfuncties van de integralen. De bijbehorende data-fitting vormt hierbij een kwadratisch programmeervraagstuk.

Deze techniek is in de loop der jaren met succes toegepast op een waaier van systemen, zoals bolhopen en galaxieën. Het oorspronkelijke doel van dit onderzoek was om de methode te gebruiken voor clusters van galaxieën, maar hierbij stootten we op een aantal tekortkomingen in het algoritme. Onze focus werd daardoor verlegd naar het oplossen van deze problemen, waarvan deze dissertatie het resultaat is.

We identificeerden drie moeilijkheden. De voornaamste is dat het algoritme een vertekening vertoont: het is meer geneigd om modellen te creëren met tangentiële banen dan modellen met radiale banen. De reden hiervoor is dat het eenvoudiger is om basiscomponenten aan de distributiefunctie toe te voegen die banen bevatten met een kleine excen-

triciteit, omdat zulke banen een vorige fit slechts wijzigen in een beperkte regio en dus heel gericht kunnen verbeteren. Componenten met meer radiale banen daarentegen hebben zowel een invloed op kleine als op grote afstanden van het centrum, zodat zulke basisfuncties een bestaande fit significanter wijzigen en dus moeilijker kunnen verbeteren. Het probleem om aldus modellen te construeren met radiale banen is met name nefast bij grote structuren zoals clusters van galaxieën, vermits hun buitenste regionen gedomineerd worden radiaal invallende sterrenstelsels.

Een tweede probleem was dat de bestaande basiscomponenten onvoldoende gesofisticeerd waren om snelheidsdispersies te genereren die overeenstemmen met waarnemingen en simulaties van grote structuren. Met name de snelheidsanisotropie, die de verhouding uitdrukt tussen tangentiële en radiale dispersies, vertoonde in de modellen een te steile overgang van centrale waarden naar waarden op grote afstand. Dit probleem kwam vooral tot uiting bij het modelleren van donkere materie-halo's.

Een derde, meer algemeen probleem dat inherent is aan elke fitting-procedure, is het feit dat de datapunten doorgaans bestaan uit een mix van grootheden (in het bijzonder dichtheid en snelheidsdispersies). Daardoor rijst de vraag hoe men deze gemengde data op een representatieve manier met elkaar kan vergelijken en hen moet laten meewegen in de fit.

Dynamisch modelleren: oplossing

Geconfronteerd met deze drie moeilijkheden zijn we op zoek gegaan naar een manier om dit te verhelpen. Onze oplossing bestaat erin om meer geavanceerde basisfuncties te ontwikkelen, die elk een anisotropie-profiel genereren dat veel algemener is dan de bestaande basisfuncties. We slaagden hierin door gebruik te maken van *vermeerderde dichtheden*, een elegante methode waarmee dynamische systemen kunnen worden beschreven, equivalent met distributiefuncties. De bekomen basiscomponenten kunnen daarbij uitgedrukt worden in termen van zogenaamde *Fox H-functies*, een heel algemene familie van speciale wiskundige functies, die een waaier van meer bekende functies omvat. Daarenboven kunnen deze functies ontwikkeld worden in machtreeksen. Dit is een bijzonder nuttige eigenschap, niet alleen omdat ze op die manier efficiënt kunnen worden berekend, maar ook omdat dit toelaat om hun asymptotisch gedrag te bestuderen.

Vermits deze componenten een snelheidsanisotropie kunnen voortbrengen die voldoende algemeen is, hoeven we deze laatste niet langer in een fit proberen te construeren. In plaats daarvan kunnen we een snelheidsanisotropie reeds op voorhand postuleren, en enkel de dichtheid te gebruiken als data in de fitting methode; voor elke anisotropie (die we in een parameterruimte kunnen laten variëren), kunnen we op deze manier een distributiefunctie genereren die deze exact voortbrengt, en aldus een parameterfamilie van fits construeren. Hiermee lossen we zowel het bias-probleem op (zodat we modellen kunnen maken met radiale banen) als het probleem van gemengde data. We demonstreren dit door onze techniek toe te passen op enkele specifieke onderwerpen.

Overzicht

Na een inleidend hoofdstuk geven we een algemeen overzicht van stellaire dynamica in Hoofdstuk 2 (grotendeels gebaseerd op werk van andere auteurs), waarbij we eveneens het modelleringsalgoritme beschrijven en de tekortkomingen die we zonet aangehaald hebben.

Vervolgens introduceren we in Hoofstuk 3 de Fox H-functie die we nodig zullen hebben voor onze distributiefuncties. Aangezien deze functie weinig bekend is in de theoretische astrofysica, besteden we de nodige aandacht aan haar eigenschappen, en we demonstreren haar kracht door verschillende eigenschappen van Sérsic en Einasto dichtheden af te leiden als Fox H-functies. Met dit wiskundig gereedschap in de hand kunnen we onze basis-distributiefuncties afleiden in Hoofdstuk 4. Deze functies blijken op zichzelf ook een algemene familie van modellen te genereren, namelijk de Veltmann modellen, en we beschrijven eveneens hun eigenschappen.

De volgende drie hoofdstukken zijn gewijd aan diverse toepassingen van onze modelleringstechniek. In Hoofdstuk 5 tonen we aan dat we distributiefuncties kunnen genereren, gebaseerd op Dehnen-McLaughlin profielen, die verscheidene "universele" eigenschappen van gesimuleerde donkere materie-halo's omvatten: een welbepaalde dichtheid, een bepaalde verhouding tussen dichtheid en dispersie die als een machtwet verloopt, en een lineaire relatie tussen het verloop van de dichtheid en de anisotropie.

In Hoofdstuk 6 bestuderen we een bepaalde theoretische eigenschap van sferische systemen, die bekend staat als de GDSAI ('global density slope – anisotropy inequality'). Een studie van Ciotti & Morganti (2010) toonde aan dat voor een grote familie van modellen het verloop van de dichtheid steeds groter is dan tweemaal de anisotropie, wat de vraag deed rijzen of deze eigenschap algemeen geldig was. Onze technieken stelden ons in staat om te bewijzen dat de ongelijkheid inderdaad geldig is voor een specifieke klasse van systemen, namelijk die met een separabele vermeerderde dichtheid, mits de centrale waarde van de anisotropie kleiner is dan $1/2$. Bovendien konden we met onze modelleringsprocedure systemen construeren die niet voldoen aan de GDSAI, met de opmerking dat deze tegenvoorbeelden dynamisch instabiel zijn. In onze studie tonen we aan dat de GDSAI in feite een speciaal geval is van algemenere restricties op de vermeerderde dichtheden. We breiden deze studie vervolgens uit om nodige en voldoende voorwaarden af te leiden waaraan systemen met een positieve distributiefunctie moeten voldoen.

Vervolgens passen we in Hoofdstuk 7 onze techniek toe op observationele data, met name een groep van dwerggalaxieën in de Fornax cluster. Onze modellen suggereren dat de gas-arme galaxieën op banen bewegen met een hoge excentriciteit, wat bewijs levert voor de hypothese dat ze hun gas hebben verloren door zogenaamde ram-pressure stripping, wanneer ze door het hete intracluster-gas in de centrale regionen van de cluster passeerden.

Een laatste hoofdstuk behandelt een zij-project, waarin we vertrekken van een familie van distributiefuncties met en zonder een superzwaar centraal zwart gat, en hieruit een verzameling discrete deeltjes genereren met behulp van een Monte Carlo algoritme (eveneens ontwikkeld door de auteur). Deze deeltjes deden vervolgens dienst als begincondities voor N-deeltjessimulaties, om de stabiliteit van deze modellen te onderzoeken. Het bleek dat de centrale zwarte gaten een stabiliserend effect hadden op deze systemen.

Alle resultaten van Hoofdstukken 3 tot en met 8 zijn gepubliceerd in een reeks artikels; een lijst van deze publicaties kan men achteraan deze dissertatie vinden.

Table of Contents

Part I

OVERVIEW

Chapter 1

Introduction

General background

All stellar structures in the universe, from solar systems, globular clusters and galaxies, to groups, clusters and superclusters of galaxies, and the dark matter haloes that surround them, are shaped by a single dominating force: gravity (see for example the large galaxy cluster Abell 1689, shown in the left panel of Fig. 1.1). Hence, the question how these systems form and behave has always been a fundamental topic in theoretical astrophysics.

Two main techniques have been developped to analyse the dynamical structure of gravitational systems. The first method involves the use of numerical N-body simulations, which enable us to understand the evolution of structure formation in the universe (e.g. the 10 billion particle Millennium-II simulation, shown in the right panel of Fig. 1.1). The second is stellar dynamics: the construction of theoretical models, by applying techniques of statistical physics to approximate discrete systems with continuous ones. In particular, one wishes to find full phase-space distribution functions, each of which completely determines a gravitational system, and study their properties.

Both approaches have advantages and limitations. The main strength of N-body simulations is their versatility. However, in order to obtain a sufficient amount of resolution one requires substantial computational power. Moreover, one has to set up suitable initial conditions if one wants to explore particular scenarios or analyse observational data. Also, it is not straightforward to gain insight into the dynamical structure of N-body systems. On the other hand, modelling techniques do allow us analyse stellar structures, for example by revealing their velocity distribution or their orbital configuration. They also can be set up to generate very specific models, with particular properties. Unfortunately, their main drawback is the fact that dynamical models are idealizations that can only be applied to simple configurations, such as (quasi-)equilibrium states, and systems with limited amounts of substructure and with a high degree of symmetry (spherical, axisymmetric, etc).

The real strength of both methods comes to light when one uses them in a complementary way. Together with observational data, the outcome of N-body simulations can be subsequently modelled and analysed. Conversely, one can generate sets of particles from a distribution function, which can serve as initial conditions in a follow-up N-body simulation. However, for this to succeed, one needs to develop algorithms that produce

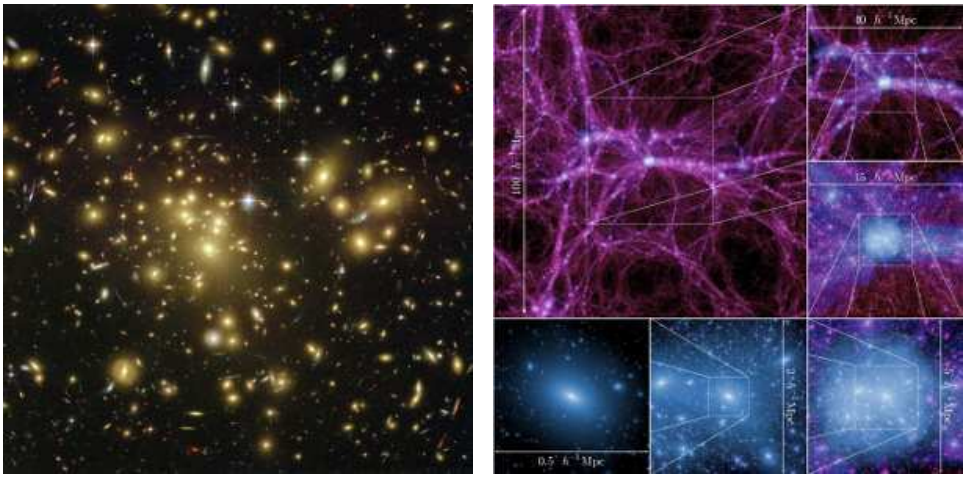

Figure 1.1 Left panel: Cluster Abell 1689 (image credit: NASA, N. Benitez (JHU), T. Broadhurst (The Hebrew University), H. Ford (JHU), M. Clampin(STScI), G. Hartig (STScI), G. Illingworth (UCO/Lick Observatory), the ACS Science Team and ESA). Right panel: Millennium-II Simulation, following 2160^3 particles in box of side length $100\,h^{-1}$ Mpc (image credit: Boylan-Kolchin et al. 2009).

sufficiently sophisticated models that can be applied to realistic systems. The aim of this dissertation is to create such an algorithm for spherical equilibrium systems. More specifically, we will construct linear combinations of analytical (in the sense that they can be expressed as Taylor expansions of elementary functions) distribution functions that can be fit to a given density and a specific (but quite general) velocity anisotropy profile, and we explore several applications. As we develop the necessary techniques, we will encounter a family of very powerful mathematical functions, the so-called Fox H-functions. As a by-product we will demonstrate the use of these functions as well.

Dynamical modelling: general principles

Let us outline how we can transform an N-body problem into a dynamical model; a more detailed treatment will be given in Section 2.1. If we can safely idealize the particles within a gravitational system as point masses with masses $m_1, \ldots, m_N$, and considering the framework of Newtonian physics within three-dimensional Euclidean space, the complete state of these particles is determined once their positions and velocities are known at a time t_0,

$$\begin{cases} \boldsymbol{r}_i(t_0) = \boldsymbol{r}_{i,0}, \\ \boldsymbol{v}_i(t_0) = \boldsymbol{v}_{i,0}, \end{cases} \qquad i = 1, \ldots, N. \tag{1.1}$$

With these initial conditions, the question of deriving the positions and velocities at any time t defines an N-*body problem*, formulated by $6N$ first-order differential equations

$$\begin{cases} \boldsymbol{v}_i = \dot{\boldsymbol{r}}_i, \\ \dot{\boldsymbol{v}}_i = -\dfrac{\partial}{\partial \boldsymbol{r}_i}\left(-G\displaystyle\sum_{j,\, j\neq i}\frac{m_j}{|\boldsymbol{r}_i-\boldsymbol{r}_j|}\right), \end{cases} \qquad i=1,\ldots,N. \tag{1.2}$$

In principle, the particles can also be influenced by an additional external force. Evidently, these equations can only be solved numerically if $N > 2$. If the number of particles is sufficiently large, we can smooth the positions of the particles into a total *mass density* $\rho_{\text{tot}}(\boldsymbol{r},t)$. The gravitational field generated by and acting upon the particles can then be expressed as a *gravitational potential*

$$\psi(\boldsymbol{r},t) = G\iiint \frac{\rho_{\text{tot}}(\boldsymbol{r}',t)}{|\boldsymbol{r}'-\boldsymbol{r}|}\,\mathrm{d}^3\boldsymbol{r}', \tag{1.3}$$

Note that we defined the potential as a positive function. We can rewrite the above equation as

$$\nabla^2\psi(\boldsymbol{r},t) = -4\pi G\rho_{\text{tot}}(\boldsymbol{r},t). \tag{1.4}$$

known as the *Poisson equation*. In this manner, every particle can be regarded as a test particle, for which the orbit is stipulated by the gravitational potential. If its initial position in six-dimensional *phase space* $(\boldsymbol{r},\boldsymbol{v})$ is known, its motion is determined by the force

$$\ddot{\boldsymbol{r}}(t) = \boldsymbol{\nabla}\psi(\boldsymbol{r},t), \tag{1.5}$$

where $\boldsymbol{\nabla}$ denotes the gradient. Following the motion of a particle in time, its position $\boldsymbol{r}(t)$ traces out an *orbit*, with an associated velocity $\boldsymbol{v}(t)$.

Instead of all particles, we can also study the motion of a subgroup of particles, with a density $\rho(\boldsymbol{r},t) \neq \rho_{\text{tot}}(\boldsymbol{r},t)$, whose motions are completely determined by the global potential. Examples of these are the behaviour of luminous matter within dark matter haloes, such as stars within a galaxy or galaxies within a cluster. In any case, if we want to treat our particles as test particles, we require that the dynamical systems are *collisionless*, i.e. they are systems where interactions between individual particles are negligible. This is a safe assumption for cold dark matter haloes; for stellar systems on the other hand, we follow Section 1.2 of Binney & Tremaine (2008) and consider the *relaxation time*

$$t_{\text{relax}} \approx \frac{0.1\,N}{\ln N} t_{\text{cross}}, \tag{1.6}$$

with $t_{\text{cross}} = R/v$ the *crossing time*, which is the time needed for a typical particle to cross the system once. The relaxation time is a measure for the timescale at which particle interactions become significant: more precisely, it is the time after which the average velocity of a particle has changed by the same order due to cumulative encounters with other particles,

thereby significantly altering its orbit compared to what it would be in a smooth gravitational field. If either N is large (such as in galaxies) or t_{cross} is large (such as in galaxy clusters), the relaxation time is indeed sufficiently large to assume a collisionless system. Such a system satisfies the *collisionless Boltzmann equation*

$$\frac{\mathrm{d}F}{\mathrm{d}t}(\boldsymbol{r},\boldsymbol{v},t) = \frac{\partial F}{\partial t}(\boldsymbol{r},\boldsymbol{v},t) + \boldsymbol{v}\cdot\frac{\partial F}{\partial \boldsymbol{r}}(\boldsymbol{r},\boldsymbol{v},t) + \boldsymbol{\nabla}\psi(\boldsymbol{r},t)\cdot\frac{\partial F}{\partial \boldsymbol{v}}(\boldsymbol{r},\boldsymbol{v},t) = 0. \tag{1.7}$$

This means that the evolution of a sample of particles within a gravitational potential is completely determined by their phase space coordinates at a given time, described by the so-called *distribution function in phase space* (hereafter DF) and denoted as $F(\boldsymbol{r},\boldsymbol{v},t)$. In other words, $F(\boldsymbol{r},\boldsymbol{v},t)\,\mathrm{d}^3\boldsymbol{r}\,\mathrm{d}^3\boldsymbol{v}$, expresses the likelihood of encountering a particle at time t in the infinitesimal volume element $\mathrm{d}^3\boldsymbol{r}\,\mathrm{d}^3\boldsymbol{v}$ centred around the coordinate $(\boldsymbol{r},\boldsymbol{v})$. Evidently, this function has only a physical meaning if it is nonnegative everywhere in its entire domain, and the corresponding system is called *consistent*. Again, such a distribution does not have to encompass all particles of the system. For instance, it can be used to describe the state of luminous matter within a dark matter halo.

Dynamical modelling: fitting the data

The general Boltzmann equation is much too complicated to solve. Fortunately, the problem simplifies significantly if we limit our study to *equilibrium systems*, wherein the potential and the DF do not depend on the time t. In other words, we will not focus on the dynamical evolution of astrophysical systems, but instead analyse their structure after they relaxed into a virialized state. As we will show in Section 2.1, the DF then reduces to a function of at most three isolating integrals of motion.

In our study, we will study primarily large structures, namely simulated data from large dark matter haloes and observational data from galaxy clusters. Such structures allow us the introduction of additional symmetries: we will only consider spherical systems with no net flow. Naturally, this is a serious restriction; real systems are not the proverbial spherical cows. However, our limitations to spherical symmetry do give us an ideal test case to develop our advanced mathematical tools and subsequently study the dynamical structure of the DFs that we will create. Also, in the case of galaxy clusters and dark matter haloes the deviations from spherical symmetry are limited enough to justify the use of our models as useful first approximations. Moreover, instead of studying the complete DFs in great detail, we can derive from them more useful quantities like the velocity distributions and their low-order moments. In future work, our techniques can be further extended to create models with rotation and axial symmetry.

With these considerations in mind, let us now pose the question what data we can extract from a given structure to create a dynamical model. For spherical systems, it is natural to express any position-velocity vector $\{\boldsymbol{r},\boldsymbol{v}\}$ either in Cartesian coordinates $\{(x,y,z),(v_x,v_y,v_z)\}$ or spherical coordinates $\{(r,\theta,\varphi),(v_r,v_\theta,v_\varphi)\}$. We shall adopt the convention that the (x,y)-plane coincides with the local celestial sphere around the system, so that the z-axis represents the line of sight, taken as positive in the direction of increasing

distance (we will assume that the angular size of the system is sufficiently small so that the lines of sight for all particles are parallel). The angles θ and φ are the standard angles of spherical coordinates, with θ the angle between the z-axis and the position vector, and φ the angle between the xz-plane and the meridional plane of the particle (see Fig. 2.1).

If we have a collection of N particles for which we the full position vectors (as in the case of dark matter haloes), we can estimate the spatial particle density at a radius r by binning a subset of m particles that lie in a shell surrounding this radius:

$$\rho(r) \approx \frac{3}{4\pi} \frac{m}{r_m^3 - r_1^3}, \tag{1.8}$$

where r_1 and r_m are the radii of the particles closest to and furthest from the centre.

If we only have observational information about the projected positions of the particles on the celestial sphere, but not their distance (as in the case of galaxies in a cluster), we can similarly estimate the projected density at a projected radius $R = \sqrt{x^2 + y^2}$:

$$\Sigma(R) \approx \frac{1}{\pi} \frac{m}{R_m^2 - R_1^2}. \tag{1.9}$$

For spherical systems, there is a 1-1 correspondence between the spatial and the projected density (see Eq. (2.69)), so that Σ can be deprojected into ρ.

The simplest useful velocity information is given by the *velocity dispersion* at a certain position and in a direction $\boldsymbol{d}$, which is the root-mean-square of the velocities in that region: $\sigma_{\boldsymbol{d}}^2 = \left\langle \left(v_{\boldsymbol{d}} - \langle v_{\boldsymbol{d}} \rangle \right)^2 \right\rangle$. Analogously to the density, we can give a simple estimate for a set of m particles as

$$\sigma_{\boldsymbol{d}}^2 \approx \frac{1}{m-1} \sum_{i=1}^{m} \left(v_{\boldsymbol{d},i} - \langle v_{\boldsymbol{d}} \rangle \right)^2, \qquad \langle v_{\boldsymbol{d}} \rangle = \frac{1}{m} \sum_{i=1}^{m} v_{\boldsymbol{d},i}, \tag{1.10}$$

although there exist more sophisticated statistical estimators (e.g. Danese et al. 1980). Again, we need to discern between systems for which we have full spatial information, and those for which only projected observational data is available. In the former case, we can construct the dispersion profiles $\sigma_r(r)$, $\sigma_\theta(r)$ and $\sigma_\varphi(r)$. In fact, for spherical systems $\sigma_\theta(r) \equiv \sigma_\varphi(r)$. It is also useful to introduce Binney's *anisotropy parameter*

$$\beta(r) = 1 - \frac{\sigma_\theta^2(r)}{\sigma_r^2(r)}. \tag{1.11}$$

In the case of observational systems, we only have velocity information along the line of sight (v_z) through redshift data. In this case, we can only construct one dispersion profile, namely the projected line-of-sight dispersion $\sigma_{\rm los}(R)$. Just as for the density, there is again a relation with the spatial dispersion (Eq. (2.75)), but this time the correspondence is not 1-1, since $\sigma_{\rm p}$ depends on a combination of σ_r and σ_θ. In other words, different combinations of the spatial dispersions can yield the same projected dispersion.

A given set of $\rho(r)$, $\sigma_r(r)$, $\sigma_\theta(r)$, and total potential $\psi(r)$ are related through the *Jeans equation*

$$\frac{\mathrm{d}\rho\sigma_r^2}{\mathrm{d}r}(r) + \frac{2\beta(r)}{r}\rho\sigma_r^2(r) = \rho(r)\frac{\mathrm{d}\psi}{\mathrm{d}r}(r). \tag{1.12}$$

This equation can be derived from the spherical Boltzmann equation, but we shall give an alternative derivation in Section 2.3.1. If the density does not trace the potential, then Eq. (1.12) can be used to find $\psi(r)$, and therefore the total mass distribution of the system. On the other hand, if both the density and the potential are known (for example, if the given density also generates the potential through Poisson's equation), then the Jeans equation shows that ρ, σ_r, and σ_θ are not independent. Similar relations exist between higher-order moments (Eq. 2.117).

In some cases, it is possible to extract more information from the data. For example, one can try to constrain the 4th-, 6th- or even 8th-order projected moments, although their statistics become increasingly worse (e.g. Gerhard 1993; van der Marel et al. 2000; Richardson & Fairbairn 2013). Alternatively, one can try to constrain the line-of-sight velocity distributions using a maximum likelihood method (Dejonghe & Merritt 1992; Wojtak et al. 2008).

But if we wish to create a full dynamical model, we have to find a way to construct the entire velocity distribution. A naive approach would be to postulate a multivariate Gaussian velocity distribution in every direction (Hernquist 1993), with dispersions constrained by the data. This approach however fails, because the resulting distributions do not obey the Boltzmann equation, and consequently do not generate equilibrium systems (Kazantzidis et al. 2004). Instead, we need a more sophisticated method to derive consistent DFs. It is important to remark though, that even under the restrictions of spherical symmetry, we can never hope to have enough data to construct unique DFs. In principle, an infinite number of DFs can be fit to a limited data set of velocity moments.

In Chapter 2 we give a general overview of dynamical modelling, which will act as the basis for all subsequent chapters. As such, most of the chapter is a summary of concepts that have been developed in previous work, in particular Dejonghe (1986). However, in the final section of the chapter we outline the key issues that have prompted the subsequent work that is presented in the rest of this dissertation.

Dynamical modelling: quadratic programming

A commonly used method to create a dynamical model is to fit individual orbits to the data with a linear programming algorithm, and build the DF as a sum of delta functions (smoothed into narrow Gaussians) of the orbital values. This is known as Schwarzschild's method (Schwarzschild 1979), and it has been applied in numerous studies (e.g. Merritt & Saha 1993; Gerhard et al. 1998; Cappellari et al. 2004; Cappellari et al. 2006; van de Ven et al. 2006; Chanamé et al. 2008; Vasiliev 2013). A schematic representation of this technique is shown in Fig. 1.2. While this method is quite general, the drawback is that one thus essentially obtains discrete systems, wherein the orbits lack an underlying physical

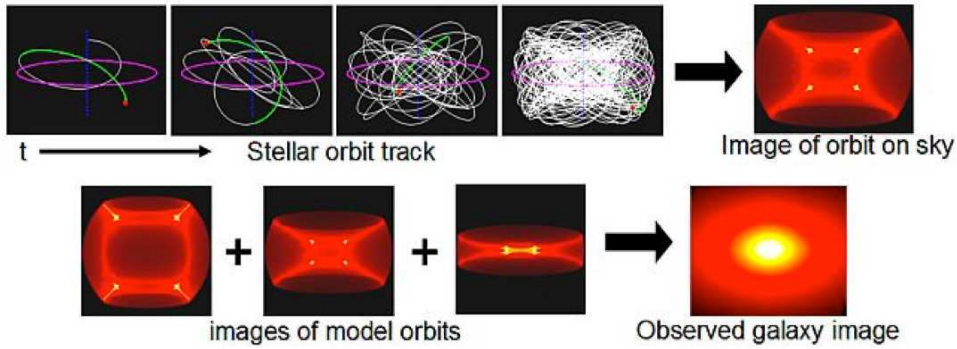

Figure 1.2 Schematic representation of Schwarzschild's modelling method (Cappellari et al. 2004).

relation. Not only are such models somewhat unphysical, but they also make subsequent integrations (to obtain observable quantities) cumbersome.

In order to create DFs that are smooth functions of the orbital elements, a more sophisticated method was developed at our department. With this algorithm, the DF is gradually built as a linear combination of a set of base functions, $F(\boldsymbol{r},\boldsymbol{v}) = \sum F_i(\boldsymbol{r},\boldsymbol{v})$, instead of individual orbits; in other words, this is an advanced version of the Schwarzschild method. By adding components, the algorithm then seeks an increasingly better fit with the data using a *quadratic programming* (QP) technique (Dejonghe 1989), which means that the model is fit to a set of data points with a χ^2 minimization procedure. This method has been used for a variety of gravitational systems, and accordingly it has been gradually extended over the years (e.g. De Rijcke & Dejonghe 1998 ; Baes et al. 2000 ; De Bruyne et al. 2001 ; Famaey et al. 2002 ; De Bruyne et al. 2004 ; Rindler-Daller et al. 2005 ; De Rijcke et al. 2006 ; see also Dejonghe et al. 2001 for a review).

Originally, we planned to apply the modelling method to clusters of galaxies (preliminary results were given in Van Hese & Dejonghe 2002). However, this work revealed that the algorithm did have its shortcomings.

The main issue was that the method was biased towards producing models that are tangentially anisotropic at their outskirts (i.e. $\beta(r) < 0$ for large r). The reason is that it is easier to add components that generate predominantly circular orbits, because they only affect the existing fit in a limited range of radii, whereas components with radial orbits will change the DF over a wide range of radii. Consequently, the algorithm tends to select the more tangential components, especially when only projected data is available for the fit. We will address this in more detail in Section 2.4. This is especially problematic for large structures, since these are formed through radial infall, thus one expects the outer regions to be dominated by radial orbits. Moreover, there is evidence from simulations and observations that many galaxies also have a significant radial anisotropy at large radii (e.g. Kronawitter et al. 2000 ; Oñorbe et al. 2007).

A second problem, which became apparent when we tried to find DFs for the Dehnen & McLaughlin (2005) systems (see Chapter 5), was that the existing base components were too simple to reproduce systems with a realistically increasing anisotropy. Even though linear combinations of components can in principle produce quite general profiles, it turned out that the transition from central to outer anisotropy in our models was too abrupt to fit the data.

A third problem concerns the fitting of mixed data: when combining different quantities, such as densities and second-order moments, it is not clear what relative importance should be given to them; also, these data are in general not independent. Naturally, this is an issue for *every* fitting procedure, not just our quadratic programming algorithm.

Overview of our main work

In this dissertation, we aim to find a solution to these problems. Our approach is to fix the velocity anisotropy profile $\beta(r)$ beforehand, and create a family of base DF components that each generate this anisotropy profile exactly, with the additional requirement that any linear combination still produces the same profile. This can be achieved using so-called *augmented moments*, explained in Section 2.3; in particular, the augmented moments of our distributions will be separable functions of their arguments. For a given $\beta(r)$ and a corresponding set of base components, the QP technique can then be used to construct a DF that fits a given spatial density $\rho(r)$ or projected density $\Sigma(R)$. If necessary, the algorithm is run for a whole parameter range of anisotropy profiles, thus constructing a collection of models, from which those DFs are selected whose derived quantities correspond best to additional data (e.g. projected dispersions). This method eliminates both the bias in the velocity anisotropy as well as the problem with mixed data. Moreover, it provides us with a mechanism to test whether a given anisotropy profile is consistent with a set of data.

This method is only effective if we manage to construct DF components that can produce sufficiently general $\beta(r)$ profiles. On the other hand, we still want our components to be analytically tractable, for two reasons: first, all the velocity moments are integrations of the DF, so the computations should be as efficient and accurate as possible; second, it is substantially easier to gain insight in the behaviour of DFs that can be expressed as series expansions. As we show in Chapter 4, we were able to find a satisfactory compromise, by constructing a family of DF components that produce velocity anisotropy profiles of the form

$$\beta(r) = \frac{\beta_0 + \beta_\infty \left(r/r_\mathrm{a}\right)^{2\delta}}{1 + \left(r/r_\mathrm{a}\right)^{2\delta}}. \tag{1.13}$$

This four-parameter family covers a wide range of systems, with anisotropies that change monotonically from a central value to a value at large radii. In principle, we can generate even more general systems, by fitting several DFs to a given density, each for different parameters of $\beta(r)$, and summing these DFs. The individual DF components that produce these anisotropy profiles generate systems of their own, governed by Veltmann density-potential pairs (Veltmann 1979). Our effort to find suitable DF components required the use

of rather sophisticated analytical tools; as it turns out, the components can be expressed in the form of a very general family of analytic functions, called Fox H-functions (Fox 1961). These encompass the vast majority of well-known special functions (elliptic functions, gamma functions, Bessel functions or hypergeometric functions, to name a few). Since these general functions are not widely known in astrophysics, we devote a separate chapter (Chapter 3) to list some of their properties, and we demonstrate their power by deriving several expressions related to Sérsic and Einasto potential-density pairs in terms of Fox H-functions, which can be used e.g. to inspect their asymptotic behaviour.

With all the necessary tools at hand, we apply our QP-method to three case studies, presented in Chapters 5, 6 and 7. First we examine the dynamical structure of simulated dark matter haloes. Such simulations have unveiled a number of 'universal' relations independent of their scale: a similar density profile (e.g. Navarro et al. 1996; Fukushige & Makino 1997; Moore et al. 1999; Jing & Suto 2000; Navarro et al. 2004; Merritt et al. 2005), a power-law behaviour of the ratio $\rho/\sigma^3(r)$ (Taylor & Navarro 2001; Rasia et al. 2004; Ascasibar et al. 2004) and a linear relation between the density slope $\gamma(r)$ and $\beta(r)$ (Hansen & Moore 2006). Dehnen & McLaughlin (2005) derived a particular family of $\{\rho(r), \beta(r)\}$ that obey these three relations. As these $\beta(r)$ profiles are of the form (1.13), we were able to extend their work by creating a family of distribution functions that generate these profiles. In this manner, it becomes possible to gain more insight into the origin of these universal relations, in terms of an underlying orbital structure.

In the next chapter, we study a more general theoretical property of spherical systems, which has become known as the global density slope – anisotropy inequality (GDSAI); in a paper by An & Evans (2006), it was proven that the central density slope and the central velocity anisotropy always satisfy the inequality $\gamma_0 \geqslant 2\beta_0$. Subsequent work by Ciotti & Morganti (2010b) showed that this equality actually held over all radii in a large class of spherical systems, thereby posing the question whether or not the inequality would be true in *every* system. Our mathematical tools allowed us to prove that the inequality in fact does hold everywhere for systems with separable augmented moments, if $\beta_0 \leqslant 1/2$. Furthermore, using our QP-method we were able to construct models with $\beta_0 > 1/2$ that violate the GDSAI. However, the velocity distributions of these counter-examples revealed that they are dynamically unstable, which suggests that stable systems do obey the GDSAI. In our analysis, we demonstrate that the GDSAI is in fact a special case of more general necessary constraints on the augmented moments in order to obtain nonnegative DFs. We then extend this study to derive a full set of necessary and sufficient consistency conditions on separable augmented moments.

In Chapter 7, we apply our modelling technique to observational data, namely a population of dwarf galaxies in the Fornax cluster. Using a study by Mori & Burkert (2000), who calculated the minimum core mass that a dwarf galaxy must have to retain its gas when subjected to a given ram pressure, we were able to construct a set of DFs for both the early-type (gas-poor) and late-type (gas-rich) dwarf galaxies, each with a different a priori fixed velocity anisotropy profile. Our models indicate that the early-type galaxies have highly eccentric orbits, which supports the hypothesis that they originated from late-type galaxies that underwent ram-pressure stripping when they passed through the hot intracluster gas in

the central region of Fornax.

These three applications demonstrate the versatility of our modelling method in the theoretical study of gravitational systems. It is worth emphasizing though that one should be cautious not to over-analyse the DFs at the fine-grained level. Instead, they should be regarded as a guiding tool to investigate the general structure of gravitational systems.

In a final chapter, we report the results of a side project, wherein we explored the reverse route, i.e. to start with given DFs that generate Hernquist profiles with and without central super-massive black holes, and extract from these several data sets of particles by means of a Monte Carlo algorithm that was also created by the author. These data sets then serve as initial conditions of N-body simulations in order to examine the radial-orbit instability of these systems. It was found that the central black holes, if sufficiently massive, do act as stabilizers of these systems.

With the exception of Chapter 2, the results presented in each chapter has been published in peer-reviewed journals:

- For Chapter 3, see Baes & van Hese (2011) and Retana-Montenegro et al. (2012);
- For Chapter 4, see Baes & van Hese (2007);
- For Chapter 5, see Van Hese et al. (2009);
- For Chapter 6, see Van Hese et al. (2011) and An et al. (2012);
- For Chapter 7, see De Rijcke et al. (2010);
- For Chapter 8, see Buyle et al. (2007).

Chapter 2

Dynamical modelling

In this chapter, we outline the basics of our dynamical modelling procedure. We define the main properties of dynamical systems, in particular spherical equilibrium systems. We then introduce the augmented moment framework, which will play a central role in the construction of our distribution functions. These sections provide a summary of the key concepts in dynamical modelling. The last section however will form the basis for the rest of this dissertation. We discuss the quadratic programming modelling algorithm as it existed prior to this work, and we discuss the shortcomings it had and the improvements that we set out to develop and use in the subsequent chapters.

2.1 Dynamical systems: from discrete to continuous models

Let us recall the discrete equations of motion (1.2) from the introductory chapter,

$$\ddot{\boldsymbol{r}}_i = -\frac{\partial}{\partial \boldsymbol{r}_i}\left(-G\sum_{j,\,j\neq i}\frac{m_j}{|\boldsymbol{r}_i-\boldsymbol{r}_j|}\right), \qquad i=1,\ldots,N. \tag{2.1}$$

These can be written in the form of a set of Lagrangian equations

$$\frac{\mathrm{d}}{\mathrm{d}t}\left(\frac{\partial \mathscr{L}}{\partial \dot{\boldsymbol{r}}_i}\right)-\frac{\partial \mathscr{L}}{\partial \boldsymbol{r}_i}=0, \qquad i=1,\ldots,N, \tag{2.2}$$

with

$$\mathscr{L}(\boldsymbol{r}_i,\dot{\boldsymbol{r}}_i)=\sum_{i=1}^{N}\left(\frac{1}{2}m_i\dot{\boldsymbol{r}}_i^2+G\sum_{j,\,j\neq i}\frac{m_i m_j}{|\boldsymbol{r}_i-\boldsymbol{r}_j|}\right). \tag{2.3}$$

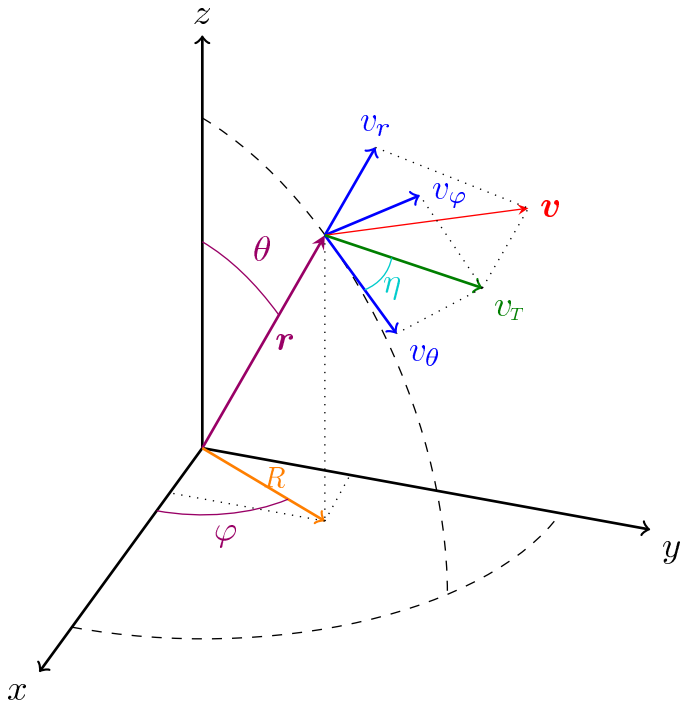

Figure 2.1 Spatial and projected coordinates for spherical systems. For observational data, we take the xy-plane as the plane of the sky, and the z-axis as the line-of-sight direction.

The transition to continuous functions can be made apparent by substituting the masses with the integrals

$$\sum_{i=1}^{N} m_i = \iiint \sum_{i=1}^{N} m_i \, \delta^3(\boldsymbol{r} - \boldsymbol{r}_i) \, \mathrm{d}^3\boldsymbol{r}. \tag{2.4}$$

In the limit $N \to \infty$, these are replaced by integrals of a density $\rho_{\mathrm{tot}}(\boldsymbol{r}, t)$, so that the Lagrangian becomes the integral of a Lagrangian density $\mathcal{L}$

$$\mathscr{L} = \iiint \rho_{\mathrm{tot}}(\boldsymbol{r}, t) \, \mathcal{L}(\boldsymbol{r}, \dot{\boldsymbol{r}}, t) \, \mathrm{d}^3\boldsymbol{r}, \tag{2.5}$$

with

$$\mathcal{L}(\boldsymbol{r}, \dot{\boldsymbol{r}}, t) = \frac{1}{2}\dot{\boldsymbol{r}}^2 + G \iiint \frac{\rho_{\mathrm{tot}}(\boldsymbol{r}', t)}{|\boldsymbol{r}' - \boldsymbol{r}|} \, \mathrm{d}^3\boldsymbol{r}'. \tag{2.6}$$

The corresponding equations of motion

$$\frac{\mathrm{d}}{\mathrm{d}t}\left(\frac{\partial \mathcal{L}}{\partial \dot{\boldsymbol{r}}}\right) - \frac{\partial \mathcal{L}}{\partial \boldsymbol{r}} = 0 \tag{2.7}$$

then lead to Eq. (1.5). As we noted in the Introduction, we can consider a subset of particles with a density $\rho(\boldsymbol{r},t)$ that doesn't necessarily generate the total gravitational potential. All the information about the positions and velocities of these particles at any given time can then be conveyed by a single phase space distribution function $F(\boldsymbol{r},\boldsymbol{v},t)$.

In the remainder of this section, we will summarize several aspects outlined in Chapter 3 & 4 of Binney & Tremaine (2008). First, we require that our particles do not change or interact (significantly) as they move through the system. This implies a conservation of probability in phase space, and just like an incompressible fluid, it is described by the continuity equation

$$\frac{\partial F}{\partial t} + \frac{\partial}{\partial \boldsymbol{r}}\left(F\dot{\boldsymbol{r}}\right) + \frac{\partial}{\partial \boldsymbol{v}}\left(F\dot{\boldsymbol{v}}\right) = 0. \tag{2.8}$$

With the aid of Hamilton's equations

$$\dot{\boldsymbol{r}} = \frac{\partial \mathcal{H}}{\partial \boldsymbol{v}}, \qquad \dot{\boldsymbol{v}} = -\frac{\partial \mathcal{H}}{\partial \boldsymbol{r}}, \tag{2.9}$$

and Eq. (1.5), it is straightforward to show that this continuity equation can be written as

$$\frac{\mathrm{d}F}{\mathrm{d}t}(\boldsymbol{r},\boldsymbol{v},t) = \frac{\partial F}{\partial t}(\boldsymbol{r},\boldsymbol{v},t) + \boldsymbol{v}\cdot\frac{\partial F}{\partial \boldsymbol{r}}(\boldsymbol{r},\boldsymbol{v},t) + \boldsymbol{\nabla}\psi(\boldsymbol{r},t)\cdot\frac{\partial F}{\partial \boldsymbol{v}}(\boldsymbol{r},\boldsymbol{v},t) = 0, \tag{2.10}$$

which is called the *collisionless Boltzmann equation*. Note also that the total time derivative is $\mathrm{d}F/\mathrm{d}t = 0$. In other words, the phase space density around a particle throughout its motion remains constant.

As mentioned in the Introduction, we will only consider *equilibrium systems*, for which the Boltzmann equation reduces to

$$\boldsymbol{v}\cdot\frac{\partial F}{\partial \boldsymbol{r}}(\boldsymbol{r},\boldsymbol{v}) + \boldsymbol{\nabla}\psi(\boldsymbol{r})\cdot\frac{\partial F}{\partial \boldsymbol{v}}(\boldsymbol{r},\boldsymbol{v}) = 0. \tag{2.11}$$

The DF will generate any observable quantity as a function $\mu(\boldsymbol{r},\boldsymbol{v})$ obtained by integrating a kernel $\bar{\mu}$ over the entire phase space, i.e.

$$\mu(\boldsymbol{r},\boldsymbol{v}) = M\int \bar{\mu}(\boldsymbol{r}',\boldsymbol{v}')\,F(\boldsymbol{r}',\boldsymbol{v}')\,\mathrm{d}^3\boldsymbol{r}'\,\mathrm{d}^3\boldsymbol{v}', \tag{2.12}$$

where M can denote the mass of the sample, or any other conversion factor (such as luminosity). In particular, the density is

$$\rho(\boldsymbol{r}) = M\iiint F(\boldsymbol{r},\boldsymbol{v})\,\mathrm{d}^3\boldsymbol{v}. \tag{2.13}$$

If the sample density represents the entire system and generates the total mass, then

$$\rho(\boldsymbol{r}) \equiv \rho_{\mathrm{tot}}(\boldsymbol{r}), \qquad M = M_{\mathrm{tot}}, \tag{2.14}$$

the model is called *self-consistent*.

Following the motion of a particle in time, its position $\boldsymbol{r}(t)$ marks out an *orbit*, with an associated velocity $\boldsymbol{v}(t)$. Any function I_i of the phase space coordinates that remains constant along all orbits is called an *integral of motion*,

$$I_i\left(\boldsymbol{r}(t),\boldsymbol{v}(t)\right) \equiv C_i. \tag{2.15}$$

The integrals themselves are clearly steady-state solutions of the collisionless Boltzmann equation, so that any function that depends on $(\boldsymbol{r},\boldsymbol{v})$ only through one or more independent integrals of motion,

$$F(\boldsymbol{r},\boldsymbol{v}) = F\left(I_1(\boldsymbol{r},\boldsymbol{v}),\ldots,I_n(\boldsymbol{r},\boldsymbol{v})\right), \tag{2.16}$$

also satisfies this equation. Indeed,

$$\frac{\mathrm{d}F}{\mathrm{d}t}(I_1,\ldots,I_n) = \boldsymbol{v}\cdot\sum_{i=1}^{n}\frac{\partial F}{\partial I_i}\frac{\partial I_i}{\partial \boldsymbol{r}}(\boldsymbol{r},\boldsymbol{v}) + \boldsymbol{\nabla}\psi(\boldsymbol{r})\cdot\sum_{i=1}^{n}\frac{\partial F}{\partial I_i}\frac{\partial I_i}{\partial \boldsymbol{v}}(\boldsymbol{r},\boldsymbol{v}) = 0, \tag{2.17}$$

and is therefore also an integral of motion. Conversely, every steady-state solution of the Boltzmann equation is itself an integral of motion, which means that any steady-state DF can be written as a function of a set of independent integrals of motion. This important property is called the *Jeans theorem*.

Furthermore, every orbit that has three independent *isolating* integrals J_1, J_2, J_3 (that is, integrals that put boundaries on the orbits in phase space) is called a *regular* orbit. We can use these integrals as Hamiltonian canonical momenta, with associated conjugate coordinates $\vartheta_1, \vartheta_2, \vartheta_3$. This six-coordinate set is called the *action-angle variables*. We find

$$\dot{J}_i = -\frac{\partial \mathcal{H}}{\partial \vartheta_i} = 0, \tag{2.18}$$

$$\dot{\vartheta}_i = \frac{\partial \mathcal{H}}{\partial J_i}, \qquad i = 1,2,3. \tag{2.19}$$

Since the Hamiltonian does not depend on ϑ_i, the latter equations imply that the $\vartheta_i(t)$ are linear functions of t, i.e. $\vartheta_i(t) = \vartheta_i(0) + C_i t$ for some constants C_i. If the orbits are bound, then the Cartesian coordinates must be periodic functions of the $\vartheta_i(t)$. Indeed, if we increase one $\vartheta_i(t)$ while keeping all other angles and actions fixed, we must eventually return to the same point in phase space where we started. We can always scale the ϑ_i such that their periods are 2π.

Under these conditions, we can prove the *strong Jeans theorem*: the DF of a steady-state stellar system in which almost all orbits are regular with non-resonant frequencies can be written as a function of only three independent isolation integrals.

Indeed, if almost all orbits are regular, then we can assume that phase space is covered by a set of action-angle variables $(\boldsymbol{\vartheta},\boldsymbol{J})$. If we write the DF in terms of these coordinates, $F(\boldsymbol{\vartheta},\boldsymbol{J})$ then any steady-state observable quantity can be expressed as

$$\langle Q\rangle = \int Q(\boldsymbol{\vartheta},\boldsymbol{J})F(\boldsymbol{\vartheta},\boldsymbol{J})\,\mathrm{d}^3\boldsymbol{\vartheta}\,\mathrm{d}^3\boldsymbol{J}. \tag{2.20}$$

From the *time averages theorem* (Binney & Tremaine 2008) it then follows that the probability $F(\boldsymbol{\vartheta}, \boldsymbol{J})\,\mathrm{d}^3\boldsymbol{\vartheta}\,\mathrm{d}^3\boldsymbol{J}$ that a particle has action-angles in $\mathrm{d}^3\boldsymbol{\vartheta}\,\mathrm{d}^3\boldsymbol{J}$ is equal to $\mathrm{d}^3\boldsymbol{\vartheta}/(2\pi)^3$ the probability that the particle has actions in $\mathrm{d}^3\boldsymbol{J}$. Therefore, the DF is independent of the angles $\boldsymbol{\vartheta}$, so that every observable quantity is a function

$$\langle Q \rangle = \int Q(\boldsymbol{\vartheta}, \boldsymbol{J}) F_J(\boldsymbol{J})\,\mathrm{d}^3\boldsymbol{\vartheta}\,\mathrm{d}^3\boldsymbol{J}, \tag{2.21}$$

where $F_J(\boldsymbol{J})$ is a DF of at most three independent isolating integrals of motion.

2.2 Spherical equilibrium systems

In our study of large structures, we will consider only spherically symmetric models. The orbits of such models have in total 4 isolating integrals (as well as one additional non-isolating integral), namely the orbital binding energy E and the angular momentum vector $\boldsymbol{L} = \boldsymbol{r} \times \boldsymbol{v}$. The conservation of the latter immediately leads to the fact that every orbit is planar, since both the position and velocity vectors are perpendicular to $\boldsymbol{L}$. Furthermore, we will limit ourselves to systems with no net rotation, so that the orbits in the system have no preferred orientation. This means that the DF can only depend on two isolating integrals, the energy E and the total angular momentum $L = |\boldsymbol{L}|$. Thus we obtain a DF of the form $F(E, L)$, with

$$E = \psi(r) - \frac{1}{2} v_r^2 - \frac{1}{2} v_T^2, \tag{2.22}$$

$$L = r v_T, \tag{2.23}$$

with

$$v_T = \sqrt{v_\theta^2 + v_\varphi^2}, \tag{2.24}$$

the transverse velocity (see Fig. 2.1), and $\psi(r)$ the positive gravitational potential; note that we defined E such that a positive value corresponds to a bounded orbit. Also note that the DF does not depend on v_θ and v_φ separately. The Poisson equation (1.4) then reduces to

$$\frac{1}{r^2} \frac{\mathrm{d}}{\mathrm{d}r} \left(r^2 \frac{\mathrm{d}\psi}{\mathrm{d}r}(r) \right) = -4\pi G \rho_{\mathrm{tot}}(r). \tag{2.25}$$

In other words, if the total mass inside a radius r of the system is given by

$$M_{\mathrm{tot}}(r) = 4\pi \int_0^r r'^2\, \rho_{\mathrm{tot}}(r')\,\mathrm{d}r', \tag{2.26}$$

we find that

$$\frac{\mathrm{d}\psi}{\mathrm{d}r}(r) = -\frac{M_{\mathrm{tot}}(r)}{r^2} \leqslant 0, \tag{2.27}$$

which means that the potential is a monotonically decreasing function of the radius, from a central value $\psi_0 = \psi(0)$, to zero at $r = +\infty$. Note that if the system extends to an infinite radius, its total mass is finite if and only if the total density falls off more steeply than $1/r^3$. Also, since $M_{\rm tot}(r)$ is a monotonically increasing function, the (negative) slope of the potential satisfies the boundaries

$$0 \leqslant -\frac{\mathrm{d}\ln\psi}{\mathrm{d}\ln r}(r) \leqslant 1, \tag{2.28}$$

and $\psi(r) \sim 1/r$ at large radii. Once a DF is known, all dynamical properties of the systems can be obtained. In the next three sections, we will derive the formulae for the orbital distributions and the velocity distributions. Examples of DFs plotted in (E, L)-space can be found in Fig. 5.5.

2.2.1 Orbits

Integral space and turning point space

Each type of orbit of a spherical system corresponds to a single pair of values (E, L). However, the converse is not generally true: not every value of the integrals corresponds to a physical orbit. Indeed, since the orbits are constrained by the isolating integrals, the motion of a particle on an orbit will be confined between two *turning point radii*, a pericentre r_- and an apocentre r_+. At these turning points, the radial velocity v_r is zero, so that

$$2r_\pm^2\big(\psi(r_\pm) - E\big) - L^2 = 0, \tag{2.29}$$

which has indeed at most two solutions if $E > 0$: the potential is a positive, monotonically decreasing function, thus the left-hand side is negative at small and large radii. It can be positive within one interval of radii, provided that L^2 is small enough. Then,

$$E = \frac{r_+^2\psi(r_+) - r_-^2\psi(r_-)}{r_+^2 - r_-^2}, \tag{2.30}$$

$$L^2 = \frac{2r_-^2 r_+^2}{r_+^2 - r_-^2}\big(\psi(r_-) - \psi(r_+)\big). \tag{2.31}$$

In other words, an orbit is also determined by the pair (r_-, r_+). A few special cases deserve our attention. Firstly, if $L = 0$, then Eq. (2.29) has only one solution, an apocentre r_+, and $v_T \equiv 0$. This means that a particle will move on a straight line, and pass through the centre, i.e. it will move on a radial orbit.

Secondly, consider the situation where L has the maximal value for which Eq. (2.29) still has a solution. In that case, the turning points will be identical, $r_- = r_+ = r_{\rm c}$, i.e. a circular orbit. The angular momentum then becomes

$$L_{\rm c}^2(r_{\rm c}) = \lim_{\substack{r_-\to r_{\rm c}\\ r_+\to r_{\rm c}}} \frac{2r_-^2 r_+^2}{r_+ + r_-}\left(-\frac{\psi(r_+) - \psi(r_-)}{r_+ - r_-}\right) = -r_{\rm c}^3\frac{\mathrm{d}\psi}{\mathrm{d}r}(r_{\rm c}), \tag{2.32}$$

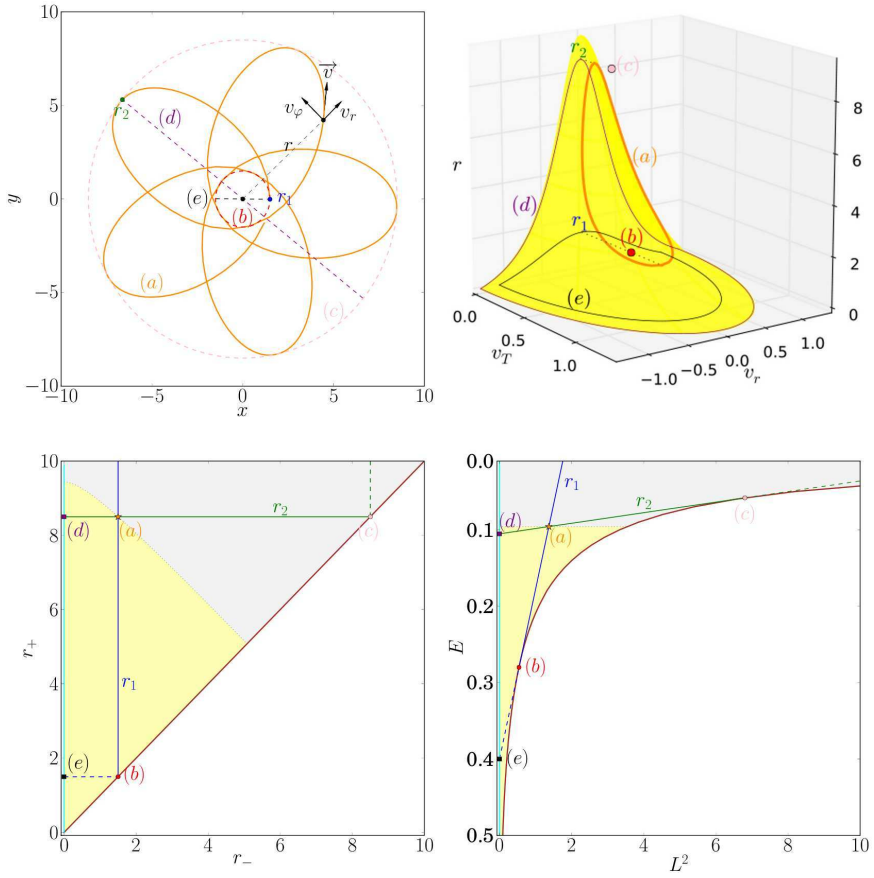

Figure 2.2 Orbits in a Herquist potential, displayed in the xy-plane (top left), the (r, v_r, v_φ) phase space (top right), the turning point space (bottom left) and the integral space (bottom right). See the text for details.

so that we can define the circular velocity v_c at radius r_c as

$$v_\mathrm{c}^2(r_\mathrm{c}) = -r_\mathrm{c}\frac{\mathrm{d}\psi}{\mathrm{d}r}(r_\mathrm{c}). \tag{2.33}$$

In this manner, the integrals of motion of a circular orbit can be expressed as

$$E_\mathrm{c} = \psi(r_\mathrm{c}) - \frac{1}{2}v_\mathrm{c}^2(r_\mathrm{c}), \tag{2.34}$$

$$L_\mathrm{c} = r_\mathrm{c}v_\mathrm{c}(r_\mathrm{c}). \tag{2.35}$$

For a given E, no orbits exist if $L > L_\mathrm{c}(E)$. In other words, the curve $L_\mathrm{c}(E)$, or equivalently $E_\mathrm{c}(L)$, marks the boundary in the integral space for physical orbits.

Finally, if $E \leqslant 0$, then the apocentre is infinite. Such unbounded orbits are not allowed in an equilibrium model, so we are constrained to $E > 0$. In fact, the easiest way to truncate a system to a finite extent $r_{\rm max}$ is to limit the DF to a cut-off energy,

$$F(E, L) \equiv 0 \qquad \text{if } E \leqslant E_0, \tag{2.36}$$

with $E_0 = \psi(r_{\rm max})$. Though one loses with this approach some tangential orbits within $r_{\rm max}$, it is a straightforward way to implement finite models. In order to alleviate notation, we implicitly assume in the remainder of this chapter that in all relevant integrations the integrands are zero for orbits with energies below a given cut-off E_0.

For any given value of E and L, the orbital motion of the particle can be readily derived (see also Section 3.1 in Binney & Tremaine 2008); without loss of generality, we can confine our orbit to the $(\theta = \pi/2)$-plane, so that

$$E = \psi(r) - \frac{1}{2}\dot{r}^2 - \frac{L^2}{2r^2}, \tag{2.37}$$

$$L = r v_\varphi = r^2 \dot{\varphi}. \tag{2.38}$$

It follows that the radial period of the orbit (i.e. the time required to travel from pericentre to apocentre and back) is

$$T_r = \int_{r_-}^{r_+} \frac{\mathrm{d}r}{\sqrt{2[\psi(r) - E] - L^2/r^2}}. \tag{2.39}$$

In this period, the azimuthal angle φ increases by an amount

$$\Delta\varphi = 2\int_{r_-}^{r_+} \frac{\mathrm{d}\varphi}{\mathrm{d}r}\,\mathrm{d}r = 2\int_{r_-}^{r_+} \frac{L}{r^2}\frac{\mathrm{d}t}{\mathrm{d}r}\,\mathrm{d}r = 2L\int_{r_-}^{r_+} \frac{\mathrm{d}r}{r^2\sqrt{2[\psi(r) - E] - L^2/r^2}}. \tag{2.40}$$

In general, the angle does not increase by some fraction of 2π after each orbital period, so that in the orbits are not closed. An example of such a rosette is given in the top left panel of Fig 2.2. Here, the orange curve (a) is a segment of the orbit of a particle with pericentre r_1 and apocentre r_2 in a Hernquist potential (see Eq. (4.101)). We also plot the circular orbits with radius r_1 (b) and r_2 (c) and the radial orbits with apocentre r_2 (d) and r_1 (e); finally, we show a tangent velocity vector $\boldsymbol{v}$ on orbit (a) and its radial and azimuthal components v_r and v_φ.

In the top right panel, the orbit (a) traces out a curve in the (r, v_r, v_φ) phase space; the yellow area indicates the locus of constant energy E associated with this orbit. The circular orbits (b) and (c) reduce to points, and the radial orbits (d) and (e) are also displayed.

In the bottom panels, the orbits (a) - (e) are represented by points in the turning point space and the integral space. The blue lines are the locus of all orbits which have r_1 as pericentre (full) or apocentre (dashed); similarly, the green lines are the locus of all orbits that have r_2 as apocentre (full) or pericentre (dashed). The locus of all radial orbits is the cyan vertical line, and the locus of all circular orbits is the brown line, which is also the boundary line of possible orbits. Finally, the light yellow area is the locus of all orbits

with E values above the energy of the orbit defined by (r_1, r_2); this area corresponds to the inside of the yellow surface in the top right panel.

Examples of DFs in turning point space can be found in Figs. 4.1, 4.2 and 5.5.

The orbital distributions

It is important to stress that $F(E, L)$ is a distribution of particles in phase space. That is, it denotes the likelihood of a particle $(\boldsymbol{r}, \boldsymbol{v})$, expressed in terms of its integrals of motion. However, it *does not* give the probability of a particular orbit with integrals (E, L). Indeed, because of spherical symmetry, phase space will consist of many orbits with the same integrals of motion. The total integrated phase space is given by

$$4\pi \int_0^{+\infty} \rho(r) r^2 \,\mathrm{d}r = 16\pi^2 \int_0^{+\infty} r^2 \,\mathrm{d}r \int_0^{\sqrt{2\psi(r)}} \mathrm{d}v_r \int_0^{\sqrt{2\psi(r)-v_r^2}} F(E, L)\, v_T \,\mathrm{d}v_T = 1, \quad (2.41)$$

where the first identity follows from Eq. (2.59) in Section 2.2.2. It is straightforward to convert the integration over the velocities into (E, L), to yield

$$16\pi^2 \int_0^{+\infty} \mathrm{d}r \int_0^{\psi(r)} \mathrm{d}E \int_0^{\sqrt{2r^2(\psi(r)-E)}} \frac{F(E, L)\, L}{\sqrt{2(\psi(r) - E) - L^2/r^2}} \,\mathrm{d}L = 1. \quad (2.42)$$

Now, if we change the order of integration, we find

$$\int_0^{\psi_0} \mathrm{d}E \int_0^{L_\mathrm{c}(E)} N(E, L) \,\mathrm{d}L = 1, \quad (2.43)$$

with $\psi_0 = \psi(0)$ the central potential (which can be infinite, when the system has a central black hole), and

$$N(E, L) = F(E, L)\, G(E, L), \quad (2.44)$$

where $N(E, L)$ is the *orbital distribution function*, and $G(E, L)$ denotes the 'density of states', i.e. the orbital density,

$$G(E, L) = 16\pi^2 L \int_{r_-(E,L)}^{r_+(E,L)} \frac{\mathrm{d}r}{\sqrt{2(\psi(r) - E) - L^2/r^2}}. \quad (2.45)$$

Examples of these orbital distributions can be found in Fig. 5.6. Integrating over L or E, we obtain respectively the *energy and angular momentum distributions*

$$N(E) = \int_0^{L_\mathrm{c}(E)} N(E, L) \,\mathrm{d}L = 4\pi \int_0^{+\infty} F_E(r, E)\, r^2 \,\mathrm{d}r, \quad (2.46)$$

$$N(L) = \int_0^{E_\mathrm{c}(L)} N(E, L) \,\mathrm{d}E = 4\pi \int_0^{+\infty} F_L(r, L)\, r^2 \,\mathrm{d}r, \quad (2.47)$$

with

$$F_E(r,E) = 2\pi \int_0^{2(\psi(r)-E)} \frac{F(E, r v_T)\,\mathrm{d}v_T^2}{\sqrt{2(\psi(r)-E)-v_T^2}}, \tag{2.48}$$

$$F_L(r,L) = \frac{4\pi}{r^2} \int_0^{\psi(r)-L^2/2r^2} \frac{F(E,L)\,L\,\mathrm{d}E}{\sqrt{2(\psi(r)-E)-L^2/r^2}}. \tag{2.49}$$

$F_E(r,E)$ essentially gives the probability that a given particle at radius r lies on an orbit with energy E; the meaning of $F_L(r,L)$ is analogous. See Figs. 5.4 and 5.8 for examples.

It is also possible to derive the orbital distributions in the turning point space (i.e. the probability density of orbits with a given peri- and apocentre), by changing in Eq. (2.42) the integration variables $\mathrm{d}E\,\mathrm{d}L$ into $\mathrm{d}r_-\,\mathrm{d}r_+$ and using the conversions (2.30) - (2.31). After some algebra, we obtain

$$N(r_-,r_+) = F(r_-,r_+)\,G(r_-,r_+), \tag{2.50}$$

with

$$G(r_-,r_+) = \frac{2r_-^2 r_+^2}{(r_+^2-r_-^2)^3} 16\pi^2 \int_{r_-}^{r_+} \frac{\mathrm{d}r}{\sqrt{2(\psi(r)-E)-L^2/r^2}} \times \\ \left|(r_+^2-r_-^2)r_+\psi'(r_+) + 2r_-^2\left(\psi(r_-)-\psi(r_+)\right)\right| \times \\ \left|(r_+^2-r_-^2)r_-\psi'(r_-) + 2r_+^2\left(\psi(r_-)-\psi(r_+)\right)\right|. \tag{2.51}$$

Examples of these distributions can be seen in Fig. 5.6.

2.2.2 Spatial velocity moments

While the orbital distributions offer us insight into the orbital structure of a system, our input data is usually in the form of positions and velocities. Ideally, we know (or postulate) some of the so-called *true (spatial) velocity moments*

$$\mu_{l,m,n}(r) = M \int_{-\infty}^{+\infty} \mathrm{d}v_r \int_{-\infty}^{+\infty} \mathrm{d}v_\theta \int_{-\infty}^{+\infty} F(E,L)\, v_r^l v_\theta^m v_\varphi^n\, \mathrm{d}v_\varphi, \tag{2.52}$$

with E and L expressed in terms of (2.22). The DF of a non-rotational spherical system is an even function of v_r, v_θ and v_φ, i.e. there is no net flow in any direction. Consequently, any moments with odd values of l, m, or n will be zero. The even lowest-order moments however are of particular significance: the spatial density is simply

$$\rho(r) = \mu_{000}(r) = M \iiint F(E,L)\,\mathrm{d}v_r\,\mathrm{d}v_\theta\,\mathrm{d}v_\varphi, \tag{2.53}$$

while the second-order velocity moments are

$$\rho(r)\sigma_r^2(r) = \mu_{200}(r) = M \iiint F(E,L)\, v_r^2 \,\mathrm{d}v_r\,\mathrm{d}v_\theta\,\mathrm{d}v_\varphi, \tag{2.54}$$

$$\rho(r)\sigma_\theta^2(r) = \mu_{020}(r) = M \iiint F(E,L)\, v_\theta^2 \,\mathrm{d}v_r\,\mathrm{d}v_\theta\,\mathrm{d}v_\varphi, \tag{2.55}$$

$$\rho(r)\sigma_\varphi^2(r) = \mu_{002}(r) = M \iiint F(E,L)\, v_\varphi^2 \,\mathrm{d}v_r\,\mathrm{d}v_\theta\,\mathrm{d}v_\varphi. \tag{2.56}$$

Evidently, the velocity dispersions σ_r, σ_θ, and σ_φ are the root-mean-squares of the radial and angular velocities, $\langle v_r^2\rangle^{1/2}$, $\langle v_\theta^2\rangle^{1/2}$, and $\langle v_\varphi^2\rangle^{1/2}$ respectively. These definitions are the continuous equivalent of the discrete quantities (1.10) from the introductory chapter.

It follows immediately that $\rho(r)\sigma_\theta^2(r) = \rho(r)\sigma_\varphi^2(r)$, and we can combine them into a transverse second-order velocity moment

$$\rho(r)\sigma_T^2(r) = \mu_{020}(r) + \mu_{002}(r) = M \int_{-\infty}^{+\infty} \mathrm{d}v_r \int_{-\infty}^{+\infty} \mathrm{d}v_\theta \int_{-\infty}^{+\infty} F(E,L)\, v_T^2 \,\mathrm{d}v_\varphi. \tag{2.57}$$

We can generalize this notion by writing the angular velocities in polar coordinates (see Fig. 2.1)

$$v_\theta = v_T \cos\eta, \qquad v_\varphi = v_T \sin\eta, \tag{2.58}$$

so that $\mathrm{d}v_\theta\,\mathrm{d}v_\varphi = v_T\,\mathrm{d}v_T\,\mathrm{d}\eta$, which allows us to introduce the so-called *anisotropic velocity moments*

$$\mu_{2n,2m}(r) = 4\pi M \int_0^{\sqrt{2\psi(r)}} \mathrm{d}v_r \int_0^{\sqrt{2\psi(r)-v_r^2}} F(E,L)\, v_r^{2n}\, v_T^{2m+1} \,\mathrm{d}v_T. \tag{2.59}$$

From these, one can easily recover the true velocity moments

$$\mu_{l,m,n}(r) = \frac{1}{\pi} B\left(m+\frac{1}{2}, n+\frac{1}{2}\right) \mu_{2l,2(m+n)}(r), \tag{2.60}$$

with

$$B(x,y) = \int_0^1 t^{x-1}(1-t)^{y-1}\,\mathrm{d}t = 2\int_0^{\pi/2} (\sin\eta)^{2x-1}(\cos\eta)^{2y-1}\,\mathrm{d}\eta, \tag{2.61}$$

the beta function. Also,

$$\rho(r) = \mu_{00}(r), \qquad \rho\sigma_r^2(r) = \mu_{20}(r), \qquad \rho\sigma_T^2(r) = 2\rho\sigma_\theta^2 = 2\rho\sigma_\varphi^2 = \mu_{02}(r). \tag{2.62}$$

In the Introduction, we defined in Eq. (1.11) a very useful shorthand known as Binney's velocity anisotropy profile, which we can also write in the form

$$\beta(r) = 1 - \frac{\sigma_T^2}{2\sigma_r^2}(r), \tag{2.63}$$

which is an indicator of whether the system contains predominantly radial orbits ($\beta(r) > 0$) or more circular orbits ($\beta(r) < 0$) at a given radius. Examples can be found in Figs. 4.1, 4.2, 5.3, 6.1 and 7.5.

Finally, we can see that the functions $\mu_{2n,0}(r)$ and $\mu_{0,2m}(r)$ are the moments of two velocity distributions, the *radial and transverse velocity distributions*, obtained by integrating the DF over one velocity component:

$$F_{v_r}(r, v_r) = 2\pi \int_0^{\sqrt{2\psi(r)-v_r^2}} F(E, L)\, v_T \, \mathrm{d}v_T, \tag{2.64}$$

$$F_{v_T}(r, v_T) = 4\pi v_T \int_0^{\sqrt{2\psi(r)-v_T^2}} F(E, L)\, \mathrm{d}v_r. \tag{2.65}$$

Evidently, their integrals are just the density

$$\rho(r) = M \int_{-\sqrt{2\psi(r)}}^{\sqrt{2\psi(r)}} F_{v_r}(r, v_r)\, \mathrm{d}v_r = M \int_0^{\sqrt{2\psi(r)}} F_{v_T}(r, v_T)\, \mathrm{d}v_T. \tag{2.66}$$

We can also derive the velocity distributions in v_θ or v_φ. These require an additional integration:

$$F_{v_\theta}(r, v_\theta) = 4 \int_0^{\sqrt{2\psi(r)-v_\theta^2}} \mathrm{d}v_\varphi \int_0^{\sqrt{2\psi(r)-v_T^2}} F(E, L)\, \mathrm{d}v_r \tag{2.67}$$

$$= \frac{1}{\pi} \int_0^{\sqrt{2\psi(r)-v_\theta^2}} \frac{1}{\sqrt{v_\theta^2 + v_\varphi^2}} F_{v_T}\left(r, \sqrt{v_\theta^2 + v_\varphi^2}\right) \mathrm{d}v_\varphi, \tag{2.68}$$

and $F_{v_\varphi}(r, v_\varphi)$ has exactly the same form. For examples, see Figs. 5.4 and 6.1.

2.2.3 Projected velocity moments

The spatial velocity distributions give us important information about the intrinsic velocity structure of the system, but unfortunately we often have much less data at our disposal. Observationally, such as for clusters of galaxies, we only have information of positions on the celestial sphere and line-of-sight velocities through redshift data. With these, we can attempt to construct some of the *projected velocity moments* as a starting point to find a suitable DF.

The *projected density* is related to the spherical density through an Abel integration,

$$\Sigma(R) = 2 \int_R^{+\infty} \rho\left(\sqrt{R^2 + z^2}\right) \mathrm{d}z = 2 \int_R^{+\infty} \frac{\rho(r)\, r}{\sqrt{r^2 - R^2}} \, \mathrm{d}r. \tag{2.69}$$

This relation can in fact be inverted, so that the spatial density can be directly derived from the projected density; we find

$$\rho(r) = -\frac{1}{\pi}\int_R^\infty \frac{\mathrm{d}\Sigma}{\mathrm{d}R}\frac{\mathrm{d}R}{\sqrt{R^2-r^2}}. \tag{2.70}$$

To obtain the second-order line-of-sight velocity moment, we start with the spatial function

$$\rho\sigma_{\rm los}^2(r) = \iiint F(E,L)\, v_z^2\, \mathrm{d}v_r\, \mathrm{d}v_\theta\, \mathrm{d}v_\varphi. \tag{2.71}$$

It can be easily seen that the projected velocity is given by

$$v_z = v_r\cos\theta - v_\theta\sin\theta. \tag{2.72}$$

Consequently,

$$\rho\sigma_{\rm los}^2(r) = \iiint F(E,L)\,\left(v_r^2(r)\,\cos^2\theta + v_\theta^2(r)\,\sin^2\theta\right)\mathrm{d}v_r\,\mathrm{d}v_\theta\,\mathrm{d}v_\varphi \tag{2.73}$$

$$= \rho\sigma_r^2(r)\,\cos^2\theta + \rho\sigma_\theta^2(r)\,\sin^2\theta, \tag{2.74}$$

where we used the fact that $\mu_{1,1,0}(r)\equiv 0$. Examples are given in Figs. 4.1, 4.2 and 7.4. With an additional Abel integration, we then obtain the projected line-of-sight velocity dispersion $\sigma_{\rm los}^2(R)$ as

$$\Sigma\sigma_{\rm los}^2(R) = 2\int_R^{+\infty}\left(\sigma_r^2(r)\,\cos^2\theta + \sigma_\theta^2(r)\,\sin^2\theta\right)\frac{\rho(r)\,r}{\sqrt{r^2-R^2}}\,\mathrm{d}r \tag{2.75}$$

$$= 2\int_R^{+\infty}\left(1-\beta(r)\frac{R^2}{r^2}\right)\frac{\rho\sigma_r^2(r)\,r}{\sqrt{r^2-R^2}}\,\mathrm{d}r. \tag{2.76}$$

Note that the line-of-sight dispersion depends on both spatial second-order moments. In principle, one can define higher-order moments in a similar way, but these are usually not well constrained by the data. There are however instances, using a maximum-likelihood estimator, where it is possible to get some information about the full *line-of-sight velocity distribution*

$$F_{\rm los}(R,v_z) = \iiint F(E,L)\,\mathrm{d}v_x\,\mathrm{d}v_y\,\mathrm{d}z. \tag{2.77}$$

An example of such a LOSVD is given in Fig. 7.6.

The central question is to seek an appropriate DF that can generate a given data set of quantities, within a gravitational potential. In the remainder of this chapter, we will develop the necessary tools to tackle this task. First, we introduce a powerful framework that will alleviate the problem substantially, namely the augmented moments. This approach was first introduced by pioneering work from Lynden-Bell (1962), and further developed by various authors (Hunter 1975; Nagai & Miyamoto 1976; Lake 1981;Dejonghe & de Zeeuw 1988; Evans et al. 1990; Hunter & Qian 1993). The most extensive treatment however was presented in Dejonghe (1986), and this study will be our main guide in the next section; we will follow a similar line of reasoning to arrive at Eq. (2.91), while the rest of the section is based on our own derivation.

2.3 The augmented moment concept

An *augmented anisotropic velocity moment* $\tilde{\mu}_{2n,2m}(\psi,r)$ is an extension of a velocity moment into a bivariate function, by treating the potential explicitly as an independent variable. The corresponding velocity moment is then simply

$$\mu_{2n,2m}(r) = \tilde{\mu}_{2n,2m}\left(\psi(r),r\right). \tag{2.78}$$

The advantage of this concept is threefold: first, we shall see that a dynamical system is completely determined by a single augmented moment, so that it can be used as an alternative to the DF. Moreover, the augmented moments can be much easier related to given data, which will enable us to impose specific properties obtained from observations. And finally, by making the potential a free variable, the functions we will derive remain the same regardless of the gravitational potential, so they can be re-used for different forms of $\psi(r)$. However, this does *not* mean that we can ignore the corresponding DFs altogether: a dynamical system is only physical if its DF is nonnegative everywhere, so this condition still needs to be checked. One can formulate equivalent consistency conditions for the augmented moments, but these are much more complicated; we explore these in Section 6.4, for systems with separable augmented moments.

Our analysis will be split in two; we will start with the general case, and then simplify the situation further.

2.3.1 General spherical systems

The distribution function

The relation between an augmented velocity moment and the DF follows directly from Eq. (2.59):

$$\tilde{\mu}_{2n,2m}(\psi,r) = 4\pi M \int_0^{\sqrt{2\psi}} \mathrm{d}v_r \int_0^{\sqrt{2\psi-v_r^2}} F(E,L)\, v_r^{2n}\, v_T^{2m+1}\, \mathrm{d}v_T \tag{2.79}$$

$$= 2\pi M \int_0^{\psi} \mathrm{d}E \int_0^{2(\psi-E)} F(E, rv_T)\left(2(\psi-E)-v_T^2\right)^{n-1/2} v_T^{2m}\, \mathrm{d}v_T^2. \tag{2.80}$$

Since both $\tilde{\mu}_{2n,2m}$ and the DF are functions of two independent variables, it is intuitively clear that they provide equivalent descriptions of a dynamical system. For a given potential $\psi(r)$, a boundary radius $r_{\max}$ and the general cut-off at $E_0 = \psi(r_{\max})$ in mind as defined in Eq. (2.36), we impose the following constraints on the augmented moments:

- The moments $\tilde{\mu}_{2n,2m}(\psi,r)$ are defined for $0 < r \leqslant r_{\max}$ and, for a given r, $E_0 \leqslant \psi \leqslant \psi(r)$;
- Within the above intervals, the $\tilde{\mu}_{2n,2m}(\psi,r)$ are C_∞ differentiable with respect to ψ and r;

- At and outside of the ψ-boundary,

$$\frac{\partial^{m+n}\tilde{\mu}_{2n,2m}}{\partial\psi^{m+n}}(\psi,r)\equiv 0 \qquad \text{for } \psi\leqslant E_0. \tag{2.81}$$

The last equation can be understood from Eq. (2.79), where v_r^2 and v_T^2 both depend on ψ.

There are several methods to derive the DF from a given augmented moment, all of them involving integral transformations; Lynden-Bell (1962) used two Laplace transforms, while Hunter (1975) adopted a Stieltjes transform, which requires an analytic continuation of the density into the complex plane. A third and particularly powerful technique consists a combination of a Laplace and a Mellin transform (Dejonghe 1986); for a general function of two variables $f(x,y)$, its Laplace-Mellin transform is given by

$$\mathcal{F}(\xi,\lambda)=\underset{x\to\xi}{\mathcal{L}}\,\underset{y\to\lambda}{\mathcal{M}}\{f(x,y)\}=\int_0^{+\infty}\int_0^{+\infty}\mathrm{e}^{-\xi x}\,y^{\lambda-1}\,f(x,y)\,\mathrm{d}x\,\mathrm{d}y. \tag{2.82}$$

Wherever we perform this transform, we will postulate that the function in question is zero outside its boundaries. The inverse transform can, at least formally, be written as a complex double integral,

$$f(x,y)=\underset{\xi\to x}{\mathcal{L}^{-1}}\,\underset{\lambda\to y}{\mathcal{M}^{-1}}\{\mathcal{F}(\xi,\lambda)\}=-\frac{1}{4\pi^2}\int_{\xi_0-i\infty}^{\xi_0+i\infty}\int_{\lambda_0-i\infty}^{\lambda_0+i\infty}\mathrm{e}^{\xi x}\,y^{-\lambda}\,\mathcal{F}(\xi,\lambda)\,\mathrm{d}\xi\,\mathrm{d}\lambda, \tag{2.83}$$

where the integrations are to be performed along paths parallel to the vertical axis, with offsets given by the real constants ξ_0 and λ_0, chosen such that they lie within a convergence strip in the complex plane that depends on the functional form of $\mathcal{F}(\xi,\lambda)$. Applied to the DF and the augmented moments, we have

$$\underset{E\to\xi}{\mathcal{L}}\,\underset{L\to\lambda}{\mathcal{M}}\{F(E,L)\}=\int_0^{+\infty}\mathrm{e}^{-\xi E}\,\mathrm{d}E\int_0^{+\infty}L^{\lambda-1}\,F(E,L)\,\mathrm{d}L, \tag{2.84}$$

$$\underset{\psi\to\xi}{\mathcal{L}}\,\underset{r\to\lambda}{\mathcal{M}}\{\tilde{\mu}_{2n,2m}(\psi,r)\}=\int_0^{+\infty}\mathrm{e}^{-\xi\psi}\,\mathrm{d}\psi\int_0^{+\infty}r^{\lambda-1}\,\tilde{\mu}_{2n,2m}(\psi,r)\,\mathrm{d}r. \tag{2.85}$$

Eq. (2.79) thus becomes

$$\begin{aligned}\underset{\psi\to\xi}{\mathcal{L}}\,\underset{r\to\lambda}{\mathcal{M}}\{\tilde{\mu}_{2n,2m}\}=4\pi M&\int_0^{+\infty}\mathrm{e}^{-\xi\psi}\,\mathrm{d}\psi\int_0^{+\infty}r^{\lambda-1}\,\mathrm{d}r\\ &\int_0^{+\infty}\mathrm{d}v_r\int_0^{+\infty}F(E,L)\,v_r^{2n}\,v_T^{2m+1}\,\mathrm{d}v_T.\end{aligned} \tag{2.86}$$

Rearranging the integrations, this can be written as

$$\begin{aligned}\underset{\psi\to\xi}{\mathcal{L}}\,\underset{r\to\lambda}{\mathcal{M}}\{\tilde{\mu}_{2n,2m}\}=4\pi M&\int_0^{+\infty}v_r^{2n}\,\mathrm{e}^{-\xi v_r^2/2}\,\mathrm{d}v_r\int_0^{+\infty}v_T^{2m+1-\lambda}\,\mathrm{e}^{-\xi v_T^2/2}\,\mathrm{d}v_T\\ &\int_0^{+\infty}\mathrm{e}^{-\xi E}\,\mathrm{d}E\int_0^{+\infty}L^{\lambda-1}\,F(E,L)\,\mathrm{d}L,\end{aligned} \tag{2.87}$$

and with the aid of the formula

$$\int_0^{+\infty} x^p \, \mathrm{e}^{-qx^2} \, \mathrm{d}x = \frac{1}{2}\Gamma\left(\frac{1+p}{2}\right) q^{-(1+p)/2} \qquad p > -1,\ q \geqslant 0, \tag{2.88}$$

the relation between both functions takes the form

$$\underset{E\to\xi}{\mathcal{L}} \underset{L\to\lambda}{\mathcal{M}} \{F\} = \frac{(\xi/2)^{m+n+(3-\lambda)/2}}{M\pi\Gamma(m+1-\lambda/2)\Gamma(n+1/2)} \underset{\psi\to\xi}{\mathcal{L}} \underset{r\to\lambda}{\mathcal{M}} \{\tilde{\mu}_{2n,2m}\}, \tag{2.89}$$

provided that $\Re\{\xi\} \geqslant 0$ and $\Re\{\lambda\} < 2(m+1)$. Naturally, the most useful of all augmented moments is the *augmented density*

$$\tilde{\rho}(\psi,r) = 2\pi M \int_0^{\psi} \mathrm{d}E \int_0^{2(\psi-E)} \frac{F(E, r v_T)}{\sqrt{2(\psi-E)-v_T^2}} \, \mathrm{d}v_T^2, \tag{2.90}$$

in which case Eq. (2.89) reduces to

$$\underset{E\to\xi}{\mathcal{L}} \underset{L\to\lambda}{\mathcal{M}} \{F(E,L)\} = \frac{(\xi/2)^{(3-\lambda)/2}}{M\pi^{3/2}\Gamma(1-\lambda/2)} \underset{\psi\to\xi}{\mathcal{L}} \underset{r\to\lambda}{\mathcal{M}} \{\tilde{\rho}(\psi,r)\}. \tag{2.91}$$

Before we analyse this relation further, we will delve deeper into the connection between the augmented moments.

The augmented velocity moments

Eliminating the DF from Eqs. (2.89) and (2.91), it follows that

$$\underset{\psi\to\xi}{\mathcal{L}} \underset{r\to\lambda}{\mathcal{M}} \{\tilde{\mu}_{2n,2m}\} = \frac{\Gamma(n+1/2)}{\sqrt{\pi}} \frac{\Gamma(m+1-\lambda/2)}{\Gamma(1-\lambda/2)} \left(\frac{2}{\xi}\right)^{m+n} \underset{\psi\to\xi}{\mathcal{L}} \underset{r\to\lambda}{\mathcal{M}} \{\tilde{\rho}\}. \tag{2.92}$$

By solving this equation, we can derive any augmented moment from the augmented density. Given that the augmented moments are only defined in the intervals $]0, r_{\max}]$ and $[E_0, \psi(r)]$, we need the Heaviside step function

$$H(x-a) = \begin{cases} 0 & \text{if } x < a, \\ 1 & \text{if } x \geqslant a, \end{cases} \tag{2.93}$$

to facilitate the calculations. First we write the Mellin transform of $\tilde{\rho}(\psi,r)$ as follows

$$\underset{r\to\lambda}{\mathcal{M}} \{\tilde{\rho}(\psi,r)\} = \int_0^{+\infty} r^{\lambda-1} \, \tilde{\rho}(\psi,r) \, \mathrm{d}r \tag{2.94}$$

$$= \frac{1}{2} \int_0^{+\infty} r^{2(\lambda/2-1-m)} \left(r^{2m} \tilde{\rho}(\psi,r)\right) \mathrm{d}r^2. \tag{2.95}$$

Integrating by parts, and with the upper boundary for r in mind, this becomes

$$\underset{r\to\lambda}{\mathcal{M}}\left\{\tilde{\rho}(\psi,r)\right\} = \frac{1/2}{\lambda/2-m}\left[r_{\max}^{\lambda}\,\tilde{\rho}(\psi,r_{\max}) - \int_0^{+\infty} r^{2(\lambda/2-m)}\,\partial_{r^2}\left(r^{2m}\tilde{\rho}\right)\mathrm{d}r^2\right], \quad (2.96)$$

where we used the shorthand notation ∂_x for the partial derivative with respect to x. The first term can be written as

$$\frac{r_{\max}^{\lambda}}{\lambda-2m}\,\tilde{\rho}(\psi,r_{\max}) = r_{\max}^{2m}\,\tilde{\rho}(\psi,r_{\max})\,\underset{r\to\lambda}{\mathcal{M}}\left\{r^{-2m}H(r-r_{\max})\right\}, \quad (2.97)$$

since $\Re\{\lambda\} < 2(m+1)$. Thus, if we limit ourselves to the region $0 < r < r_{\max}$, we can ignore this term. In this manner, we obtain after m integrations by parts

$$\underset{r\to\lambda}{\mathcal{M}}\left\{\tilde{\rho}(\psi,r)\right\} = \frac{1/2}{(m-\lambda/2)\cdots(1-\lambda/2)}\int_0^{+\infty} r^{2(\lambda/2-1)}\,\partial_{r^2}^{m}\left(r^{2m}\tilde{\rho}(\psi,r)\right)\mathrm{d}r^2 \quad (2.98)$$

$$= \frac{\Gamma(1-\lambda/2)}{\Gamma(m+1-\lambda/2)}\,\underset{r\to\lambda}{\mathcal{M}}\left\{\partial_{r^2}^{m}\left(r^{2m}\tilde{\rho}(\psi,r)\right)\right\}. \quad (2.99)$$

The above trick eliminates the Mellin transforms from Eq. (2.92), leaving only the Laplace transforms,

$$\underset{\psi\to\xi}{\mathcal{L}}\left\{\tilde{\mu}_{2n,2m}\right\} = \frac{\Gamma(n+1/2)}{\sqrt{\pi}}\left(\frac{2}{\xi}\right)^{m+n}\underset{\psi\to\xi}{\mathcal{L}}\left\{\partial_{r^2}^{m}\left(r^{2m}\tilde{\rho}\right)\right\}. \quad (2.100)$$

We can tackle the Laplace transform of $\tilde{\mu}_{2n,2m}(\psi,r)$ in a similar way. Recalling that the ψ-dependent parts of the augmented moments are defined in the interval $[E_0,\psi(r)]$, we find

$$\underset{\psi\to\xi}{\mathcal{L}}\left\{\tilde{\mu}_{2n,2m}\right\} = \int_0^{+\infty}\mathrm{e}^{-\xi\psi}\,\tilde{\mu}_{2n,2m}(\psi,r)\,\mathrm{d}\psi \quad (2.101)$$

$$= \left[-\frac{1}{\xi}\,\mathrm{e}^{-\xi\psi}\,\tilde{\mu}_{2n,2m}(\psi,r)\right]_{E_0}^{\psi(r)} + \frac{1}{\xi}\int_0^{+\infty}\mathrm{e}^{-\xi\psi}\,\partial_{\psi}\left(\tilde{\mu}_{2n,2m}\right)\mathrm{d}\psi. \quad (2.102)$$

The first part reduces to

$$-\frac{1}{\xi}\tilde{\mu}_{2n,2m}(\psi(r),r)\,\mathrm{e}^{-\xi\psi(r)} = -\tilde{\mu}_{2n,2m}(\psi(r),r)\,\underset{\psi\to\xi}{\mathcal{L}}\left\{H(\psi-\psi(r))\right\} \quad (2.103)$$

where we used the conditions (2.81). So once again, if we only consider the region $\psi < \psi(r)$, this term can be omitted. Repeating the above procedure up to $m+n$ integrations by parts, we find

$$\underset{\psi\to\xi}{\mathcal{L}}\left\{\tilde{\mu}_{2n,2m}\right\} = \frac{1}{\xi^{m+n}}\,\underset{\psi\to\xi}{\mathcal{L}}\left\{\partial_{\psi}^{m+n}\left(\tilde{\mu}_{2n,2m}(\psi,r)\right)\right\}, \quad (2.104)$$

and Eq. (2.100) reduces to the elegant relation

$$\partial_\psi^{m+n}\left(\tilde{\mu}_{2n,2m}(\psi,r)\right) = \frac{2^{m+n}}{\sqrt{\pi}}\Gamma(n+1/2)\,\partial_{r^2}^m\left(r^{2m}\tilde{\rho}(\psi,r)\right). \tag{2.105}$$

Assuming that these functions are continuous, the relation is also valid at the boundaries $r = r_{\max}$ and $\psi = \psi(r)$ (and at the origin $r = 0$, if the functions are finite there). Finally, after $m+n$ integrations, we find

$$\tilde{\mu}_{2n,2m}(\psi,r) = \frac{2^{m+n}}{\sqrt{\pi}}\frac{\Gamma(n+1/2)}{\Gamma(m+n)}\int_0^\psi (\psi-\psi')^{m+n-1}\,\partial_{r^2}^m\left(r^{2m}\tilde{\rho}(\psi',r)\right)\mathrm{d}\psi'. \tag{2.106}$$

Using an additional integration by parts, we can write this equation in the alternative form

$$\tilde{\mu}_{2n,2m}(\psi,r) = \frac{(1/2)_n}{(m+n)!}\int_0^\psi \left(2(\psi-\psi')\right)^{m+n}\partial_{r^2}^m\left(r^{2m}\,\partial_{\psi'}(\tilde{\rho})\right)\mathrm{d}\psi', \tag{2.107}$$

where we also introduced the Pochhammer symbol for the rising factorial,

$$(x)_k = x(x+1)\cdots(x+k-1) = \prod_{i=1}^{k}(x+i-1) = \frac{\Gamma(x+k)}{\Gamma(x)}. \tag{2.108}$$

Relation between the velocity moments

We can show from Eq. (2.105) that the velocity moments of a dynamical system are not independent. We have

$$\partial_\psi^{m+n}\left(\tilde{\mu}_{2n,2m}\right) = \frac{2^{m+n}}{\sqrt{\pi}}\Gamma(n+1/2)\,\partial_{r^2}^m\left(r^2\,r^{2(m-1)}\tilde{\rho}\right) \tag{2.109}$$

$$= \frac{2^{m+n}}{\sqrt{\pi}}\Gamma(n+1/2)\sum_{i=0}^{m}\binom{m}{i}\partial_{r^2}^i\left(r^2\right)\partial_{r^2}^{m-i}\left(r^{2(m-1)}\tilde{\rho}\right) \tag{2.110}$$

$$= \frac{2^{m+n}}{\sqrt{\pi}}\Gamma(n+1/2)\left[r^2\,\partial_{r^2}^m\left(r^{2(m-1)}\tilde{\rho}\right) + m\,\partial_{r^2}^{m-1}\left(r^{2(m-1)}\tilde{\rho}\right)\right] \tag{2.111}$$

$$= \frac{2^{m+n}}{2^{m+n-1}}\left[\partial_\psi^{m+n-1}\left(r^2\,\partial_{r^2}\left(\tilde{\mu}_{2n,2(m-1)}\right) + m\,\tilde{\mu}_{2n,2(m-1)}\right)\right]. \tag{2.112}$$

Furthermore,

$$\partial_\psi^{m+n}\left(\tilde{\mu}_{2n,2m}\right) = \frac{2^{m+n}}{2^{m+n-1}}\frac{\Gamma(n+1/2)}{\Gamma(n-1/2)}\,\partial_\psi^{m+n-1}\left(\tilde{\mu}_{2(n-1),2m}\right). \tag{2.113}$$

Both equations can be simplified and combined into

$$\partial_\psi\left(\tilde{\mu}_{2n,2m}(\psi,r)\right) = 2m\,\tilde{\mu}_{2n,2(m-1)}(\psi,r) + r\,\partial_r\left(\tilde{\mu}_{2n,2(m-1)}(\psi,r)\right) \tag{2.114}$$

$$= (2n-1)\,\tilde{\mu}_{2(n-1),2m}(\psi,r). \tag{2.115}$$

Within a potential $\psi(r)$, the derivative of a velocity moment is given by

$$\frac{\mathrm{d}\mu_{2n,2m}}{\mathrm{d}r}(r) = \frac{\partial\tilde{\mu}_{2n,2m}}{\partial r}(\psi(r),r) + \frac{\partial\tilde{\mu}_{2n,2m}}{\partial\psi}(\psi(r),r)\,\frac{\mathrm{d}\psi}{\mathrm{d}r}(r), \tag{2.116}$$

so that we obtain the *general Jeans equations*

$$\begin{aligned} r\frac{\mathrm{d}}{\mathrm{d}r}\mu_{2n,2(m-1)}(r) &= (2n-1)\,\mu_{2(n-1),2m}(r) - 2m\,\mu_{2n,2(m-1)}(r) \\ &\quad + (2n-1)\,r\,\mu_{2(n-1),2(m-1)}(r)\,\frac{\mathrm{d}\psi}{\mathrm{d}r}(r). \end{aligned} \tag{2.117}$$

These equations are a direct consequence of the collisionless Boltzmann equation. The best-known of them is the case $m = n = 1$, which connects the density and the velocity dispersions.

The augmented dispersions; the Jeans equation

The augmented dispersions are derived from Eq. (2.106),

$$\tilde{\sigma}_r^2(\psi,r) = \frac{\tilde{\mu}_{20}(\psi,r)}{\tilde{\mu}_{00}(\psi,r)} = \frac{1}{\tilde{\rho}(\psi,r)}\int_0^\psi \tilde{\rho}(\psi',r)\,\mathrm{d}\psi', \tag{2.118}$$

$$\tilde{\sigma}_T^2(\psi,r) = \frac{\tilde{\mu}_{02}(\psi,r)}{\tilde{\mu}_{00}(\psi,r)} = \frac{2}{\tilde{\rho}(\psi,r)}\int_0^\psi \partial_{r^2}\left(r^2\,\tilde{\rho}(\psi',r)\right)\mathrm{d}\psi', \tag{2.119}$$

$$2\tilde{\beta}(\psi,r) = 2 - \frac{\tilde{\sigma}_T^2(\psi,r)}{\tilde{\sigma}_r^2(\psi,r)} = -r\frac{\int_0^\psi \partial_r\left(\tilde{\rho}(\psi',r)\right)\mathrm{d}\psi'}{\int_0^\psi \tilde{\rho}(\psi',r)\,\mathrm{d}\psi'}, \tag{2.120}$$

where $\tilde{\beta}(\psi,r)$ is an augmented version of the velocity anisotropy profile. A useful alternative formulation are the pair

$$\tilde{\rho}(\psi,r) = \frac{\partial\tilde{\mu}_{20}}{\partial\psi}(\psi,r), \tag{2.121}$$

$$2\tilde{\beta}(\psi,r) = -\frac{\partial\ln\tilde{\mu}_{20}}{\partial\ln r}(\psi,r). \tag{2.122}$$

The derivative of the radial second-order moment follows from Eq. (2.116),

$$\frac{\mathrm{d}\rho\sigma_r^2}{\mathrm{d}r}(r) = \frac{\partial\tilde{\mu}_{20}}{\partial r}(\psi(r),r) + \frac{\partial\tilde{\mu}_{20}}{\partial\psi}(\psi(r),r)\,\frac{\mathrm{d}\psi}{\mathrm{d}r}(r), \tag{2.123}$$

so that, when $\psi(r)$ is known, Eqs. (2.121) - (2.122) can be combined to

$$\frac{\mathrm{d}\rho\sigma_r^2}{\mathrm{d}r}(r) + \frac{2\beta(r)}{r}\rho\sigma_r^2(r) = \rho(r)\frac{\mathrm{d}\psi}{\mathrm{d}r}(r). \tag{2.124}$$

This special case of Eq. (2.117) is the often-used *second-order Jeans equation*. If we recall the definitions of the density slope $\gamma(r)$ and the circular velocity $v_\mathrm{c}(r)$, and we introduce the function $\kappa(r)$,

$$\gamma(r) = -\frac{\mathrm{d}\ln\rho}{\mathrm{d}\ln r}(r), \qquad \kappa(r) = -\frac{\mathrm{d}\ln\sigma_r^2}{\mathrm{d}\ln r}(r), \qquad v_\mathrm{c}^2(r) = -r\frac{\mathrm{d}\psi}{\mathrm{d}r}(r), \tag{2.125}$$

then we can rewrite the Jeans equation as

$$\sigma_r^2(r)\left(\gamma(r) - 2\beta(r) + \kappa(r)\right) = v_\mathrm{c}^2(r). \tag{2.126}$$

For a given potential, one of the three profiles $\rho(r)$, $\sigma_r(r)$ and $\sigma_T(r)$ is thus determined by the other two. However, they do not determine the entire DF. It is important to emphasize this: a given pair $\rho(r)$ and $\beta(r)$, for instance, can be generated by infinitely many DFs. Indeed, if we define for example a function $\tau(\psi, r)$ for which $\tau(\psi(r), r) \equiv 1$, and extend a given $\tilde{\mu}_{20}$ to $\tilde{\mu}_{20}(\psi, r, \tau)$, we obtain

$$\tilde{\rho}(\psi, r) = \frac{\partial\tilde{\mu}_{20}}{\partial\psi}(\psi, r, \tau) + \frac{\partial\tilde{\mu}_{20}}{\partial\tau}\frac{\partial\tau}{\partial\psi}(\psi, r, \tau), \tag{2.127}$$

$$2\tilde{\beta}(\psi, r) = -\frac{\partial\ln\tilde{\mu}_{20}}{\partial\ln r}(\psi, r, \tau) - \frac{\partial\ln\tilde{\mu}_{20}}{\partial\ln\tau}\frac{\partial\ln\tau}{\partial\ln r}(\psi, r, \tau), \tag{2.128}$$

Then simply the condition

$$\frac{\partial\tilde{\mu}_{20}}{\partial\tau}(\psi(r), r, 1) \equiv 0, \tag{2.129}$$

will generate the same $\rho(r)$ and $\beta(r)$. Examples can be found in Dejonghe (1987). So how many moments are required to determine the DF? Let us examine the fourth-order moments from Eq. (2.117),

$$r\frac{\mathrm{d}\mu_{40}}{\mathrm{d}r}(r) = 3\,\mu_{22}(r) - 2\,\mu_{40}(r) + 3r\,\mu_{20}(r)\,\frac{\mathrm{d}\psi}{\mathrm{d}r}(r), \tag{2.130}$$

$$r\frac{\mathrm{d}\mu_{22}}{\mathrm{d}r}(r) = \mu_{04}(r) - 4\,\mu_{22}(r) + r\,\mu_{02}(r)\,\frac{\mathrm{d}\psi}{\mathrm{d}r}(r). \tag{2.131}$$

Clearly, the second-order moments $\mu_{20}(r)$ and $\mu_{02}(r)$ do not determine the fourth-order moments: we have two equations for the three unknowns $\mu_{40}(r)$, $\mu_{22}(r)$ and $\mu_{04}(r)$. However, if in addition one of the fourth-order moments is known, the other two can be derived. This remains true for higher-order moments: if one velocity moment of every order is known, then all others can be calculated, so that the entire DF is determined. In the next paragraph, we show how the radial velocity moments alone generate a dynamical system, by exploring the radial velocity distribution.

The radial velocity distribution

The radial velocity distribution (2.64) can be derived directly from the augmented density. First we define the auxiliary function

$$\widetilde{F}_{v_r^2}(\psi,r,v_r^2)=\frac{1}{|v_r|}\widetilde{F}_{v_r}(\psi,r,v_r)=\frac{2\pi}{|v_r|}\int_0^{\sqrt{2\psi-v_r^2}}F(E,L)\,v_T\,\mathrm{d}v_T, \tag{2.132}$$

such that

$$\begin{aligned}\int_{-\infty}^{+\infty}\widetilde{F}_{v_r}(\psi,r,v_r)\,\mathrm{d}v_r&=\int_0^{+\infty}\widetilde{F}_{v_r^2}(\psi,r,v_r^2)\,\mathrm{d}v_r^2\\&=\int_0^{+\infty}2v_r\,\widetilde{F}_{v_r^2}(\psi,r,v_r^2)\,\mathrm{d}v_r=\int_{-\infty}^{+\infty}|v_r|\,\widetilde{F}_{v_r^2}(\psi,r,v_r^2)\,\mathrm{d}v_r.\end{aligned} \tag{2.133}$$

Its Laplace transform is given by

$$\mathop{\mathcal{L}}_{v_r^2\to s}\left\{\widetilde{F}_{v_r^2}(\psi,r,v_r^2)\right\}=\int_0^{+\infty}\mathrm{e}^{-sv_r^2}\,\widetilde{F}_{v_r^2}(\psi,r)\,\mathrm{d}v_r^2 \tag{2.134}$$

$$=2\int_0^{+\infty}\sum_{n=0}^{\infty}\frac{(-s)^n}{n!}v_r^{2n}\widetilde{F}_{v_r}(\psi,r)\,\mathrm{d}v_r \tag{2.135}$$

$$=\frac{1}{M}\sum_{n=0}^{\infty}\frac{(-s)^n}{n!}\tilde{\mu}_{2n,0}(\psi,r). \tag{2.136}$$

As expected, all radial velocity moments are needed to determine the radial velocity distribution. With the use of Eq. (2.107), we find

$$\mathop{\mathcal{L}}_{v_r^2\to s}\left\{\widetilde{F}_{v_r^2}(\psi,r,v_r^2)\right\}=\frac{1}{M}\int_0^{\psi}\sum_{n=0}^{\infty}\frac{(1/2)_n}{n!\,n!}\big(-2s(\psi-\psi')\big)^n\,\frac{\partial\tilde{\rho}}{\partial\psi'}(\psi',r)\,\mathrm{d}\psi' \tag{2.137}$$

$$=\frac{1}{M}\int_0^{\psi}{}_1F_1\big(1/2,1;-2s(\psi-\psi')\big)\,\frac{\partial\tilde{\rho}}{\partial\psi'}(\psi',r)\,\mathrm{d}\psi', \tag{2.138}$$

where we introduced the confluent hypergeometric function of the first kind,

$${}_1F_1(a,b;z)=\frac{\Gamma(b)}{\Gamma(a)\,\Gamma(b-a)}\int_0^1\mathrm{e}^{zt}\,t^{a-1}(1-t)^{b-a-1}\mathrm{d}t,\qquad b>a>0, \tag{2.139}$$

with z a complex number. Evidently, its inverse Laplace transform is

$$\mathop{\mathcal{L}^{-1}}_{z\to t}\left\{{}_1F_1(a,b;-z)\right\}=\begin{cases}\dfrac{\Gamma(b)}{\Gamma(a)\,\Gamma(b-a)}t^{a-1}(1-t)^{b-a-1} & 0<t<1,\\ 0 & t\geqslant 1.\end{cases} \tag{2.140}$$

Also, for a real constant $c > 0$,

$$ {}_1F_1(a,b;-cz) = \frac{\Gamma(b)}{\Gamma(a)\,\Gamma(b-a)}\frac{1}{c}\int_0^c \mathrm{e}^{-zt}\left(\frac{t}{c}\right)^{a-1}\left(1-\frac{t}{c}\right)^{b-a-1}\mathrm{d}t, \tag{2.141} $$

which leads to the property

$$ \underset{z\to t}{\mathcal{L}^{-1}}\left\{{}_1F_1(a,b;-cz)\right\} = \frac{1}{c}\underset{z\to \frac{t}{c}}{\mathcal{L}^{-1}}\left\{{}_1F_1(a,b;-z)\right\}. \tag{2.142} $$

In this manner we can eliminate the Laplace transform in Eq. (2.138),

$$ \widetilde{F}_{v_r^2}(\psi,r,v_r^2) = \frac{1}{M}\int_0^\psi \frac{1}{2(\psi-\psi')}\underset{s\to\frac{v_r^2}{2(\psi-\psi')}}{\mathcal{L}^{-1}}\left\{{}_1F_1(1/2,1;-s)\right\}\frac{\partial\tilde{\rho}}{\partial\psi'}(\psi',r)\,\mathrm{d}\psi' \tag{2.143} $$

$$ = \frac{1}{M\pi\,|v_r|}\int_0^{\psi-v_r^2/2}\frac{1}{\sqrt{2(\psi-\psi')}}\left(1-\frac{v_r^2}{2(\psi-\psi')}\right)^{-1/2}\frac{\partial\tilde{\rho}}{\partial\psi'}\,\mathrm{d}\psi'. \tag{2.144} $$

Finally, from Eq. (2.132), we obtain the augmented radial velocity distribution,

$$ \widetilde{F}_{v_r}(\psi,r,v_r) = \frac{1}{\sqrt{2}M\pi}\int_0^{\psi-v_r^2/2}\left(\psi-\frac{v_r^2}{2}-\psi'\right)^{-1/2}\frac{\partial\tilde{\rho}}{\partial\psi'}(\psi',r)\,\mathrm{d}\psi'. \tag{2.145} $$

Note also that F_{v_r} does not depend on ψ and v_r independently, but on the combination $\psi - v_r^2/2$. This is no surprise, as this term is found solely in the energy-part of the DF. So if we write, for a given potential, the observational radial velocity distribution as

$$ \widetilde{F}_{v_r}(\psi(r),r,v_r) \equiv F_{v_r}(u,r), \qquad \text{with} \quad u = \psi(r) - v_r^2/2, \tag{2.146} $$

then we can apply an Abel inversion to Eq. (2.145), leading to

$$ \frac{\partial\tilde{\rho}}{\partial\psi}(\psi,r) = \sqrt{2}M\int_0^\psi (\psi-u)^{-1/2}\frac{\partial F_{v_r}}{\partial u}(u,r)\,\mathrm{d}u, \tag{2.147} $$

and

$$ \tilde{\rho}(\psi,r) = \sqrt{8}M\int_0^\psi \sqrt{\psi-u}\,\frac{\partial F_{v_r}}{\partial u}(u,r)\,\mathrm{d}u. \tag{2.148} $$

In other words, the radial velocity distribution $F_{v_r}(r,v_r)$ does determine the augmented density $\tilde{\rho}(\psi,r)$, and thus the DF. Similarly, the transverse velocity distribution $F_{v_T}(r,v_T)$ also generates a dynamical system, although the terms $\partial_{r^2}^m\left(r^{2m}\tilde{\rho}\right)$ prevent us to write a similar general formula. We will encounter Eq. (2.147) again when we discuss the global density slope – velocity anisotropy inequality in Chapter 6.

After this short detour, it is time to further examine the DF.

Back to the distribution function

As we mentioned, even though an augmented moment contains the same amount of information as the DF, we still need to know the latter to verify that it is nonnegative everywhere, i.e. that the dynamical system is physical. To calculate it, we need to invert the Laplace-Mellin transform in Eq. (2.91),

$$F(E,L) = \frac{-1}{4M\pi^{7/2}} \int_{\xi_0-i\infty}^{\xi_0+i\infty} \int_{\lambda_0-i\infty}^{\lambda_0+i\infty} \mathrm{e}^{\xi E} L^{-\lambda} \frac{(\xi/2)^{(3-\lambda)/2}}{\Gamma(1-\lambda/2)} \underset{\psi\to\xi}{\mathcal{L}} \underset{r\to\lambda}{\mathcal{M}} \{\tilde{\rho}\} \,\mathrm{d}\xi \,\mathrm{d}\lambda. \quad (2.149)$$

In general, this inversion has to be performed numerically. Unfortunately, this procedure is mathematically unstable. This can be understood by noting that the density, Eq. (2.53), is an integration of the distribution function over velocity space. As a result, the augmented density will generally be much smoother than the distribution function. The inversion thus involves the tricky job to "unsmooth" the augmented density. For a more precise mathematical demonstration of the unstable character of the inversion formulae, with examples, we refer to Dejonghe (1986).

So how can we avoid these problems? The solution is to build a dynamical system as a sum of simpler components, for which Eq. (2.149) can be solved analytically (in the sense that the functions can be written as power series). The 'base functions' we will construct are of a particular, very useful class: their augmented moments are separable functions.

2.3.2 Separable systems

Nearly all self-consistent dynamical models found in the literature are actually analytical separable systems (e.g. the isochrone sphere of Hénon 1960, the Cuddeford-Louis models of Cuddeford & Louis 1995, the Plummer models of Dejonghe 1987, the Hernquist models of Baes & Dejonghe 2002, the hypervirial models of Evans & An 2005, and the γ-models of Buyle et al. 2007). In all these models, the augmented density is a separable function of ψ and r,

$$\tilde{\rho}(\psi,r) = f(\psi)\, g(r). \quad (2.150)$$

Examples of such separable augmented densities are displayed in Fig. 2.3, which shows three functions that generate the same Hernquist density-potential pair (4.101) - (4.102), but produce different anisotropy profiles. It immediately follows that every augmented moment is a separable function,

$$\tilde{\mu}_{2n,2m}(\psi,r) = \frac{2^{m+n}}{\sqrt{\pi}} \frac{\Gamma(n+1/2)}{\Gamma(m+n)} \mathrm{d}_{r^2}^m \left(r^{2m} g(r)\right) \int_0^{\psi} (\psi-\psi')^{m+n-1} f(\psi')\,\mathrm{d}\psi'. \quad (2.151)$$

This means that, in contrast with general spherical models, a separable system is completely determined by just two observational moments: from two equations, one can derive the two

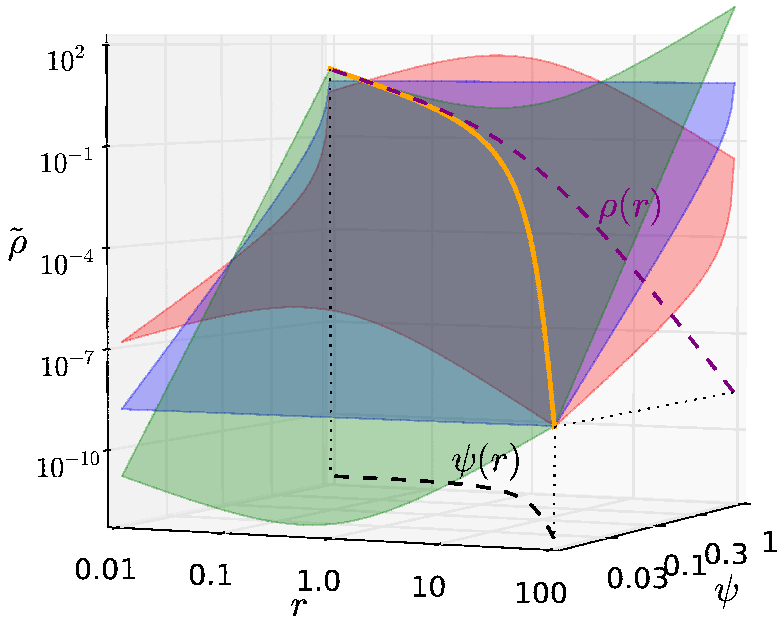

Figure 2.3 Three separable augmented densities of the form (4.111). They intersect in the orange curve, which means that each of these generate the same Hernquist density-potential pair (black and purple curves); however, they produce different anisotropy profiles: $(\beta_0, \beta_\infty) = (0,0)$ (blue), $(-0.5, 1)$ (red) and $(0.5, -1)$ (green).

functions $f(\psi)$ and $g(r)$. Again, our main attention goes out to the augmented density and the dispersion profiles

$$\tilde{\sigma}_r^2(\psi) = \frac{1}{f(\psi)} \int_0^\psi f(\psi')\, \mathrm{d}\psi', \tag{2.152}$$

$$\tilde{\sigma}_T^2(\psi, r) = \left(1 + \frac{1}{2}\frac{\mathrm{d}\ln g}{\mathrm{d}\ln r}\right) \frac{2}{f(\psi)} \int_0^\psi f(\psi')\, \mathrm{d}\psi'. \tag{2.153}$$

Note that the augmented radial dispersion only depends on ψ. An important property of separable systems is that the corresponding anisotropy profile is only a function of r,

$$\beta(r) = -\frac{1}{2}\frac{\mathrm{d}\ln g}{\mathrm{d}\ln r}(r). \tag{2.154}$$

Because of this, $\beta(r)$ can be written in terms of any radial velocity moment. Together with Eq. (2.113), we find

$$\frac{\partial\tilde{\mu}_{2n,0}}{\partial\psi}(\psi,r) = (2n-1)\tilde{\mu}_{2(n-1),0}(\psi,r), \tag{2.155}$$

$$\beta(r) = -\frac{1}{2}\frac{\partial\ln\tilde{\mu}_{2n,0}}{\partial\ln r}(r), \tag{2.156}$$

which can be combined into a simple form of the general Jeans equations,

$$\frac{\mathrm{d}\,\mu_{2n,0}}{\mathrm{d}r}(r) + \frac{2\beta(r)}{r}\mu_{2n,0}(r) = (2n-1)\mu_{2(n-1),0}(r)\,\frac{\mathrm{d}\psi}{\mathrm{d}r}(r). \tag{2.157}$$

This is a very convenient property: it offers us in principle the opportunity to construct dynamical models with a given potential $\psi(r)$, a density profile $\rho(r)$ and an anisotropy profile $\beta(r)$. First we solve Eq. (2.154) for $g(r)$. Next we invert the gravitational potential as $r(\psi)$ and we set

$$\overline{g}(\psi) = g(r(\psi)), \tag{2.158}$$

$$\overline{\rho}(\psi) = \rho(r(\psi)), \tag{2.159}$$

$$f(\psi) = \frac{\overline{\rho}(\psi)}{\overline{g}(\psi)}, \tag{2.160}$$

so that the augmented density $\tilde{\rho}(\psi,r) = f(\psi)\,g(r)$ defines the desired model. Clearly this procedure cannot in general be performed analytically. The inversion (2.149) has nevertheless become less daunting; it reduces to the form

$$\underset{L\to\lambda}{\mathcal{M}}\{F(E,L)\} = \frac{1}{2M\pi^{5/2}i}\int_{\xi_0-i\infty}^{\xi_0+i\infty}\mathrm{e}^{\xi E}\,\frac{(\xi/2)^{(3-\lambda)/2}}{\Gamma(1-\lambda/2)}\,\underset{\psi\to\xi}{\mathcal{L}}\{f(\psi)\}\,\underset{r\to\lambda}{\mathcal{M}}\{g(r)\}\,\mathrm{d}\xi. \tag{2.161}$$

So, can the DF be recovered without numerical problems? In a few cases, it can. A widely used example is a DF of the form

$$F(E,L) = \begin{cases} h(Q)\left(\dfrac{L}{r_\mathrm{a}}\right)^{-2\beta_0} & Q = E - \dfrac{L^2}{2r_\mathrm{a}^2} > 0, \\ 0 & Q \leqslant 0, \end{cases} \tag{2.162}$$

with r_a the so-called anisotropy radius. This model has been defined by Cuddeford (1991), who in turn derived it as an extension of the system considered by Osipkov (1979) and Merritt (1985), where $\beta_0 = 0$. The augmented density for this model is given by

$$\tilde{\rho}(\psi,r) = 2\pi M\int_0^{\psi}\mathrm{d}Q\int_0^{2(\psi-Q)}\frac{h(Q)\,u^{-2\beta_0}}{\sqrt{2(\psi-Q)-u^2}}\left(\frac{r}{r_\mathrm{a}}\right)^{-2\beta_0}\left(1+\frac{r^2}{r_\mathrm{a}^2}\right)^{\beta_0-1}\mathrm{d}u^2, \tag{2.163}$$

with

$$u^2 = \left(1 + \frac{r^2}{r_\mathrm{a}^2}\right) v_r^2. \tag{2.164}$$

Thus the system is indeed separable, with

$$f(\psi) = (2\pi)^{3/2} 2^{-\beta_0} M \frac{\Gamma(1-\beta_0)}{\Gamma(3/2-\beta_0)} \int_0^\psi (\psi - Q)^{1/2-\beta_0} h(Q)\, \mathrm{d}Q, \tag{2.165}$$

and

$$g(r) = \left(\frac{r}{r_\mathrm{a}}\right)^{-2\beta_0} \left(1 + \frac{r^2}{r_\mathrm{a}^2}\right)^{\beta_0 - 1}. \tag{2.166}$$

From $g(r)$, we can derive the anisotropy profile

$$\beta(r) = \frac{\beta_0 + (r/r_\mathrm{a})^2}{1 + (r/r_\mathrm{a})^2}. \tag{2.167}$$

This is a monotonically increasing anisotropy, from a central value $\beta(0) = \beta_0$ (justifying the notation) to purely radial orbits at infinity $\beta_\infty = 1$. The function $h(Q)$ can be derived from $f(\psi)$ by means of an Abel-related inversion (Cuddeford 1991),

$$h(Q) = \frac{2^{\beta_0}}{(2\pi)^{3/2} M \Gamma(1-\alpha)\Gamma(1-\beta_0)} \left(\int_0^Q \frac{\mathrm{d}^{n+1} f}{\mathrm{d}\psi^{n+1}} \frac{\mathrm{d}\psi}{(Q-\psi)^\alpha} + \frac{1}{Q^\alpha} \frac{\mathrm{d}^n f}{\mathrm{d}\psi^n}(0) \right), \tag{2.168}$$

where we denoted $n = \lfloor 3/2 - \beta_0 \rfloor$ and $\alpha = 3/2 - \beta_0 - n$ as the integer floor and fractional part of $3/2 - \beta_0$. The Cuddeford models contain a few special cases of the anisotropy profiles:

1. Models that are isotropic at the centre, i.e. $\beta_0 = 0$, so that $F(E,L) = h(Q)$. These are the *Osipkov-Merritt models*.

2. Models with constant anisotropy, i.e. $r_\mathrm{a} \to +\infty$:

$$\tilde{\rho}(\psi, r) = f(\psi) r^{-2\beta_0}, \qquad \beta(r) \equiv \beta_0, \qquad F(E,L) = h(E)\, L^{-2\beta_0}. \tag{2.169}$$

3. Isotropic models, i.e. both $\beta_0 = 0$ and $r_\mathrm{a} \to +\infty$. In this case the augmented density is only a function of ψ, i.e. $\tilde{\rho}(\psi)$, and the DF is the Eddington integral

$$F(E) = \frac{1}{\sqrt{8}\pi^2 M} \left(\int_0^E \frac{\mathrm{d}^2 \tilde{\rho}}{\mathrm{d}\psi^2} \frac{\mathrm{d}\psi}{\sqrt{E-\psi}} + \frac{1}{\sqrt{E}} \frac{\mathrm{d}\tilde{\rho}}{\mathrm{d}\psi}(0) \right). \tag{2.170}$$

Recall from Eqs. (2.127) - (2.129) that these are not the only spherical models with such anisotropy profiles. They are the only *separable* systems of this form, though.

The popularity of Osipkov-Merritt-Cuddeford-type models is easy to see: Kazantzidis et al. (2004) argued the importance to work with dynamical equilibrium models as their velocity distributions are often highly non-Maxwellian, and Cuddeford models are straightforward to implement, they can be applied to any density, and their anisotropy profiles Eq. (2.167) are general enough to try and model a broad range of gravitational systems.

For instance, structure formation by radial infall and virialization in the central regions lead to dark matter haloes with central isotropy and more radial orbits at the outskirts (Cole & Lacey 1996; Colín et al. 2000; Fukushige & Makino 1997; Diemand et al. 2005). Moreover, there is evidence from simulations and observations that many galaxies also have a significant radial anisotropy at large radii (e.g. Kronawitter et al. 2000; Oñorbe et al. 2007), while their inner regions range from isotropic to tangential, depending on the dynamical processes that shape their nucleus (Quinlan et al. 1995; Quinlan & Hernquist 1997; Gebhardt et al. 2003).

However, the Osipkov-Merritt anisotropy profiles are too steep to describe these systems adequately. For example, Mamon & Łokas (2005) showed that simulated dark matter haloes are not completely radial at infinity (i.e. $\beta_\infty < 1$) and the transition from inner to outer anisotropies is too abrupt; these authors suggested a profile of the form

$$\beta(r) = \frac{1}{2}\frac{r/r_\mathrm{a}}{1+r/r_\mathrm{a}}. \tag{2.171}$$

On a dynamical note, the $h(Q)$-part of the associated DFs creates unphysical cut-off boundary for orbits with $Q < 0$. Hence, the Osipkov-Merritt framework is too limited to model dark matter haloes, and a more extensive method is needed. And lastly, it has been noted that the tangential velocity dispersion undergoes a jump as r increases past r_a.

Because of these issues, we would like to construct models with different anisotropy profiles that resemble more closely the observational data. Yet, we still need to avoid the numerical instabilities involved in Eq. (2.149), so we focus on simpler functions that allow an analytical inversion. More sophisticated models can then be constructed as linear combinations of simpler components.

A set of very simple components that has been widely used in fitting dynamical models is the set of Fricke components (Fricke 1952; Hénon 1973), defined by the augmented mass density

$$\tilde{\rho}(r,\psi) = \begin{cases} r^{-2\beta}(\psi - E_0)^p & \psi > E_0, \\ \\ 0 & \psi \leqslant E_0. \end{cases} \tag{2.172}$$

Inserting this simple form of the augmented mass density into Eq. (2.168), it translates into a distribution function that is also a simple double power-law,

$$F(E,L) = \frac{2^\beta}{(2\pi)^{3/2}}\frac{\Gamma(1+p)}{\Gamma(1-\beta)\,\Gamma(p+\beta-1/2)}L^{-2\beta}(E-E_0)^{p+\beta-3/2}, \tag{2.173}$$

provided that $p+\beta-3/2>0$. The corresponding self-consistent models are also called the generalized polytropes, and were examined by Barnes et al. (1986) and Nguyen & Lingam (2013). Moreover, the hypervirial models (Evans & An 2005) form a sub-family of them. A more sophisticated set of components is given by the Plummer models (Dejonghe 1987),

$$\tilde{\rho}(r,\psi)=\frac{3}{4\pi}\psi^{5-2\beta_\infty}\left(1+\frac{r^2}{r_\mathrm{a}^2}\right)^{-2\beta_\infty}. \tag{2.174}$$

These components generate self-consistent Plummer systems with a monotonic, centrally isotropic $\beta(r)$ profile. The Fricke and Plummer components have been further generalized (see De Rijcke 2000) into functions of the form

$$\tilde{\rho}(r,\psi)=\begin{cases}(\psi-E_0)^p\left(\dfrac{r}{r_\mathrm{a}}\right)^{-2\beta_0}\left(1+\dfrac{r^2}{r_\mathrm{a}^2}\right)^{\beta_0-\beta_\infty}, & \psi>E_0,\\ 0 & \psi\leqslant E_0,\end{cases} \tag{2.175}$$

which produce anisotropy profiles that extend the Cuddeford profiles to varying values of β_∞, i.e.

$$\beta(r)=\frac{\beta_0+\beta_\infty(r/r_\mathrm{a})^2}{1+(r/r_\mathrm{a})^2}. \tag{2.176}$$

However, these anisotropy profiles still change more steeply from β_0 to β_∞ than profiles found in observations and simulations, like e.g. Eq. (2.171). Also, if the central potential ψ_0 is finite, then the components (2.175) will generate densities with finite central values if $\beta_0=0$, so that a finite sum of them cannot generate models with a central cusp. Worse, the central densities becomes zero (thus unphysical) if $\beta_0<0$.

These and other issues raised in the next section prompted us to extend these generalized Plummer components even further, which we describe in Chapter 4. Indeed, as we stated in the Introduction, our goal is to create DFs that can produce four-parameter anisotropy profiles of the form

$$\beta(r)=\frac{\beta_0+\beta_\infty\,(r/r_\mathrm{a})^{2\delta}}{1+(r/r_\mathrm{a})^{2\delta}}, \tag{2.177}$$

with $0<\delta\leqslant 1$. To make this possible, we shall need to develop several tools. The first step is an algorithm to create sums of components and to fit them to given data, which is the subject of the next section.

2.4 Quadratic programming

Recall the general observable quantities derived from the DF, Eq. (2.12), applied to spherical systems. Because they are linear functions, we can construct them as sums of simpler

base functions,

$$\mu(\boldsymbol{r},\boldsymbol{v}) = \int \bar{\mu}(\boldsymbol{r}',\boldsymbol{v}')\,F(E,L)\,\mathrm{d}^3\boldsymbol{r}'\,\mathrm{d}^3\boldsymbol{v}', \tag{2.178}$$

$$= \sum_{i=1}^{n} a_i \int \bar{\mu}(\boldsymbol{r}',\boldsymbol{v}')\,F_i(E,L)\,\mathrm{d}^3\boldsymbol{r}'\,\mathrm{d}^3\boldsymbol{v}' = \sum_{i=1}^{n} a_i\,\mu_i(\boldsymbol{r},\boldsymbol{v}). \tag{2.179}$$

Now, suppose we want to fit a dynamical model to a given gravitational system (derived from observations, simulations or theory; see the Introduction), from which we have extracted a set of N_{data} data points,

$$\mu_{\text{obs}}^{[m]}(\boldsymbol{r}_m,\boldsymbol{v}_m), \qquad m = 1,\ldots,N_{\text{data}}. \tag{2.180}$$

We emphasize with the superscript $[m]$ that the data can consist of different quantities. Furthermore, we postulate a gravitational potential $\psi(r)$. To model these data, we first construct a library of N_{lib} separable base functions,

$$f_i(\psi)\,g_i(r) \longleftrightarrow F_i(E,L), \qquad i = 1,N_{\text{lib}}, \tag{2.181}$$

and we calculate the corresponding values (with the aid of the augmented densities),

$$\mu_i^{[m]}(\boldsymbol{r}_m,\boldsymbol{v}_m) = \int_{\substack{\boldsymbol{r}=\boldsymbol{r}_m\\ \boldsymbol{v}=\boldsymbol{v}_m}} \bar{\mu}^{[m]}(\boldsymbol{r}',\boldsymbol{v}')\,F_i(E,L)\,\mathrm{d}^3\boldsymbol{r}'\,\mathrm{d}^3\boldsymbol{v}', \tag{2.182}$$

for $m = 1,\ldots,N_{\text{data}}$ and $i = 1,N_{\text{lib}}$. The library can for example consist of the generalized Plummer functions of Eq. (2.175), with varying parameter values. Our aim is now to construct a linear combination of N components from this library that provides an adequate fit to the given data. This fit is obtained by the χ^2 minimization

$$\chi^2_N = \min_{a_1,\ldots,a_N} \frac{1}{N_{\text{data}}} \sum_{m=1}^{N_{\text{data}}} w_m \left(\mu_{\text{obs}}^{[m]}(\boldsymbol{r}_m,\boldsymbol{v}_m) - \sum_{i=1}^{N} a_i\,\mu_i^{[m]}(\boldsymbol{r}_m,\boldsymbol{v}_m) \right)^2, \tag{2.183}$$

with weights $w_m > 0$ to give more or less importance to certain data points; for example, their values can be adjusted according to the error bars on the data points. For any set of N components, we are thus faced with a quadratic function of the coefficients a_i,

$$\chi^2_N = \min_{a_1,\ldots,a_N} f(\boldsymbol{a}), \tag{2.184}$$

with $\boldsymbol{a} = (a_1, \ldots, a_N)$ and

$$f(\boldsymbol{a}) = \left(\boldsymbol{a}^T A \boldsymbol{a} - 2B\boldsymbol{a} + C\right), \tag{2.185}$$

$$A_{ij} = \sum_{m=1}^{N_{\text{data}}} w_m \, \mu_i^{[m]}(\boldsymbol{r}_m, \boldsymbol{v}_m) \, \mu_j^{[m]}(\boldsymbol{r}_m, \boldsymbol{v}_m), \tag{2.186}$$

$$B_i = \sum_{m=1}^{N_{\text{data}}} w_m \, \mu_{\text{obs}}^{[m]}(\boldsymbol{r}_m, \boldsymbol{v}_m) \, \mu_i^{[m]}(\boldsymbol{r}_m, \boldsymbol{v}_m), \tag{2.187}$$

$$C = \sum_{m=1}^{N_{\text{data}}} w_m \left(\mu_{\text{obs}}^{[m]}(\boldsymbol{r}_m, \boldsymbol{v}_m)\right)^2. \tag{2.188}$$

Of course, we also require that the resulting fit defines a physical model, so we have to impose the condition

$$\sum_{i=1}^{N} a_i \, F_i(E, L) \geqslant 0 \tag{2.189}$$

on the DF, for all values of E and L. In practice, this means that we impose on a grid of J values (E_j, L_j) the conditions

$$\sum_{i=1}^{N} a_i \, F_i(E_j, L_j) \geqslant 0 \qquad \text{for } j = 1, \ldots, J. \tag{2.190}$$

Finally, we might want to limit the coefficients further with a set of N_{con} additional linear constraints,

$$l_k \leqslant \sum_{i=1}^{N} D_{ki} \, a_i \leqslant u_k, \qquad k = 1, \ldots, N_{\text{con}}. \tag{2.191}$$

Such constraints can for instance be useful to keep the coefficients between some lower and upper boundaries, so that he resulting linear combination of components can be computed with sufficient accuracy and without too much computational costs.

The matrix A is positive definite, so that $f(\boldsymbol{a})$ is a convex function; in this case the quadratic program has a unique global minimizer if there exists some feasible vector $\boldsymbol{a}$ (satisfying the constraints) and if $f(\boldsymbol{a})$ is bounded below on the feasible region. The equations (2.184) - (2.191) hence define a quadratic programming (QP) problem, which can be solved by a specialized numerical routine (in particular, we used the code provided by the `NAG` Library).

We still need a procedure to select N components out of the N_{lib} library functions that provide a good fit. It would be much too time consuming to try all possible combinations; instead we make use of the algorithm `GALS`, developed at our department, that builds a suitable set incrementally in N steps (Dejonghe 1989):

1. In the first step, every component is selected in turn from the library and used for a one-dimensional QP fit. From these $N_{\rm lib}$ fits, the component with the lowest χ^2_1 is then retained as the permanent first element of our best-fitting set.

2. In the second step, the remaining $N_{\rm lib}-1$ library components are again in turn selected and added to the first element, and $N_{\rm lib}-1$ two-dimensional QP fits are performed. The component that leads to the lowest χ^2_2 becomes the permanent second element of the best-fitting set.

3. In each next iteration, the best-fitting set is extended by adding the component from the library that yields the most improvement of the fit, until the set contains N elements. In other words, suppose we have obtained the best-fitting set of $N-1$ base functions. Then, we add in turn the remaining $N_{\rm lib}-N+1$ components from the library, and calculate the coefficients for each combination by means of N-dimensional QP fits. The set with the lowest χ^2_N, and corresponding coefficients $a_1,\ldots,a_N$ is the final best-fitting model, generated by

$$\tilde{\rho}(\psi,r) = \sum_{i=1}^{N} a_i\, f_i(\psi)\, g_i(r), \tag{2.192}$$

$$F(E,L) = \sum_{i=1}^{N} a_i\, F_i(E,L). \tag{2.193}$$

Note that this procedure does not in general find the best possible fit from a given library, but that is not important. What matters is that it strives to obtain a satisfactory fit, in a computationally efficient way.

This method has several other advantages. The resulting DFs will be smooth functions of E and L, unlike for example the results obtained by Schwarzschild's method (Schwarzschild 1979), where one ends up with a collection of discrete orbits. Our DFs also remain analytically tractable, simplifying the computation of all subsequent quantities. Furthermore, only a limited number of data points are required, rather than entire profiles. This enables us to apply the technique to theoretical profiles as well as data extracted from simulations. Moreover, if all data are of the same type, then the χ^2-values have a statistical goodness-of-fit meaning. While on the other hand a variety of different quantities can be mixed together in the fitting procedure, the resulting χ^2s lose their statistical interpretation, they still indicate the adequacy of the fits. And finally, as long as the base library is large and diverse enough, then even sums of simple Fricke components allow — in theory at least — dynamical models with a wide variation of velocity distributions. After all, any spherical DF can be decomposed into a double-power series of E and L by means of a two-dimensional Laurent series, so one should be able to approximate it by a finite sum of Fricke components (or more sophisticated base functions that are specifically designed for certain modelling tasks).

Over the years, the `GALS` routine has been applied successfully to a variety of gravitational systems, like globular clusters and galaxies (see the references in the Introduction).

Unfortunately, the algorithm also has a number of serious caveats. First of all, not all data lend themselves easily to be molded into functions of the DF. For example, the most complete observational knowledge of a system usually comes from its projected density (possibly derived from individual positions) as well as line-of-sight velocities. Ideally, these should be combined into a LOSVD; and for galaxy photometry and spectra, this can be done (De Rijcke 2000). For discrete systems however, like galaxy clusters, the positions and redshifts are too sparse to create an accurate two-dimensional LOSVD. So instead, we are forced to clump the data together into (projected) velocity moments, consequently not utilizing the full potential of the available information. Fortunately, we can resolve this by subjecting the best-fitting QP-models a posteriori to additional goodness-of-fit tests, like for instance a penalized maximum likelihood algorithm.

Alas, mixing different quantities into the χ^2-fitting creates issues of deeper concern. We already mentioned that such a χ^2 has no longer a statistical meaning. More importantly, it is unclear how to assign suitable weights w_m to heterogeneous data: what relative importance should be given to different quantities to obtain an adequate fit? Basically, we're comparing apples and oranges. Also, bear in mind that the constructed quantities, and the error bars on them, are not independent: they are assembled from the underlying (observational, theoretical) data and thus depend on each other in complex ways. Evidently, this problem is not specific to the QP-algorithm, it is a general concern in *any* fitting procedure.

But there is an even bigger Achilles heel. As we said, in theory any suitable library should be able to produce models of any kind. Practice, however, has taught that when we try to fit to projected data, it is generally difficult to construct models with a strong radial anisotropy at large radii; we encountered this difficulty in our early attempts to fit galaxy distributions in rich clusters (Van Hese & Dejonghe 2002). The reason for this problem is that one needs to populate the model with radial orbits that reach large radii. Since such orbits also contribute to the density at small radii, it requires a delicate fine-tuning of the different components to both satisfy the density and anisotropy constraints at small radii while still retaining the radial anisotropy at large radii. By contrast, tangential orbits only affect the density in very limited ranges of the radius. This means that if one only knows the velocity dispersion in one direction (like e.g. the projected, the radial or the transverse velocity dispersion), or if one thus know all velocity dispersions yet with significant error bars, then the `GALS` fitting procedure will be biased towards models with tangential, rather than radial outskirts. In fact, the iterative nature of the algorithm worsens the bias in each successive step, because every new component has to work together with the set of base functions that is gathered in the previous step; it will in general be easier to incorporate a tangential component into the existing set than a radial one. This bias is of less concern in models of globular clusters or galaxies, but it is nefast for large scale structures, which are thought to develop by means of radial infall.

When we have data on the spatial dispersions $\sigma_r(r)$ and $\sigma_T(r)$ instead of the projected dispersions alone, the bias is less problematic. But even so, another issue became apparent: the existing components (2.175) each produce anisotropy profiles of the form (2.176). The transition in these profiles from the central value β_0 to the value at infinity β_∞ is much steeper than profiles found in observations and simulations, like Eq. (2.171). Even though

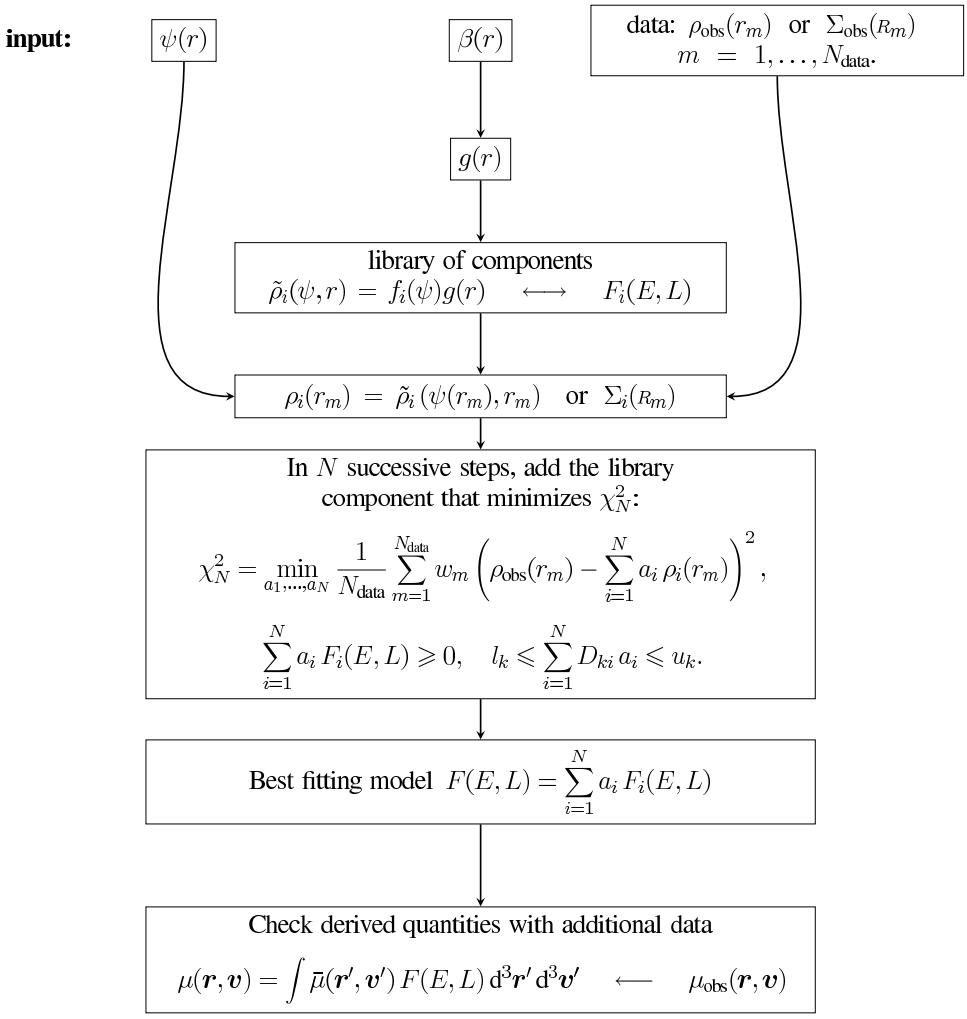

Figure 2.4 Schematic overview of our QP-algorithm.

linear combinations of these components can produce more general anisotropy profiles, it turned out that they remained too steep to obtain adequate fits. This prompted us to construct more advanced base components.

What can be done about these concerns? The solution is to predetermine the velocity moments beforehand, eliminating them from the fitting procedure. Recall that a separable system is determined by just two moments. We can use this property to our advantage; let us postulate an anisotropy profile $\beta(r)$, within a given potential $\psi(r)$, that is realistic, yet

simple enough to allow the construction of a library of $N_{\rm lib}$ base functions

$$\tilde{\rho}_i(\psi,r) = f_i(\psi)\, g(r), \tag{2.194}$$

$$\beta(r) = -\frac{1}{2}\frac{\mathrm{d}\ln g}{\mathrm{d}\ln r}(r), \tag{2.195}$$

that correspond to analytically tractable DFs $F_i(E,L)$. If we have a set of $N_{\rm data}$ density data points $\rho_{\rm obs}(r_m)$ available, then we can fit a model using the QP-algorithm

$$\chi^2_N = \min_{a_1,\ldots,a_N} \frac{1}{N_{\rm data}} \sum_{m=1}^{N_{\rm data}} w_m \left(\rho_{\rm obs}(r_m) - \sum_{i=1}^{N} a_i\, f_i\left(\psi(r_m)\right)\, g(r_m) \right)^2 . \tag{2.196}$$

The procedure can also be performed with projected densities. Note that the resulting model is still separable, $\tilde{\rho}(\psi,r) = f(\psi)\, g(r)$, with $f(\psi) = \sum_i a_i\, f_i(\psi)$. And since all components have a priori the same $g(r)$, their linear combination will automatically still generate the desired anisotropy profile $\beta(r)$. In this manner, we can construct an unbiased fit for a set of anisotropy profiles. If the data contain more information, we can discriminate between the obtained fits with further comparisons between every model and the data, e.g. with a maximum likelihood algorithm as previously mentioned. Thus we have derived a mechanism to test whether a given anisotropy profile is consistent with a certain data set. A schematic overview of the procedure is displayed in Fig. 2.4.

This immediately raises two remarks. First, our modelling procedure is now confined to finding only separable systems, and one can object that this puts severe limits on our results. True, if the data are detailed enough to impose significant constraints on the higher-order velocity moments, then our technique might be too restrictive. However, this is rarely the case; one usually has to deal with the opposite problem of degeneracy.

The second problem is of course that the fitting now no longer works with the simple components mentioned in the previous section, so that we are forced to design more intricate base functions with general enough anisotropy profiles. This is the topic of Chapter 4, where we will extend the generalized Plummer systems.

But before that, we note that the above two objections can in principle be — partially — resolved by constructing linear combinations of models that are fitted to the same density, but have different anisotropies. Thus one would be able to create a non-separable model with the same density, but a more general $\beta(r)$. But such a sum of sums of course increases the number of components, which makes accurate computations more difficult.

This concludes our introductory part. We have laid out the necessary mathematical machinery to create spherical dynamical models to a given set of data, which will be the topic of the next two chapters. In Chapter 4, we shall develop the family of library base functions for our QP-algorithm. However, these DFs will be expressed as so-called Fox H-functions, and we discuss these first in the next chapter.

Part II

CONSTRUCTION

Chapter 3

Fox H-functions, applied to kinematical profiles

Before we construct our distribution functions, we first introduce a very powerful analytical tool, the Fox H-function. We will demonstrate its use by deriving several analytical expressions related to very common potential-density pairs: the Sérsic, Einasto and double power-law profiles. The main results of this chapter are found in Baes & van Hese (2011) and Retana-Montenegro et al. (2012). Section 3.5.1 is based on work by E. Retana-Montenegro and F. Frutos-Alfaro; Sections 3.4.1, 3.4.4 and 3.5.4 are based on work by M. Baes; the rest of the material was worked out by the author.

3.1 Definition of the Fox H-function

In the previous chapter, we outlined a method to derive spherical distribution functions from (separable) augmented densities, where we encountered the *Mellin transform* (2.82)

$$\mathcal{F}(u) = \underset{x\to u}{\mathcal{M}}\{f(x)\} = \int_0^{+\infty} x^{u-1}\,f(x)\,\mathrm{d}x. \tag{3.1}$$

Wherever we perform this transform, we will postulate that the function in question is zero outside its boundaries. The inverse transform can, at least formally, be written as a complex integral,

$$f(x) = \underset{u\to x}{\mathcal{M}^{-1}}\{\mathcal{F}(u)\} = \frac{1}{2\pi i}\int_{u_0-i\infty}^{u_0+i\infty} x^{-u}\,\mathcal{F}(u)\,\mathrm{d}u, \tag{3.2}$$

where the integration is to be performed along a vertical line $u_0 = \text{const}$ in the complex plane within the strip of analyticity of $\mathcal{F}(u)$. As can be seen in Eq. (2.161), the distribution functions that we seek will indeed be inverse Mellin transforms of certain functions.

Since our aim is to find DFs that are advanced yet still computationally tractable, it is worthwhile to explore for which functional forms the integration can be performed. It turns out that a very broad range of special functions can be written as inverse Mellin integrals involving a product of gamma functions, known as *Mellin-Barnes integrals*. The work of Barnes (1908) focused on hypergeometric functions, but an important generalization was obtained by Meijer (1946). The broad class of functions that he considered has become known as *Meijer G-functions* (see also Mathai 1993 ; Gradshteyn & Ryzhik 1965),

$$G_{p,q}^{m,n}\left(z\,\middle|\,\begin{matrix}a_1,\ldots,a_p\\ b_1,\ldots,b_q\end{matrix}\right)= \frac{1}{2\pi i}\int_{\mathcal{C}}\frac{\prod_{j=1}^{m}\Gamma(b_j+s)\prod_{j=1}^{n}\Gamma(1-a_j-s)}{\prod_{j=n+1}^{p}\Gamma(a_j+s)\prod_{j=m+1}^{q}\Gamma(1-b_j-s)}\,z^{-s}\,\mathrm{d}s. \quad (3.3)$$

Here $0\leqslant n\leqslant p$, $1\leqslant m\leqslant q$ and $z^{-s}=\exp\{-s\ln|z|+i\arg z\}$. The possible contours $\mathcal{C}$ for which the integrals exist can be more general than vertical lines (see below). This family does indeed encompass many commonly used special functions, such as exponentials, Bessel functions, hypergeometric functions, and elliptic integrals. Nonetheless, we will require for our purposes a further extension, the lesser-known *Fox H-functions* (Fox 1961 ; Mathai 1993 ; Kilbas & Saigo 1999 ; Mathai et al. 2009),

$$H_{p,q}^{m,n}\left(z\,\middle|\,\begin{matrix}(a_1,A_1),\ldots,(a_p,A_p)\\ (b_1,B_1),\ldots,(b_q,B_q)\end{matrix}\right)= \frac{1}{2\pi i}\int_{\mathcal{C}}\frac{\prod_{j=1}^{m}\Gamma(b_j+B_js)\prod_{j=1}^{n}\Gamma(1-a_j-A_js)}{\prod_{j=n+1}^{p}\Gamma(a_j+A_js)\prod_{j=m+1}^{q}\Gamma(1-b_j-B_js)}\,z^{-s}\,\mathrm{d}s, \quad (3.4)$$

with $A_l,\ B_i$ positive real numbers. These functions evidently include all special functions generated by Meijer G-functions, but include also many other special functions, such as generalized Mittag-Leffler functions and generalized Bessel functions.

Note that if $A_1,\ldots,A_p$ and $B_1,\ldots,B_q$ are rational numbers, the Fox H-function can be written as a Meijer G-function, using the multiplication formula for the gamma function (see Eq. (4.40)). Since every real number can be approximated by a rational number to arbitrary precision, it is not surprising that Fox H and Meijer G-functions share many properties.

The integration path $\mathcal{C}$ is a contour separating the poles of the gamma functions $\Gamma(b_i+B_is)$ from the poles of the gamma functions $\Gamma(1-a_l-A_ls)$. We therefore require that these poles do not coincide, that is

$$A_l(b_i+\mu)\neq B_i(a_l-\nu-1),\quad i=1,\ldots,m;\ \ l=1,\ldots,n;\ \ \mu,\nu=0,1,2,\ldots \quad (3.5)$$

If we further define the quantities

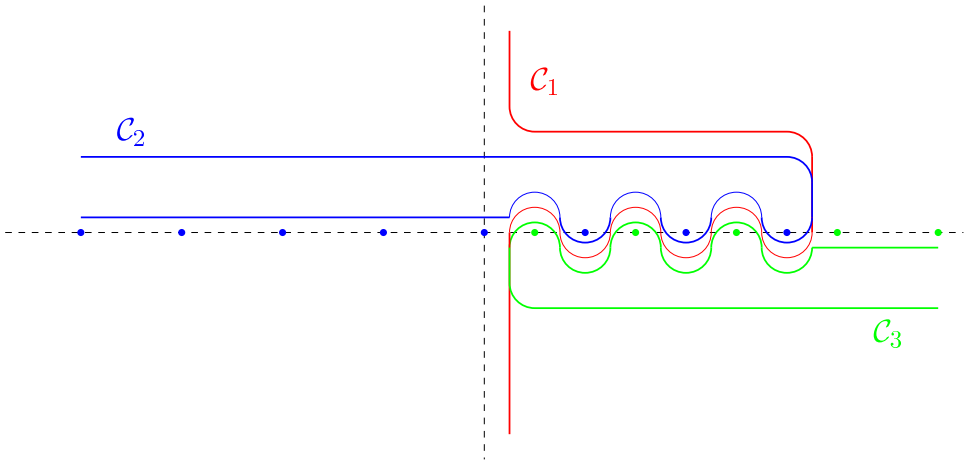

Figure 3.1 An illustration of the three contour paths $\mathcal{C}_1$, $\mathcal{C}_2$ and $\mathcal{C}_3$ for a simple Fox H-function, defined in Eq. (3.18).

$$\alpha = \sum_{j=1}^{n} A_j - \sum_{j=n+1}^{p} A_j + \sum_{j=1}^{m} B_j - \sum_{j=m+1}^{q} B_j, \tag{3.6}$$

$$\beta = \left[\prod_{j=1}^{p} (A_j)^{-A_j}\right] \left[\prod_{j=1}^{q} (B_j)^{B_j}\right], \tag{3.7}$$

$$\Delta = \sum_{j=1}^{q} B_j - \sum_{j=1}^{p} A_j, \tag{3.8}$$

$$\delta = \sum_{j=1}^{q} b_j - \sum_{j=1}^{p} a_j + \frac{p-q}{2}, \tag{3.9}$$

then the functions exist under one of the following conditions:

1. A contour $\mathcal{C}_1$ starting at a point $\gamma_0 - i\infty$ and going to $\gamma_0 + i\infty$ for some real value γ_0, such that all the poles of $\Gamma(b_i + B_i s),\ \ i = 1,\ldots,m$ are separated from those of $\Gamma(1 - a_l - A_l s),\ \ l = 1,\ldots,n$. The integral exists if either

   $$\alpha > 0,\ \ |\arg z| < \frac{\pi}{2}\alpha, \tag{3.10}$$

   or

   $$\alpha = 0,\ \ \gamma_0 \Delta + \Re\{\delta\} < -1,\ \ \arg z = 0,\ \ z \neq 0. \tag{3.11}$$

   In the special case where all the poles of $\Gamma(b_i + B_i s)$ lie to the left of all the poles of $\Gamma(1 - a_l - A_l s)$, or vice versa, then we can choose $\mathcal{C}_1$ to be a vertical line, so that the integral is an inverse Mellin-Barnes transform.

2. A loop $\mathcal{C}_2$ beginning and ending at $-\infty$ and encircling all the poles of $\Gamma(b_i+B_i s),\ i=1,\ldots,m$ once in the positive direction, but none of the poles of $\Gamma(1-a_l-A_l s),\ l=1,\ldots,n$, provided that

$$\Delta>0,\ \ z\neq 0, \tag{3.12}$$

or

$$\Delta=0,\ \ 0<|z|<\beta, \tag{3.13}$$

or

$$\Delta=0,\ \ |z|=\beta,\ \ \Re\{\delta\}<-1. \tag{3.14}$$

3. A loop $\mathcal{C}_3$ beginning and ending at $+\infty$ and encircling all the poles of $\Gamma(1-a_l-A_l s),\ \ l=1,\ldots,n$ once in the negative direction, but none of the poles of $\Gamma(b_i+B_i s),\ \ i=1,\ldots,m$, provided that

$$\Delta<0,\ \ z\neq 0, \tag{3.15}$$

or

$$\Delta=0,\ \ |z|>\beta, \tag{3.16}$$

or

$$\Delta=0,\ \ |z|=\beta,\ \ \Re\{\delta\}<-1. \tag{3.17}$$

If the integral exists on more than one path, then the result will be the same for each of those paths. We illustrate these three paths in Fig. 3.1 for the simple example

$$H^{1,1}_{1,1}\left(z\,\middle|\,\begin{matrix}(\frac{1}{2},1)\\(-3,1)\end{matrix}\right)=\frac{1}{2\pi i}\int_{\mathcal{C}}\Gamma(s-3)\,\Gamma\left(\frac{1}{2}-s\right)z^{-s}\,\mathrm{d}s, \tag{3.18}$$

where the poles $\{3-\mu;\ \mu=1,2,\ldots\}$ are indicated by the blue dots, and $\{1/2+\nu;\ \nu=1,2,\ldots\}$ are the green dots.

3.2 Illustrative examples

As we mentioned, a very broad range of special functions can be obtained as particular cases of Meijer G-functions and Fox H-functions (see Chapter 3 in Mathai 1993 and Section 1.8 in Mathai et al. 2009 for an overview). They include, for example, exponential functions,

$$\mathrm{e}^{-z}=\frac{1}{2\pi i}\int_{\mathcal{C}}\Gamma(s)\,z^{-s}\,\mathrm{d}s, \tag{3.19}$$

binomial series,

$$(1-z)^{-a} = \frac{1}{\Gamma(a)} \frac{1}{2\pi i} \int_{\mathcal{C}} \Gamma(-s)\, \Gamma(s+a)\, (-z)^{-s}\, \mathrm{d}s, \tag{3.20}$$

confluent hypergeometric functions,

$${}_1F_1(a,b;z) = \frac{\Gamma(b)}{\Gamma(a)} \frac{1}{2\pi i} \int_{\mathcal{C}} \frac{\Gamma(s)\, \Gamma(a-s)}{\Gamma(b-s)}\, (-z)^{-s}\, \mathrm{d}s, \tag{3.21}$$

Gaussian hypergeometric functions,

$${}_2F_1(a,b;c;z) = \frac{\Gamma(c)}{\Gamma(a)\Gamma(b)} \frac{1}{2\pi i} \int_{\mathcal{C}} \frac{\Gamma(s)\, \Gamma(a-s)\, \Gamma(b-s)}{\Gamma(c-s)}\, (-z)^{-s}\, \mathrm{d}s, \tag{3.22}$$

generalized hypergeometric functions,

$${}_pF_q(a_1 \dots a_p; b_1 \dots b_q; z) = \frac{\prod_{j=1}^{q} \Gamma(b_j)}{\prod_{j=1}^{p} \Gamma(a_j)} \frac{1}{2\pi i} \int_{\mathcal{C}} \frac{\Gamma(s) \prod_{j=1}^{p} \Gamma(a_j - s)}{\prod_{j=1}^{q} \Gamma(b_j - s)}\, z^{-s}\, \mathrm{d}s, \tag{3.23}$$

and Mittag-Leffler functions,

$$E_\alpha(z) = \sum_{k=0}^{\infty} \frac{z^k}{\Gamma(\alpha k + 1)} = \frac{1}{2\pi i} \int_{\mathcal{C}} \frac{\Gamma(s)\, \Gamma(1-s)}{\Gamma(1-\alpha s)}\, (-z)^{-s}\, \mathrm{d}s, \tag{3.24}$$

to name a few. Other functions, like beta functions, Bessel functions and elliptic functions, are special cases of hypergeometric functions, hence these are included as well.

3.3 Series expansions

The real strength of the Fox H-function is that, under the conditions for the paths $\mathcal{C}_2$ or $\mathcal{C}_3$ listed in Section 3.1, the integral can be evaluated using the powerful Residue Theorem. This allows us to evaluate and study it as a series expansion. Let us write the function in the form

$$H_{p,q}^{m,n}\left(z \,\middle|\, \begin{matrix} (\boldsymbol{a}, \boldsymbol{A}) \\ (\boldsymbol{b}, \boldsymbol{B}) \end{matrix} \right) = \frac{1}{2\pi i} \int_{\mathcal{C}} \varphi(s)\, z^{-s}\, \mathrm{d}s, \tag{3.25}$$

with

$$\varphi(s) = \frac{\prod_{j=1}^{m} \Gamma(b_j + B_j s) \prod_{j=1}^{n} \Gamma(1 - a_j - A_j s)}{\prod_{j=m+1}^{q} \Gamma(1 - b_j - B_j s) \prod_{j=n+1}^{p} \Gamma(a_j + A_j s)}. \tag{3.26}$$

First we examine the integration along $\mathcal{C}_2$, encircling the poles of the functions $\Gamma(b_i + B_i s),\ \ i = 1, \ldots, m$. With the short-hand notation

$$\beta_{i,k_i} = -(b_i + k_i)/B_i, \qquad i = 1, \ldots, m, \quad k_i = 0, \ldots, +\infty, \tag{3.27}$$

we obtain

$$H_{p,q}^{m,n}\left(z \,\middle|\, \begin{array}{c}(\boldsymbol{a},\boldsymbol{A})\\(\boldsymbol{b},\boldsymbol{B})\end{array}\right) = \sum_{i=1}^{m}\sum_{k_i=0}^{\infty} \operatorname*{Res}_{s=\beta_{i,k_i}} \left\{\varphi(s)\, z^{-s}\right\}. \tag{3.28}$$

If β_{i,k_i} is a simple pole, then the corresponding residue is fairly straightforward: we find

$$\operatorname*{Res}_{s=\beta_{i,k_i}} \left\{\varphi(s)\, z^{-s}\right\} = \lim_{s\to\beta_{i,k_i}} \left\{(s-\beta_{i,k_i})\,\varphi(s)\, z^{-s}\right\} = \varphi_i(\beta_{i,k_i})\,\frac{(-1)^{k_i}}{k_i!}\,\frac{z^{-\beta_{i,k_i}}}{B_i}, \tag{3.29}$$

where $\varphi_i(s)$ is $\varphi(s)/\Gamma(b_i + B_i s)$. As a result, if all gamma functions $\Gamma(b_i + B_i s)$ have only single poles, we obtain the series expansion,

$$H_{p,q}^{m,n}\left(z \,\middle|\, \begin{array}{c}(\boldsymbol{a},\boldsymbol{A})\\(\boldsymbol{b},\boldsymbol{B})\end{array}\right) = \sum_{i=1}^{m}\sum_{k_i=0}^{\infty} \frac{(-1)^{k_i}}{k_i!\,B_i}\, \frac{\prod_{j=1,j\neq i}^{m}\Gamma\left(b_j - B_j\frac{b_i+k_i}{B_i}\right)\prod_{j=1}^{n}\Gamma\left(1-a_j+A_j\frac{b_i+k_i}{B_i}\right)}{\prod_{j=m+1}^{q}\Gamma\left(1-b_j+B_j\frac{b_i+k_i}{B_i}\right)\prod_{j=n+1}^{p}\Gamma\left(a_j-A_j\frac{b_i+k_i}{B_i}\right)}\, z^{(b_i+k_i)/B_i} \tag{3.30}$$

in agreement with Eq. (3.4) in Kilbas & Saigo (1999).

The integration along the path $\mathcal{C}_3$, encircling the poles of $\Gamma(1 - a_l - A_l s),\ \ i = 1, \ldots, n$ is completely analogous:

$$H_{p,q}^{m,n}\left(z \,\middle|\, \begin{array}{c}(\boldsymbol{a},\boldsymbol{A})\\(\boldsymbol{b},\boldsymbol{B})\end{array}\right) = \sum_{l=1}^{m}\sum_{k_l=0}^{\infty} \frac{(-1)^{k_l}}{k_l!\,A_l} \times \frac{\prod_{j=1}^{m}\Gamma\left(b_j + B_j\frac{1-a_l+k_l}{A_l}\right)\prod_{j=1,j\neq l}^{n}\Gamma\left(1-a_j-A_j\frac{1-a_l+k_l}{A_l}\right)}{\prod_{j=m+1}^{q}\Gamma\left(1-b_j-B_j\frac{1-a_l+k_l}{A_l}\right)\prod_{j=n+1}^{p}\Gamma\left(a_j+A_j\frac{1-a_l+k_l}{A_l}\right)}\, z^{-(1-a_l+k_l)/A_l} \tag{3.31}$$

in agreement with Eq. (3.12) in Kilbas & Saigo (1999).

However, if two or more gamma functions share a pole, then this pole is of higher order, and the calculation becomes more involved. Kilbas & Saigo (1999) demonstrate that the Fox H-function can then be expressed as a logarithmic-power series rather than a simple

power series. They present a generic expression valid for all orders of pole multiplicity. Here, we present a less general, but more explicit, series expansion for the path $\mathcal{C}_2$ in the case that two gamma functions $\Gamma(b_j + B_j s)$ share some of their poles. Without loss of generality, we can place these two gamma functions at the front, so that we can write

$$\varphi(s) = \Gamma(b_1 + B_1 s)\,\Gamma(b_2 + B_2 s)\,\phi(s), \tag{3.32}$$

with

$$\phi(s) = \frac{\prod_{j=3}^{m}\Gamma(b_j + B_j s)\prod_{j=1}^{n}\Gamma(1 - a_j - A_j s)}{\prod_{j=m+1}^{q}\Gamma(1 - b_j - B_j s)\prod_{j=n+1}^{p}\Gamma(a_j + A_j s)}. \tag{3.33}$$

Now, suppose there is a tuple (k_1, k_2) of indices so that

$$\beta_{1,k_1} = \beta_{2,k_2}. \tag{3.34}$$

The residue of this second-order pole is then, after some algebra,

$$\operatorname*{Res}_{s=\beta_{1,k_1}}\left\{\varphi(s)\,z^{-s}\right\} = \lim_{s\to\beta_{1,k_1}}\left\{\frac{\mathrm{d}}{\mathrm{d}s}\left[(s-\beta_{1,k_1})^2\,\varphi(s)\,z^{-s}\right]\right\}, \tag{3.35}$$

$$= \left[-\ln z + B_1\psi(k_1+1) + B_2\psi(k_2+1) + \frac{\phi'(\beta_{1,k_1})}{\phi(\beta_{1,k_1})}\right] \times \tag{3.36}$$

$$\phi(\beta_{1,k_1})\,\frac{(-1)^{k_1}(-1)^{k_2}}{(k_1)!\,(k_2)!}\,\frac{z^{-\beta_{1,k_1}}}{B_1 B_2}, \tag{3.37}$$

with

$$\psi(s) = \frac{\Gamma'(s)}{\Gamma(s)}, \tag{3.38}$$

the so-called *digamma function*. Moreover, note that $\phi(s)$ is a product and quotient of gamma functions, so that $\phi'(s)/\phi(s)$ can also be expressed as a sum of digamma functions. This means that all the machinery is available to express the Fox H-function as the rather daunting-looking series expansion

$$H_{p,q}^{m,n}\left(z\,\middle|\,\begin{matrix}(\boldsymbol{a},\boldsymbol{A})\\(\boldsymbol{b},\boldsymbol{B})\end{matrix}\right) =$$

$$\sum_{i,k_i}{}' \frac{(-1)^{k_i}}{k_i!\,B_i}\,\frac{\prod_{j=1,j\neq i}^{m}\Gamma\left(b_j - B_j\frac{b_i+k_i}{B_i}\right)\prod_{j=1}^{n}\Gamma\left(1-a_j+A_j\frac{b_i+k_i}{B_i}\right)}{\prod_{j=m+1}^{q}\Gamma\left(1-b_j+B_j\frac{b_i+k_i}{B_i}\right)\prod_{j=n+1}^{p}\Gamma\left(a_j-A_j\frac{b_i+k_i}{B_i}\right)}\,z^{(b_i+k_i)/B_i}$$

$$+\sum_{k_1}{}'' \frac{(-1)^{k_1+k_2}}{k_1!\,k_2!\,B_1 B_2}\,\frac{\prod_{j=3}^{m}\Gamma\left(b_j - B_j\frac{b_i+k_1}{B_i}\right)\prod_{j=1}^{n}\Gamma\left(1-a_j+A_j\frac{b_i+k_1}{B_i}\right)}{\prod_{j=m+1}^{q}\Gamma\left(1-b_j+B_j\frac{b_i+k_1}{B_i}\right)\prod_{j=n+1}^{p}\Gamma\left(a_j-A_j\frac{b_i+k_1}{B_i}\right)}\times$$

$$z^{(b_i+k_1)/B_i}\left(C_{k_1} - \ln z\right), \tag{3.39}$$

with the constants C_{k_1} defined as

$$\begin{aligned} C_{k_1} = {} & B_1\psi(k_1+1) + B_2\psi(k_2+1) \\ & + \sum_{j=3}^{m} B_j\psi\left(b_j - B_j\tfrac{b_1+k_1}{B_1}\right) - \sum_{j=1}^{n} A_j\psi\left(1-a_j + A_j\tfrac{b_1+k_1}{B_1}\right) \\ & + \sum_{j=m+1}^{q} B_j\psi\left(1-b_j + B_j\tfrac{b_1+k_1}{B_1}\right) - \sum_{j=n+1}^{p} A_j\psi\left(a_j - A_j\tfrac{b_1+k_1}{B_1}\right). \end{aligned} \tag{3.40}$$

The prime in the first summation in Eq. (3.39) indicates that this sum covers only the single poles, and the double prime in the second summation indicates that this summation runs over the second-order poles. In the latter summation, we set $k_2 = B_2(b_1+k_1)/B_1 - b_2$. Alternatively, one can use k_2 as summation index and set $k_1 = B_1(b_2+k_2)/B_2 - b_1$.

For the integration path $\mathcal{C}_3$, one can obtain completely analogous equations involving the poles of $\Gamma(1-a_l-A_l s),\ \ l=1,\ldots,n$, but we shall not need these in our subsequent work. In principle, one can extend this scheme further, when more gamma functions have poles in common, although it is clear that the calculations can become substantially elaborate.

For numerical implementations though, one can always "cheat" when the gamma functions share poles, by changing some of the relevant parameters $(\boldsymbol{a},\boldsymbol{A},\boldsymbol{b},\boldsymbol{B})$ by small constants in such a way that all the poles become simple and (3.30) - (3.30) can be used. This is how commercial software packages like `Maple`® and `Mathematica`® deal with Meijer G-functions.

To conclude this section, we list several useful properties of the digamma function:

$$\psi(s) = -\gamma - \frac{1}{s} + s\sum_{k=1}^{\infty}\frac{1}{k(s+k)}, \tag{3.41}$$

$$\psi(s+m) = \psi(s) + \frac{1}{s} + \frac{1}{s+1} + \cdots + \frac{1}{s+m-1}, \tag{3.42}$$

$$\psi(ms) = \ln m + \frac{1}{m}\sum_{k=0}^{m-1}\psi(s+k/m), \tag{3.43}$$

$$\psi(1+m) = 1 + \frac{1}{2} + \cdots + \frac{1}{m} - \gamma, \tag{3.44}$$

$$\psi(1/2) = -\gamma - 2\ln 2, \tag{3.45}$$

with $\gamma \approx 0.57721566$ the Euler-Mascheroni constant. Let us now examine how we can put all that horsepower to use, deriving various quantities related to two widely-used density-potential pairs. We will start with the Sérsic model.

3.4 Analytical expressions for the deprojected Sérsic model

3.4.1 Introduction

The Sersic (1968) surface brightness profile has become the preferred model to describe the surface brightness profile of early-type galaxies and the bulges of spiral galaxies (e.g. Davies et al. 1988; Caon et al. 1993; D'Onofrio et al. 1994; Cellone et al. 1994; Andredakis et al. 1995; Prugniel & Simien 1997; Möllenhoff & Heidt 2001; Graham & Guzmán 2003; Allen et al. 2006; Gadotti 2009), and it has also been used to describe disc galaxy mergers (Aceves et al. 2006). Due to this popularity, many analytical properties of this model have been discussed in the literature, for certain parameter values (Ciotti 1991; Ciotti & Lanzoni 1997; Ciotti & Bertin 1999; Trujillo et al. 2001; Mazure & Capelato 2002; Cardone 2004; Graham & Driver 2005; Elíasdóttir & Möller 2007; Baes & Gentile 2011).

An important inconvenience of the Sérsic model is that its deprojected luminosity density, i.e. the spatial 3D luminosity density $\rho(r)$ that projects on the plane of the sky to the Sérsic surface brightness profile, cannot be expressed using elementary functions or even in terms of standard special functions (for a numerical deprojection using series expansions, see Bendinelli et al. 1993). It was long thought that no analytical expression could be obtained, when quite unexpectedly, Mazure & Capelato (2002) came up with an analytical expression for $\rho(r)$ in terms of the Meijer G-function for all integer Sérsic indices m. Baes & Gentile (2011) took this analysis one step further and showed that the deprojection of the Sérsic surface brightness profile for general values of m can be solved elegantly using Mellin integral transforms and gives rise to a Mellin-Barnes integral.

The result is that the Sérsic luminosity density can be written compactly in terms of a Fox H-function, which reduces to a Meijer G-function for all rational values of m. Using this property, Baes & Gentile (2011) calculated a number of additional properties of the Sérsic model for rational m, including the asymptotic expansion of the luminosity density at small and large radii, the cumulative light profile and the gravitational potential.

In this section, we extend and complete the analysis that was presented in Mazure & Capelato (2002) and Baes & Gentile (2011): we will provide compact and elegant expressions for the density, potential and luminosity profiles in terms of the general Fox H-function, which are valid for *all* values of the Sérsic index m rather than just for integer or rational m. We also present a completely general series expansion of these functions that enables both a numerical evaluation and a straightforward analytical study of their asymptotic behaviour.

3.4.2 Analytical properties of the Sérsic model

The Sérsic model is defined by the intensity profile projected on the plane of the sky,

$$I(R) = I_0 \exp\left[-b\left(\frac{R}{R_\mathrm{e}}\right)^{1/m}\right], \tag{3.46}$$

which generalizes the de Vaucouleurs $R^{1/4}$ model (de Vaucouleurs 1948). The 3D, deprojected luminosity density $\rho(r)$ of a spherically symmetric system can be recovered from the surface brightness profile $I(R)$ using the standard deprojection formula (2.70)

$$\rho(r) = -\frac{1}{\pi}\int_r^\infty \frac{\mathrm{d}I}{\mathrm{d}R}\,\frac{\mathrm{d}R}{\sqrt{R^2-r^2}}. \tag{3.47}$$

Substituting the Sérsic profile (3.46) into (3.47) we obtain an integral that cannot readily be evaluated using the standard ways or look-up tables. Baes & Gentile (2011) applied a Mellin integral transform technique to convert this integral to a Mellin-Barnes contour integral,

$$\rho(r) = \frac{2m\,I_0}{\sqrt{\pi}}\,r^{-1}\,\frac{1}{2\pi i}\int_{\mathcal{C}} \frac{\Gamma(2mx)\,\Gamma\left(\frac{1}{2}+x\right)}{\Gamma(x)}\left(\frac{b^m r}{R_\mathrm{e}}\right)^{-2x}\mathrm{d}x, \tag{3.48}$$

or, given the definition (3.4), to the compact expression

$$\rho(r) = \frac{2m\,I_0\,b^m}{\sqrt{\pi}\,R_\mathrm{e}}\,u^{-1}\,H^{2,0}_{1,2}\left(u^2\,\middle|\,\begin{matrix}(0,1)\\(0,2m),(\frac{1}{2},1)\end{matrix}\right), \tag{3.49}$$

where we have used the reduced coordinate

$$u = \frac{b^m r}{R_\mathrm{e}}. \tag{3.50}$$

As a check on this formula, Baes & Gentile (2011) calculated the total luminosity of the Sérsic model for rational m by integrating the luminosity density over the entire space. To obtain the results, they used the integration properties of the Meijer G-function, combined with several applications of Gauss' multiplication theorem. As a generalization of this result, and as a nice example of the power of the Fox H-function, we calculate the total luminosity from the general formula (3.49), i.e.

$$L = 4\pi\int_0^\infty \rho(r)\,r^2\,\mathrm{d}r = \frac{4m\sqrt{\pi}\,I_0\,R_\mathrm{e}^2}{b^{2m}}\int_0^\infty H^{2,0}_{1,2}\left(t\,\middle|\,\begin{matrix}(0,1)\\(0,2m),(\frac{1}{2},1)\end{matrix}\right)\mathrm{d}t. \tag{3.51}$$

To evaluate this integral, recall that the Fox H-function is an inverse Mellin transform of a combination of gamma functions. As a result, the Mellin transform of a Fox H-function reads

$$\int_0^\infty H^{m,n}_{p,q}\left(z\,\middle|\,\begin{matrix}(\boldsymbol{a},\boldsymbol{A})\\(\boldsymbol{b},\boldsymbol{B})\end{matrix}\right)z^{s-1}\,\mathrm{d}z = \frac{\prod_{j=1}^m\Gamma(b_j+B_j s)\prod_{j=1}^n\Gamma(1-a_j-A_j s)}{\prod_{j=m+1}^q\Gamma(1-b_j-B_j s)\prod_{j=n+1}^p\Gamma(a_j+A_j s)}.$$

(3.52)

Applying this to (3.51) with $s = 1$, we obtain

$$L = \frac{4m\sqrt{\pi}\, I_0\, R_\mathrm{e}^2}{b^{2m}}\, \frac{\Gamma(2m)\,\Gamma(\frac{3}{2})}{\Gamma(1)} = \frac{\pi\, I_0\, R_\mathrm{e}^2\, \Gamma(2m+1)}{b^{2m}}, \tag{3.53}$$

in agreement with the value obtained by integrating the surface brightness profile (3.46) over the plane of the sky.

From the luminosity density, a number of other important quantities can be derived, most importantly the cumulative luminosity profile $L(r)$ and the gravitational potential $\psi(r)$,

$$L(r) = 4\pi \int_0^r \rho(r')\, r'^2\, \mathrm{d}r'. \tag{3.54}$$

$$\psi(r) = G\Upsilon \int_r^\infty \frac{L(r')\, \mathrm{d}r'}{r'^2}, \tag{3.55}$$

where Υ is the mass-to-light ratio. Mazure & Capelato (2002) and Baes & Gentile (2011) calculated these quantities for the Sérsic model for integer and rational values of the Sérsic parameter, respectively, using the integration properties of the Meijer G-function. It is, however, possible to calculate these properties for general m in an elegant way by directly applying the integrations on the Mellin-Barnes integral form of the luminosity density. We obtain for the cumulative luminosity profile

$$\begin{aligned}
L(r) &= 8m\sqrt{\pi}\, I_0 \int_0^r \left[\frac{1}{2\pi i} \int_{\mathcal{C}} \frac{\Gamma(2m\,x)\,\Gamma\left(\frac{1}{2}+x\right)}{\Gamma(x)} \left(\frac{b^m r'}{R_\mathrm{e}} \right)^{-2x} \mathrm{d}x \right] r'\, \mathrm{d}r' \\
&= 8m\sqrt{\pi}\, I_0\, \frac{1}{2\pi i} \int_{\mathcal{C}} \frac{\Gamma(2m\,x)\,\Gamma\left(\frac{1}{2}+x\right)}{\Gamma(x)} \left(\frac{b^m}{R_\mathrm{e}} \right)^{-2x} \left[\int_0^r r'^{1-2x}\, \mathrm{d}r' \right] \mathrm{d}x \\
&= 4m\sqrt{\pi}\, I_0\, r^2 \frac{1}{2\pi i} \int_{\mathcal{C}} \frac{\Gamma(2m\,x)\,\Gamma\left(\frac{1}{2}+x\right)\,\Gamma(1-x)}{\Gamma(x)\,\Gamma(2-x)}\, u^{-2x}\, \mathrm{d}x \\
&= \frac{4m\sqrt{\pi}\, I_0\, R_\mathrm{e}^2}{b^{2m}}\, u^2\, H^{2,1}_{2,3}\left(u^2 \,\middle|\, \begin{matrix} (0,1),(0,1) \\ (0,2m),(\frac{1}{2},1),(-1,1) \end{matrix} \right).
\end{aligned} \tag{3.56}$$

For the gravitational potential we find after a similar calculation

$$\psi(r) = \frac{2m\sqrt{\pi}\, G\Upsilon\, I_0\, R_\mathrm{e}}{b^m}\, u\, H^{2,1}_{2,3}\left(u^2 \,\middle|\, \begin{matrix} (0,1),(0,1) \\ (0,2m),(-\frac{1}{2},1),(-1,1) \end{matrix} \right). \tag{3.57}$$

The formulae (3.49), (3.56) and (3.57) form a triplet of formulae that describe three important spatial properties of the Sérsic model in a compact way.

A straightforward way of checking these formulae is to look at the model that corresponds to $m = \frac{1}{2}$. In this case, all components of the vectors $\boldsymbol{A}$ and $\boldsymbol{B}$ are equal to one,

such that the Fox H-function reduces to a Meijer G-function. We find

$$\rho(r) = \frac{I_0\sqrt{b}}{\sqrt{\pi}\,R_\mathrm{e}}\,u^{-1}\,G^{2,0}_{1,2}\left(u^2\,\middle|\,\begin{matrix}0\\0,\frac{1}{2}\end{matrix}\right) = \frac{I_0\sqrt{b}}{\sqrt{\pi}\,R_\mathrm{e}}\,\mathrm{e}^{-u^2}, \tag{3.58}$$

$$L(r) = \frac{2\sqrt{\pi}\,I_0\,R_\mathrm{e}^2}{b}\,u^2\,G^{2,1}_{2,3}\left(u^2\,\middle|\,\begin{matrix}0,0\\0,\frac{1}{2},-1\end{matrix}\right) = \frac{\pi\,I_0\,R_\mathrm{e}^2}{b}\,\left[\mathrm{erf}\,u - \frac{2}{\sqrt{\pi}}\,u\,\mathrm{e}^{-u^2}\right], \tag{3.59}$$

$$\psi(r) = \frac{\sqrt{\pi}\,G\Upsilon\,I_0\,R_\mathrm{e}}{\sqrt{b}}\,u\,G^{2,1}_{2,3}\left(u^2\,\middle|\,\begin{matrix}0,0\\0,-\frac{1}{2},-1\end{matrix}\right) = \frac{\pi\,G\Upsilon\,I_0\,R_\mathrm{e}}{\sqrt{b}}\,\frac{\mathrm{erf}\,u}{u}. \tag{3.60}$$

These expressions can also be derived by substituting the intensity $I(R) = I_0\,\mathrm{e}^{-bR^2/R_\mathrm{e}^2}$ into the expressions (3.47), (3.54) and (3.55) and directly evaluating the resulting integrals. More generally, one can check that the formulae (3.49), (3.56) and (3.57) reduce to the Eqs. (22), (40) and (44) of Baes & Gentile (2011) for rational values of m.

3.4.3 Explicit series expansions

While the expressions (3.49), (3.56) and (3.57) form an triplet of compact formulae that are useful for analytical work, they are not readily useful to numerically evaluate the spatial properties of the Sérsic model. For rational values of m, the Fox H-functions reduce to Meijer G-functions, and some numerical software packages have this function now implemented. However, the numerical evaluation of Meijer G-functions with large parameter vectors (which easily occurs in our case for rational values of m, as can be seen in Baes & Gentile 2011), proves to be difficult, in particular in cases where second-order poles are present in the integrand of the inverse Mellin transform. Moreover, for general values of m, the expressions (3.49), (3.56) and (3.57) cannot be written in terms of the Meijer G-function or any other special function, and we are not aware of any implementations in numerical software that can evaluate general Fox H-functions.

In this subsection, we derive explicit series expansions for $\rho(r)$, $L(r)$ and $\psi(r)$, which both enable a numerical calculation and again highlight the power of Fox H-function as a useful mathematical tool. Note that for all three profiles we find $\Delta = 2m > 0$, with Δ defined in (3.9). This means that we can perform the integrations along the paths $\mathcal{C}_2$.

The form of the series expansions depends on the multiplicity of the poles of the gamma functions $\Gamma(b_j + B_j s)$. For $\rho(r)$ and $L(r)$, the poles of these gamma functions are found at $-k_1/2m$ and $-1/2-k_2$ with k_1 and k_2 any natural number. The gamma functions corresponding to the expression of the potential $\psi(r)$ contain the same poles with an additional pole at $1/2$. The good news is that each pole can at most occur twice, the bad news is that this happens quite often: for all integer m and rational $m = p/q$ where the denominator q of the fraction is odd, double poles do occur.

Let us first consider the case where m is non-rational or rational with an even denominator. The gamma functions then have simple poles, so that the expansions are power

series, given by Eq. (3.30). We find

$$\rho(r) = \frac{2m\,I_0\,b^m}{\sqrt{\pi}\,R_{\rm e}} \left[\sum_{k=1}^{\infty} \frac{\Gamma\left(\frac{1}{2}-\frac{k}{2m}\right)}{\Gamma\left(-\frac{k}{2m}\right)} \frac{(-1)^k}{k!} \frac{u^{k/m-1}}{2m} + \sum_{k=0}^{\infty} \frac{\Gamma(-m-2mk)}{\Gamma\left(-\frac{1}{2}-k\right)} \frac{(-1)^k}{k!} u^{2k} \right], \quad (3.61)$$

$$L(r) = \frac{4m\sqrt{\pi}\,I_0\,R_{\rm e}^2}{b^{2m}} \left[\sum_{k=1}^{\infty} \frac{\Gamma\left(\frac{1}{2}-\frac{k}{2m}\right)}{\Gamma\left(-\frac{k}{2m}\right)} \frac{(-1)^k}{k!} \frac{u^{k/m+2}}{k+2m} + \sum_{k=0}^{\infty} \frac{2\,\Gamma(-m-2mk)}{\Gamma\left(-\frac{1}{2}-k\right)} \frac{(-1)^k}{k!} \frac{u^{2k+3}}{2k+3} \right], \quad (3.62)$$

$$\psi(r) = \frac{2m\sqrt{\pi}\,G\Upsilon\,I_0\,R_{\rm e}}{b^m} \left[\sum_{k=1}^{\infty} \frac{\Gamma\left(-\frac{1}{2}-\frac{k}{2m}\right)}{\Gamma\left(-\frac{k}{2m}\right)} \frac{(-1)^k}{k!} \frac{u^{k/m+1}}{k+2m} + \sum_{k=0}^{\infty} \frac{2\,\Gamma(m-2mk)}{\Gamma\left(\frac{1}{2}-k\right)} \frac{(-1)^k}{k!} \frac{u^{2k}}{2k+1} \right]. \quad (3.63)$$

Notice that the term $k=0$ in the first sums is omitted, since the factors $\Gamma(0)$ in the denominator make those terms vanish. In fact, if m is a rational number p/q with q even, then the terms in the first sums for which $k = 0,\ p,\ 2p, \ldots$ vanish; if $p = 1$, these first sums vanish completely. A particularly interesting case is (again) $m = \frac{1}{2}$, where we find

$$\rho(r) = \frac{I_0\sqrt{b}}{\sqrt{\pi}\,R_{\rm e}} \sum_{k=0}^{\infty} \frac{(-1)^k}{k!} u^{2k} = \frac{I_0\sqrt{b}}{\sqrt{\pi}\,R_{\rm e}}\,{\rm e}^{-u^2}, \quad (3.64)$$

$$L(r) = \frac{4\sqrt{\pi}\,I_0\,R_{\rm e}^2}{b} \sum_{k=0}^{\infty} \frac{(-1)^k}{k!} \frac{u^{3+2k}}{2k+3} = \frac{\pi\,I_0\,R_{\rm e}^2}{b} \left[{\rm erf}\,u - \frac{2}{\sqrt{\pi}}\,u\,{\rm e}^{-u^2} \right], \quad (3.65)$$

$$\psi(r) = \frac{2\sqrt{\pi}\,G\Upsilon\,I_0\,R_{\rm e}}{\sqrt{b}} \sum_{k=0}^{\infty} \frac{(-1)^k}{k!} \frac{u^{2k}}{2k+1} = \frac{\pi\,G\Upsilon\,I_0\,R_{\rm e}}{\sqrt{b}}\,\frac{{\rm erf}\,u}{u}, \quad (3.66)$$

in agreement with formulae (3.58), (3.59) and (3.60).

When the Sérsic index m is integer or rational with an odd denominator, two of the gamma functions $\Gamma(b_j + B_j s)$ in $\rho(r)$, $L(r)$ and $\psi(r)$ share some of their poles, and the expansions of the Fox H-functions become logarithmic-power series of the form (3.39). If

we define $k_0 = (q+1)/2$, one obtains after quite some algebra

$$\rho(r) = \frac{2m\,I_0\,b^m}{\sqrt{\pi}\,R_\mathrm{e}} \left\{ \sum_{\substack{k=1 \\ k \bmod p \neq 0}}^{\infty} \frac{\Gamma\left(\frac{1}{2}-\frac{k}{2m}\right)}{\Gamma\left(-\frac{k}{2m}\right)} \frac{(-1)^k}{k!} \frac{u^{k/m-1}}{2m} + \right.$$
$$\sum_{\substack{k=0 \\ (k+k_0) \bmod q \neq 0}}^{\infty} \frac{\Gamma(-m-2mk)}{\Gamma\left(-\frac{1}{2}-k\right)} \frac{(-1)^k}{k!} u^{2k} - \frac{1}{\sqrt{\pi}} \sum_{\substack{k=0 \\ (k+k_0) \bmod q = 0}}^{\infty} \frac{(-1)^p}{2m} \frac{(2k+1)!}{(2km+m)!\,k!\,k!} \left(\frac{u}{2}\right)^{2k} \times$$
$$\left. \left[-\ln\left(\frac{u}{2}\right) + \psi(k+1) + m\,\psi(2km+m) - \psi(2k+1) \right] \right\}, \quad (3.67)$$

$$L(r) = \frac{4m\sqrt{\pi}\,I_0\,R_\mathrm{e}^2}{b^{2m}} \left\{ \sum_{\substack{k=1 \\ k \bmod p \neq 0}}^{\infty} \frac{\Gamma\left(\frac{1}{2}-\frac{k}{2m}\right)}{\Gamma\left(-\frac{k}{2m}\right)} \frac{(-1)^k}{k!} \frac{u^{k/m+2}}{k+2m} + \right.$$
$$\sum_{\substack{k=0 \\ (k+k_0) \bmod q \neq 0}}^{\infty} \frac{2\Gamma(-m-2mk)}{\Gamma\left(-\frac{1}{2}-k\right)} \frac{(-1)^k}{k!} \frac{u^{2k+3}}{2k+3} -$$
$$\frac{u^3}{\sqrt{\pi}} \sum_{\substack{k=0 \\ (k+k_0) \bmod q = 0}}^{\infty} \frac{(-1)^p}{2km+3m} \frac{(2k+1)!}{(2km+m)!\,k!\,k!} \left(\frac{u}{2}\right)^{2k} \times$$
$$\left. \left[-\ln\left(\frac{u}{2}\right) + \frac{1}{2k+3} + \psi(k+1) + m\,\psi(2km+m) - \psi(2k+1) \right] \right\}, \quad (3.68)$$

$$\psi(r) = \frac{2m\sqrt{\pi}\,G\,\Upsilon\,I_0\,R_\mathrm{e}}{b^m} \left\{ \sum_{\substack{k=1 \\ k \bmod p \neq 0}}^{\infty} \frac{\Gamma\left(-\frac{1}{2}-\frac{k}{2m}\right)}{\Gamma\left(-\frac{k}{2m}\right)} \frac{(-1)^k}{k!} \frac{u^{k/m+1}}{k+2m} + \frac{2\Gamma(m)}{\sqrt{\pi}} - \right.$$
$$\sum_{\substack{k=0 \\ (k+k_0) \bmod q \neq 0}}^{\infty} \frac{2\Gamma(-m-2mk)}{\Gamma\left(-\frac{1}{2}-k\right)} \frac{(-1)^k}{(k+1)!} \frac{u^{2k+2}}{2k+3} +$$
$$\frac{u^2}{\sqrt{\pi}} \sum_{\substack{k=0 \\ (k+k_0) \bmod q = 0}}^{\infty} \frac{(-1)^p}{2km+3m} \frac{(2k+1)!}{(2km+m)!\,k!\,(k+1)!} \left(\frac{u}{2}\right)^{2k} \times$$
$$\left. \left[-\ln\left(\frac{u}{2}\right) + \frac{1}{2k+2} + \frac{1}{2k+3} + \psi(k+1) + m\,\psi(2km+m) - \psi(2k+1) \right] \right\}. \quad (3.69)$$

In these expressions, we again used the digamma function (3.38). In $\psi(r)$, the third term $2\Gamma(m)/\sqrt{\pi}$ corresponds with the residue of the pole $\frac{1}{2}$. Again, the terms in the first sums for which $k = 0,\ p,\ 2p, \ldots$ vanish, and these first sums vanish completely if $p = 1$. On the other hand, if $q = 1$, i.e. if m is an integer value, the second sums vanish, since then the integrands for $\rho(r)$ and $L(r)$ have no simple poles β_{2,k_2}, while for $\psi(r)$ only the pole $\frac{1}{2}$ remains as a single pole. On the crossroad of these two cases we have $m = 1$: for this model, both the first and second sums in the expansions (3.67) - (3.69) vanish completely, apart from a single term for the potential. Astrophysically, the Sérsic model with $m = 1$ corresponds to a model with an exponential surface brightness profile, often used for the description of low-luminosity elliptical galaxies and pseudo-bulges. Baes & Gentile (2011) calculated the luminosity density of the exponential model by directly deprojecting the surface brightness profile and through its representation as a Meijer G-function. For the luminosity density we get

$$\rho(r) = \frac{I_0\, b}{\pi\, R_\mathrm{e}} \sum_{k=0}^{\infty} \frac{1}{k!\, k!} \left(\frac{u}{2}\right)^{2k} \left[-\ln\left(\frac{u}{2}\right) + \psi(k+1)\right] = \frac{I_0\, b}{\pi\, R_\mathrm{e}}\, K_0(u), \tag{3.70}$$

with $K_\nu(z)$ the modified Bessel function of the second kind (Section 8.4 in Gradshteyn & Ryzhik 1965). This expression is in agreement with equation (24) of Baes & Gentile (2011). Similarly, we obtain for the cumulative luminosity

$$\begin{aligned} L(r) &= \frac{4\, I_0\, R_\mathrm{e}^2}{b^2} \sum_{k=0}^{\infty} \frac{8}{(2k+3)\, k!\, k!} \left(\frac{u}{2}\right)^{2k+3} \left[-\ln\left(\frac{u}{2}\right) + \frac{1}{2k+3} + \psi(k+1)\right] \\ &= \frac{2\pi\, I_0\, R_\mathrm{e}^2}{b^2}\, u \left[K_2(u)\, L_1(u) + K_1(u)\, L_2(u) - \frac{4}{3\pi}\, u\, K_1(u)\right], \end{aligned} \tag{3.71}$$

with $L_\nu(u)$ the modified Struve function (Section 8.5 in Gradshteyn & Ryzhik 1965). Finally, for the potential of the exponential model we get the expansion

$$\begin{aligned} \psi(r) &= \frac{4G\Upsilon\, I_0\, R_\mathrm{e}}{b} \left\{1 - \sum_{k=0}^{\infty} \frac{2}{(2k+3)\, k!\, (k+1)!} \left(\frac{u}{2}\right)^{2k+2} \times \right. \\ &\left. \left[-\ln\left(\frac{u}{2}\right) + \frac{1}{2k+3} + \frac{1}{2k+2} + \psi(k+1)\right]\right\} \\ &= \frac{2\pi G\Upsilon\, I_0\, R_\mathrm{e}}{b} \left[K_2(u)\, L_1(u) + K_1(u)\, L_2(u) + \frac{2}{3\pi}\, u\, K_1(u)\right]. \end{aligned} \tag{3.72}$$

These last two expressions can also be obtained by substituting the luminosity density (3.70) into the recipes (3.54) and (3.55).

3.4.4 Asymptotic behaviour

With all the explicit power series of Section 3.4.3 available, it is fairly straightforward to examine the asymptotic behaviour of the spatial function of the Sérsic model at small

radii, generalizing the results of Baes & Gentile (2011). The density has the following rich behaviour, depending on the value of m:

$$\rho(r) \sim \frac{I_0\, b^m}{\pi\, R_\mathrm{e}} \left[\Gamma(1-m) + \frac{1}{2}\,\Gamma(1-3m)\, u^2\right] \qquad \text{for } 0 < m < \tfrac{1}{3} \text{ or } m = \tfrac{1}{2}, \tag{3.73a}$$

$$\rho(r) \sim \frac{I_0\, b^{1/3}}{\pi\, R_\mathrm{e}} \left[\Gamma\left(\frac{2}{3}\right) - \frac{1}{2}\left(3\ln\left(\frac{u}{2}\right) + \gamma + \frac{3}{2}\right) u^2\right] \qquad \text{for } m = \tfrac{1}{3}, \tag{3.73b}$$

$$\rho(r) \sim \frac{I_0\, b^m}{\pi\, R_\mathrm{e}} \left[\Gamma(1-m) + \frac{\sqrt{\pi}}{2m}\, \frac{\Gamma\left(\frac{1}{2} - \frac{1}{2m}\right)}{\Gamma\left(1 - \frac{1}{2m}\right)}\, u^{1/m-1}\right] \qquad \text{for } \tfrac{1}{3} < m < 1 \text{ and } m \neq \tfrac{1}{2}, \tag{3.73c}$$

$$\rho(r) \sim \frac{I_0\, b}{\pi\, R_\mathrm{e}} \left[-\ln\left(\frac{u}{2}\right) - \gamma\right] \qquad \text{for } m = 1, \tag{3.73d}$$

$$\rho(r) \sim \frac{I_0\, b^m}{\sqrt{\pi}\, R_\mathrm{e}}\, \frac{1}{2m}\, \frac{\Gamma\left(\frac{1}{2} - \frac{1}{2m}\right)}{\Gamma\left(1 - \frac{1}{2m}\right)}\, u^{1/m-1} \qquad \text{for } m > 1. \tag{3.73e}$$

with again γ the Euler-Mascheroni constant. The luminosity behaves as

$$L(r) \sim \frac{4\, I_0\, R_\mathrm{e}^2}{3\, b^{2m}}\, \Gamma(1-m)\, u^3 \qquad \text{for } m < 1, \tag{3.74a}$$

$$L(r) \sim \frac{4\, I_0\, R_\mathrm{e}^2}{3\, b^2} \left[-\ln\left(\frac{u}{2}\right) - \gamma + \frac{1}{3}\right] u^3 \qquad \text{for } m = 1, \tag{3.74b}$$

$$L(r) \sim \frac{I_0\, R_\mathrm{e}^2}{b^{2m}}\, \frac{2\sqrt{\pi}}{2m+1}\, \frac{\Gamma\left(\frac{1}{2} - \frac{1}{2m}\right)}{\Gamma\left(1 - \frac{1}{2m}\right)}\, u^{1/m+2} \qquad \text{for } m > 1. \tag{3.74c}$$

Finally, the potential approaches $r \to 0$ as

$$\psi(r) \sim \frac{G\Upsilon I_0 R_\mathrm{e}}{b^m}\left[4\Gamma(1+m) - \frac{2}{3}\Gamma(1-m)\,u^2\right] \qquad \text{for } m<1, \tag{3.75a}$$

$$\psi(r) \sim \frac{G\Upsilon I_0 R_\mathrm{e}}{b}\left[4 + \frac{2}{3}\left(\ln\left(\frac{u}{2}\right)+\gamma-\frac{5}{6}\right)u^2\right] \qquad \text{for } m=1, \tag{3.75b}$$

$$\psi(r) \sim \frac{G\Upsilon I_0 R_\mathrm{e}}{b^m}\left[4\Gamma(1+m) + \frac{\sqrt{\pi}}{2m+1}\,\frac{\Gamma\left(-\frac{1}{2}-\frac{1}{2m}\right)}{\Gamma\left(1-\frac{1}{2m}\right)}\,u^{1/m+1}\right] \qquad \text{for } m>1. \tag{3.75c}$$

If we set $r=0$ in the expressions (3.75), we recover the central potential

$$\psi_0 = \frac{4G\Upsilon I_0 R_\mathrm{e}}{b^m}\,\Gamma(m+1), \tag{3.76}$$

for every real value $m>0$, in agreement with Eq. (12) of Ciotti (1991).

3.5 Analytical expressions for the Einasto model

3.5.1 Introduction

Einasto models (Einasto & Haud 1989) are closely related to Sérsic profiles, so that we can study their analytical properties in a similar way. Einasto profiles have gradually gained popularity in the description of simulated dark matter haloes (Navarro et al. 2004; Merritt et al. 2005; Merritt et al. 2006; Graham et al. 2006; Gao et al. 2008; Duffy et al. 2008; Stadel et al. 2009; Navarro et al. 2010), as their central behaviour appears in some cases to match high-resolution simulations more closely than double power-law models (which we will study in the next chapters). Nevertheless, there is still tension with observations of dwarf galaxies, which favour density profiles with a flat central core, a discrepancy known as the cusp-core problem (see de Blok 2010 for a review).

Some aspects of the Einasto model have been presented by several authors (Mamon & Łokas 2005; Cardone et al. 2005; Merritt et al. 2006; Dhar & Williams 2010). The most complete study of the properties of the Einasto model is the work by Cardone et al. (2005), who provide a set of analytical expressions for quantities such as the mass profile and gravitational potential and discuss the dynamical structure for both isotropic and anisotropic cases. Nevertheless, the Einasto model has not been studied analytically as extensively as the Sérsic models, and several properties still have to be further investigated in more detail.

The most important lacuna concerns the surface density on the plane of the sky, an important quantity that defines the lensing properties of a dark matter halo. Since gravitational lensing is an important tool to investigate the differences between theory and observation, we will also provide analytical formulae that describe the lensing properties of Einasto models. We published these results as part of a collaboration (Retana-Montenegro et al. 2012), and in the following sections we will focus on our work within this study.

3.5.2 Analytical properties of the Einasto model

Spatial properties

The Einasto profile is characterized by a power-law logarithmic slope,

$$\gamma(r) \equiv -\frac{\mathrm{d}\ln\rho}{\mathrm{d}\ln r}(r) \propto r^{1/n}, \tag{3.77}$$

with n, which we call the Einasto index, a positive number defining the steepness of the power-law. Integrating leads to the general density profile

$$\rho(r) = \rho_\mathrm{s} \exp\left\{-d_n\left[\left(\frac{r}{r_\mathrm{s}}\right)^{1/n} - 1\right]\right\}, \tag{3.78}$$

where r_s represents the radius of the sphere that contains half of the total mass, ρ_s is the mass density at $r = \mathrm{r_s}$, and d_n is a numerical constant that ensures that r_s is indeed the half-mass radius. Equivalently, we can write

$$\rho(r) = \rho_0 \exp\left[-\left(\frac{r}{h}\right)^{1/n}\right]. \tag{3.79}$$

Here, we introduced the central density

$$\rho_0 = \rho_s\, \mathrm{e}^{d_n}, \tag{3.80}$$

and the scale length

$$h = \frac{r_\mathrm{s}}{d_n^n}. \tag{3.81}$$

The total mass that corresponds with the Einasto density can be found as

$$M = 4\pi\,\rho_0\, h^3\, n\,\Gamma(3n). \tag{3.82}$$

If we use this formula to replace the central density ρ_0 by the total mass M as a parameter in the definition of the Einasto models, we get

$$\rho(r) = \frac{M}{4\pi\, h^3\, n\,\Gamma(3n)}\, \mathrm{e}^{-s^{1/n}}, \tag{3.83}$$

with

$$s = (d_n)^n \, \frac{r}{r_s} = \frac{r}{h}. \tag{3.84}$$

At small radii, the density profile behaves as

$$\rho(r) = \frac{M}{4\pi \, h^3 \, n \Gamma(3n)} \left(1 - s^{1/n} + \cdots\right). \tag{3.85}$$

The cumulative mass profile

$$M(r) = 4\pi \int_0^r \rho(r') \, r'^2 \, \mathrm{d}r', \tag{3.86}$$

is then, for the Einasto density,

$$M(r) = M \left[1 - \frac{\Gamma(3n, s^{1/n})}{\Gamma(3n)}\right], \tag{3.87}$$

where $\Gamma(\alpha, x)$ is the incomplete gamma function,

$$\Gamma(\alpha, x) = \int_x^\infty t^{\alpha-1} \, \mathrm{e}^{-t} \, \mathrm{d}t. \tag{3.88}$$

Given the radius of the sphere that encloses half of the total mass, we find that d_n is the (numerical) solution of the equation

$$2\,\Gamma(3n, d_n) = \Gamma(3n). \tag{3.89}$$

The spherical gravitational potential can be calculated from Eq. (3.87)

$$\psi(r) = \int_r^\infty \frac{M(r')}{r'^2} \, \mathrm{d}r', \tag{3.90}$$

and we obtain the profile

$$\psi(r) = \frac{GM}{h} \, s^{-1} \left[1 - \frac{\Gamma(3n, s^{1/n})}{\Gamma(3n)} + \frac{s\,\Gamma(2n, s^{1/n})}{\Gamma(3n)}\right]. \tag{3.91}$$

Evidently, the Einasto model has a finite potential well, given by

$$\psi_0 = \frac{GM}{h} \, \frac{\Gamma(2n)}{\Gamma(3n)}. \tag{3.92}$$

Projected properties

The surface mass density of a spherically symmetric lens is given by integrating along the line of sight of the 3D density profile:

$$\Sigma(R) = 2\int_R^\infty \frac{\rho(r)\, r\, \mathrm{d}r}{\sqrt{r^2 - R^2}}. \tag{3.93}$$

Inserting Eq. (3.79) into the above expression, we obtain

$$\Sigma(x) = 2\,\rho_0\, h \int_x^\infty \frac{\mathrm{e}^{-s^{1/n}}\, s\, \mathrm{d}s}{\sqrt{s^2 - x^2}}, \tag{3.94}$$

where we have introduced the quantities $x = R/h$ and $s = r/h$.

As discussed by Cardone et al. (2005) and Dhar & Williams (2010), the integral (3.94) cannot be expressed in terms of elementary or even the most regular functions for all the values of n. Only the central surface mass density can be evaluated analytically as

$$\Sigma(0) = 2n\,\rho_0\, h\, \Gamma(n)\,. \tag{3.95}$$

This situation is very similar to the deprojection of the Sérsic surface brightness profile. The obvious similarity between these two cases invites us to apply the same Mellin transform technique as for the Sérsic profiles. We obtain

$$\Sigma(x) = 2n\sqrt{\pi}\,\rho_0\, h\, x\, \frac{1}{2\pi i}\int_{\mathcal{C}} \frac{\Gamma(2ny)\,\Gamma\left(-\frac{1}{2}+y\right)}{\Gamma(y)} \left[x^2\right]^{-y} \mathrm{d}y. \tag{3.96}$$

which can be written in the following compact form

$$\Sigma(x) = 2n\sqrt{\pi}\,\rho_0\, h\, x\, H^{2,0}_{1,2}\left(x^2 \,\middle|\, \begin{matrix}(0,1)\\ (0,2n),(-\frac{1}{2},1)\end{matrix}\right). \tag{3.97}$$

An important quantity for gravitational lensing studies is the cumulative surface mass density, i.e. the total mass contained in a infinite cylinder with radius R,

$$M(R) = 2\pi \int_0^R \Sigma(R')\, R'\, \mathrm{d}R'. \tag{3.98}$$

We find,

$$M(x) = 2n\,\pi^{3/2}\,\rho_0\, h^3\, x^3\, H^{2,1}_{2,3}\left(x^2 \,\middle|\, \begin{matrix}(-\frac{1}{2},1),(0,1)\\ (0,2n),(-\frac{1}{2},1),(-\frac{3}{2},1)\end{matrix}\right). \tag{3.99}$$

Lensing properties

In the context of spherically symmetric lenses, the *deflection angle* of a gravitational lens is defined as (Schneider et al. 1992)

$$\alpha(x) = \frac{2}{x}\int_0^x x' \frac{\Sigma(x')}{\Sigma_{\rm crit}}\,{\rm d}x' = \frac{2}{x}\int_0^x x'\,\kappa(x')\,{\rm d}x', \tag{3.100}$$

where

$$\kappa = \frac{\Sigma(x)}{\Sigma_{\rm crit}}, \tag{3.101}$$

is the convergence and $\Sigma_{\rm crit}$ is the critical surface mass density defined by

$$\Sigma_{\rm crit} \equiv \frac{c^2\,D_{\rm S}}{4\pi\,G\,D_{\rm L}\,D_{\rm LS}}, \tag{3.102}$$

with c the speed of light, G the gravitational constant, and $D_{\rm L}$, $D_{\rm S}$ and $D_{\rm LS}$ are the angular distances from observer to lens, from observer to source, and from lens to source, respectively. Evidently, the deflection angle is related to the integrated mass as

$$\alpha(x) = \frac{M(x)}{\pi\,h^2\,\Sigma_{\rm crit} x}. \tag{3.103}$$

Introducing the central convergence, $\kappa_{\rm c}$, a parameter that determines the lensing properties of the Einasto profile,

$$\kappa_{\rm c} \equiv \frac{\Sigma(0)}{\Sigma_{\rm crit}} = \frac{2\,\rho_0\,h\,n\,\Gamma(n)}{\Sigma_{\rm crit}}, \tag{3.104}$$

we can write $\alpha(x)$ in the form

$$\alpha(x) = \frac{\kappa_{\rm c}\sqrt{\pi}}{\Gamma(n)}\,x^2\,H^{2,1}_{2,3}\left(x^2\,\middle|\,\begin{matrix}(-\frac{1}{2},1),(0,1)\\(0,2n),(-\frac{1}{2},1),(-\frac{3}{2},1)\end{matrix}\right). \tag{3.105}$$

with a completely analogous behaviour as $M(x)$ in Eq. (3.99).

The *deflection potential* $\bar{\psi}(x)$ for a spherically symmetric lens is the integral of the deflection angle

$$\bar{\psi}(x) = \int_0^x \alpha(x')\,{\rm d}x'. \tag{3.106}$$

Inserting Eq. (3.99) into (3.106), we obtain again a result that can be re-expressed as a Fox H-function

$$\bar{\psi}(x) = \frac{\kappa_{\rm c}\sqrt{\pi}}{2\Gamma(n)}\,x^3\,H^{2,2}_{3,4}\left(x^2\,\middle|\,\begin{matrix}(-\frac{1}{2},1),(-\frac{1}{2},1),(0,1)\\(0,2n),(-\frac{1}{2},1),(-\frac{3}{2},1),(-\frac{3}{2},1)\end{matrix}\right). \tag{3.107}$$

For other lensing properties of the Einasto profile, such as magnification and shear, we refer to Retana-Montenegro et al. (2012).

3.5.3 Explicit series expansions

The derivation of the series expansions for $\Sigma(x)$, $M(x)$ and $\bar{\psi}(x)$ is completely analogous to the Sérsic case. We find $\Delta = 2n > 0$, so that we have to choose again the integration path $\mathcal{C}_2$. Likewise, the form of the series expansion depends on the multiplicity of the poles of the gamma functions $\Gamma(b_j + B_j s)$. These poles are $-k_1/2n$ and $1/2 - k_2$, with k_1 and k_2 any natural number. We encounter again two cases:

Case 1: if n is either non-rational or a rational number p/q with an even denominator (and p, q coprime), all poles are simple and the expansion is a power series (3.30),

$$\Sigma(x) = 2n\sqrt{\pi}\,\rho_0\,h\left[\sum_{k=1}^{\infty}\frac{\Gamma\left(-\frac{1}{2}-\frac{k}{2n}\right)}{\Gamma\left(-\frac{k}{2n}\right)}\,\frac{(-1)^k}{k!}\,\frac{x^{k/n+1}}{2n} + \sum_{k=0}^{\infty}\frac{\Gamma(n-2nk)}{\Gamma\left(\frac{1}{2}-k\right)}\,\frac{(-1)^k}{k!}\,x^{2k}\right], \quad (3.108)$$

the mass is

$$M(x) = 2n\,\pi^{3/2}\,\rho_0\,h^3\left[-\sum_{k=1}^{\infty}\frac{\Gamma\left(-\frac{3}{2}-\frac{k}{2n}\right)}{\Gamma\left(-\frac{k}{2n}\right)}\,\frac{(-1)^k}{k!}\,\frac{x^{k/n+3}}{2n} + \sum_{k=0}^{\infty}\frac{\Gamma(n-2nk)}{\Gamma\left(\frac{1}{2}-k\right)}\,\frac{(-1)^k}{(k+1)!}\,x^{2k+2}\right], \quad (3.109)$$

and the deflection potential is

$$\bar{\psi}(x) = \frac{\kappa_{\rm c}\sqrt{\pi}}{2\,\Gamma(n)}\left[-\sum_{k=1}^{\infty}\frac{\Gamma\left(-\frac{3}{2}-\frac{k}{2n}\right)}{\Gamma\left(-\frac{k}{2n}\right)}\,\frac{(-1)^k}{k!}\,\frac{x^{k/n+3}}{3n+k} + \sum_{k=0}^{\infty}\frac{\Gamma(n-2nk)}{\Gamma\left(\frac{1}{2}-k\right)}\,\frac{(-1)^k}{(k+1)!}\,\frac{x^{2k+2}}{k+1}\right]. \quad (3.110)$$

Case 2: if n is integer or a rational number p/q with an odd denominator, some poles are of second order, and the expansion is a logarithmic-power series (3.39). If we define

$k_0 = \frac{q-1}{2}$, then we obtain after some algebra,

$$\Sigma(x) = 2n\sqrt{\pi}\,\rho_0\,h\left[\sum_{\substack{k=1\\ k \bmod p\neq 0}}^{\infty} \frac{\Gamma\left(-\frac{1}{2}-\frac{k}{2n}\right)}{\Gamma\left(-\frac{k}{2n}\right)}\,\frac{(-1)^k}{k!}\,\frac{x^{k/n+1}}{2n} + \frac{\Gamma(n)}{\sqrt{\pi}} + \sum_{\substack{k=1\\ (k+k_0) \bmod q\neq 0}}^{\infty} \frac{\Gamma(n-2nk)}{\Gamma\left(\frac{1}{2}-k\right)}\,\frac{(-1)^k}{k!}\,x^{2k}\right] + 2\,\rho_0\,h \sum_{\substack{k=0\\ (k+k_0) \bmod q=0}}^{\infty} \frac{(-1)^p\,(2k)!}{(2nk-n)!\,k!\,k!}\left(\frac{x}{2}\right)^{2k} \times \left[-\ln\left(\frac{x}{2}\right) - \frac{1}{2k} + \psi(k+1) + n\,\psi(2nk-n) - \psi(2k-1)\right], \quad (3.111)$$

for the mass we find

$$M(x) = 2n\,\pi^{3/2}\,\rho_0\,h^3\,x^2\left[-\sum_{\substack{k=1\\ k \bmod p\neq 0}}^{\infty} \frac{\Gamma\left(-\frac{3}{2}-\frac{k}{2n}\right)}{\Gamma\left(-\frac{k}{2n}\right)}\,\frac{(-1)^k}{k!}\,\frac{x^{k/n+1}}{2n} + \frac{\Gamma(n)}{\sqrt{\pi}} + \sum_{\substack{k=1\\ (k+k_0) \bmod q\neq 0}}^{\infty} \frac{\Gamma(n-2nk)}{\Gamma\left(\frac{1}{2}-k\right)}\,\frac{(-1)^k}{(k+1)!}\,x^{2k}\right] + 2\pi\,\rho_0\,h^3\,x^2 \sum_{\substack{k=0\\ (k+k_0) \bmod q=0}}^{\infty} \frac{(-1)^p\,(2k)!}{(2nk-n)!\,k!\,(k+1)!}\left(\frac{x}{2}\right)^{2k} \times \left[-\ln\left(\frac{x}{2}\right) - \frac{1}{2k} - \frac{1}{2k+2} + \psi(k+2) + n\,\psi(2nk-n) - \psi(2k-1)\right], \quad (3.112)$$

and the deflection potential becomes

$$\bar{\psi}(x) = \frac{\kappa_c\sqrt{\pi}}{2\Gamma(n)}\,x^2\left[-\sum_{\substack{k=1\\ k \bmod p\neq 0}}^{\infty} \frac{\Gamma\left(-\frac{3}{2}-\frac{k}{2n}\right)}{\Gamma\left(-\frac{k}{2n}\right)}\,\frac{(-1)^k}{k!}\,\frac{x^{k/n+1}}{3n+k} + \frac{\Gamma(n)}{\sqrt{\pi}} + \sum_{\substack{k=1\\ (k+k_0) \bmod q\neq 0}}^{\infty} \frac{\Gamma(n-2nk)}{\Gamma\left(\frac{1}{2}-k\right)}\,\frac{(-1)^k}{(k+1)!}\,\frac{x^{2k}}{k+1}\right] + \frac{\kappa_c}{2\Gamma(n)}\,x^2 \sum_{\substack{k=0\\ (k+k_0) \bmod q=0}}^{\infty} \frac{(-1)^p\,(2k)!}{(2nk-n)!\,(k+1)!\,(k+1)!}\left(\frac{x}{2}\right)^{2k} \times \left[-\ln\left(\frac{x}{2}\right) - \frac{1}{2k} + \psi(k+2) + n\,\psi(2nk-n) - \psi(2k-1)\right]. \quad (3.113)$$

For particular values of n, these series will simplify and reduce to more elementary functions. Examples for simple cases like $n = 1$ and $n = 1/2$ are given in Retana-Montenegro et al. (2012).

3.5.4 Asymptotic behaviour

The series expansions allow us to directly investigate the behaviour of Einasto models at small radii. It follows that the central asymptotic behaviour of the surface density $\Sigma(x)$ depends on the value of n. If $n < 1$, we find the following expansion at small radii $(x \ll 1)$

$$\Sigma(x) \sim \rho_0\, h \left[2\Gamma(n+1) + \Gamma(1-n)\, x^2 \right]. \tag{3.114}$$

If $n = 1$, then the expansion has the form

$$\Sigma(x) \sim \rho_0\, h \left[2 + \left(2\ln\left(\tfrac{1}{2}\right) - 1 \right) x^2 \right]. \tag{3.115}$$

Finally, if $n > 1$, the central surface density behaves as

$$\Sigma(x) \sim \rho_0\, h \left[2\Gamma(n+1) - \frac{\sqrt{\pi}}{n+1}\, \frac{\Gamma\left(\frac{n-1}{2n}\right)}{\Gamma\left(\frac{2n-1}{2n}\right)}\, x^{1+\frac{1}{n}} \right]. \tag{3.116}$$

The behaviour of the cumulative surface mass $M(x)$ is more straightforward. At small radii, we find the asymptotic expression

$$M(x) \sim 2\pi\, \rho_0\, h^3\, \Gamma(n+1)\, x^2. \tag{3.117}$$

The slope is not unexpected, given that the Einasto models have a finite central surface mass density. The asymptotic behaviour of the Fox H-function at large radii is described in Kilbas & Saigo (1999). We obtain the following expansions $(x \gg 1)$

$$\Sigma(x) \sim \sqrt{8n\,\pi}\, \rho_0\, h\, \mathrm{e}^{-x^{1/n}}\, x^{1-\frac{1}{2n}}, \tag{3.118}$$

and

$$M(x) \sim 4\pi\, \rho_0\, h^3\, n\, \Gamma(3n) - 2(2\pi n)^{3/2}\, \rho_0\, h^3\, \mathrm{e}^{-x^{1/n}}\, x^{3-\frac{3}{2n}}. \tag{3.119}$$

3.5.5 Conclusions

As we demonstrated, the Fox H-functions are a powerful tool obtain analytical expression for various quantities related to well-known theoretical models, in casu Sérsic and Einasto profiles. These expressions can be readily implemented in numerical codes for arbitrary-precision calculations; moreover, they enable us to derive the asymptotic behaviour of these functions in a straightforward manner, which is very helpful to understand their properties.

In the next chapter, we return to our dynamical modelling problem. As we said, our aim is to construct a family of sophisticated yet analytically tractable DF components. The Fox H-functions will prove invaluable for this task.

Chapter 4

A DF family of Fox H-components

We now have all the necessary mathematical tools to construct a family of distribution functions, which will generate models with a very general 4-parameter anisotropy profile. These DFs themselves form self-consistent Veltmann models, and will serve as base functions to build more general dynamical models. The results in this chapter are published in Baes & van Hese (2007). The specific DFs for the Plummer and Hernquist models were worked out by M. Baes; the rest of the material was developed by the author.

4.1 Motivation

In Section 2.4, we outlined our method to construct DFs as linear combinations of base components, $F(E,L)=\sum_{i=1}^{N}F_i(E,L)$, each of which have separable augmented densities that generate the same a priori given anisotropy profile,

$$\tilde{\rho}_i(\psi,r)=f_i(\psi)\,g(r), \tag{4.1}$$

$$\beta(r)=-\frac{1}{2}\frac{\mathrm{d}\ln g}{\mathrm{d}\ln r}(r). \tag{4.2}$$

As we stated, the existing set of components (2.175) that was already implemented, is not sufficiently general for our purposes. Indeed, we would like our base functions to be capable of fitting a wide variety of gravitational systems. In particular, we wish to optimize them to model the large family of double power-law densities, also referred to as the Zhao models or $\alpha\beta\gamma$-models (Hernquist 1990 ; Zhao 1996),

$$\rho(r)=\frac{\rho_\mathrm{s}}{(r/r_\mathrm{s})^{\gamma_0}\left(1+(r/r_\mathrm{s})^{\eta}\right)^{(\gamma_\infty-\gamma_0)/\eta}}. \tag{4.3}$$

These densities have an central slope γ_0, an outer slope γ_∞, a transition rate η, a scale radius r_s and a factor ρ_s defined so that $\rho_\mathrm{s}=2^{(\gamma_\infty-\gamma_0)/\eta}\rho(r_\mathrm{s})$. With the auxiliary notation

$$\chi=\frac{(r/r_\mathrm{s})^{\eta}}{1+(r/r_\mathrm{s})^{\eta}}, \tag{4.4}$$

we can write these densities in the form

$$\rho(r) = \rho_\mathrm{s}\left(\chi^{-\gamma_0/\eta}(1-\chi)^{\gamma_\infty/\eta}\right), \tag{4.5}$$

or in terms of the logarithmic slope,

$$\gamma(r) = -\frac{\mathrm{d}\ln\rho}{\mathrm{d}\ln r}(r) = \frac{\gamma_0+\gamma_\infty\,(r/r_\mathrm{s})^\eta}{1+(r/r_\mathrm{s})^\eta} = \gamma_0(1-\chi)+\gamma_\infty\chi. \tag{4.6}$$

The corresponding integrated mass can be easily calculated,

$$M(r) = \frac{4\pi}{\eta}\rho_\mathrm{s}r_\mathrm{s}^3\,B_\chi\left(\frac{3-\gamma_0}{\eta},\frac{\gamma_\infty-3}{\eta}\right), \tag{4.7}$$

where we used the incomplete beta function

$$B_x(a,b) = \int_0^x t^{a-1}(1-t)^{b-1}\,\mathrm{d}t = x^a\sum_{n=0}^{\infty}\frac{(1-b)_n}{n!\,(a+n)}x^n. \tag{4.8}$$

As required, systems with $\gamma_\infty > 3$ have a finite mass at infinite radius. In self-consistent systems, the double power-law densities are, through Poisson's equation, equivalent with the gravitational potentials (Zhao 1996)

$$\psi(r) = \frac{4\pi G}{\eta}\rho_\mathrm{s}r_\mathrm{s}^2\left[\frac{r_\mathrm{s}}{r}B_\chi\left(\frac{3-\gamma_0}{\eta},\frac{\gamma_\infty-3}{\eta}\right)+B_{1-\chi}\left(\frac{\gamma_\infty-2}{\eta},\frac{2-\gamma_0}{\eta}\right)\right]. \tag{4.9}$$

These potentials are thus analytically tractable; also note the condition $0\leqslant\gamma_0\leqslant 2$. The family encompasses a wide variety of profiles, including some of the best-known systems:

$(\gamma_0,\gamma_\infty,\eta)$	Name	Reference
$(0,5,2)$	Plummer sphere	Plummer (1911)
$(1,4,1)$	Hernquist profile	Hernquist (1990)
$(2,4,1)$	Jaffe profile	Jaffe (1983)
$(1,3,1)$	NFW profile	Navarro et al. (1997)
$(2-\eta,3+\eta,\eta)$	α-profile	Veltmann (1979)
$(\gamma,4,1)$	γ-profile	Dehnen (1993)
$(1-\eta/2+\beta_0,3+\eta,\eta)$	Dehnen-McLaughlin profile	Dehnen & McLaughlin (2005)

More importantly, we wish to create base functions that generate observationally realistic anisotropy profiles. The logical choice is an extension of the profiles generated by the generalized Plummer functions Eq. (2.176). The obvious generalization is

$$\beta(r) = \frac{\beta_0+\beta_\infty\,(r/r_\mathrm{a})^{2\delta}}{1+(r/r_\mathrm{a})^{2\delta}}, \tag{4.10}$$

with $0 < \delta \leqslant 1$. These profiles extend the anisotropies described in Eq. (2.171), as well as the Cuddeford anisotropies (2.167). Furthermore, when combined with the density slopes Eq. (4.6), they allow the construction of dynamical models where $\beta(r)$ is a linear function of $\gamma(r)$; this occurs when $\eta = 2\delta$ and $r_\mathrm{a} = r_\mathrm{s}$. Numerical simulations have revealed that dark matter haloes obey this striking relation (Hansen & Moore 2006), and it is one of the key features of the dynamical models that we will create in Chapter 6.

To summarize, we want to construct separable augmented densities for which the DFs can be computed analytically, yet are sophisticated enough to

1. generate the $\beta(r)$ profiles of Eq. (4.10);
2. be able to model densities with either central cusps or cores;
3. be able to model systems with either finite or infinite extent;
4. be optimized to model the family of double power-law profiles of Eq. (4.3).

These requirements lead quite naturally to a family of base functions of the form

$$\tilde{\rho}(\psi, r) = \rho_0 \left(\frac{\psi - E_0}{\psi_0 - E_0}\right)^p \left[1 - \left(\frac{\psi - E_0}{\psi_0 - E_0}\right)^s\right]^q \left(\frac{r}{r_\mathrm{a}}\right)^{-2\beta_0} \left(1 + \frac{r^{2\delta}}{r_\mathrm{a}^{2\delta}}\right)^{\beta_\delta}, \tag{4.11}$$

for $\psi > E_0$, with

$$\beta_\delta = \frac{\beta_0 - \beta_\infty}{\delta}. \tag{4.12}$$

In other words, we have a separable system with

$$f(\psi) = \rho_0 \left(\frac{\psi - E_0}{\psi_0 - E_0}\right)^p \left[1 - \left(\frac{\psi - E_0}{\psi_0 - E_0}\right)^s\right]^q, \tag{4.13}$$

$$g(r) = \left(\frac{r}{r_\mathrm{a}}\right)^{-2\beta_0} \left(1 + \frac{r^{2\delta}}{r_\mathrm{a}^{2\delta}}\right)^{\beta_\delta}, \tag{4.14}$$

with $g(r)$ derived from (4.2) and (4.10). These functions have a normalizing factor ρ_0 and eight parameters: $E_0 = \psi(r_\mathrm{max})$ determines the extent, for a given potential $\psi(r)$, $p \geqslant 0$ controls the behaviour at large radii, $q \leqslant 0$ controls the inner slope (where we assume that the potential is finite at the centre), $s > 0$ defines a transition rate between them, and the four remaining parameters β_0, β_∞, δ and r_a generate the anisotropy profile. Note that the central behaviour of the density not only depends on q, but also on β_0.

If the functions extend to infinity, i.e. $E_0 = 0$, we have to ensure a finite total mass. On the other hand, if $E_0 > 0$, we impose that the corresponding DF is zero at the boundary $E = E_0$. This leads to the following conditions:

$$p + 2\beta_\infty > 3 \qquad \text{if } E_0 = 0, \tag{4.15}$$

$$p + \beta_\infty > 3/2 \qquad \text{if } E_0 > 0, \tag{4.16}$$

where the latter condition can be seen by inspection of the DF series expansion in Eq. (4.54) in Section 4.2.2. Of course, one can trivially extend these augmented densities to more general $\beta(r)$ profiles by taking finite sums

$$g(r) = \sum_{j=1}^{n} c_j g_j(r), \tag{4.17}$$

with c_j positive constants and $g_j(r)$ of the form (4.14) but each with different parameter values. We will not consider such extensions in the rest of this dissertation.

While the augmented densities (4.11) are particularly suitable to fit double power-law profiles, they can be used without problems for other densities, as we will demonstrate in Chapter 7.

In the following sections, we will derive the DF and moments that correspond with these components. We start with a detailed calculation of the distribution function.

4.2 Derivation of the distribution function

4.2.1 Integral form

Let us first tackle the simpler function

$$\tilde{\rho}(\psi, r) = \rho_0 \left(\frac{\psi - E_0}{\psi_0 - E_0}\right)^p \left(\frac{r}{r_\mathrm{a}}\right)^{-2\beta_0} \left(1 + \frac{r^{2\delta}}{r_\mathrm{a}^{2\delta}}\right)^{\beta_\delta}. \tag{4.18}$$

We have to consider several cases, depending on the parameter β_δ.

Case 1: β_δ is a natural number

First we consider the special case where β_δ is zero or a natural number. Then the augmented density is simply a finite sum of positive Fricke components Eq. (2.172),

$$\tilde{\rho}(\psi, r) = \rho_0 \left(\frac{\psi - E_0}{\psi_0 - E_0}\right)^p \sum_{k=0}^{\beta_\delta} \binom{\beta_\delta}{k} \left(\frac{r}{r_\mathrm{a}}\right)^{-2\beta_0 + 2k\delta}, \tag{4.19}$$

which leads immediately to

$$F(E, L) = \frac{\rho_0}{M\big(2\pi(\psi_0 - E_0)\big)^{3/2}} \left(\frac{E - E_0}{\psi_0 - E_0}\right)^{p-3/2} \times \sum_{k=0}^{\beta_\delta} \binom{\beta_\delta}{k} \frac{\Gamma(1+p)}{\Gamma(1 - \beta_0 + k\delta)\,\Gamma(p - 1/2 + \beta_0 - k\delta)} \left(\frac{L^2}{2r_\mathrm{a}^2(E - E_0)}\right)^{-\beta_0 + k\delta}, \tag{4.20}$$

for $E > E_0$. This series is a special case of Eq. (4.54). It is clear that the conditions (4.15) - (4.16) guarantee that all the gamma functions are positive, so that the entire DF is nonnegative everywhere.

Case 2: $\beta_\delta < 0$

When $\beta_\delta < 0$ we can apply the Laplace-Mellin formalism: the connection between the distribution function and the augmented density is given by Eq. (2.91),

$$\underset{E\to\xi}{\mathcal{L}}\,\underset{L\to\lambda}{\mathcal{M}}\{F(E,L)\} = \frac{2^{\lambda/2}}{M(2\pi)^{3/2}}\frac{\xi^{(3-\lambda)/2}}{\Gamma\left(1-\frac{\lambda}{2}\right)}\,\underset{\psi\to\xi}{\mathcal{L}}\{f(\psi)\}\,\underset{r\to\lambda}{\mathcal{M}}\{g(r)\}\,. \tag{4.21}$$

Since the augmented density is a separable function of ψ and r, the transforms can be calculated separately: we find

$$\underset{\psi\to\xi}{\mathcal{L}}\{(\psi-E_0)^p\} = \int_{E_0}^{+\infty} \mathrm{e}^{-\xi\psi}(\psi-E_0)^p\,\mathrm{d}\psi = \Gamma(1+p)\,\frac{\mathrm{e}^{-\xi E_0}}{\xi^{1+p}}, \tag{4.22}$$

and

$$\begin{aligned}\underset{r\to\lambda}{\mathcal{M}}\{g(r)\} &= \int_0^{+\infty} r^{\lambda-1}\left(\frac{r}{r_\mathrm{a}}\right)^{-2\beta_0}\left(1+\frac{r^{2\delta}}{r_\mathrm{a}^{2\delta}}\right)^{-(\beta_\infty-\beta_0)/\delta}\mathrm{d}r,\\ &= \frac{r_\mathrm{a}^\lambda}{2\delta}\,B\left(\frac{\lambda-2\beta_0}{2\delta},\frac{2\beta_\infty-\lambda}{2\delta}\right),\end{aligned} \tag{4.23}$$

which is valid if we choose λ to lie in the convergence strip $2\beta_0 < \lambda < 2\beta_\infty$. Thus

$$\begin{aligned}\underset{E\to\xi}{\mathcal{L}}\,\underset{L\to\lambda}{\mathcal{M}}\{F(E,L)\} = \frac{\rho_0}{M(2\pi)^{3/2}}\,\frac{\Gamma(1+p)}{(\psi_0-E_0)^p}\,\times\\ \frac{r_\mathrm{a}^\lambda}{2\delta}\,\frac{2^{\lambda/2}}{\Gamma\left(1-\frac{\lambda}{2}\right)}\,B\left(\frac{\lambda-2\beta_0}{2\delta},\frac{2\beta_\infty-\lambda}{2\delta}\right)\mathrm{e}^{-\xi E_0}\,\xi^{(1-\lambda)/2-p}.\end{aligned} \tag{4.24}$$

The inversion of the Laplace transform is straightforward,

$$\begin{aligned}\underset{\xi\to E}{\mathcal{L}^{-1}}\left\{\mathrm{e}^{-\xi E_0}\,\xi^{(1-\lambda)/2-p}\right\} &= \frac{1}{2\pi i}\int_{\xi_0-i\infty}^{\xi_0+i\infty}\mathrm{e}^{\xi(E-E_0)}\,\xi^{(1-\lambda)/2-p}\,\mathrm{d}\xi\\ &= \frac{(E-E_0)^{p-(3-\lambda)/2}}{\Gamma\left(p-\frac{1-\lambda}{2}\right)},\end{aligned} \tag{4.25}$$

leaving us with the inversion of the Mellin transform,

$$F(E,L) = \frac{\rho_0}{M\big(2\pi(\psi_0-E_0)\big)^{3/2}} \frac{\Gamma(1+p)}{\delta\Gamma(-\beta_\delta)} \left(\frac{E-E_0}{\psi_0-E_0}\right)^{p-3/2} \times \underset{\lambda\to L}{\mathcal{M}^{-1}} \left\{ \frac{1}{2} \frac{\Gamma\Big(\frac{\lambda-2\beta_0}{2\delta}\Big)\,\Gamma\Big(\frac{2\beta_\infty-\lambda}{2\delta}\Big)}{\Gamma\big(1-\frac{\lambda}{2}\big)\,\Gamma\big(p-\frac{1-\lambda}{2}\big)} \big(2r_{\mathrm{a}}^2(E-E_0)\big)^{\lambda/2} \right\}, \tag{4.26}$$

$$= \frac{\rho_0}{M\big(2\pi(\psi_0-E_0)\big)^{3/2}} \frac{\Gamma(1+p)}{\delta\Gamma(-\beta_\delta)} \left(\frac{E-E_0}{\psi_0-E_0}\right)^{p-3/2} \times \frac{1}{2\pi i} \int_{s_0-i\infty}^{s_0+i\infty} \frac{\Gamma\Big(\frac{s-\beta_0}{\delta}\Big)\Gamma\Big(\frac{\beta_\infty-s}{\delta}\Big)}{\Gamma\big(1-s\big)\Gamma\big(p-\frac{1}{2}+s\big)} \left(\frac{L^2}{2r_{\mathrm{a}}^2(E-E_0)}\right)^{-s} \mathrm{d}s, \tag{4.27}$$

with $s=\lambda/2$ and s_0 a real constant to be chosen such that the integral exists. At last, we come to the point where we can put our tools of Chapter 3 to use. Indeed, we recognize in the last equation a Fox H-function (3.4):

$$F(E,L) = \frac{\rho_0}{M\big(2\pi(\psi_0-E_0)\big)^{3/2}} \frac{\Gamma(1+p)}{\delta\Gamma(-\beta_\delta)} \left(\frac{E-E_0}{\psi_0-E_0}\right)^{p-3/2} \times H_{2,2}^{1,1}\left(\frac{L^2}{2r_{\mathrm{a}}^2(E-E_0)} \,\middle|\, \begin{matrix} \Big(1-\frac{\beta_\infty}{\delta},\frac{1}{\delta}\Big), \Big(p-\frac{1}{2},1\Big) \\ \Big(-\frac{\beta_0}{\delta},\frac{1}{\delta}\Big) \quad , \quad \Big(0,1\Big) \end{matrix} \right), \tag{4.28}$$

or equivalently,

$$F(E,L) = \frac{\rho_0}{M\big(2\pi(\psi_0-E_0)\big)^{3/2}} \frac{\Gamma(1+p)}{\Gamma(-\beta_\delta)} \left(\frac{E-E_0}{\psi_0-E_0}\right)^{p-3/2} \times H_{2,2}^{1,1}\left(\left(\frac{L^2}{2r_{\mathrm{a}}^2(E-E_0)}\right)^{\delta} \,\middle|\, \begin{matrix} \Big(1-\frac{\beta_\infty}{\delta},1\Big), \Big(p-\frac{1}{2},\delta\Big) \\ \Big(-\frac{\beta_0}{\delta},1\Big) \quad , \quad \Big(0,\delta\Big) \end{matrix} \right). \tag{4.29}$$

Even though the integration path of the inverse Mellin transform is normally defined as in Eq. (4.27), the integration in the specific case of a Fox H-function can be performed along three possible paths $\mathcal{C}$, which are equivalent: if the integral converges for more than one of these three paths, then the result is the same. If the integral converges for only one path, then that is the only one to be considered. Using the definitions (3.9), which we will give a

prime to avoid notational confusion, we have

$$\alpha' = \frac{2}{\delta} - 2, \tag{4.30}$$

$$\beta' = 1, \tag{4.31}$$

$$\Delta' = 0, \tag{4.32}$$

$$\delta' = -p - \frac{1}{2} - \beta_\delta, \tag{4.33}$$

So that the possible integration contours are

- a path $\mathcal{C}_1$ from $-i\infty$ to $i\infty$, such that the poles of $\Gamma\left(\frac{s-\beta_0}{\delta}\right)$ lie on one side and the poles of $\Gamma\left(\frac{\beta_\infty - s}{\delta}\right)$ lie on the other side. The convergence is absolute if $\delta < 1$ or if $\delta = 1$ and $p - \frac{1}{2} + \beta_\delta > 0$. Previous work showed that in addition, if $\delta = 1$ and $p + \frac{1}{2} + \beta_\delta > 0$ the integral is semi-convergent for $L^2 \neq 2r_\mathrm{a}^2(E - E_0)$ (Dejonghe 1986).

- a loop $\mathcal{C}_2$, starting and ending at $-\infty$, that encircles the poles of $\Gamma\left(\frac{s-\beta_0}{\delta}\right)$ once in the positive direction and none of the poles of $\Gamma\left(\frac{\beta_\infty - s}{\delta}\right)$. The integral then converges if $p - \frac{1}{2} + \beta_\delta > 0$ and $L^2 < 2r_\mathrm{a}^2(E - E_0)$.

- a loop $\mathcal{C}_3$, starting and ending at $+\infty$, that encircles the poles of $\Gamma\left(\frac{\beta_\infty - s}{\delta}\right)$ once in the negative direction and none of the poles of $\Gamma\left(\frac{s-\beta_0}{\delta}\right)$. The integral then converges if $p - \frac{1}{2} + \beta_\delta > 0$ and $L^2 > 2r_\mathrm{a}^2(E - E_0)$.

It can easily be seen that the convergence criterion for path $\mathcal{C}_1$ ensures a well-defined DF, i.e. continuous and nonnegative. Indeed, in this case the contour is a line parallel to the imaginary axis from $s_0 - i\infty$ to $s_0 + i\infty$ with $\beta_0 < s_0 < \beta_\infty$. On this path, the real parts of all the gamma functions are positive; this is trivial to see for $\Gamma((s-\beta_0)/\delta)$, $\Gamma((\beta_\infty - s)/\delta)$, and $\Gamma(1-s)$. Furthermore, the conditions Eqs. (4.15) - (4.16) ensure that the real part of $p - \frac{1}{2} + s$ is positive if s_0 is chosen sufficiently close to β_∞. Hence, the distribution function is again nonnegative everywhere.

Case 3: $\beta_\delta > 0$ and not a natural number

In the case of $\beta_\delta > 0$ and not a natural number, the Mellin transform does not exist. However, we can solve this problem by rewriting the augmented density in a similar way as Eq. (4.19): defining n as the smallest natural number such that $n > \beta_\delta$, we obtain

$$\tilde{\rho}(\psi, r) = \rho_0 \left(\frac{\psi - E_0}{\psi_0 - E_0}\right)^p \sum_{k=0}^{n} \binom{n}{k} \left(\frac{r}{r_\mathrm{a}}\right)^{-2\beta_0 + 2k\delta} \left(1 + \frac{r^{2\delta}}{r_\mathrm{a}^{2\delta}}\right)^{\beta_\delta - n}. \tag{4.34}$$

For the individual terms the Laplace-Mellin formalism does apply, and the DF becomes

$$F(E,L) = \frac{\rho_0}{M\big(2\pi(\psi_0 - E_0)\big)^{3/2}} \frac{\Gamma(1+p)}{\delta\Gamma(n-\beta_\delta)} \left(\frac{E-E_0}{\psi_0-E_0}\right)^{p-3/2} \times$$
$$\sum_{k=0}^{n} \binom{n}{k} \frac{1}{2\pi i} \int_{\mathcal{C}_{(k)}} \frac{\Gamma\Big(\frac{s-\beta_0}{\delta}+k\Big)\Gamma\Big(\frac{\beta_\infty - s}{\delta}+n-k\Big)}{\Gamma\big(1-s\big)\Gamma\big(p-\frac{1}{2}+s\big)} \left(\frac{L^2}{2r_{\mathrm{a}}^2(E-E_0)}\right)^{-s} \mathrm{d}s. \quad (4.35)$$

Now, it is easily observed that we can choose each of the integration paths $\mathcal{C}_{(k)}$ to be identical, as the contours $\mathcal{C}_1$, $\mathcal{C}_2$ or $\mathcal{C}_3$ defined above. Therefore, the summation can be performed inside the integral. Using the Pochhammer symbol from Eq. (2.108) with its properties

$$\Gamma(x+k) = (x)_k \Gamma(x), \qquad \text{and} \qquad \Gamma(x-k) = (-1)^k \frac{\Gamma(x)}{(1-x)_k}, \quad (4.36)$$

we find

$$\sum_{k=0}^{n} \binom{n}{k} \Gamma\left(\frac{s-\beta_0}{\delta}+k\right) \Gamma\left(\frac{\beta_\infty - s}{\delta}+n-k\right) =$$
$$\Gamma\left(\frac{s-\beta_0}{\delta}\right) \Gamma\left(\frac{\beta_\infty - s}{\delta}+n\right) {}_2F_1\left(-n, \frac{s-\beta_0}{\delta}, \frac{s-\beta_\infty}{\delta}+1-n; 1\right). \quad (4.37)$$

Finally, with the identity

$${}_2F_1(-n,b,c;1) = \frac{(c-b)_n}{(c)_n}, \quad (4.38)$$

the equation for the distribution function also reduces to Eq. (4.28).

If the convergence criterion for path $\mathcal{C}_1$ is valid, then every contour $\mathcal{C}_{(k)}$ can be taken as a line $s_k - i\infty$ to $s_k + i\infty$ with $\beta_0 - k\delta < s_k < \beta_\infty + (n-k)\delta$. Following the same reasoning as with $\beta_\delta < 0$, one can verify that the real part of the integrand is positive for each k, so that the distribution function is once again well-defined.

4.2.2 A practical series expansion

For practical purposes, we would like to write these DFs in the form of series expansions. Following Section 3.3, we can use the Residue Theorem on the paths $\mathcal{C}_2$ (if $L^2 < 2r_{\mathrm{a}}^2(E-E_0)$) and $\mathcal{C}_3$ (if $L^2 > 2r_{\mathrm{a}}^2(E-E_0)$). Since these loops encircle gamma functions with simple poles, the series follow immediately from Eqs. (3.30) and (3.31), and we obtain (4.53) and (4.54), respectively.

It is also instructive to examine the special case where δ is a rational number. It turns out that the Fox H-functions then reduce to Meijer G-functions, which can be written as sums of hypergeometric series. Indeed, if $\delta = \frac{m}{n}$, we can write

$$F(E,L) = \frac{\rho_0}{M\big(2\pi(\psi_0 - E_0)\big)^{3/2}} \frac{n\Gamma(1+p)}{\Gamma(-\beta_\delta)} \left(\frac{E-E_0}{\psi_0 - E_0}\right)^{p-3/2} \times \\ \frac{1}{2\pi i} \int_{\mathcal{C}} \frac{\Gamma\big(-\frac{n}{m}\beta_0 + ns\big)\Gamma\big(\frac{n}{m}\beta_\infty - ns\big)}{\Gamma\big(1-ms\big)\Gamma\big(p-\frac{1}{2}+ms\big)} \left(\frac{L^2}{2r_{\mathrm{a}}^2(E-E_0)}\right)^{-ms} \mathrm{d}s. \quad (4.39)$$

Now, using the multiplication formula for the gamma function

$$\Gamma(kx) = (2\pi)^{(1-k)/2} k^{kx-1/2} \prod_{l=0}^{k-1} \Gamma\left(x + \frac{l}{k}\right), \quad (4.40)$$

we can write the integral in the form of a Meijer G-function (Gradshteyn & Ryzhik 1965):

$$F(E,L) = \frac{\rho_0}{M\big(2\pi(\psi_0 - E_0)\big)^{3/2}} \frac{\Gamma(1+p)}{\Gamma(-\beta_\delta)} \left(\frac{E-E_0}{\psi_0 - E_0}\right)^{p-3/2} \times \\ \frac{n^{n(\beta_\infty - \beta_0)/m}}{(2\pi)^{n-m} m^{p-1/2}} G^{n,n}_{m+n,m+n}\left(\left(\frac{L^2}{2r_{\mathrm{a}}^2(E-E_0)}\right)^m \middle| \begin{matrix} a_1, \ldots, a_{m+n} \\ b_1, \ldots, b_{m+n} \end{matrix}\right), \quad (4.41)$$

with

$$\begin{aligned} a_i &= -\frac{i-1}{n} + \frac{m-\beta_\infty}{m} && \text{for } i = 1,\ldots,n, \\ a_{n+i} &= \frac{i-1}{m} + \frac{p-1/2}{m} && \text{for } i = 1,\ldots,m, \\ b_i &= \frac{i-1}{n} - \frac{\beta_0}{m} && \text{for } i = 1,\ldots,n, \\ b_{n+i} &= -\frac{i-1}{m} + \frac{m-1}{m} && \text{for } i = 1,\ldots,m. \end{aligned} \quad (4.42)$$

Since for a general Meijer G-function

$$G^{m,n}_{p,q}\left(z \middle| \begin{matrix} a_1, \ldots, a_p \\ b_1, \ldots, b_q \end{matrix}\right), \quad (4.43)$$

with $p = q$ and $z, \boldsymbol{a}, \boldsymbol{b}$ real, the integral convergences for path $\mathcal{C}_1$ (Mathai 1993) if $|\arg z| < \varepsilon\pi$, with

$$\varepsilon = m + n - \frac{1}{2}(p+q) > 0, \quad (4.44)$$

or if $|\arg z| = \varepsilon\pi \geqslant 0$, with

$$\varepsilon = m+n-\frac{1}{2}(p+q) = 0, \qquad \text{and} \qquad \sum_{i=0}^{q} b_i - \sum_{i=0}^{p} a_i < -1, \tag{4.45}$$

we indeed obtain the conditions $\delta < 1$ or $\delta = 1$ and $p - \frac{1}{2} + \beta_\delta > 0$.

This Meijer G-function can be calculated as a sum of generalized hypergeometric functions (Gradshteyn & Ryzhik 1965). For $z < 1$ the following equation is valid:

$$G^{n,n}_{m+n,m+n}\left(z^m \,\middle|\, \begin{matrix}\boldsymbol{a}\\ \boldsymbol{b}\end{matrix}\right) = \sum_{i=1}^{n} \frac{\prod_{l=1}^{n}{}' \Gamma(b_l - b_i) \prod_{l=1}^{n} \Gamma(1+b_i-a_l)}{\prod_{l=n+1}^{m+n} \Gamma(1+b_i-b_l) \prod_{l=n+1}^{m+n} \Gamma(a_l-b_i)} z^{mb_i} \times$$
$$ {}_{m+n}F_{m+n-1}\big(1+b_i-a_1,\ldots,1+b_i-a_{m+n};$$
$$1+b_i-b_1,\ldots,*,\ldots,1+b_i-b_{m+n};(-1)^{m+n}z^m\big), \tag{4.46}$$

where the prime by the product symbol denotes the omission of the product when $i = l$, and the asterisk in the hypergeometric function indicates the omission on the ith parameter. Analogously, the equation for $z > 1$ reads

$$G^{n,n}_{m+n,m+n}\left(z^m \,\middle|\, \begin{matrix}\boldsymbol{a}\\ \boldsymbol{b}\end{matrix}\right) = \sum_{i=1}^{n} \frac{\prod_{l=1}^{n}{}' \Gamma(a_i - a_l) \prod_{l=1}^{n} \Gamma(1+b_l-a_i)}{\prod_{l=n+1}^{m+n} \Gamma(1+a_l-a_i) \prod_{l=n+1}^{m+n} \Gamma(a_i-b_l)} z^{m(a_i-1)} \times$$
$$ {}_{m+n}F_{m+n-1}\big(1+b_1-a_i,\ldots,1+b_{m+n}-a_i;$$
$$1+a_1-a_i,\ldots,*,\ldots,1+a_{m+n}-a_i;(-1)^{m+n}z^{-m}\big), \tag{4.47}$$

With the coefficients from Eq. (4.42), we obtain for $L^2 < 2r_{\mathrm{a}}^2 E$,

$$
\begin{aligned}
G^{n,n}_{m+n,m+n}\left(\left(\frac{L^2}{2r_{\mathrm{a}}^2(E-E_0)}\right)^m \middle| \begin{matrix}\boldsymbol{a}\\ \boldsymbol{b}\end{matrix}\right) = \\
\sum_{i=0}^{n-1} \frac{\prod_{l=0}^{n-1}{}' \Gamma\left(\frac{l-i}{n}\right) \prod_{l=0}^{n-1} \Gamma\left(\frac{\beta_\infty-\beta_0}{m}+\frac{l+i}{n}\right)}{\prod_{l=0}^{m-1} \Gamma\left(\frac{1-\beta_0+l}{m}+\frac{i}{n}\right) \prod_{l=0}^{m-1} \Gamma\left(\frac{p+\beta_0-1/2+l}{m}-\frac{i}{n}\right)} \times \\
\sum_{j=0}^{\infty} \frac{\prod_{l=0}^{n-1} \left(\frac{\beta_\infty-\beta_0}{m}+\frac{l+i}{n}\right)_j \prod_{l=0}^{m-1} \left(1-\frac{p+\beta_0-1/2+l}{m}+\frac{i}{n}\right)_j}{\prod_{l=0}^{n-1} \left(1-\frac{l-i}{n}\right)_j \prod_{l=0}^{m-1} \left(\frac{1-\beta_0+l}{m}+\frac{i}{n}\right)_j} \times \\
(-1)^{(m+n)j} \left(\frac{L^2}{2r_{\mathrm{a}}^2(E-E_0)}\right)^{-\beta_0+i\delta+mj} .
\end{aligned}
\tag{4.48}
$$

Now, with the aid of the identities

$$
\Gamma(x)\,\Gamma(1-x) = \frac{\pi}{\sin(\pi x)}, \tag{4.49}
$$

and

$$
\prod_{k=1}^{n-1} \sin\left(\frac{k\pi}{n}\right) = \frac{n}{2^{n-1}}, \tag{4.50}
$$

we can simplify this expression to

$$
\begin{aligned}
G^{n,n}_{m+n,m+n}\left(\left(\frac{L^2}{2r_{\mathrm{a}}^2(E-E_0)}\right)^m \middle| \begin{matrix}\boldsymbol{a}\\ \boldsymbol{b}\end{matrix}\right) = \\
\sum_{i=0}^{n-1} \sum_{j=0}^{\infty} \frac{\prod_{l=0}^{n-1} \Gamma\left(\frac{\beta_\infty-\beta_0}{m}+\frac{l+i+nj}{n}\right)}{\prod_{l=0}^{n-1} \Gamma\left(\frac{1+l}{n}+\frac{i+nj}{n}\right)} \times \\
\frac{1}{\prod_{l=0}^{m-1} \Gamma\left(\frac{1-\beta_0+l}{m}+\frac{i+nj}{n}\right) \prod_{l=0}^{m-1} \Gamma\left(\frac{p+\beta_0-1/2+l}{m}-\frac{i+nj}{n}\right)} \times \\
\frac{(2\pi)^{n-1}}{n} (-1)^{i+nj} \left(\frac{L^2}{2r_{\mathrm{a}}^2(E-E_0)}\right)^{-\beta_0+i\delta+mj} ,
\end{aligned}
\tag{4.51}
$$

so that, using again Eq. (4.40), the distribution function reduces to

$$F(E,L) = \frac{\rho_0}{M\big(2\pi(\psi_0-E_0)\big)^{3/2}} \frac{\Gamma(1+p)}{\Gamma(-\beta_\delta)} \left(\frac{E-E_0}{\psi_0-E_0}\right)^{p-3/2} \times \sum_{i=0}^{n-1}\sum_{j=0}^{\infty} \frac{\Gamma\Big(\frac{\beta_\infty-\beta_0}{\delta}+i+jn\Big)}{\Gamma(p+\beta_0-1/2-i\delta-jm)\Gamma(1-\beta_0+i\delta+jm)} \times \frac{(-1)^{i+nj}}{\Gamma(1+i+jn)} \left(\frac{L^2}{2r_\mathrm{a}^2(E-E_0)}\right)^{-\beta_0+i\delta+mj}. \tag{4.52}$$

Finally, the double summation can be grouped into a single index $k=i+nj$, and we obtain for $L^2 < 2r_\mathrm{a}^2(E-E_0)$,

$$F(E,L) = \frac{\rho_0}{M\big(2\pi(\psi_0-E_0)\big)^{3/2}} \left(\frac{E-E_0}{\psi_0-E_0}\right)^{p-3/2} \times \sum_{k=0}^{\infty} \binom{\beta_\delta}{k} \frac{\Gamma(1+p)}{\Gamma(1-\beta_0+k\delta)\Gamma(p-1/2+\beta_0-k\delta)} \left(\frac{L^2}{2r_\mathrm{a}^2(E-E_0)}\right)^{-\beta_0+k\delta}. \tag{4.53}$$

Similarly, for $L^2 > 2r_\mathrm{a}^2(E-E_0)$, we find

$$F(E,L) = \frac{\rho_0}{M\big(2\pi(\psi_0-E_0)\big)^{3/2}} \left(\frac{E-E_0}{\psi_0-E_0}\right)^{p-3/2} \times \sum_{k=0}^{\infty} \binom{\beta_\delta}{k} \frac{\Gamma(1+p)}{\Gamma(1-\beta_\infty-k\delta)\Gamma(p-1/2+\beta_\infty+k\delta)} \left(\frac{L^2}{2r_\mathrm{a}^2(E-E_0)}\right)^{-\beta_\infty-k\delta}. \tag{4.54}$$

Although these expressions have been derived for rational values of δ, they remain valid for any real value, since these functions are continuous in δ; indeed, as we mentioned above, they follow directly from Eqs. (3.30) and (3.31).

4.2.3 Extension to systems with a central cusp

The set of power-law components presented in the previous subsection is very adequate to fit a broad class of models. It is however, not fit to construct dynamical models for systems that have a central density cusp and $\beta_0 \leqslant 0$. For such systems, we need the general form (4.11),

$$\tilde{\rho}(\psi,r) = \rho_0 \left(\frac{\psi-E_0}{\psi_0-E_0}\right)^p \left[1-\left(\frac{\psi-E_0}{\psi_0-E_0}\right)^s\right]^q \left(\frac{r}{r_\mathrm{a}}\right)^{-2\beta_0} \left(1+\frac{r^{2\delta}}{r_\mathrm{a}^{2\delta}}\right)^{\beta_\delta}, \tag{4.55}$$

with $q < 0$. Fortunately, this generalization is trivial, since we can expand the q-dependent factor as a power series,

$$\tilde{\rho}(\psi,r) = \rho_0 \sum_{j=0}^{\infty} (-1)^j \binom{q}{j} \left(\frac{\psi - E_0}{\psi_0 - E_0}\right)^{p+js} \left(\frac{r}{r_\mathrm{a}}\right)^{-2\beta_0} \left(1 + \frac{r^{2\delta}}{r_\mathrm{a}^{2\delta}}\right)^{\beta_\delta}, \tag{4.56}$$

which is nothing more than a positive sum of terms that all have the form (4.18). Thus, our condition $q \leqslant 0$ is sufficient to obtain a well-defined DF, which we can write down immediately,

$$F(E,L) = \frac{\rho_0}{M\big(2\pi(\psi_0 - E_0)\big)^{3/2}} \sum_{j=0}^{\infty} (-1)^j \binom{q}{j} \frac{\Gamma(1+p+js)}{\delta\,\Gamma(-\beta_\delta)} \left(\frac{E - E_0}{\psi_0 - E_0}\right)^{p+js-3/2} \times H_{2,2}^{1,1}\left(\frac{L^2}{2r_\mathrm{a}^2(E - E_0)} \,\middle|\, \begin{matrix} \left(1 - \frac{\beta_\infty}{\delta}, \frac{1}{\delta}\right), \left(p + js - \frac{1}{2}, 1\right) \\ \left(-\frac{\beta_0}{\delta}, \frac{1}{\delta}\right) \quad , \quad \left(0,1\right) \end{matrix}\right), \tag{4.57}$$

or explicitly,

$$F(E,L) = \frac{\rho_0}{M\big(2\pi(\psi_0 - E_0)\big)^{3/2}} \sum_{j=0}^{\infty} (-1)^j \binom{q}{j} \Gamma(1+p+js) \left(\frac{E - E_0}{\psi_0 - E_0}\right)^{p+js-3/2} \times \sum_{k=0}^{\infty} \binom{\beta_\delta}{k} \frac{1}{\Gamma(1-\beta_k)\Gamma(p+js-1/2+\beta_k)} \left(\frac{L^2}{2r_\mathrm{a}^2(E - E_0)}\right)^{-\beta_k}, \tag{4.58}$$

with

$$\beta_k = \begin{cases} \beta_0 - k\delta & \text{for } L^2 < 2r_\mathrm{a}^2(E - E_0), \\ \beta_\infty + k\delta & \text{for } L^2 > 2r_\mathrm{a}^2(E - E_0). \end{cases} \tag{4.59}$$

These DFs will diverge in the limit $E \to \psi_0$, if $q < 0$. For practical implementations, the double summation $\sum_j \sum_k$ can be computed by changing the indices to $\sum_l \sum_{j+k=l}$. For each value of l one then evaluates the inner summation, which consists of the $l+1$ terms ($j = 0$,$k = l$), ($j = 1$,$k = l-1$),..., ($j = l$,$k = 0$). The index l is increased until the total (outer) sum alters by less than a required numerical error δF; due to the double summation, the computational time is an inverse quadratic function of δF.

4.2.4 Velocity moments

In order to derive the corresponding velocity moments, we develop $g(r)$ in (4.55) into a series expansion as well. This expansion must be split into two regimes:

$$\tilde{\rho}(\psi,r) = \rho_0 \sum_{j=0}^{\infty} (-1)^j \binom{q}{j} \left(\frac{\psi - E_0}{\psi_0 - E_0}\right)^{p+js} \sum_{k=0}^{\infty} \binom{\beta_\delta}{k} \left(\frac{r}{r_\mathrm{a}}\right)^{-2\beta_k}, \tag{4.60}$$

with

$$\beta_k = \begin{cases} \beta_0 - k\delta & \text{for } (r < r_\mathrm{a}) \text{ or } (r = r_\mathrm{a} \text{ and } \beta_0 > \beta_\infty), \\ \beta_\infty + k\delta & \text{for } (r > r_\mathrm{a}) \text{ or } (r = r_\mathrm{a} \text{ and } \beta_0 < \beta_\infty). \end{cases} \tag{4.61}$$

When we plug this into the equations (2.106) for the augmented moments, we obtain

$$\tilde{\mu}_{2n,2m}(\psi,r) = \rho_0 \frac{2^{m+n}}{\sqrt{\pi}} (\psi - E_0)^{m+n} \sum_{k=0}^{\infty} \binom{\beta_\delta}{k} \frac{\Gamma(m+1-\beta_k)}{\Gamma(1-\beta_k)} \left(\frac{r}{r_\mathrm{a}}\right)^{-2\beta_k} \times \sum_{j=0}^{\infty} (-1)^j \binom{q}{j} \frac{\Gamma(n+1/2)\Gamma(1+p+js)}{\Gamma(m+n+1+p+js)} \left(\frac{\psi - E_0}{\psi_0 - E_0}\right)^{p+js}. \tag{4.62}$$

In particular, the radial second-order moment reduces to

$$\tilde{\mu}_{2,0}(\psi,r) = \rho_0 \left(\frac{r}{r_\mathrm{a}}\right)^{-2\beta_0} \left(1 + \frac{r^{2\delta}}{r_\mathrm{a}^{2\delta}}\right)^{\beta_\delta} \sum_{j=0}^{\infty} (-1)^j \binom{q}{j} \frac{(\psi - E_0)}{1+p+js} \left(\frac{\psi - E_0}{\psi_0 - E_0}\right)^{p+js}, \tag{4.63}$$

and this allows us to derive the augmented velocity dispersions (2.152) and (2.153),

$$\tilde{\sigma}_r^2(\psi) = \frac{(\psi_0 - E_0)}{s} \left(\frac{\psi - E_0}{\psi_0 - E_0}\right)^p \left[1 - \left(\frac{\psi - E_0}{\psi_0 - E_0}\right)^s\right]^q B_\chi\left(\frac{1+p}{s}, 1+q\right), \tag{4.64}$$

$$\tilde{\sigma}_T^2(\psi,r) = 2\frac{(1-\beta_0) + (1-\beta_\infty)(r/r_\mathrm{a})^{2\delta}}{1 + (r/r_\mathrm{a})^{2\delta}} \tilde{\sigma}_r^2(\psi), \tag{4.65}$$

where we used the incomplete beta function (4.8), and

$$\chi = \left(\frac{\psi - E_0}{\psi_0 - E_0}\right)^s. \tag{4.66}$$

The radial velocity distribution (2.64) can be derived by calculating the integral (2.145). We obtain

$$\widetilde{F}_{v_r}(\psi,r,v_r) = \frac{\rho_0}{\sqrt{2\pi}M} \frac{1}{\sqrt{\psi_0 - E_0}} \left(\frac{r}{r_\mathrm{a}}\right)^{-2\beta_0} \left(1 + \frac{r^{2\delta}}{r_\mathrm{a}^{2\delta}}\right)^{\beta_\delta} \times \sum_{j=0}^{\infty} (-1)^j \binom{q}{j} \frac{\Gamma(p+js+1)}{\Gamma(p+js+1/2)} \left(\frac{\psi - E_0 - v_r^2/2}{\psi_0 - E_0}\right)^{p+js-1/2}. \tag{4.67}$$

Note that this function is separable in r and $\psi - E_0 - v_r^2/2$. To obtain the transverse velocity distribution, we need to solve the integral (2.65) with the series expansion (4.58). We find

$$\widetilde{F}_{v_T}(\psi,r,v_T) = \frac{\rho_0}{M}\frac{v_T}{(\psi_0-E_0)}\sum_{j=0}^{\infty}(-1)^j\binom{q}{j}\Gamma(1+p+js)\left(\frac{\psi-E_0-v_T^2/2}{\psi_0-E_0}\right)^{p+js-1} \times \sum_{k=0}^{\infty}\binom{\beta_\delta}{k}\frac{1}{\Gamma(1-\beta_k)\Gamma(p+js+\beta_k)}\left(\frac{r^2}{r_\mathrm{a}^2}\frac{v_T^2/2}{(\psi-E_0-v_T^2/2)}\right)^{-\beta_k}. \quad (4.68)$$

As a sanity check, one can verify that indeed

$$\tilde{\rho}(\psi,r) = M\int_{-\sqrt{2(\psi-E_0)}}^{\sqrt{2(\psi-E_0)}}\widetilde{F}_{v_r}(\psi,r,v_r)\,\mathrm{d}v_r = M\int_0^{\sqrt{2(\psi-E_0)}}\widetilde{F}_{v_T}(\psi,r,v_r)\,\mathrm{d}v_T. \quad (4.69)$$

The velocity distributions $F_{v_\theta}(r,v_\theta)$ and $F_{v_\varphi}(r,v_\varphi)$ can be derived from $F_{v_T}(\psi,r,v_T)$ by the numerical integration (2.67). It is straightforward to check that for isotropic models $\beta_\delta = 0$ they are identical to $F_{v_r}(\psi,r,v_r)$.

Finally, the marginal distributions of E and L (2.48) - (2.49) become

$$\widetilde{F}_E(\psi,r,E) = \frac{\rho_0}{M}\frac{\sqrt{\psi-E}}{(\psi_0-E_0)^{3/2}}\sum_{j=0}^{\infty}(-1)^j\binom{q}{j}\Gamma(1+p+js)\left(\frac{E-E_0}{\psi_0-E_0}\right)^{p+js-3/2} \times \sum_{k=0}^{\infty}\binom{\beta_\delta}{k}\frac{1}{\Gamma(3/2-\beta_k)\Gamma(p-1/2+js+\beta_k)}\left(\frac{r^2}{r_\mathrm{a}^2}\frac{(\psi-E)}{(E-E_0)}\right)^{-\beta_k}, \quad (4.70)$$

and

$$\widetilde{F}_L(\psi,r,L) = \frac{\rho_0}{M}\frac{L/r^2}{(\psi-E_0)}\sum_{j=0}^{\infty}(-1)^j\binom{q}{j}\Gamma(1+p+js)\left(\frac{\psi-E_0-L^2/2r^2}{\psi_0-E_0}\right)^{p+js-1} \times \sum_{k=0}^{\infty}\binom{\beta_\delta}{k}\frac{1}{\Gamma(1-\beta_k)\Gamma(p+js+\beta_k)}\left(\frac{1}{r_\mathrm{a}^2}\frac{L^2/2}{2(\psi-E_0-L^2/2r^2)}\right)^{-\beta_k}. \quad (4.71)$$

Note that $\widetilde{F}_L(\psi,r,L)$ is essentially the same as $\widetilde{F}_{v_T}(\psi,r,v_T)$, with $L = rv_T$.

4.3 Self-consistent analytical models

At the beginning of this chapter, we claimed that the family of Fox H-components Eq. (4.11) is particularly suited to generate the double power-law models. Before we use their full potential with the QP-algorithm, we demonstrate our claim by showing that the individual

components actually generate an important subfamily of the double power-law models, i.e. there are self-consistent models such that

$$\rho(r) = \tilde{\rho}(\psi(r), r), \tag{4.72}$$

with $\psi(r)$ of the form Eq. (4.9), $\rho(r)$ of the form Eq. (4.3), $\beta(r)$ of the form Eq. (4.10) and $\tilde{\rho}(\psi, r)$ of the form Eq. (4.11). The existence of such analytical dynamical models is a significant step forward in our quest for simple but realistic dynamical models that can e.g. be used as a framework in which to initiate detailed numerical simulations.

4.3.1 A family of anisotropic Plummer models

One of the most obvious candidates is the Plummer sphere (Plummer 1911), as this model has a rather straightforward potential-density pair

$$\psi(r) = \frac{GM_{\rm tot}}{\sqrt{r_{\rm s}^2 + r^2}}, \tag{4.73}$$

$$\rho(r) = \frac{3M_{\rm tot}}{4\pi r_{\rm s}^3}\left(1 + \frac{r^2}{r_{\rm s}^2}\right)^{-5/2}. \tag{4.74}$$

This system, like all double power-law models, has infinite extent, so we have to set $E_0 = 0$. When we further combine these functions with the expressions (4.11) and (4.10), we obtain the condition

$$\frac{3M_{\rm tot}}{4\pi r_{\rm s}^3}\left(1 + \frac{r^2}{r_{\rm s}^2}\right)^{-5/2} = \rho_0\left(1 + \frac{r^2}{r_{\rm s}^2}\right)^{-p/2}\left[1 - \left(1 + \frac{r^2}{r_{\rm s}^2}\right)^{-s/2}\right]^q \left(\frac{r}{r_{\rm a}}\right)^{-2\beta_0}\left(1 + \frac{r^{2\delta}}{r_{\rm a}^{2\delta}}\right)^{-(\beta_\infty - \beta_0)/\delta}. \tag{4.75}$$

A straightforward solution is obviously given by

$$\rho_0 = \frac{3M_{\rm tot}}{4\pi r_{\rm s}^3}, \tag{4.76}$$

$$p = 5, \tag{4.77}$$

$$q = \beta_0 = \beta_\infty = 0, \tag{4.78}$$

which yields the isotropic Plummer model, defined by

$$\tilde{\rho}(\psi) = \frac{3M_{\rm tot}}{4\pi r_{\rm s}^3}\left(\frac{r_{\rm s}\psi}{GM_{\rm tot}}\right)^5. \tag{4.79}$$

$$F(E) = \frac{3}{7\pi^3 (GM_{\rm tot} r_{\rm s})^{3/2}}\left(\frac{2r_{\rm s}E}{GM_{\rm tot}}\right)^{7/2}. \tag{4.80}$$

Our goal, however, is to determine the most general subspace of the $(E_0, p, q, s, \beta_0, \beta_\infty, \delta, r_\mathrm{a})$ parameter space such that the condition Eq. (4.75) is satisfied for all r. In particular we aim for a subspace of the parameter space that has no restrictions on β_0 and β_∞, such that we obtain a family of dynamical models with an arbitrary anisotropy at small and large radii. It is obvious from Eq. (4.75) that, in order to find non-trivial solutions, we have to set

$$E_0 = 0, \tag{4.81}$$
$$s = 2\delta = 2, \tag{4.82}$$
$$r_\mathrm{a} = r_\mathrm{s}. \tag{4.83}$$

We then obtain the requirement

$$\frac{3M_\mathrm{tot}}{4\pi r_\mathrm{s}^3 \rho_0} \left(\frac{r^2}{r_\mathrm{s}^2}\right)^{\beta_0 - q} \left(1 + \frac{r^2}{r_\mathrm{s}^2}\right)^{-5/2 + p/2 + q + \beta_\infty - \beta_0} \equiv 1. \tag{4.84}$$

The left- and right-hand side are identical for all values of r if

$$\rho_0 = \frac{3M_\mathrm{tot}}{4\pi r_\mathrm{s}^3}, \tag{4.85}$$
$$p = 5 - 2\beta_\infty, \tag{4.86}$$
$$q = \beta_0. \tag{4.87}$$

We now have constructed a general two-parameter family of self-consistent Plummer models with the augmented density profile

$$\tilde{\rho}(\psi, r) = \frac{3M_\mathrm{tot}}{4\pi r_\mathrm{s}^3} \left(\frac{r_\mathrm{s}\psi}{GM_\mathrm{tot}}\right)^{5-2\beta_\infty} \times \left[1 - \left(\frac{r_\mathrm{s}\psi}{GM_\mathrm{tot}}\right)^2\right]^{\beta_0} \left(\frac{r^2}{r_\mathrm{s}^2}\right)^{-\beta_0} \left(1 + \frac{r^2}{r_\mathrm{s}^2}\right)^{-(\beta_\infty - \beta_0)}. \tag{4.88}$$

From the condition $q \leqslant 0$ it follows that the central anisotropy has to satisfy $\beta_0 \leqslant 0$. This is in fact a special case of the cusp slope-central anisotropy theorem of An & Evans (2006): a model without a density cusp cannot have a radial velocity anisotropy in the centre. The anisotropy at large radii can take any value $\beta_\infty \leqslant 1$. By construction, the anisotropy profile of this family of models reads

$$\beta(r) = \frac{\beta_0 + \beta_\infty (r/r_\mathrm{s})^2}{1 + (r/r_\mathrm{s})^2}. \tag{4.89}$$

Note that this $\beta(r)$ is a linear function of the density slope

$$\gamma(r) = 5\frac{r^2}{r_\mathrm{s}^2 + r^2}. \tag{4.90}$$

The radial velocity dispersion profile can be written as

$$\sigma_r^2(r) = \frac{GM_{\rm tot}}{2r_{\rm s}} \left(\frac{r^2}{r_{\rm s}^2}\right)^{-\beta_0} \left(1+\frac{r^2}{r_{\rm s}^2}\right)^{5/2-(\beta_\infty-\beta_0)} B_{\frac{r_{\rm s}^2}{r_{\rm s}^2+r^2}}(3-\beta_\infty, 1+\beta_0). \tag{4.91}$$

At large radii, the radial velocity dispersion profile shows a r^{-1} behaviour for all values of the parameters β_0 and β_∞,

$$\sigma_r^2(r) \sim \frac{1}{6-2\beta_\infty} \frac{GM_{\rm tot}}{r}, \tag{4.92}$$

The asymptotic behaviour at small radii is

$$\sigma_r^2(r) \sim \begin{cases} -\dfrac{GM_{\rm tot}}{r_{\rm s}} \dfrac{1}{1+\beta_0} \dfrac{r^2}{r_{\rm s}^2} & \text{if } \beta_0 < -1, \\ \dfrac{GM_{\rm tot}}{2r_{\rm s}} B(3-\beta_\infty, 1+\beta_0) \left(\dfrac{r^2}{r_{\rm s}^2}\right)^{-\beta_0} & \text{if } \beta_0 > -1. \end{cases} \tag{4.93}$$

Except for the models that are isotropic in the centre, the radial velocity dispersions hence always tend to zero at small radii. The asymptotic behaviour of the tangential velocity dispersions $\sigma_\theta(r) = \sigma_\varphi(r)$ follows immediately. At large radii we obtain

$$\sigma_\theta^2(r) = \sigma_\varphi^2(r) \sim \frac{1-\beta_\infty}{6-2\beta_\infty} \frac{GM_{\rm tot}}{r}, \tag{4.94}$$

whereas at small radii

$$\sigma_\theta^2(r) = \sigma_\varphi^2(r) \sim \begin{cases} -\dfrac{GM_{\rm tot}}{r_{\rm s}} \dfrac{1-\beta_0}{1+\beta_0} \dfrac{r^2}{r_{\rm s}^2} & \text{if } \beta_0 < -1, \\ \dfrac{1-\beta_0}{2} \dfrac{GM_{\rm tot}}{r_{\rm s}} B(3-\beta_\infty, 1+\beta_0) \left(\dfrac{r^2}{r_{\rm s}^2}\right)^{-\beta_0} & \text{if } \beta_0 > -1. \end{cases} \tag{4.95}$$

In the top panels of Fig. 4.1 we plot the radial and tangential velocity dispersions for a set of anisotropic Plummer models. The three models in this figure all have the same anisotropy $\beta_\infty = \frac{1}{2}$ at large radii, but a different central anisotropy. Apart from the radial and transverse velocity dispersion, we also plot the line-of-sight velocity dispersion $\sigma_{\rm los}(R)$ on the plane of the sky, derived from Eq. (2.75). The distribution function for our set of Plummer models can be written as

$$F(E,L) = \frac{3}{2(2\pi)^{5/2}} \frac{1}{(GM_{\rm tot}r_{\rm s})^{3/2}} \sum_{j=0}^{\infty} (-1)^j \binom{\beta_0}{j} \frac{\Gamma(6+2j-2\beta_\infty)}{\Gamma(\beta_\infty-\beta_0)} \times \left(\frac{r_{\rm s}E}{GM_{\rm tot}}\right)^{7/2+2j-2\beta_\infty} \mathbb{H}\left(-\beta_0, \beta_\infty, \frac{9}{2}+2j-2\beta_\infty, 1; \frac{L^2}{2r_{\rm s}^2E}\right), \tag{4.96}$$

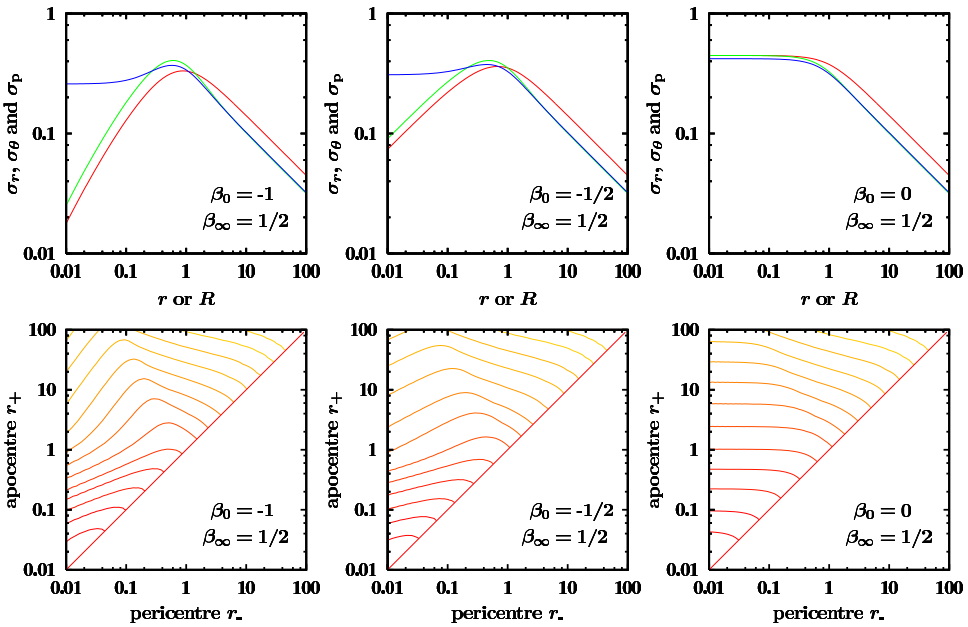

Figure 4.1 *Top.* Radial (red), tangential (green) and line-of-sight (blue) velocity dispersion profiles for three Plummer models with anisotropy values β_0 and β_∞ displayed in the figures. *Bottom.* The distribution function of these models, represented by isoprobability contours in turning point space. High values are indicated by red contours, low values by yellow contours. In all plots, we have used normalized units with $G = M_{\rm tot} = r_{\rm s} = 1$.

where the function $\mathbb{H}(a,b,c,d;x)$ is defined as (Dejonghe 1986)

$$\mathbb{H}(a,b,c,d;x) = G^{1,1}_{2,2}\left(x\left|\begin{matrix}1-b,c\\a,1-d\end{matrix}\right.\right) \equiv H^{1,1}_{2,2}\left(x\left|\begin{matrix}(1-b,1),(c,1)\\(a,1),(1-d,1)\end{matrix}\right.\right), \tag{4.97}$$

with $G^{m,n}_{p,q}(x)$ the Meijer G-function. This $\mathbb{H}$-function can conveniently be expressed as

$$\mathbb{H}(a,b,c,d;x) = \begin{cases} \dfrac{\Gamma(a+b)}{\Gamma(c-a)\Gamma(a+d)}\, x^a\, {}_2F_1(a+b,1+a-c;a+d;x) & \text{if } x<1,\\[2ex] \dfrac{\Gamma(a+b)}{\Gamma(d-b)\Gamma(b+c)}\left(\dfrac{1}{x}\right)^b {}_2F_1\left(a+b,1+b-d;b+c;\dfrac{1}{x}\right) & \text{if } x>1. \end{cases} \tag{4.98}$$

In the bottom panels of Fig. 4.1 we plot the DF as a contour plot in the turning point space for the same models as the upper panels. The change in anisotropy from tangentially anisotropic at small radii to radially anisotropic at large radii can easily be seen in the slope of these contours.

An interesting subset of models in our two-parameter family of Plummer models is the one-parameter family with $\beta_0 = 0$. These models are isotropic in the inner regions and become anisotropic at large radii. Their augmented density is given by

$$\tilde{\rho}(\psi, r) = \frac{3M_{\rm tot}}{4\pi r_{\rm s}^3} \left(\frac{r_{\rm s}\psi}{GM_{\rm tot}} \right)^{5-2\beta_\infty} \left(1 + \frac{r^2}{r_{\rm s}^2} \right)^{-\beta_\infty}. \tag{4.99}$$

and in the expression for the distribution function (4.96) only the term corresponding to $j = 0$ remains

$$F(E, L) = \frac{3}{2(2\pi)^{5/2}} \frac{1}{(GM_{\rm tot}\, r_{\rm s})^{3/2}} \frac{\Gamma(6-2\beta_\infty)}{\Gamma(\beta_\infty)} \times \left(\frac{r_{\rm s}E}{GM_{\rm tot}} \right)^{7/2-2\beta_\infty} \mathbb{H}\left(0, \beta_\infty, \frac{9}{2} - 2\beta_\infty, 1; \frac{L^2}{2r_{\rm s}^2 E} \right). \tag{4.100}$$

This subfamily of our current set of Plummer models was already presented by Dejonghe (1987). Most of the kinematical properties, including the projected properties such as dispersions and higher-order moments of the line profiles, can be calculated completely analytically.

4.3.2 A family of anisotropic Hernquist models

Another very popular and simple potential-density pair is the Hernquist model (Hernquist 1990), defined by

$$\psi(r) = \frac{GM_{\rm tot}}{r_{\rm s} + r}, \tag{4.101}$$

$$\rho(r) = \frac{M_{\rm tot}}{2\pi} \frac{r_{\rm s}}{r(r_{\rm s}+r)^3}. \tag{4.102}$$

Contrary to the Plummer model, this model has a central r^{-1} density cusp and a more realistic r^{-4} behaviour at large radii. We can do the same exercise for the Hernquist model as we did for the Plummer model. If we combine the potential-density pair (4.101) - (4.102) with expressions (4.11) and (4.10), we obtain $E_0 = 0$ and

$$\frac{M_{\rm tot}}{2\pi r_{\rm s}^3} \left(\frac{r}{r_{\rm s}} \right)^{-1} \left(1 + \frac{r}{r_{\rm s}} \right)^{-3} = \rho_0 \left(1 + \frac{r}{r_{\rm s}} \right)^{-p} \times \left[1 - \left(1 + \frac{r}{r_{\rm s}} \right)^{-s} \right]^q \left(\frac{r}{r_{\rm a}} \right)^{-2\beta_0} \left(1 + \frac{r^{2\delta}}{r_{\rm a}^{2\delta}} \right)^{-(\beta_\infty - \beta_0)/\delta}. \tag{4.103}$$

Similarly as for the Plummer model, it is clear that we will only be able to find a general non-trivial solution if we set

$$E_0 = 0, \tag{4.104}$$
$$s = 2\delta = 1, \tag{4.105}$$
$$r_\mathrm{a} = r_\mathrm{s}. \tag{4.106}$$

This yields the equation

$$\frac{M_\mathrm{tot}}{2\pi r_\mathrm{s}^3 \rho_0} \left(\frac{r}{r_\mathrm{s}}\right)^{-1-q+2\beta_0} \left(1+\frac{r}{r_\mathrm{s}}\right)^{-3+p+q+2\beta_\infty-2\beta_0} \equiv 1, \tag{4.107}$$

from which we find

$$\rho_0 = \frac{M_\mathrm{tot}}{2\pi r_\mathrm{s}^3}, \tag{4.108}$$
$$p = 4-2\beta_\infty, \tag{4.109}$$
$$q = 2\beta_0 - 1. \tag{4.110}$$

We have now defined a two-parameter family of self-consistent Hernquist models with augmented density

$$\tilde{\rho}(\psi, r) = \frac{M_\mathrm{tot}}{2\pi r_\mathrm{s}^3} \left(\frac{r_\mathrm{s}\psi}{GM_\mathrm{tot}}\right)^{4-2\beta_\infty} \times \left(1-\frac{r_\mathrm{s}\psi}{GM_\mathrm{tot}}\right)^{2\beta_0-1} \left(\frac{r}{r_\mathrm{s}}\right)^{-2\beta_0} \left(1+\frac{r}{r_\mathrm{s}}\right)^{-2(\beta_\infty-\beta_0)}. \tag{4.111}$$

The parameter β_∞ can assume all values, whereas the central anisotropy β_0 is limited to $\beta_0 \leqslant 1/2$, in agreement with the cusp slope-central anisotropy theorem of An & Evans (2006). By construction, the anisotropy profile of this family of Hernquist models reads

$$\beta(r) = \frac{\beta_0 r_\mathrm{s} + \beta_\infty r}{r_\mathrm{s}+r}, \tag{4.112}$$

which is again a linear function of the density slope

$$\gamma(r) = \frac{r_\mathrm{s}+4r}{r_\mathrm{s}+r}. \tag{4.113}$$

The radial dispersion profile reads

$$\sigma_r^2(r) = \frac{GM_\mathrm{tot}}{r_\mathrm{s}} \left(\frac{r}{r_\mathrm{s}}\right)^{1-2\beta_0} \left(1+\frac{r}{r_\mathrm{s}}\right)^{3-2(\beta_\infty-\beta_0)} B_{\frac{r_\mathrm{s}}{r_\mathrm{s}+r}}(5-2\beta_\infty, 2\beta_0). \tag{4.114}$$

At large radii, the radial velocity dispersion profile falls as r^{-1},

$$\sigma_r^2(r) \sim \frac{1}{5-2\beta_\infty}\,\frac{GM_{\rm tot}}{r}, \tag{4.115}$$

whereas the asymptotic behaviour at small radii is

$$\sigma_r^2(r) \sim \begin{cases} -\dfrac{GM_{\rm tot}}{r_{\rm s}}\,\dfrac{1}{2\beta_0}\,\dfrac{r}{r_{\rm s}} & \text{if } \beta_0 < 0, \\ \dfrac{GM_{\rm tot}}{r_{\rm s}}\,B(5-2\beta_\infty, 2\beta_0)\left(\dfrac{r}{r_{\rm s}}\right)^{1-2\beta_0} & \text{if } \beta_0 > 0. \end{cases} \tag{4.116}$$

The radial velocity dispersion hence always disappears in the centre, except for the models with the largest allowed central anisotropy ($\beta_0 = 1/2$) where it reaches a finite value. For the asymptotic behaviour of the tangential velocity dispersions $\sigma_\theta(r) = \sigma_\varphi(r)$ at large radii we obtain

$$\sigma_\theta^2(r) = \sigma_\varphi^2(r) \sim \frac{1-\beta_\infty}{5-2\beta_\infty}\,\frac{GM_{\rm tot}}{r}, \tag{4.117}$$

whereas at small radii

$$\sigma_\theta^2(r) = \sigma_\varphi^2(r) \sim \begin{cases} \dfrac{GM_{\rm tot}}{r_{\rm s}}\,\dfrac{\beta_0-1}{2\beta_0}\,\dfrac{r}{r_{\rm s}} & \text{if } \beta_0 < 0, \\ \dfrac{GM_{\rm tot}}{r_{\rm s}}\,(1-\beta_0)\,B(5-2\beta_\infty, 2\beta_0)\left(\dfrac{r}{r_{\rm s}}\right)^{1-2\beta_0} & \text{if } \beta_0 > 0. \end{cases} \tag{4.118}$$

The distribution function can most conveniently be written as a series of hypergeometric functions

$$\begin{aligned} F(E,L) = &\frac{1}{(2\pi)^{5/2}}\,\frac{1}{(GM_{\rm tot}r_{\rm s})^{3/2}}\left(\frac{r_{\rm s}E}{GM_{\rm tot}}\right)^{5/2-2\beta_\infty} \times \\ &\sum_{k=0}^{\infty}\binom{\beta_\delta}{k}\,\frac{\Gamma(5-2\beta_\infty)}{\Gamma\left(1-\beta_0+\frac{k}{2}\right)\Gamma\left(\frac{7}{2}-2\beta_\infty+\beta_0-\frac{k}{2}\right)}\left(\frac{L^2}{2r_{\rm s}^2E}\right)^{-\beta_0+k/2} \times \\ &{}_2F_1\left(5-2\beta_\infty, 1-2\beta_0; \frac{7}{2}-\beta_\infty+\frac{k}{2}; \frac{r_{\rm s}E}{GM_{\rm tot}}\right) \end{aligned} \tag{4.119}$$

if $L^2 < 2r_{\rm s}^2E$, and as

$$\begin{aligned} F(E,L) = &\frac{1}{(2\pi)^{5/2}}\,\frac{1}{(GM_{\rm tot}r_{\rm s})^{3/2}}\left(\frac{r_{\rm s}E}{GM_{\rm tot}}\right)^{5/2-2\beta_\infty} \times \\ &\sum_{k=0}^{\infty}\binom{\beta_\delta}{k}\,\frac{\Gamma(5-2\beta_\infty)}{\Gamma\left(1-\beta_\infty-\frac{k}{2}\right)\Gamma\left(\frac{7}{2}-\beta_\infty+\frac{k}{2}\right)}\left(\frac{L^2}{2r_{\rm s}^2E}\right)^{-\beta_\infty-k/2} \times \\ &{}_2F_1\left(5-2\beta_\infty, 1-2\beta_0; \frac{7}{2}-2\beta_\infty+\beta_0-\frac{k}{2}; \frac{r_{\rm s}E}{GM_{\rm tot}}\right) \end{aligned} \tag{4.120}$$

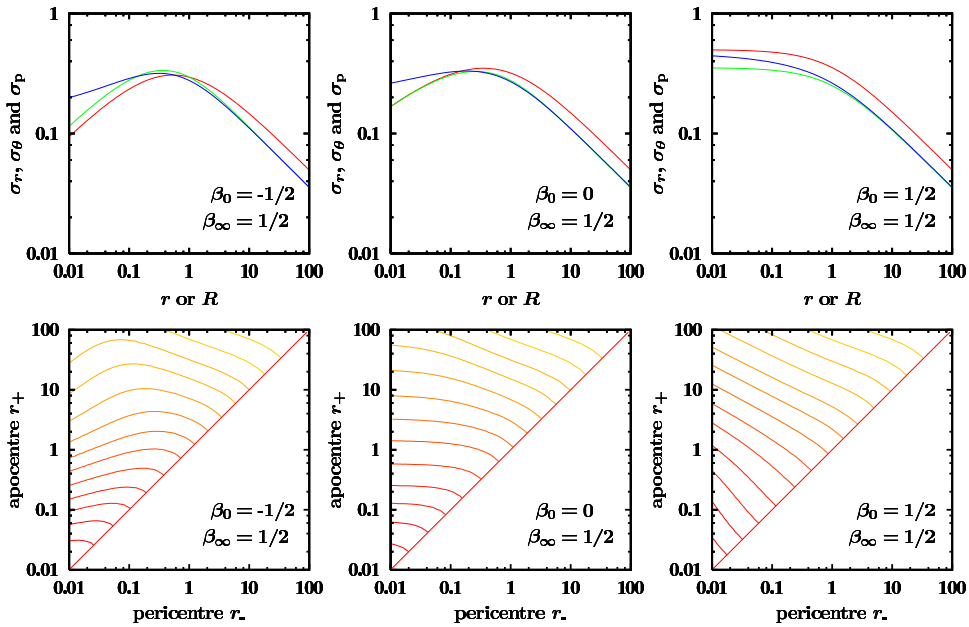

Figure 4.2 *Top.* Radial (red), tangential (green) and line-of-sight (blue) velocity dispersion profiles for three Hernquist models with anisotropy values β_0 and β_∞ displayed in the figures. *Bottom.* The distribution function of these models, represented by isoprobability contours in turning point space. High values are indicated by red contours, low values by yellow contours. In all plots, we have used normalized units with $G = M_{\rm tot} = r_{\rm s} = 1$.

if $L^2 > 2r_{\rm s}^2 E$. These sums only contain a finite number of terms if β_δ is a positive integer number, i.e. when $(\beta_0 - \beta_\infty)$ is a positive integer or half-integer number. This particular subset of models, in which the outer regions are always more tangentially anisotropic than the central regions, has already been discussed by Baes & Dejonghe (2002).

In a similar manner as for the Plummer model, we plot in Fig. 4.2 the velocity dispersions and the distribution function for three Hernquist models with the same anisotropy β_∞ but different anisotropy β_0.

4.3.3 Generalization to a family of anisotropic Veltmann models

It is well-known that the Plummer and the Hernquist potential-density pairs can be generalized to a one-parameter family of models characterized by

$$\psi(r) = \frac{GM_{\rm tot}}{(r_{\rm s}^{\eta} + r^{\eta})^{1/\eta}}, \tag{4.121}$$

$$\rho(r) = \frac{(1+\lambda)\, M_{\rm tot}}{4\pi} \frac{r_{\rm s}^{\eta}}{r^{2-\eta}\,(r_{\rm s}^{\eta} + r^{\eta})^{2+1/\eta}}. \tag{4.122}$$

This potential-density pair was first described by Veltmann (1979) and is a special subset (the α-models) of the general set of Zhao models (4.3). This potential-density pair has regained much interest because it supports dynamical models that are hypervirial, i.e. in which the virial relation is not only satisfied on a global but also on a local level (Evans & An 2005; Iguchi et al. 2006; Sota et al. 2006). The parameter η, lying in the range $0 < \eta \leqslant 2$, determines the slope of the central density cusp. We easily recognize the Plummer model with $\eta = 2$ as the only core-density member of the family and the Hernquist model as the model with $\eta = 1$.

We can now repeat the same exercise as for the Plummer and Hernquist models. After a little bit of algebra, we find that the parameters

$$E_0 = 0, \tag{4.123}$$

$$\rho_0 = \frac{(1+\eta)\, M_{\rm tot}}{4\pi r_{\rm s}^3}, \tag{4.124}$$

$$p = 3 + \eta - 2\beta_{\infty}, \tag{4.125}$$

$$q = 1 + \frac{2\,(\beta_0 - 1)}{\eta}, \tag{4.126}$$

$$s = 2\delta = \eta, \tag{4.127}$$

$$r_{\rm a} = r_{\rm s}, \tag{4.128}$$

are the general solution for the condition of self-consistency. Notice that the initial condition $q \leqslant 0$ implies $\beta_0 \leqslant 1 - \eta/2$, which is again in correspondence with the cusp slope-central anisotropy theorem (An & Evans 2006). In other words, for this family the condition $q \leqslant 0$ is also necessary to yield physical models. In this manner we have constructed a three-parameter family of dynamical models defined by the augmented density

$$\tilde{\rho}(\psi, r) = \frac{(1+\eta)\, M_{\rm tot}}{4\pi r_{\rm s}^3} \left(\frac{r_{\rm s}\psi}{GM_{\rm tot}}\right)^{3+\eta-2\beta_{\infty}} \times \left[1 - \left(\frac{r_{\rm s}\psi}{GM_{\rm tot}}\right)^{\eta}\right]^{1+2(\beta_0-1)/\eta} \left(\frac{r^{\eta}}{r_{\rm s}^{\eta}}\right)^{-2\beta_0/\eta} \left(1 + \frac{r^{\eta}}{r_{\rm s}^{\eta}}\right)^{-2(\beta_{\infty}-\beta_0)/\eta}. \tag{4.129}$$

This augmented density self-consistently supports the one-parameter potential-density pair (4.121) - (4.122) and has by construction an anisotropy profile

$$\beta(r) = \frac{\beta_0 r_\mathrm{s}^\eta + \beta_\infty r^\eta}{r_\mathrm{s}^\eta + r^\eta}, \tag{4.130}$$

which varies smoothly from β_0 in the centre towards β_∞ at large radii. Once again, the anisotropy is a linear function of the density slope

$$\gamma(r) = \frac{(2-\eta) r_\mathrm{s}^\eta + (3+\eta) r^\eta}{r_\mathrm{s}^\eta + r^\eta}. \tag{4.131}$$

The radial velocity dispersion can be written as

$$\sigma_r^2(r) = \frac{G M_\mathrm{tot}}{\eta r_\mathrm{s}} \left(\frac{r^\eta}{r_\mathrm{s}^\eta}\right)^{-1+2(1-\beta_0)/\eta} \times \left(1+\frac{r^\eta}{r_\mathrm{s}^\eta}\right)^{2+(1-2(\beta_\infty-\beta_0))/\eta} B_{\frac{r_\mathrm{s}^\eta}{r_\mathrm{s}^\eta+r^\eta}} \left(1+\frac{2\,(2-\beta_\infty)}{\eta}, 2-\frac{2\,(1-\beta_0)}{\eta}\right). \tag{4.132}$$

For general values of η, the distribution function cannot be simplified and should be taken as in Eqs. (4.57) - (4.58) with the values (4.124) - (4.128). For rational values of η however, distribution function simplifies to a sum of generalized hypergeometric functions. One such case is the model with $\eta = 1/2$, for which we obtain the potential-density pair

$$\psi(r) = \frac{G M_\mathrm{tot}}{\left(\sqrt{r_\mathrm{s}} + \sqrt{r}\right)^2}, \tag{4.133}$$

$$\rho(r) = \frac{3 M_\mathrm{tot}}{8\pi} \frac{\sqrt{r_\mathrm{s}}}{r^{3/2}\left(\sqrt{r_\mathrm{s}} + \sqrt{r}\right)^4}. \tag{4.134}$$

This model has a central density cups with a slope $\rho(r) \propto r^{-3/2}$, which has been obtained by numerical simulations for dark matter haloes in a CDM cosmological model (Moore et al. 1998).

This concludes our construction and analysis of our DF components. These provide a significant extension of previously implemented DFs, and in principle they can be extended even more (Lingam & Nguyen 2014). We now have all the necessary tools to use our modelling technique in several applications, building general DFs as linear combinations of our components, fitting given data sets. We will cover this work in the next three chapters: in Chapter 5, we model Dehnen & McLaughlin (2005) dark matter haloes, in Chapter 6, we study the global density slope – anisotropy inequality (GDSAI), and in Chapter 7, we examine the orbits of certain dwarf galaxies in the Fornax cluster and their link to ram-pressure stripping.

Part III

APPLICATIONS

Chapter 5

Dark matter haloes with universal properties

With the DFs derived in the previous chapter, we now demonstrate that we can construct dynamical models with very general anisotropy profiles, using the quadratic programming algorithm described in Chapter 2. In particular, we will construct self-consistent models with Dehnen-McLaughlin haloes. These models are characterized by three "universal" properties, commonly encountered in CDM simulations. The main results in this chapter are published in Van Hese et al. (2009), but we will also include extra material; all the work presented here has been carried out by the author.

5.1 Results from cosmological simulations

As N-body simulations of cold dark matter haloes have become more detailed (see Springel 2005 for an overview), several common characteristics have emerged over a large range of mass scales. We highlight three of these "universal" properties.

Firstly, numerous cosmological studies revealed similar density profiles over several orders of magnitude in halo mass. Many simulations (e.g. Dubinski & Carlberg 1991; Crone et al. 1994; Navarro et al. 1996; Fukushige & Makino 1997; Carlberg et al. 1997; Navarro et al. 1997; Moore et al. 1998; Moore et al. 1999; Jing & Suto 2000) hinted at densities with a mild central cusp and an a $\rho(r) \propto r^{-3}$ falloff at large radii, but more recent studies showed that the central density slope does vary somewhat with halo mass, ranging from no inner slope for galaxy-sized haloes to $\sim r^{-0.4}$ in cluster-sized haloes (Navarro et al. 2010; Del Popolo 2010; Del Popolo 2012). Two types of profiles are widely used to describe these densities: the Einasto models (Einasto & Haud 1989; Navarro et al. 2004; Merritt et al. 2005; Gao et al. 2008; Stadel et al. 2009; see also Section 3.5) and the double power-law profiles (also known as generalized NFW profiles, see citations above), which are part of the Zhao family that we introduced in Eq. (4.3). The difference between these two families however is minimal, especially outside the central region (An & Zhao

2013). As we derived in the previous chapters the appropriate tools to describe the double power-law profiles, one such model will be the focus of our modelling in the subsequent sections.

A second relation was found by Taylor & Navarro (2001). These authors identified that a particular ratio between the density and the (total) velocity dispersion, the quantity $Q(r) = \rho/\sigma^3(r)$ (which has become known as the pseudo phase-space density), behaves as a power-law over 2-3 orders of magnitude in radius inside the virial radius,

$$Q(r) \propto r^{-\alpha}. \tag{5.1}$$

Other studies (e.g. Rasia et al. 2004; Ascasibar et al. 2004; Navarro et al. 2010; Ludlow et al. 2010; Ludlow et al. 2011) have confirmed the scale-free nature of $Q(r)$, and their results indicate that its slope lies in the range $\alpha = 1.90 \pm 0.05$. This property is remarkable since the density $\rho(r)$ nor the velocity dispersion $\sigma(r)$ separately show a power-law behaviour. It should be noted though that Schmidt et al. (2008) called the universality of this property into question, and suggested a more general ratio $\rho/\sigma_d^{\varepsilon}(r)$, with dispersions in other directions and with different powers ε.

Finally, the velocity anisotropy profiles $\beta(r)$ of dark matter systems also evolve towards a similar shape, steepening gradually from isotropic in the centre to radially anisotropic in the outer regions. Hansen & Moore (2006) and Hansen & Stadel (2006) discovered a nearly linear relation between the logarithmic density slope $\gamma(r)$ and the velocity anisotropy profile; they proposed the $\beta - \gamma$ relation

$$\beta(\gamma) \simeq 1 - 1.15(1 + \gamma/6). \tag{5.2}$$

Why do dark matter haloes share these properties? How are they connected? Various ideas have been proposed, such as phase mixing, violent relaxation (Lynden-Bell 1967; Kandrup et al. 2003), statistical mechanics (Hjorth & Williams 2010), radial orbit instabilities (Henriksen 2007; Henriksen 2009), adiabatic contraction (Dalal et al. 2010), self-similar collapse (Lapi & Cavaliere 2011; Alard 2013), and entropy effects (He 2012). But the puzzle remains unsolved. A popular approach to tackle the problem is to investigate whether solutions of the Jeans equation (2.124) exist that encompass the observed properties of dark matter haloes (e.g. Zait et al. 2008; Hansen et al. 2010). In a very interesting study, Dehnen & McLaughlin (2005) analysed the anisotropic Jeans equation constrained by a slightly different form of the pseudo phase-space density, namely $Q_r(r) = \rho/\sigma_r^3$ with $\sigma_r(r)$ the radial velocity dispersion. They found a special solution, namely an analytical self-consistent potential-density pair of the form (4.3) with an exactly linear $\beta - \gamma$ relation. In other words, their corresponding anisotropy profile is given by Eq. (4.10)

$$\beta(r) = \frac{\beta_0 + \beta_\infty (r/r_\mathrm{a})^{2\delta}}{1 + (r/r_\mathrm{a})^{2\delta}}, \tag{5.3}$$

with $r_\mathrm{a} = r_\mathrm{s}$ and $2\delta = \eta$, the same form for which we developed our DF components. These Jeans models satisfy the three universal relations mentioned above, but they don't provide any additional information.

With the QP-algorithm and the components derived in the previous chapter, we have the tools to take the analytical study of dark matter systems a step further, i.e. to look for full dynamical models that encompass the universal properties found in N-body simulations. In concreto, we will construct DFs with a separable augmented density that generate the spatial density and anisotropy profiles of the Dehnen-McLaughlin haloes with high accuracy. Naturally, such dynamical models are an idealization; actual DM haloes are more "grainy" than smooth DFs (Zemp et al. 2009), so we shouldn't over-analyse these models. Nevertheless, by mapping their orbital and velocity structure, we provide an additional way to gain more insight into the properties of DM haloes.

It is also interesting to note that, just prior to our publication, Wojtak et al. (2008) presented a similar approach to generate dynamical models for potential-density pairs with a fairly general anisotropy profile. Instead of the augmented density, they proposed to express the DF as a separable function of the form $f_E(E)\, f_L(L)$, with

$$f_L(L) = L^{-2\beta_0} \left(1 + \frac{L^2}{2L_0^2}\right)^{\beta_0 - \beta_\infty}, \tag{5.4}$$

a double power-law function with three parameters β_0, β_∞, and L_0. Once their values have been determined, they derive the function $f_E(E)$ from the observed density profile by a numerical inversion. This technique yields a three-parameter anisotropy profile that resembles Eq. (5.3), where L_0 has a similar role as r_a, and a fixed transition rate $0.5 < \delta < 1$. The authors applied their method to an NFW density. This approach is slightly simpler than ours, but it does have a caveat: they mention a bias towards too high kurtosis values, indicating that three parameters are not sufficient to produce realistic models. The reason is likely due to their transition rate, which is lower than that of an Osipkov-Merritt system, but still higher than the $\delta \sim 0.5$ value found in simulations and observations (Mamon & Łokas 2005). Our four-parameter anisotropy profiles, with δ as an extra free parameter, are able to solve this problem.

5.2 The Dehnen-McLaughlin haloes

In the context of dark matter halo studies, the model derived by Dehnen & McLaughlin (2005) is of particular interest. We summarize their main results in this section. Instead of fitting a parametrized density profile to N-body simulations, they investigated the solution space of the Jeans equation to search for models that explicitly obey the power-law behaviour of the pseudo phase-space density. With the extra condition of a linear $\beta - \gamma$ relation they found a critical solution that satisfies the condition

$$\frac{\rho}{\sigma_r^\varepsilon}(r) = \frac{\rho}{\sigma_r^\varepsilon}(r_\mathrm{s}) \left(\frac{r}{r_\mathrm{s}}\right)^{-\alpha_\mathrm{crit}}, \tag{5.5}$$

with r_s a scale radius. In the remainder of the chapter, we adopt the common value $\varepsilon = 3$ and use the notation

$$Q_r(r) = \frac{\rho}{\sigma_r^3}(r). \tag{5.6}$$

Dehnen & McLaughlin derived for this case the exponent

$$\alpha_\mathrm{crit} = \eta + \frac{3}{2}, \tag{5.7}$$

$$\eta = \frac{4-2\beta_0}{9}. \tag{5.8}$$

The corresponding potential-density pair is part of the Zhao family (4.3) - (4.9), namely

$$\psi(r) = \frac{GM_\mathrm{tot}}{r_\mathrm{s}}\,\frac{1}{\eta}\,B_{\frac{1}{1+x^\eta}}\left(\frac{1}{\eta}, \frac{1-\beta_0}{\eta}+\frac{1}{2}\right), \tag{5.9}$$

$$\rho(r) = \frac{4+\eta-2\beta_0}{8\pi}\,\frac{M_\mathrm{tot}}{r_\mathrm{s}^3}\,x^{-\gamma_0}\,(1+x^\eta)^{-(\gamma_\infty-\gamma_0)/\eta}, \tag{5.10}$$

where $x = r/r_\mathrm{s}$, $B_y(a,b)$ is the incomplete beta function, and

$$\gamma_0 = \frac{7+10\beta_0}{9}, \tag{5.11}$$

$$\gamma_\infty = \frac{31-2\beta_0}{9}. \tag{5.12}$$

The density can be equivalently written in terms of the slope $\gamma(r)$, which has the same elegant form as the velocity anisotropy profile $\beta(r)$

$$\gamma(r) = \frac{\gamma_0+\gamma_\infty x^\eta}{1+x^\eta}, \tag{5.13}$$

$$\beta(r) = \frac{\beta_0+\beta_\infty x^\eta}{1+x^\eta}. \tag{5.14}$$

Finally, the authors derived the corresponding velocity dispersions

$$\sigma_r^2(r) = \frac{1}{4+\eta-2\beta_\infty}\,\frac{GM_\mathrm{tot}}{r_\mathrm{s}}\,x^{-1}\left(\frac{x^\eta}{1+x^\eta}\right)^{(\gamma_\infty-\gamma_0)/\eta-2}, \tag{5.15}$$

$$\sigma_\theta^2(r) = \sigma_\varphi^2(r) = \frac{1}{2}\sigma_T^2(r) = \big(1-\beta(r)\big)\,\sigma_r^2(r). \tag{5.16}$$

To summarize, these haloes are determined by five parameters: the exponent in the pseudo phase space density ε, two scaling constants i.e. the total mass M_tot and a scale-length r_s, and the asymptotic anisotropy parameters β_0 and β_∞. The authors also noticed the remarkable property that the shape of the density profile (and hence the gravitational potential) only depends on β_0 and not on β_∞.

While the Dehnen-McLaughlin halo profiles are derived from theoretical considerations, they also closely fit adequately galaxy-sized and certain cluster-sized haloes generated by N-body simulations (Diemand et al. 2005 ; Merritt et al. 2006). However, the density and velocity dispersions alone do not determine the complete dynamical state of dark matter systems. In other words, these profiles need to be incorporated into self-consistent dynamical models, described by nonnegative DFs.

5.3 The modelling technique

5.3.1 Quadratic programming

As we explained in Section 2.4, we will build our DFs as linear combinations of base functions, selected from a parameter library of components

$$F(E,L) = \sum_{i=1}^{N} a_i\, F_i(E,L), \tag{5.17}$$

with a corresponding separable augmented density of the form

$$\tilde{\rho}(\psi,r) = \sum_{i=1}^{N} a_i\, f_i(\psi)\, g(r). \tag{5.18}$$

Consider the potential $\psi(r)$ given by Eq. (5.9), the anisotropy profile $\beta(r)$ stated by Eq. (5.14) and a set of $N_{\rm data}$ data points $\rho_{\rm obs}(r_m)$, with $m = 1,\ldots,N_{\rm data}$, drawn from the density profile Eq. (5.10). To model these data, we thus first construct a library of $N_{\rm lib}$ base functions of the form (4.55),

$$\tilde{\rho}_i(\psi,r) = \rho_{0,i} \left(\frac{\psi}{\psi_0}\right)^{p_i} \left(1-\frac{\psi^{s_i}}{\psi_0^{s_i}}\right)^{q_i} \left(\frac{r}{r_{\rm a}}\right)^{-2\beta_0} \left(1+\frac{r^{2\delta}}{r_{\rm a}^{2\delta}}\right)^{\beta_\delta}, \tag{5.19}$$

where the normalization constants $\rho_{0,i}$ are chosen such that the total mass of the components is unity,

$$M_i = 4\pi \int_0^{+\infty} \tilde{\rho}_i(\psi(r),r)\, r^2\, {\rm d}r = 1. \tag{5.20}$$

These functions extend to infinity, i.e. $E_0 = 0$. The four parameters that determine the anisotropy profile (5.3) are fixed, with β_0 and β_∞ to be chosen freely, and

$$r_{\rm a} = r_{\rm s}, \tag{5.21}$$

$$2\delta = \eta, \tag{5.22}$$

to match (5.14). Since all components have a priori the desired $\beta(r)$, all that remains is to fit the $f(\psi)$-part of these functions to the data extracted from the density (5.10). Our library of base functions will therefore be constructed with three parameters p_i, q_i and s_i, which respectively determine the asymptotic behaviour at infinity, the inner slope and the transition rate between these two regions. They satisfy the conditions $p_i + 2\beta_\infty > 3$, $q_i \leqslant 0$ and $s_i > 0$. For each component, we then calculate the corresponding densities in the given data points,

$$\rho_i(r_m) = \tilde{\rho}_i\left(\psi(r_m), r_m\right). \tag{5.23}$$

The DFs are then built in N steps. In each successive step, the previous best-fitting set is preserved and extended by adding the one component from the remaining library that yields the most improvement of the fit, minimizing the quantity

$$\chi^2_N = \frac{1}{N_{\text{data}}} \sum_{m=1}^{N_{\text{data}}} w_m \left(\rho_{\text{obs}}(r_m) - \sum_{i=1}^{N} a_i\, \rho_i(r_m) \right)^2, \tag{5.24}$$

where we set $w_m = 1/\rho^2_{\text{obs}}(r_m)$.

5.3.2 The library of components

Every given Dehnen-McLaughlin halo requires a specific component library. In particular, the parameters p_i, q_i are constrained by the potential. If we examine the asymptotic behaviour of the Dehnen-McLaughlin potential (5.9) in more detail, we find

$$\begin{array}{lcll} \psi(r) & \sim & \psi_0 - a\, r^{(11-10\beta_0)/9} + \cdots & \text{for} \quad r \to 0, \\ \psi(r) & \sim & r^{-1} & \text{for} \quad r \to \infty. \end{array} \tag{5.25}$$

Introducing these asymptotic expansions in the expression (5.19) we find for the inner and outer slopes of the density

$$\begin{array}{lcll} \tilde{\rho}_i(\psi(r), r) & \sim & r^{-2\beta_0 + q_i(11-10\beta_0)/9} & \text{for} \quad r \to 0, \\ \tilde{\rho}_i(\psi(r), r) & \sim & r^{-2\beta_\infty - p_i} & \text{for} \quad r \to \infty. \end{array} \tag{5.26}$$

Evidently, the parameters p_i stipulate the density slope at large radii. Because the models fall as $r^{-\gamma_\infty}$, no components can be used in the fitting routine that fall less rapidly. Using Eq. (5.12), this puts a boundary on the p_i,

$$p_i \geqslant \frac{31 - 2\beta_0 - 18\beta_\infty}{9} \equiv p_{\min}(\beta_0, \beta_\infty). \tag{5.27}$$

Conversely, the density slope at small radii depends on the parameters q_i. The density diverges toward the centre as $r^{-\gamma_0}$, and we cannot use components in the fitting routine that have a steeper slope. Thus we obtain from Eq. (5.11)

$$q_i \geqslant -\frac{7 - 8\beta_0}{11 - 10\beta_0} \equiv q_{\min}(\beta_0). \tag{5.28}$$

So if a fit to a halo has at least one component with parameter $p_{\min}$ and one with $q_{\min}$, this fit has the same slope as the given density at small and large radii.

Finally, the parameters s_i have a similar role as δ, in the sense that they control the transition rate between the inner and outer density slopes. Their value can be chosen freely, but we found that excellent results are obtained with a single fixed value

$$s_i \equiv 2\delta = \eta, \tag{5.29}$$

for all components. This is the same choice as the Veltmann models. It thus further facilitates the fitting process, leaving only p_i and q_i as free parameters, and it also simplifies the computation of the DF components

$$F_i(E,L) = \frac{\rho_{0,i}}{M_i(2\pi\psi_0)^{3/2}} \sum_{j=0}^{\infty} (-1)^j \binom{q_i}{j} \Gamma(1+p_i+j\eta) \left(\frac{E}{\psi_0}\right)^{p_i+j\eta-3/2} \times \sum_{k=0}^{\infty} \binom{\beta_\delta}{k} \frac{1}{\Gamma(1-\beta_k)\Gamma(p_i+j\eta-1/2+\beta_k)} \left(\frac{L^2}{2r_{\mathrm{a}}^2 E}\right)^{-\beta_k}, \tag{5.30}$$

with β_k given by Eq. (4.59).

5.4 Results

5.4.1 The minimization

Now that we have derived the necessary mathematical tools, we can present the results for the Dehnen-McLaughlin haloes. Without loss of generality, we can work in dimensionless units $G = M_{\mathrm{tot}} = r_{\mathrm{s}} = r_{\mathrm{a}} = 1$, and we limit ourselves to $\varepsilon = 3$. Consequently, the models are determined by the anisotropy parameters β_0 and β_∞. Although we are able to generate models with arbitrary values for these parameters, realistic dark matter haloes are nearly isotopic near the centre and radially anisotropic at large radii, so that we concentrate on six representative models with $\beta_0 = 0$ and $\beta_\infty = 0$, 0.2, 0.4, 0.6, 0.8, 1. We verified that the modelling procedure works equally well for models with non-zero values of β_0. Finally, it is evident from Eq. (5.8) that $\beta_0 = 0$ sets the parameters $s_i \equiv 2\delta = \eta = 4/9$.

As we demonstrated above, the very specific form of the base functions (5.19) simplifies our QP-algorithm considerably for these models. Only the parameters p_i and q_i remain to construct a library of components, and we have found that sets of only 30 components are sufficient to extract excellent fits from. Recalling Eqs. (5.27) and (5.28), the parameters p_i take five values, ranging from $p_{\min}(0,\beta_\infty)$ to 10 or 12, depending on the model, and the parameters q_i take six values from $q_{\min}(0)$, -0.5, -0.4, -0.3, -0.15, 0. The minimum values for p_i lie between $p_{\min}(0,0) \simeq 3.444$ and $p_{\min}(0,1) \simeq 1.444$, while $q_{\min}(0) \simeq -0.636$.

Table 5.1. Components of the six QP-models: $\beta_\infty = 0$, 0.2 and 0.4.

$\beta_\infty = 0.0$	$p_i = 3.4\overline{4}$, 4, 5, 7.5, 10		$q_i = -0.\overline{63}$, -0.5, -0.4, -0.3, -0.15, 0		
$a_{10,i}$	0.2047	-0.0380	-0.5411	1.6652	0.0414
	-3.8806	0.1312	2.5207	-0.2684	1.1652
ρ_{0i}	0.0053	1.9783	0.0009	2.5540	0.4890
	3.0677	0.0384	3.6728	6.1920	0.0008
p_i	4.0000	10.0000	3.4444	10.0000	7.5000
	10.0000	5.0000	10.0000	10.0000	3.4444
q_i	-0.6364	-0.6364	0.0000	-0.5000	-0.6364
	-0.4000	-0.6364	-0.3000	0.0000	-0.6364
χ^2_N	0.44×10^{0}	0.17×10^{0}	0.67×10^{-1}	0.33×10^{-1}	0.24×10^{-2}
	0.17×10^{-2}	0.53×10^{-4}	0.36×10^{-4}	0.48×10^{-5}	0.82×10^{-7}
$\beta_\infty = 0.2$	$p_i = 3.0\overline{4}$, 4, 5, 7.5, 10		$q_i = -0.\overline{63}$, -0.5, -0.4, -0.3, -0.15, 0		
$a_{10,i}$	-0.1534	15.5467	-0.0006	0.4549	-0.2707
	74.2329	-88.6417	0.5880	-0.7724	0.0165
ρ_{0i}	0.0238	0.0017	3.4087	4.4609	11.3269
	0.0014	0.0015	8.6356	5.4102	0.9797
p_i	4.0000	3.0444	10.0000	10.0000	10.0000
	3.0444	3.0444	10.0000	10.0000	7.5000
q_i	-0.6364	0.0000	-0.6364	-0.5000	0.0000
	-0.6364	-0.5000	-0.1500	-0.4000	-0.6364
χ^2_N	0.48×10^{0}	0.27×10^{0}	0.43×10^{-1}	0.93×10^{-2}	0.13×10^{-2}
	0.88×10^{-3}	0.10×10^{-4}	0.95×10^{-5}	0.48×10^{-5}	0.32×10^{-7}
$\beta_\infty = 0.4$	$p_i = 2.6\overline{4}$, 4, 5, 8, 12		$q_i = -0.\overline{63}$, -0.5, -0.4, -0.3, -0.15, 0		
$a_{10,i}$	8.2375	-1.4318	-0.0467	0.2297	2.2705
	-0.0111	0.1299	10.3097	-0.3108	-18.3771
ρ_{0i}	0.0832	0.0032	10.9019	14.9246	0.0028
	2.4301	23.3335	0.1015	18.6978	0.0934
p_i	4.0000	2.6444	12.0000	12.0000	2.6444
	8.0000	12.0000	4.0000	12.0000	4.0000
q_i	-0.6364	0.0000	-0.6364	-0.5000	-0.6364
	-0.6364	-0.3000	-0.4000	-0.4000	-0.5000
χ^2_N	0.48×10^{0}	0.18×10^{0}	0.28×10^{-1}	0.93×10^{-2}	0.42×10^{-2}
	0.14×10^{-3}	0.36×10^{-4}	0.13×10^{-4}	0.68×10^{-5}	0.24×10^{-6}

Table 5.2. Components of the six QP-models: $\beta_\infty = 0.6$, 0.8 and 1.

$\beta_\infty = 0.6$	$p_i = 2.2\overline{4}$, 3.5, 5, 8, 12		$q_i = -0.\overline{63}$, -0.5, -0.4, -0.3, -0.15, 0		
$a_{10,i}$	0.3552	2.0738	-0.0094	0.0086	16.3498
	-17.4861	0.0731	-0.3019	-0.2109	0.1477
ρ_{0i}	0.1222	0.0063	16.7922	23.2672	0.0053
	0.0055	4.3156	0.1372	8.0592	10.5109
p_i	3.5000	2.2444	12.0000	12.0000	2.2444
	2.2444	8.0000	3.5000	8.0000	8.0000
q_i	-0.6364	0.0000	-0.6364	-0.5000	-0.6364
	-0.5000	-0.6364	-0.5000	-0.3000	-0.1500
χ^2_N	0.44×10^{0}	0.15×10^{0}	0.18×10^{-1}	0.67×10^{-2}	0.31×10^{-2}
	0.16×10^{-4}	0.13×10^{-4}	0.10×10^{-4}	0.17×10^{-5}	0.20×10^{-6}
$\beta_\infty = 0.8$	$p_i = 1.8\overline{4}$, 3, 5, 8, 12		$q_i = -0.\overline{63}$, -0.5, -0.4, -0.3, -0.15, 0		
$a_{10,i}$	-0.0321	-6.1421	0.0008	-0.0013	24.5830
	-100.0000	-0.0163	-0.0926	40.5233	42.1774
ρ_{0i}	0.1791	0.0121	25.3820	35.5933	0.0101
	0.0109	2.3877	0.2367	0.0105	0.0116
p_i	3.0000	1.8444	12.0000	12.0000	1.8444
	1.8444	5.0000	3.0000	1.8444	1.8444
q_i	-0.6364	0.0000	-0.6364	-0.5000	-0.6364
	-0.4000	-0.3000	-0.3000	-0.5000	-0.1500
χ^2_N	0.40×10^{0}	0.11×10^{0}	0.11×10^{-1}	0.46×10^{-2}	0.22×10^{-2}
	0.66×10^{-5}	0.26×10^{-5}	0.13×10^{-5}	0.47×10^{-6}	0.24×10^{-6}
$\beta_\infty = 1.0$	$p_i = 1.4\overline{4}$, 3, 5, 8, 12		$q_i = -0.\overline{63}$, -0.5, -0.4, -0.3, -0.15, 0		
$a_{10,i}$	-5.2047	0.1086	62.6962	40.1800	-0.0002
	0.0003	-96.6969	-0.1234	0.0273	0.0128
ρ_{0i}	0.0192	2.9967	0.0201	0.0213	37.6938
	44.2497	0.0207	3.7237	7.8118	0.8543
p_i	1.4444	5.0000	1.4444	1.4444	12.0000
	8.0000	1.4444	5.0000	5.0000	3.0000
q_i	-0.6364	-0.6364	-0.5000	-0.3000	-0.6364
	0.0000	-0.4000	-0.5000	0.0000	-0.1500
χ^2_N	0.35×10^{0}	0.36×10^{-1}	0.10×10^{-1}	0.24×10^{-3}	0.41×10^{-4}
	0.16×10^{-4}	0.13×10^{-4}	0.45×10^{-6}	0.89×10^{-7}	0.22×10^{-8}

Finally, we put additional constraints of the form (2.191) on the coefficients, namely

$$-100 \leqslant a_i \leqslant 100, \qquad \forall i. \tag{5.31}$$

These constraints are not necessary for the fitting, but they greatly reduce the computational cost in the calculation of the DF. The reason for this is straightforward: if the components are computed with numerical errors $\delta_i F_i$ then the total numerical error of the DF is

$$\delta F(E,L) \sim \sum_{i=1}^{N} |a|_i \, \delta_i F_i(E,L). \tag{5.32}$$

The higher the absolute values of the coefficients $|a|_i$, the smaller the errors $\delta_i F_i$ need to be to obtain a given δF, which increases the computational time. Sensible boundary values (5.31) enable efficient calculations of the DF, while maintaining satisfactory fits.

Naturally, the resulting DF also needs to be physical, i.e. nonnegative everywhere in phase space. We found that all our DFs automatically satisfy this condition without imposing explicit constraints.

For each model, we extracted $N_{\text{data}} = 25$ values of the density $\rho_{\text{obs}}(r_m)$ (5.10), at radii r_m, distributed logarithmically between $10^{-3}\ r_s$ and $10^4\ r_s$. Evidently, this range is much larger than the virialized region in N-body simulations, where the profiles are valid. This larger range is therefore not intended to be realistic, but rather to demonstrate that our models are accurate up to arbitrary distances. Furthermore, this makes it possible to create discrete equilibrium systems from the DFs, by means of Monte Carlo simulators, that trace very closely the Dehnen-McLaughlin haloes. After calculating the densities of every library component at these radii $\tilde{\rho}_i(\psi(r_m), r_m)$ (5.19), we can perform the QP-procedure for the six values of β_∞, constructing iteratively the best-fitting linear combination (2.183).

Our results for the six models are displayed in Tables 5.1 and 5.2. Each header lists β_∞ and the values of p_i and q_i of the 30 library components that are used for the construction of the specific model. Below each header, the parameters of the subsequently selected fitting functions are given, from 1 to 10, with corresponding values χ^2_1 to χ^2_{10}. The coefficients a_i are those of the final fit with 10 components. It can be checked that for each model

$$\sum_{i=1}^{10} a_i \simeq M_{\text{tot}} = 1. \tag{5.33}$$

Combining this result with Eqs. (5.32) and (5.31), it can be seen that if $N = 10$, the numerical errors of the base functions $\delta_i F_i$ need at most be a factor 10^3 smaller than a given error δF, allowing efficient computations of the DF with sufficient accuracy.

The resulting χ^2_N values for each model are also displayed in Fig. 5.1. Evidently, $N = 10$ components are more than sufficient to obtain very accurate dynamical models. As an example, Fig. 5.2 shows the 10 individual components of the QP-model with $\beta_\infty = 0.4$. Although this fit has the highest χ^2_{10} of our set, its total density is a very close approximation to the given data over the entire range in radius.

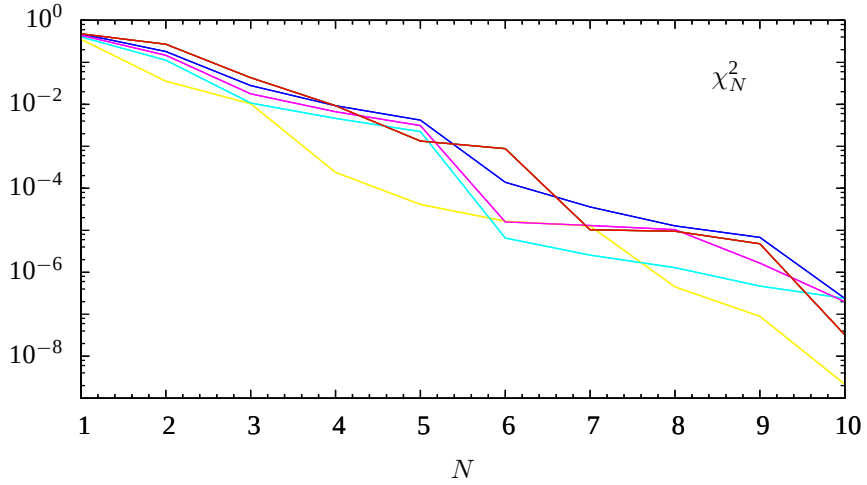

Figure 5.1 The obtained χ^2_N for the six QP-models, explicitly as a function of the number of components in the fit. The different curves correspond to $\beta_\infty = 0$, 0.2, 0.4, 0.6, 0.8 and 1, with respective colours red, green, blue, magenta, cyan and yellow.

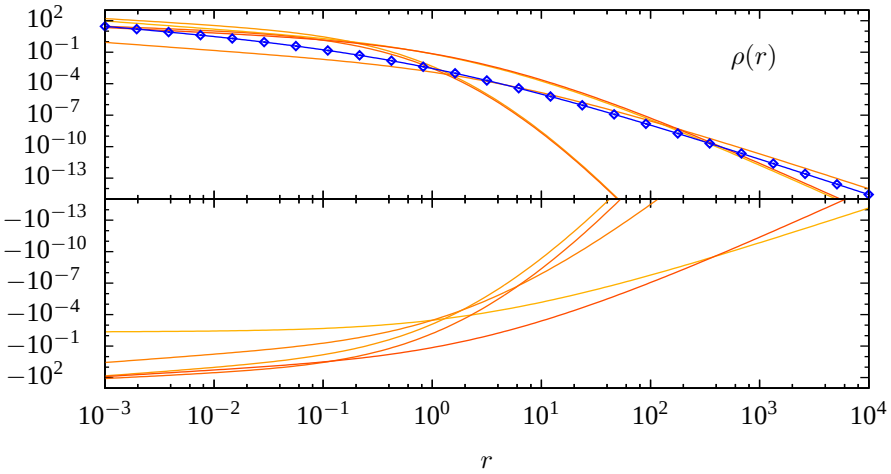

Figure 5.2 The 10 individual components of the fitted density for the QP-model with $\beta_0 = 0$ and $\beta_\infty = 0.4$. Their sum is the QP-density (blue curve), fitting the 25 data points (blue dots).

5.4.2 The velocity moments

Fig. 5.3 displays several moments for our six models, with 10 components. The top row shows the density $\rho(r)$, the pseudo phase-space density $Q_r(r)$ and the $\beta - \gamma$ relation. Be-

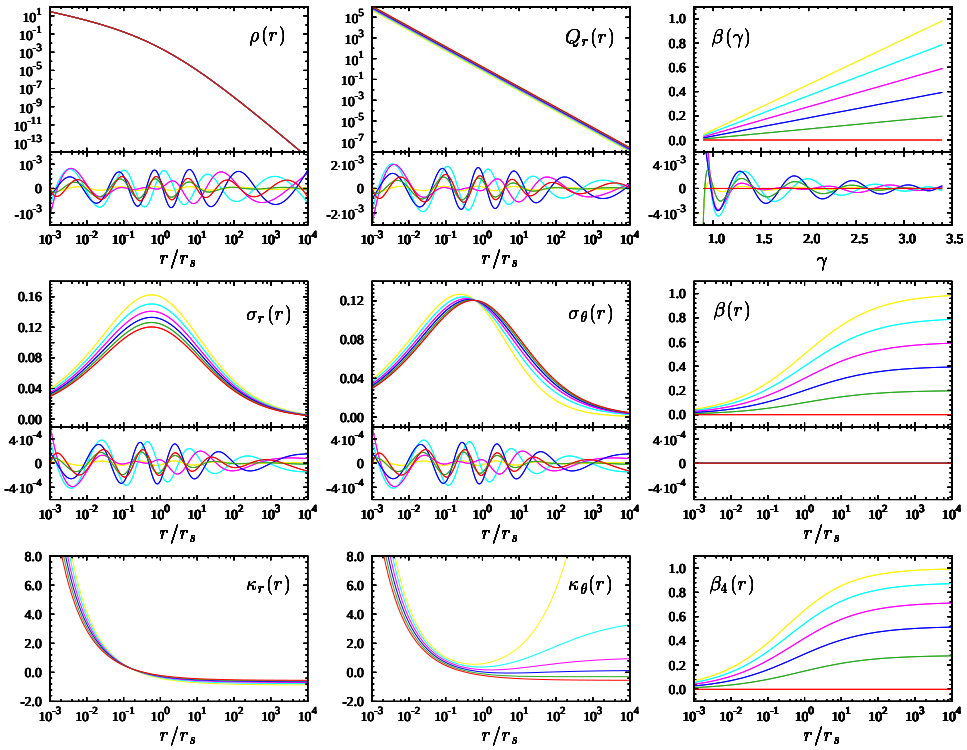

Figure 5.3 The most important moments for our set of representative models with 10 components. Top row: the density $\rho(r)$, the pseudo phase-space density $Q_r(r)$ and the $\beta-\gamma$ relation. Below each graph, the relative errors with respect to the theoretical profiles is shown. Middle row: the radial velocity dispersion $\sigma_r(r)$, the tangential velocity dispersion $\sigma_\theta(r)$, and the anisotropy $\beta(r)$, also with the relative errors. Bottom row: the radial kurtosis $\kappa_r(r)$, the tangential kurtosis $\kappa_\theta(r)$, and fourth-order anisotropy $\beta_4(r)$. The models and colouring are the same as in Fig. 5.1.

low each graph, we calculated the residual errors between the QP-fits and the theoretical curves, i.e. for each profile $f(r)$ we have

$$\Delta f(r) = \frac{f_{\rm obs}(r) - f_{\rm QP}(r)}{f_{\rm obs}(r)}. \tag{5.34}$$

As can be seen, the relative errors on the densities are less than 10^{-3} along 7 orders of magnitude in radius, and the correct asymptotic slopes of the models ensure excellent fits even beyond this range. The power-law trend of $Q_r(r)$ and the $\beta-\gamma$ relations are also reproduced very accurately with errors $\sim 10^{-3}$. Note that the small offset between the pseudo phase-space density profiles for the different models is due to the dependence of σ_r

on β_∞.

In the central row, we display the velocity dispersion profiles $\sigma_r(r)$, $\sigma_\theta(r)$ and the anisotropies $\beta(r)$. It is striking that, while these quantities were not used in the fit, the deviations of these moments from the theoretical values are even smaller. Evidently, since the models have the anisotropies (5.14) by construction, the $\beta(r)$ profiles are exact, without errors. Note also that all tangential velocity dispersion profiles $\sigma_\theta(r)$ intersect at a common radius $r = r_{\rm s}\,(9/11)^{1/\eta}$.

While the density and dispersions are defined by the Dehnen-McLaughlin haloes, the higher-order moments are determined by the QP-models. The fourth-order moments, derived from Eq. (4.62), allow us to derive the radial and tangential kurtosis,

$$\kappa_r(r) = \frac{\langle v_r^4 \rangle}{\sigma_r^4}(r) - 3, \tag{5.35}$$

$$\kappa_\theta(r) = \frac{\langle v_\theta^4 \rangle}{\sigma_\theta^4}(r) - 3, \tag{5.36}$$

and the fourth-order anisotropy

$$\beta_4(r) = 1 - \frac{\langle v_\theta^4 \rangle}{\langle v_r^4 \rangle}(r), \tag{5.37}$$

Interestingly, as a result of the separable form of the augmented densities, we find that the $\beta_4(r)$ profiles are only a function of the $\beta(r)$,

$$\beta_4(r) = \frac{1}{2}\beta(r)\big(3-\beta(r)\big) + \frac{1}{2\beta_\delta}\big(\beta_0-\beta(r)\big)\big(\beta_\infty-\beta(r)\big). \tag{5.38}$$

These profiles are shown in the bottom row of Fig. 5.3. We can use these kurtosis values to get a general idea about the non-Gaussianity of the velocity distributions at a certain radius; in the next section, we will show these distributions in full. Our radial kurtosis values are very large in the centre, which indicates that the v_r-distributions are significantly peaked (leptokurtic) at small radii. The $\kappa_r(r)$ curves decrease rapidly as a function of radius: they reach zero at radii between 0.26-0.36 and become negative at larger radii, leading to flat-topped (platykurtic) radial velocity distributions. This behaviour is in accordance with N-body simulations (Kazantzidis et al. 2004; Wojtak et al. 2005). Clearly, the value of β_∞ has little influence on the radial kurtosis, as in the case of $Q_r(r)$. In contrast, the tangential kurtosis $\kappa_\theta(r)$ curves do depend significantly on β_∞. All v_θ-distributions are highly peaked at small radii. For $\beta_\infty < 0.4$ the tangential kurtosis decreases to slightly negative values, i.e. at larger radii the tangential velocity distributions become slightly flat-topped. If $\beta_\infty > 0.4$, the $\kappa_\theta(r)$ profiles reach a minimum value and increase again for larger radii, in other words, the v_θ distributions will be peaked at large radii for the radially anisotropic models.

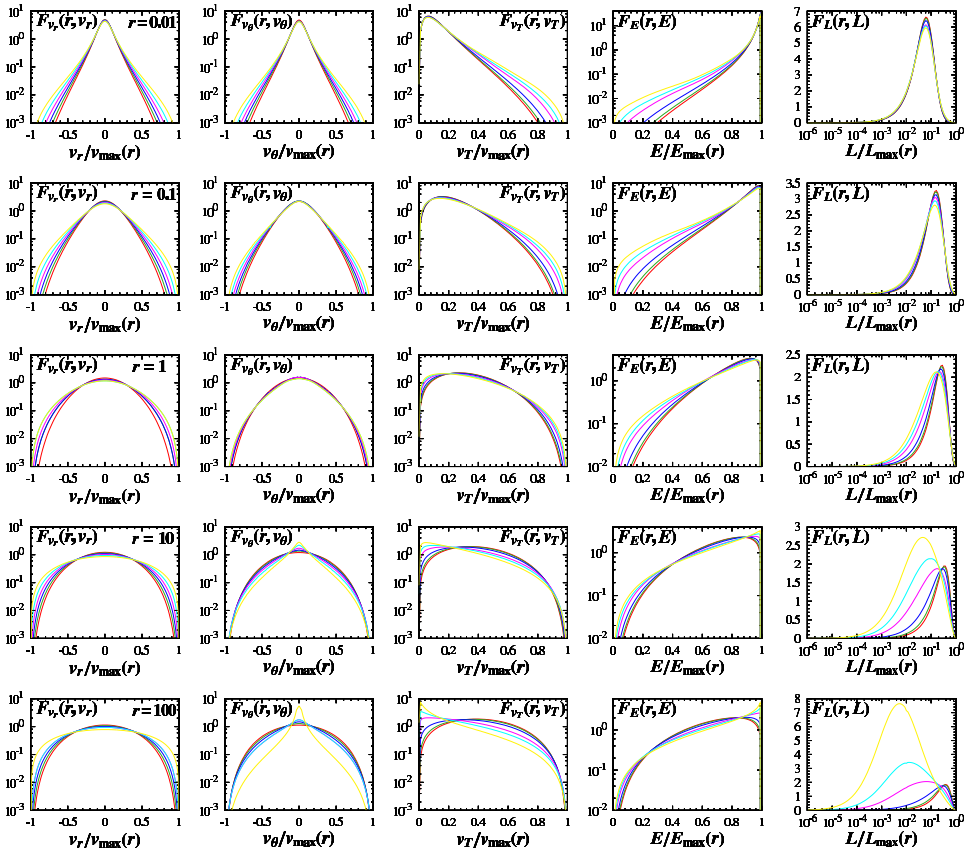

Figure 5.4 The distributions of the velocities v_r, v_θ, v_T, and the integrals E, L at different radii: $r = 0.01,\ 0.1,\ 1,\ 10,\ 100$ (rows).

5.4.3 The distributions of the velocities and orbital integrals

In Fig. 5.4, we show the full velocity distributions $F_{v_r}(r, v_r)$, $F_{v_\theta}(r, v_\theta)$, and $F_{v_T}(r, v_T)$, defined in (2.64), (2.67) and (2.65) respectively and calculated using the augmented functions (4.67) and (4.68). The velocities at a given r have been normalized to $v_{\rm max}(r) = \sqrt{2\psi(r)}$. We also display the orbital distributions $F_E(r, E)$ and $F_L(r, L)$, defined in (2.48) and (2.49), and calculated from (4.70) and (4.71). These functions are plotted at five different radii: $r = 0.01,\ 0.1,\ 1,\ 10,\ 100$; all the distributions have been normalized.

Inspection of $F_{v_r}(r, v_r)$ and $F_{v_\theta}(r, v_\theta)$ confirms the conclusions we reached based on the kurtosis values alone: at small radii, both velocity distributions are sharply peaked.

The v_r then broadens as r increases, indicating that orbits with high v_r (and thus high eccentricity) become more prevalent. The v_θ distribution also broadens as r approaches r_s, but as r further increases, the distributions narrow again somewhat, especially the models with high β_∞, which show a strong peak at large radii. It would be interesting to examine more closely whether these distributions are in agreement with those found in simulations (Hansen et al. 2006; Hansen & Sparre 2012).

When we look at the energy distributions $F_E(r, E)$, we see that at large radii the models with high radial anisotropy ($\beta_\infty > 0.6$) show a peak towards $E_\mathrm{max}(r) = \psi(r)$, which is the energy of a radial orbit with apocentre r; this is what we expect, as these models are populated with highly eccentric orbits at their outskirts. Since those orbits have small pericentres, they also contribute to the population of orbits near the centre. This must be compensated by a higher abundance of low-energy orbits near the centre, for those models.

Since $L = rv_T$, the distributions $F_{v_T}(r, v_T)$ and $F_L(r, L)$ are essentially equivalent. Note though that the y-axis for the former is logarithmic, while for the latter the x-axis is logarithmic. At small radii, the models with high radial anisotropy contain relatively more circular orbits (v_T or L large) than the other models. Near $r = r_\mathrm{s} = 1$, the orbital populations become more similar in all models, while at large radii the distributions diverge significantly: again, models with high values of β_∞ are dominated by eccentric orbits at their outskirts.

5.4.4 The distribution functions

The six top panels of Fig. 5.5 show the DFs $F(E, L)$ of our radially anisotropic systems with $\beta_0 = 0$ and $\beta_\infty = 0, \ldots, 1$, expressed as logarithmic isoprobability contours and a logarithmic colour gradient in the integral space, with L scaled to L_s, denoting the angular momentum of a circular orbit with radius r_s. All models are clearly physical, i.e. the DFs are nonnegative everywhere. This means that the Dehnen-McLaughlin Jeans models can indeed be realized by full dynamical models. Moreover, contrary to the Osipkov-Merritt models, these functions fill the entire integral space. In the isotropic case, the contours are horizontal (no dependence on angular momentum), and their orientation alters gradually with increasing β_∞ in an intuitive way, as orbits with high eccentricities (i.e. low angular momentum) become more abundant.

Alternatively, we can express these DFs in (r_-, r_+) turning point space, with r_- and r_+ the respective pericentres and apocentres of the particle orbits. These distributions are shown by means of logarithmic contours in the bottom panels of Fig. 5.5. Because of the central isotropy, the DFs are similar near the centre. However, the contours of orbits with high apocentres become increasingly steeper functions of r_- for larger anisotropies β_∞. In particular, the structure of the isotropic model is striking: the isoprobability contours are equidistant to a high degree of accuracy. Consequently, along the lines of equal eccentricity

$$e = \frac{r_+ - r_-}{r_+ + r_-}, \tag{5.39}$$

the isotropic DF has (near) power-law profiles as a function of r_- or r_+.

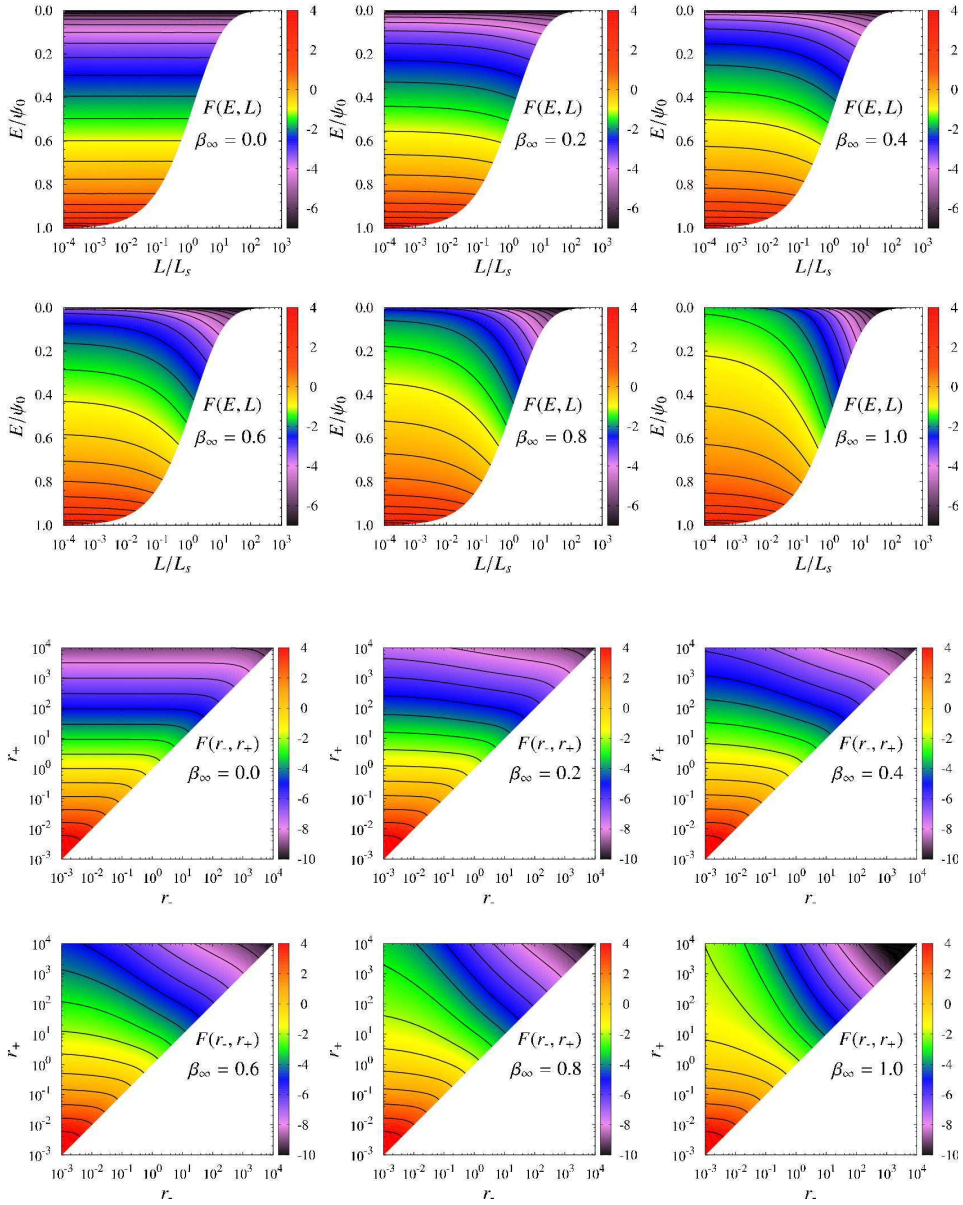

Figure 5.5 The phase space DFs of the six models, expressed as logarithmic isoprobability contours in the integral space (top panels) and turning point space (bottom panels). The contour lines are drawn at the same values for all DFs. The energy is scaled to the central potential and the angular momentum is scaled to the angular momentum L_s of a circular orbit at radius r_s.

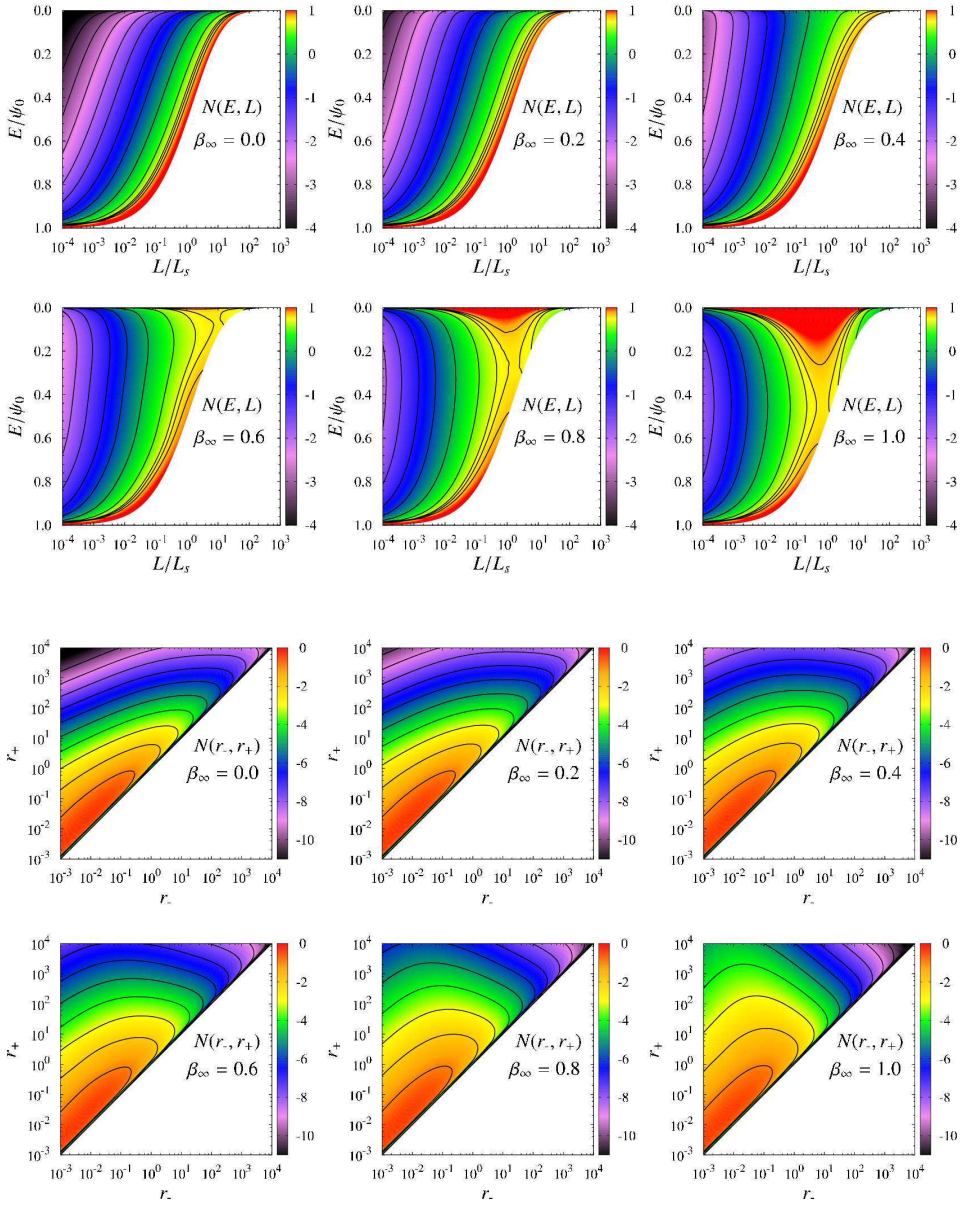

Figure 5.6 The orbital DFs of the six models, expressed as logarithmic isoprobability contours in the integral space (top panels) and turning point space (bottom panels). The contour lines are drawn at the same values for all DFs. The energy is scaled to the central potential and the angular momentum is scaled to the angular momentum L_s of a circular orbit at radius r_s.

A closer inspection of all six models reveals that in fact all contours become nearly equidistant for $r_- = r_+$. In other words, the distribution of circular orbits with radius r, which we denote as $F_c(r)$, follows closely a power-law. We show these profiles, as well as their slopes, in Fig. 5.7. While the slopes do vary with radius, this variation is very small, and for all models the slopes lie in the range 2.1-2.4. We stress that these features are not a property of the individual components in our modelling library, but an actual characteristic of the fits. It is unclear how to interpret these intriguing results, and a more systematic study with different haloes and anisotropy profiles might unravel if this property is linked to the linear $\beta - \gamma$ relation, the power-law behaviour of $Q_r(r)$ or the density profiles. It would also be very interesting to investigate these distributions in N-body simulations.

As we explained in Section 2.2.1, the DFs express the probability distributions of particles in phase space, but not in the integral space nor the turning point space. It is therefore instructive to view the true orbital distributions $N(E, L)$, given by Eq. (2.44), that describe the likelihood to find an orbit with energy E and angular momentum L.

The results are displayed in the top panels of Fig. 5.6 as logarithmic isoprobability contours and a logarithmic colour gradient in the integral space. Note that the contour lines are almost parallel in the isotropic case with high probability for near-circular orbits. For increasing β_∞, the contours gradually become steeper functions of L. The number of circular orbits (high L) with low binding energies E decreases, whereas the the number of orbits with low E and intermediate L significantly increases. As a result, models with $\beta_\infty > 0.5$ form a saddle point in these regions.

Similarly, we can derive the orbital distributions in turning point space, $N(r_-, r_+)$, given by Eq. (2.50), which express the probability to find an orbit with pericentre r_- and apocentre r_+. As shown in the bottom panels of Fig. 5.6, these functions are very regular,

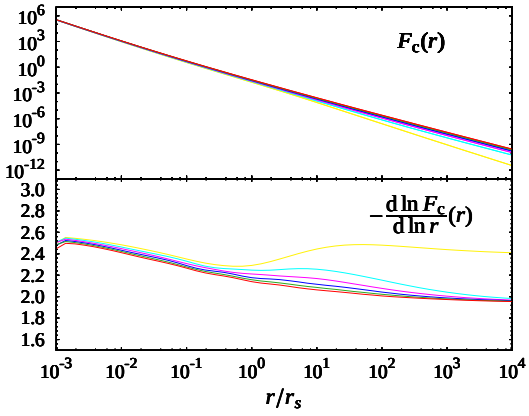

Figure 5.7 The phase space distribution of circular orbits for the QP-models, as a function of the radius. These profiles follow closely a power-law behaviour. The bottom panel shows the slowly changing slope as a function of the radius.

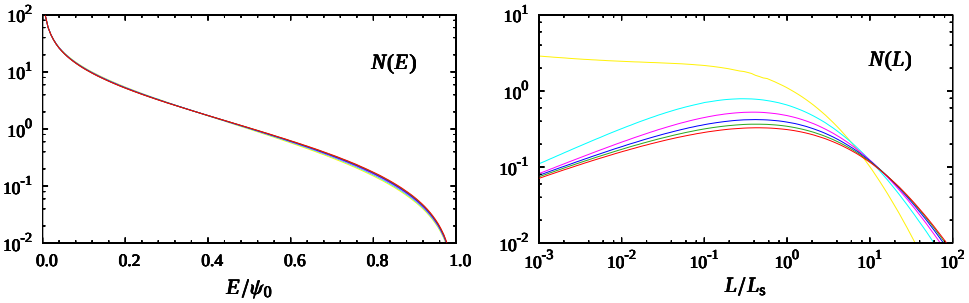

Figure 5.8 The energy and angular momentum distributions of the six QP-models with 10 components. The angular momenta are scaled to the values L_s of a circular orbit with radius r_s. The models and grayscaling are the same as in Fig. 5.1.

with high probabilities near the centre, and an increasing number of eccentric orbits for larger β_∞.

5.4.5 The marginal distributions

We conclude the discussion of our Dehnen-McLaughlin DFs with an analysis of the marginal distributions. The differential energy and angular momentum distributions $N(E)$ and $N(L)$ are the integrals of the orbital distributions, given by Eqs. (2.46) - (2.47).

These curves are displayed in Fig. 5.8. The differential energy distributions are all monotonously decreasing functions of E. It is striking that these profiles are almost identical, regardless of the anisotropy β_∞. This result reinforces previous dynamical studies (Binney 1982), and suggests that $\rho(r)$, $Q_r(r)$ and $\kappa_r(r)$ are linked to a universal differential energy distribution, independent of β_∞, caused by the same physical processes.

In contrast, the angular momentum distributions depend on β_∞, most notably for high radial anisotropies. For increasing values of β_∞, the fraction of orbits with low angular momentum increases. Bullock et al. (2001) proposed a universal form for the integrated angular momentum distribution in dark matter haloes $M(L)$. Alternatively, Sharma & Steinmetz (2005) found a differential distribution

$$N_\mathrm{ss}(L) = \frac{1}{L_\mathrm{d}^a \Gamma(a)} L^{a-1} \mathrm{e}^{-L/L_\mathrm{d}}. \tag{5.40}$$

Our models indicate a similar profile, with $a > 0.9$, although the functions (5.40) fall steeper than ours as L increases.

This concludes our dynamical modelling of dark matter haloes with Dehnen-McLaughlin profiles. One of the characteristic properties of these models is the linear relation between the density slope and the velocity anisotropy. This is a special case of a more general property; indeed, it turns out that most spherical dynamical systems obey the so-called

global density slope – anisotropy inequality, or GDSAI. With our mathematical tools, we were able to give a complete analysis of this relation for systems with separable augmented densities. This will be the topic of the next chapter.

Chapter 6

The global density slope – anisotropy inequality

In this chapter, we investigate some theoretical properties of spherical dynamical models, namely the relation between the density slope and the anisotropy profile. Using the augmented density concept, we show that $\gamma(r) \geqslant 2\beta(r)$ at all radii, for separable systems with $\beta_0 \leqslant 1/2$. In addition, we investigate the consistency requirements of spherical models with separable augmented densities. The results of this chapter are published in Van Hese et al. (2011) and An et al. (2012); all the work presented here has been carried out by the author.

6.1 Introduction

Recalling the definition of the density slope and the velocity anisotropy profile

$$\gamma(r) = -\frac{\mathrm{d}\ln\rho}{\mathrm{d}\ln r}(r), \tag{6.1}$$

$$\beta(r) = 1 - \frac{\sigma_\theta^2(r)}{\sigma_r^2(r)}, \tag{6.2}$$

several theoretical studies addressed the question whether any general statements can be made about the relation between these two quantities. It was found that systems with a steeper density profile can support more radial anisotropy than flatter models. First, An & Evans (2006) proved that the central inequality $\gamma_0 \geqslant 2\beta_0$ is a necessary condition for a consistent spherical dynamical model (i.e. a nonnegative DF). More recently, Ciotti & Morganti (2009), Ciotti & Morganti (2010a) and Ciotti & Morganti (2010b) showed that $\gamma(r) \geqslant 2\beta(r)$ at all radii (hereafter called the Global Density Slope – Anisotropy Relation, GDSAI) is a necessary condition for consistency, if $\beta_0 \leqslant 1/2$, in several families of dynamical models: multi-component Osipkov-Merritt systems (Osipkov 1979; Merritt 1985), Cuddeford systems (Cuddeford 1991), Cuddeford-Louis models (Cuddeford & Louis 1995), the Plummer models of Dejonghe (1987), the Hernquist models of

Baes & Dejonghe (2002), and the models we introduced in Baes & van Hese (2007) (see Section 4.3). Their proof is based on the fact that all these models are characterized by having a separable augmented density (see Section 2.3.2). They also noted that at that time no counter-examples of the GDSAI were known, but remarked that in the case of Cuddeford models with a central anisotropy $\beta_0 > 1/2$ the GDSAI is only a sufficient condition, so that possible counter-examples could be found in this range of values.

These results pose the question under which conditions the GDSAI holds for all spherical systems. In this chapter, we make advancements by providing a complete analysis of the GDSAI for all well-behaved systems with a separable augmented density. This group includes all aforementioned models, as well as the hypervirial models of Evans & An (2005), the γ-models of Buyle et al. (2007) and the Dehnen-McLaughlin systems discussed in Chapter 5 and Van Hese et al. (2009), among others. First, we show that the GDSAI holds for all separable systems, if $\beta_0 \leqslant 1/2$, by proving an equivalent criterion formulated by Ciotti & Morganti (2010b). In this manner, we extend their previous results. In fact, the GDSAI is a special case of more general conditions.

Furthermore, we use our QP-algorithm to show that counter-examples of the GDSAI do exist for separable systems with $\beta_0 > 1/2$, in other words, we demonstrate that the GDSAI is not a universal property. However, the velocity distributions of these models are extreme, and all counter-examples are very likely dynamically unstable.

Recently, Barber & Zhao (2014) extended our results by constructing models with non-separable augmented densities that also violate the GDSAI, even if $\beta_0 \leqslant 1/2$. However, their systems have densities that *increase* for large radii, which is quite unrealistic behaviour. This strengthens the impression that stable equilibrium systems do obey the GDSAI.

In Section 6.2, we briefly repeat some aspects of spherical dynamical systems that we will use for our proof in Section 6.3. Our analysis shows that the GDSAI is actually a special case of more general constraints on the ψ-part of the separable augmented density. In Section 6.4, we extend this study by deriving a full set of necessary and sufficient conditions on the augmented densities for consistent separable models, which we simplify to a set of sufficient consistency conditions.

6.2 Dynamical systems

Let us recall that from the DF, we can obtain the anisotropic velocity moments (2.59)

$$\mu_{2n,2m}(r) = 2\pi M \iint F(E,L)\, v_r^{2n}\, v_T^{2m+1}\, \mathrm{d}v_r\, \mathrm{d}v_T. \tag{6.3}$$

In particular, the density and the second-order moments are

$$\rho(r) = \mu_{00}(r), \qquad \rho\sigma_r^2(r) = \mu_{20}(r), \qquad \rho\sigma_T^2(r) = \mu_{02}(r), \tag{6.4}$$

and $\sigma_T^2(r) = 2\sigma_\theta^2(r)$. Spherical dynamical models satisfy the Jeans equation (2.124)

$$\frac{\mathrm{d}\rho\sigma_r^2}{\mathrm{d}r}(r) + \frac{2\beta(r)}{r}\rho\sigma_r^2(r) = \rho(r)\frac{\mathrm{d}\psi}{\mathrm{d}r}(r), \tag{6.5}$$

which can be written as

$$\sigma_r^2(r)\left(\gamma(r) - 2\beta(r) + \kappa(r)\right) = v_c^2(r), \tag{6.6}$$

with

$$\kappa(r) = -\frac{\mathrm{d}\ln\sigma_r^2}{\mathrm{d}\ln r}(r), \qquad v_c^2(r) = -r\frac{\mathrm{d}\psi}{\mathrm{d}r}(r). \tag{6.7}$$

Evidently, it follows that

$$\gamma(r) - 2\beta(r) + \kappa(r) \geqslant 0, \qquad \forall r. \tag{6.8}$$

Ciotti & Morganti (2010a) and Ciotti & Morganti (2010b) showed that several systems satisfy a stronger condition, the GDSAI

$$\gamma(r) - 2\beta(r) \geqslant 0, \qquad \forall r, \tag{6.9}$$

and they pose the question whether this condition holds for all spherical systems. Naturally, the inequality is valid outside the radius r_2 where $\gamma(r_2) = 2$. It is also valid at $r = 0$, as was proven by An & Evans (2006). In Section 2.3, we introduced the powerful framework of augmented velocity moments $\tilde{\mu}_{2n,2m}(\psi, r)$ as an equivalent way to describe gravitational systems. In particular, we will consider the augmented density $\tilde{\rho}(\psi, r)$,

$$\tilde{\rho}(\psi, r) = 2\pi M \int_0^{\psi} \mathrm{d}E \int_0^{2(\psi - E)} \frac{F(E, r v_T)}{\sqrt{2(\psi - E) - v_T^2}}\,\mathrm{d}v_T^2. \tag{6.10}$$

The strength of the augmented density framework lies in its direct connection to observable quantities like the velocity moments. For instance, the augmented velocity dispersion profiles are given by

$$\tilde{\sigma}_r^2(\psi, r) = \frac{1}{\tilde{\rho}(\psi, r)} \int_0^{\psi} \tilde{\rho}(\psi', r)\,\mathrm{d}\psi', \tag{6.11}$$

$$\tilde{\sigma_T}^2(\psi, r) = \frac{2}{\tilde{\rho}(\psi, r)} \int_0^{\psi} D_{r^2}\left[r^2\,\tilde{\rho}(\psi', r)\right]\mathrm{d}\psi', \tag{6.12}$$

where D_{r^2} denotes the derivative with respect to r^2. The observed density and dispersions are then simply recovered from

$$\rho(r) = \tilde{\rho}(\psi(r), r), \tag{6.13}$$

$$\sigma_r^2(r) = \tilde{\sigma}_r^2(\psi(r), r), \tag{6.14}$$

$$\sigma_T^2(r) = \tilde{\sigma_T}^2(\psi(r), r), \tag{6.15}$$

and the density slope is

$$\gamma(r) = -\frac{r}{\rho}\frac{\partial\tilde{\rho}}{\partial r}(\psi(r),r) - \frac{r}{\rho}\frac{\mathrm{d}\psi}{\mathrm{d}r}(r)\,\frac{\partial\tilde{\rho}}{\partial\psi}(\psi(r),r). \tag{6.16}$$

As remarked in the Introduction, Ciotti & Morganti have examined the GDSAI in several systems with a separable augmented density, i.e. systems of the form

$$\tilde{\rho}(\psi,r) = f(\psi)\,g(r), \qquad 0 \leqslant \psi \leqslant \psi_0, \tag{6.17}$$

with $\psi_0 = \psi(0)$ (for convenience, we will assume systems with infinite extent). For such models, the dispersion profiles simplify to

$$\tilde{\sigma}_r^2(\psi) = \frac{1}{f(\psi)}\int_0^\psi f(\psi')\,\mathrm{d}\psi', \tag{6.18}$$

$$\tilde{\sigma_T}^2(\psi,r) = \left(1+\frac{1}{2}\frac{\mathrm{d}\ln g}{\mathrm{d}\ln r}\right)\frac{2}{f(\psi)}\int_0^\psi f(\psi')\,\mathrm{d}\psi', \tag{6.19}$$

and the velocity anisotropy profile of these systems has the simple form

$$\beta(r) = -\frac{1}{2}\frac{\mathrm{d}\ln g}{\mathrm{d}\ln r}(r). \tag{6.20}$$

As we demonstrated in the previous chapters, this property provides a very elegant way to construct dynamical models with a given potential, density and velocity anisotropy. Indeed, separable systems are completely determined by $\psi(r)$, $\rho(r)$ and $\beta(r)$, since $g(r)$ is defined by Eq. (6.20) and, by inverting $\psi(r)$, the function $f(\psi)$ follows from

$$f(\psi) = \frac{\rho(r(\psi))}{g(r(\psi))}. \tag{6.21}$$

However, one still needs to verify whether the corresponding DF is nonnegative everywhere. Eq. (6.16) now reduces to

$$\gamma(r) = -\frac{\mathrm{d}\ln g}{\mathrm{d}\ln r}(r) - \frac{\mathrm{d}\ln\psi}{\mathrm{d}\ln r}(r)\,\frac{\mathrm{d}\ln f}{\mathrm{d}\ln\psi}(\psi(r)), \tag{6.22}$$

so that we obtain

$$\frac{\mathrm{d}f}{\mathrm{d}\psi}(\psi(r)) = \frac{f(\psi(r))}{v_c^2(r)}\left(\gamma(r) - 2\beta(r)\right). \tag{6.23}$$

In other words, as remarked by Ciotti & Morganti, the GDSAI

$$\gamma(r) \geqslant 2\beta(r), \qquad \forall r \geqslant 0, \tag{6.24}$$

is for separable systems equivalent to the statement

$$\frac{\mathrm{d}f}{\mathrm{d}\psi} \geqslant 0, \qquad \forall\, 0 \leqslant \psi \leqslant \psi_0. \tag{6.25}$$

The question thus becomes whether this inequality is valid for all separable systems. In the following section, we will prove that this is indeed the case, if $\beta_0 \leqslant 1/2$.

6.3 Analysis of the GDSAI for separable systems

Following the reasoning of An & Evans (2006), we assume that any well-behaved DF can be written in the form

$$F(E,L) = L^{-2\beta_0}\left(F_0(E) + F_1(E,L)\right), \tag{6.26}$$

with

$$F_1(E,0) \equiv 0, \quad \forall\, 0 \leqslant E \leqslant \psi_0. \tag{6.27}$$

The function $L^{-2\beta_0}F_0(E)$ in this Ansatz can be understood as the leading term of a Laurent series expansion in L at $L = 0$. Towards the centre $r \to 0$, the DF is dominated by this term, which has the form of a system with constant anisotropy (2.169). Consequently, the central anisotropy of the entire model indeed equals β_0. Since the DF has to be nonnegative everywhere, it follows immediately that $F_0(E) \geqslant 0\ \forall E$ is a necessary condition to obtain a physically meaningful DF.

If we consider separable systems, the corresponding augmented density then has the form

$$\tilde{\rho}(\psi,r) = f(\psi)\, r^{-2\beta_0}\left(1 + g_1(r)\right), \quad \text{with } g_1(0) = 0. \tag{6.28}$$

By changing in Eq. (6.10) the integration variable v_T to $u^2 = \frac{v_T^2}{2(\psi-E)}$, the relation between the augmented density and the DF (6.10) can be written as

$$\tilde{\rho}(\psi,r) = 2\pi\, 2^{1/2-\beta_0} r^{-2\beta_0} M \int_0^1 \frac{u^{-2\beta_0}}{\sqrt{1-u^2}}\,\mathrm{d}u^2 \times \int_0^\psi (\psi-E)^{1/2-\beta_0}\left(F_0(E) + F_1\left(E, ru\sqrt{2(\psi-E)}\right)\right)\mathrm{d}E. \tag{6.29}$$

In separable systems, it follows that

$$f(\psi) = \frac{\tilde{\rho}(\psi,r)}{g(r)}. \tag{6.30}$$

Since the left-hand side of this equation is independent of the radius r, the right-hand side does not depend on r either. The equality is therefore valid for all values r; in particular, we can take the limit of r towards the centre,

$$f(\psi) = \lim_{r\to 0} \frac{\tilde{\rho}(\psi,r)}{g(r)} = \lim_{r\to 0} r^{2\beta_0}\tilde{\rho}(\psi,r). \tag{6.31}$$

This property is the key element to prove the GDSAI when $\beta_0 \leqslant 1/2$: using (6.27) and (6.31), it follows from Eq. (6.29) that

$$f(\psi) = (2\pi)^{3/2} 2^{-\beta_0} M \frac{\Gamma(1-\beta_0)}{\Gamma(3/2-\beta_0)} \int_0^\psi (\psi-E)^{1/2-\beta_0} F_0(E)\,\mathrm{d}E. \tag{6.32}$$

Remarkably, the function $f(\psi)$ thus only depends on $F_0(E)$ and β_0. In other words, for separable systems the function $F_1(E,L)$ has no influence on the GDSAI. Concrete examples of this behaviour are furnished in the systems considered by Ciotti & Morganti. For instance, the equivalent function $B(\psi_\mathrm{T})$ in Ciotti & Morganti (2010b) for generalized Cuddeford systems does not depend on the anisotropy radius r_a (see their Eq. (13)).

The value of β_0 splits our further analysis into three cases: $\beta_0 < 1/2$, $\beta_0 = 1/2$, and $\beta_0 > 1/2$.

6.3.1 Proof for $\beta_0 < 1/2$

If $\beta_0 < 1/2$, the derivative of $f(\psi)$ becomes

$$\frac{\mathrm{d}f}{\mathrm{d}\psi}(\psi) = (2\pi)^{3/2} 2^{-\beta_0} M \frac{\Gamma(1-\beta_0)}{\Gamma(3/2-\beta_0)} \left[\lim_{E\to\psi} (\psi - E)^{1/2-\beta_0} F_0(E) + \left(\frac{1}{2} - \beta_0\right) \int_0^\psi (\psi - E)^{-1/2-\beta_0} F_0(E)\,\mathrm{d}E \right]. \quad (6.33)$$

Let us examine the first term inside the brackets: if

$$\lim_{E\to\psi} (\psi - E)^{1/2-\beta_0} F_0(E) > 0, \quad (6.34)$$

then

$$\lim_{E\to\psi} (\psi - E)^{-1/2-\beta_0} F_0(E) \sim \lim_{E\to\psi} (\psi - E)^{-a} \quad \text{with } a \geqslant 1, \quad (6.35)$$

so that

$$\int_0^\psi (\psi - E)^{-1/2-\beta_0} F_0(E)\,\mathrm{d}E = +\infty. \quad (6.36)$$

In other words, if the limit is nonzero, then the integral in the second term becomes infinite, and the condition (6.25) holds trivially. If on the other hand the limit term is zero, the equation simplifies to

$$\frac{\mathrm{d}f}{\mathrm{d}\psi}(\psi) = (2\pi)^{3/2} 2^{-\beta_0} M \frac{\Gamma(1-\beta_0)}{\Gamma(1/2-\beta_0)} \int_0^\psi \frac{F_0(E)}{(\psi - E)^{1/2+\beta_0}}\,\mathrm{d}E \geqslant 0, \quad (6.37)$$

so again (6.25) holds, and the GDSAI is proven.

The above relation can be generalized further: if $n = \lfloor 3/2 - \beta_0 \rfloor$ and $\alpha = 3/2 - \beta_0 - n$ are the integer floor and fractional part of $3/2 - \beta_0$, then

$$\frac{\mathrm{d}^k f}{\mathrm{d}\psi^k}(\psi) = (2\pi)^{3/2} 2^{-\beta_0} M \frac{\Gamma(1-\beta_0)}{\Gamma(3/2-\beta_0-k)} \times \int_0^\psi (\psi - E)^{1/2-\beta_0-k} F_0(E) \geqslant 0, \qquad 0 \leqslant k \leqslant n, \quad (6.38)$$

so the inequalities

$$\frac{\mathrm{d}^k f}{\mathrm{d}\psi^k}(\psi) \geqslant 0, \qquad \forall\, 0 \leqslant \psi \leqslant \psi_0, \quad 0 \leqslant k \leqslant n = \lfloor 3/2 - \beta_0 \rfloor, \tag{6.39}$$

are necessary conditions to obtain a separable system with a nonnegative DF. This extends the results obtained by Ciotti & Morganti (2010a) for multi-component Cuddeford models. The GDSAI is thus a special case of the more general requirements (6.38).

6.3.2 Proof for $\beta_0 = 1/2$

When $\beta_0 = 1/2$, Eq. (6.32) reduces to

$$f(\psi) = 2\pi^2 M \int_0^\psi F_0(E)\,\mathrm{d}E. \tag{6.40}$$

The derivative is then simply

$$\frac{\mathrm{d}f}{\mathrm{d}\psi}(\psi) = 2\pi^2 M\, F_0(\psi) \geqslant 0, \tag{6.41}$$

so evidently, the GDSAI is again a necessary condition for a physical dynamical model.

6.3.3 Counter-examples for $\beta_0 > 1/2$

The proof is not applicable to systems with $\beta_0 > 1/2$. Indeed, the derivative has the same form as Eq. (6.33), but now the two terms inside the brackets are respectively $+\infty$ and $-\infty$ when $F_0(E) > 0$, so their sum is undetermined. However, we can rewrite Eq. (6.32) using integration by parts as

$$f(\psi) = (2\pi)^{3/2} 2^{-\beta_0} M \frac{\Gamma(1-\beta_0)}{\Gamma(5/2-\beta_0)} \left[\psi^{3/2-\beta_0} F_0(0) + \int_0^\psi (\psi - E)^{3/2-\beta_0} F_0'(E)\,\mathrm{d}E \right], \tag{6.42}$$

where $F_0'(E)$ denotes the derivative of $F_0(E)$. After differentiation, we then obtain

$$\frac{\mathrm{d}f}{\mathrm{d}\psi}(\psi) = (2\pi)^{3/2} 2^{-\beta_0} M \frac{\Gamma(1-\beta_0)}{\Gamma(3/2-\beta_0)} \left[\psi^{1/2-\beta_0} F_0(0) + \int_0^\psi (\psi - E)^{1/2-\beta_0} F_0'(E)\,\mathrm{d}E \right]. \tag{6.43}$$

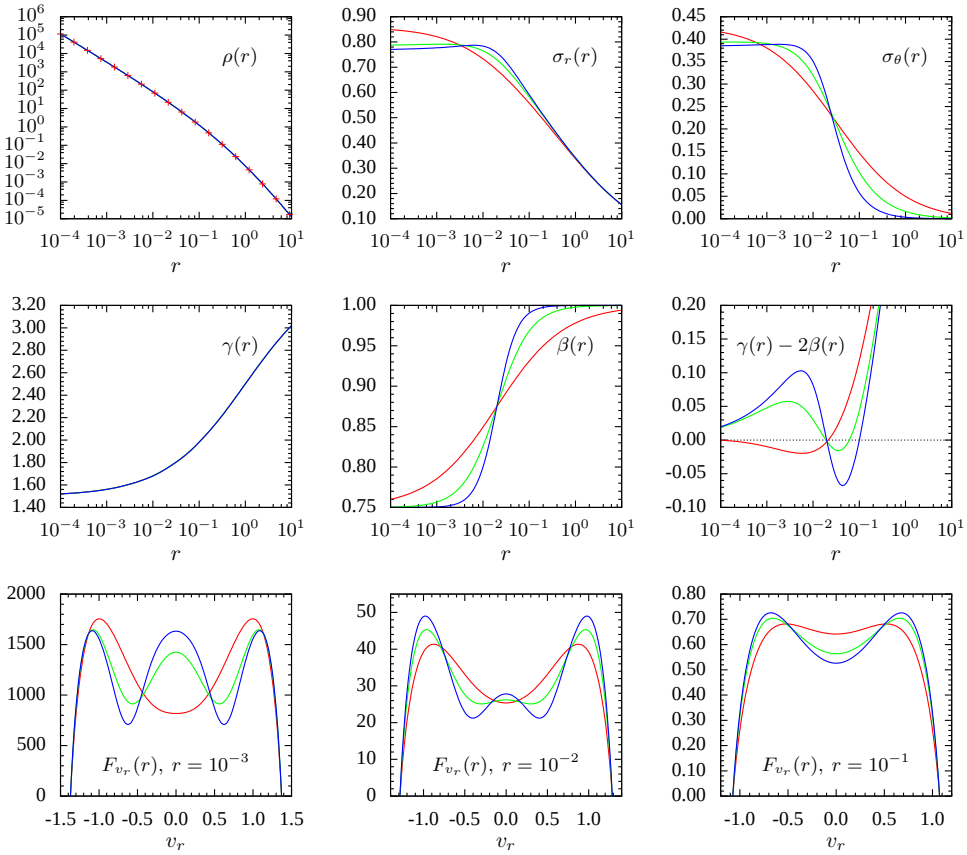

Figure 6.1 Three models for which the GDSAI does not hold: $\delta = 0.3$ (red), $\delta = 0.6$ (green), and $\delta = 1.0$ (blue). In the first panel, the density data points are also displayed.

Thus, separable systems with a monotonically increasing $F_0(E)$ (i.e. $F_0'(E) \geqslant 0 \quad \forall E$), satisfy the GDSAI. Again, this is an extension of the results for generalized Cuddeford systems found by Ciotti & Morganti (2010b).

Yet, the GDSAI is no longer a necessary condition for a physical model, which raises the question whether systems can be found for which the global inequality does not hold. To this aim, we consider the potential-density pair

$$\psi(r) = \frac{GM_{\text{tot}}}{(1+\sqrt{r})^2}, \tag{6.44}$$

$$\rho(r) = \frac{3M}{8\pi} \frac{1}{r^{3/2}\,(1+\sqrt{r})^4}, \tag{6.45}$$

with corresponding density slope

$$\gamma(r) = \frac{3/2 + 7/2\sqrt{r}}{1+\sqrt{r}}, \tag{6.46}$$

which is part of the family of Veltmann models that we studied in Section 4.3.3; this potential-density pair was also discussed by Moore et al. (1998). If $M_{\rm tot} = M$, then the system is also self-consistent. For this pair, we construct physical DFs that generate our four-parameter anisotropy profiles

$$\beta(r) = \frac{\beta_0 + \beta_\infty (r/r_{\rm a})^{2\delta}}{1+(r/r_{\rm a})^{2\delta}}, \tag{6.47}$$

with $0 < \delta \leqslant 1$, so that

$$\tilde{\rho}(\psi, r) = f(\psi) \left(\frac{r}{r_{\rm a}}\right)^{-2\beta_0} \left(1 + \frac{r^{2\delta}}{r_{\rm a}^{2\delta}}\right)^{\beta_\delta}, \tag{6.48}$$

with

$$\beta_\delta = \frac{\beta_0 - \beta_\infty}{\delta}. \tag{6.49}$$

Yet this time, we are interested in models with a non-linear $\gamma - \beta$ relation, so we put our QP-machinery to work (Sections 2.4 and 5.3.1). In particular, we created models with $N = 12$ components, fitting 25 density data points extracted from Eq. (6.45).

With this technique, we obtain several dynamical models with nonnegative DFs that violate the GDSAI; three of them are shown in Fig. 6.1. All three share the anisotropy parameters $\beta_0 = 0.75$, $\beta_\infty = 1$ and $r_{\rm a} = 0.02$, but have different values for δ: 0.3, 0.6 and 1.0 respectively; note that the latter is a Cuddeford-type model. For the model with $\delta = 0.3$, we find that $\gamma(r) < 2\beta(r)$ for radii in the interval $]0, 0.021]$, with a minimum around $r = 0.0057$ (note that the centre is a local maximum, for which $\gamma_0 = 2\beta_0$). In the model with $\delta = 0.6$, the $\gamma - \beta$ relation reaches a local maximum around $r = 0.0028$, and the GDSAI does not hold in the interval $[0.019, 0.061]$, with a minimum around $r = 0.036$. Finally the largest $\gamma - \beta$ fluctuations occur in the Cuddeford model ($\delta = 1$), with a local maximum around $r = 0.0054$, and a GDSAI violation within $[0.019, 0.100]$, with a minimum for $r = 0.044$.

Evidently, we require rather extreme parameter values to obtain these (modest) violations, while maintaining nonnegative DFs. The central anisotropy β_0 has to be high, and the profile $\beta(r)$ has to increase very rapidly. It is therefore safe to assume that the self-consistent variants of these models are dynamically unstable. This can be seen from the standard criterion for radial-orbit instability: $2K_r/K_T = 2\langle v_r^2\rangle / \langle v_T^2\rangle = 5.45$, 8.26 and 10.42 for the three models, which is much higher than the $\simeq 2$ threshold for similar models (see Merritt 1999 for an overview). Further evidence of dynamical instability is given by the radial velocity distributions

$$F_{v_r}(r) = 2\pi M \int_0^{\sqrt{2\psi(r) - v_r^2}} F(E, L)\, v_T \, {\rm d}v_T. \tag{6.50}$$

As shown in the bottom row of Fig. 6.1, these profiles have two or three peaks at small radii. These are indications of Hénon instabilities (see Barnes et al. 1986; Merritt 1999). In theory, if the systems are instead not self-consistent but embedded in a massive dark matter halo, they might withstand these instabilities; however, one can safely argue that such equilibrium systems are too extreme to arise in structure formation.

6.3.4 The inverse relation

Finally, we remark that the function $F_0(E)$ can be derived from $f(\psi)$ by means of an Abel-related inversion (see Eq. (2.168), and Cuddeford 1991; An & Evans 2006), which holds for all values of $\beta_0 < 1$,

$$F_0(E) = \frac{2^{\beta_0}}{(2\pi)^{3/2} M \Gamma(1-\alpha)\,\Gamma(1-\beta_0)} \times \left(\int_0^E \frac{\mathrm{d}^{n+1} f}{\mathrm{d}\psi^{n+1}} \frac{\mathrm{d}\psi}{(E-\psi)^{\alpha}} + \frac{1}{E^{\alpha}} \frac{\mathrm{d}^n f}{\mathrm{d}\psi^n}(0) \right), \quad (6.51)$$

where again $n = \lfloor 3/2 - \beta_0 \rfloor$ and $\alpha = 3/2 - \beta_0 - n$ are the integer floor and fractional part of $3/2 - \beta_0$. Thus the additional condition

$$\frac{\mathrm{d}^{n+1} f}{\mathrm{d}\psi^{n+1}}(\psi) \geqslant 0, \qquad \forall\, 0 \leqslant \psi \leqslant \psi_0, \quad (6.52)$$

is sufficient to obtain a nonnegative $F_0(E)$. As Ciotti & Pellegrini (1992) and Ciotti & Morganti (2010a) showed, this also implies that the entire DF $F(E, L)$ is nonnegative in the case of (generalized) Cuddeford systems. If fact, we can define the *fractional derivative* (Samko et al. 1993)

$$\frac{\mathrm{d}^{n+\alpha} f}{\mathrm{d}\psi^{n+\alpha}}(\psi) = \frac{1}{\Gamma(1-\alpha)} \int_0^{\psi} \frac{\mathrm{d}^{n+1} f}{\mathrm{d}\psi'^{n+1}} \frac{\mathrm{d}\psi}{(\psi - \psi')^{\alpha}}, \quad (6.53)$$

so that the condition

$$\frac{\mathrm{d}^{n+\alpha} f}{\mathrm{d}\psi^{n+\alpha}}(\psi) \geqslant 0, \qquad \forall\, 0 \leqslant \psi \leqslant \psi_0, \quad (6.54)$$

together with (6.39), is necessary and sufficient for a nonnegative $F_0(E)$, and a nonnegative generalized Cuddeford DF. However, these conditions alone are not sufficient to guarantee consistent DFs for all separable systems, since the behaviour of $F_1(E, L)$ might still lead to negative values of the DF. In fact, there are also additional constraints on $g(r)$, and we will explore this in the next section.

The function $F_0(E)$ can be interpreted in various ways: it can be thought of as the distribution of particles at purely radial orbits, as the distribution of particles at the centre,

or as the energy distribution of the constant-anisotropy component of the DF. A remarkable consequence is that, if a separable system has a given potential $\psi(r)$ and density $\rho(r)$, then knowledge of $F_0(E)$ alone is sufficient to construct the complete DF of the system. Indeed, we showed that $F_0(E)$ is equivalent to $f(\psi)$, and in combination with $\rho(r)$, the function $g(r) = \rho(r)/f(\psi(r))$ can also be derived, determining the augmented density $f(\psi)\,g(r)$ and thus $F(E, L)$.

The next step would be to investigate the GDSAI for general, non-separable spherical models. One possible approach would be to consider a spherical systems as a linear combination of separable systems. In fact, an analytic $\tilde{\rho}(\psi, r)$ or $F(E, L)$ can be written as a double sum of power-law functions, by means of a two-dimensional Laurent series expansion. An alternative approach would be to ask the following question: given a spherical dynamical system with a given $\psi(r)$ and a non-separable dynamical model that generates $\rho(r)$ and $\beta(r)$, does there always exist a separable model with a nonnegative DF that generates the same density and anisotropy? If so, then then same GDSAI analysis applies as presented here.

Recent work by Barber & Zhao (2014) indicates that the answer is no: they were able to construct consistent non-separable systems with $\beta_0 \leqslant 1/2$ that do violate the GDSAI. However, the densities of their systems increase at large radii, so their models are not physically realistic.

6.4 Conditions on the augmented density for a consistent separable model

6.4.1 Consistency requirements

An essential requirement for a physical dynamical model is the nonnegativity of the DF over the relevant phase space. In turn, this consistency requirement puts constraints on the derived quantities, like the potential, density and velocity anisotropy. In other words, the underlying DF determines the boundaries wherein the observable quantities can vary, and which properties they should have to guarantee a physical model.

Our analysis of the GDSAI revealed a set of constraints on $f(\psi)$ that are necessary for a consistent model. An (2011) demonstrated that there are necessary conditions for $g(r)$ as well:

$$\mathrm{d}^m_{r^2}\left(r^{2m} g(r)\right) \geqslant 0, \qquad \forall\, m. \tag{6.55}$$

These conditions are however not sufficient. In this section, we will derive the full set of necessary and sufficient conditions for consistent separable models. This set is too complicated for practical purposes, but we will be able to simplify them into sufficient conditions.

We now pose the question: which constraints are the augmented moments subjected to, in order to guarantee a nonnegative DF? This problem is related to the so-called *Haus-*

dorff moment problem (Hausdorff 1921 ; Hausdorff 1921) in probability theory: consider a function $F(x)$ over a closed interval $[0,h]$, with the sequence of moments[1]

$$\mu_n = \int_0^h x^n\, F(x)\,\mathrm{d}x, \tag{6.56}$$

then $F(x)$ defines a nonnegative distribution if and only if the difference sequences satisfy the equations

$$(-1)^k \Delta^k \mu_n \geqslant 0, \qquad \forall\, n,k \geqslant 0, \tag{6.57}$$

with Δ the difference operator defined as

$$\Delta^k \mu_n = \sum_{i=0}^{k} \binom{k}{i} (-h)^i\, \mu_{n+k-i} = \sum_{j=0}^{k} \binom{k}{j} (-h)^{k-j}\, \mu_{n+j}. \tag{6.58}$$

In other words, we require that

$$\mu_n \geqslant 0, \tag{6.59}$$

$$-\mu_{n+1} + h\mu_n \geqslant 0, \tag{6.60}$$

$$\mu_{n+2} - 2h\mu_{n+1} + h^2\mu_n \geqslant 0, \tag{6.61}$$

and so forth, for all n. We can apply this to the phase-space DF of a spherical gravitational system.

6.4.2 Necessary and sufficient conditions

We showed in Section 6.3 that the constraints (6.39) and (6.54) are necessary to obtain a corresponding nonnegative DF. Now, let us in addition assume that

$$\frac{\mathrm{d}^l f}{\mathrm{d}\psi^l}(\psi) \geqslant 0, \qquad 0 \leqslant \psi \leqslant \psi_0, \quad 0 \leqslant l \leqslant \lfloor \lambda \rfloor, \tag{6.62}$$

$$\frac{\mathrm{d}^\lambda f}{\mathrm{d}\psi^\lambda}(\psi) \geqslant 0, \tag{6.63}$$

where $\lambda \geqslant 3/2 - \beta_0$. We will also assume the boundary conditions

$$\frac{\mathrm{d}^l f}{\mathrm{d}\psi^l}(0) = 0, \qquad 0 \leqslant l \leqslant \lfloor \lambda \rfloor. \tag{6.64}$$

Now consider the functions

$$\widetilde{F}_{2m}(\psi, r, v_r) = 2\pi M \int_0^{\sqrt{2\psi - v_r^2}} F(E,L)\, v_T^{2m+1}\, \mathrm{d}v_T. \tag{6.65}$$

[1]The original Hausdorff moment problem applies to distributions in the interval $[0,1]$, but the extension to a general upper bound h follows simply by changing the integration variables.

Note that the function with $m = 0$ is the radial velocity distribution (up to the factor M). Also, the functions do not depend on ψ and v_r separately, but only on the combination

$$u = \psi - v_r^2/2. \tag{6.66}$$

We can thus write the above equation as

$$\widetilde{F}_{2m}(u,r) = \pi M \int_0^{2u} F(u - v_T^2/2, r\, v_T)\, v_T^{2m}\, \mathrm{d}v_T^2. \tag{6.67}$$

These functions can be expressed in terms of the velocity moments. Indeed,

$$\tilde{\mu}_{0,2m}(\psi,r) = 2\int_0^{\sqrt{2\psi}} \widetilde{F}_{2m}(\psi,r,v_r)\,\mathrm{d}v_r \tag{6.68}$$

$$= \int_0^{2\psi} \frac{\widetilde{F}_{2m}(\psi,r,v_r)}{|v_r|}\,\mathrm{d}v_r^2 \tag{6.69}$$

$$= \sqrt{2}\int_0^{\psi} \frac{\widetilde{F}_{2m}(u,r)}{\sqrt{\psi-u}}\,\mathrm{d}u. \tag{6.70}$$

The last equation is evidently an Abel integral, which can be inverted to yield

$$\widetilde{F}_{2m}(u,r) = \frac{1}{\sqrt{2}\pi}\int_0^u \frac{1}{\sqrt{u-\psi'}}\,\partial_{\psi'}\left(\tilde{\mu}_{0,2m}(\psi',r)\right)\mathrm{d}\psi'. \tag{6.71}$$

With the aid of Eq. (2.151), this can be written for separable systems as

$$\widetilde{F}_{2m}(u,r) = \frac{2^m}{\sqrt{2}\pi\,\Gamma(m)}\,\mathrm{d}^m_{r^2}(r^{2m}g)\int_0^u \mathrm{d}\psi' \int_0^{\psi'} \frac{(\psi'-\psi'')^{m-1}}{\sqrt{u-\psi'}}\,\mathrm{d}_{\psi''}(f)\,\mathrm{d}\psi'', \tag{6.72}$$

for $m > 0$. By changing the order of the integrations, we obtain

$$\widetilde{F}_{2m}(u,r) = \frac{2^m}{\sqrt{2}\pi\,\Gamma(m)}\,\mathrm{d}^m_{r^2}(r^{2m}g)\int_0^u \mathrm{d}_{\psi'}(f)\,\mathrm{d}\psi' \int_{\psi'}^u \frac{(\psi''-\psi')^{m-1}}{\sqrt{u-\psi''}}\,\mathrm{d}\psi'' \tag{6.73}$$

$$= \frac{1}{\sqrt{\pi}\,\Gamma(m+1/2)}\,\mathrm{d}^m_{r^2}(r^{2m}g)\int_0^u \left[2(u-\psi)\right]^{m-1/2}\mathrm{d}_{\psi}(f)\,\mathrm{d}\psi, \tag{6.74}$$

which is also valid for $m = 0$. We can write this equation in a more general form using the conditions (6.62) - (6.63) and the inversion of the fractional derivative (6.53)

$$f(\psi) = \frac{1}{\Gamma(\lambda)}\int_0^{\psi} (\psi-\psi')^{\lambda-1}\,\mathrm{d}^{\lambda}_{\psi'}(f)\,\mathrm{d}\psi' \tag{6.75}$$

$$\mathrm{d}_{\psi}(f) = \frac{1}{\Gamma(\lambda-1)}\int_0^{\psi} (\psi-\psi')^{\lambda-2}\,\mathrm{d}^{\lambda}_{\psi'}(f)\,\mathrm{d}\psi', \tag{6.76}$$

for $\lambda > 1$. When we plug this into (6.74) and again change the order of the integrations, we get

$$\widetilde{F}_{2m}(u,r) = \frac{2^{m-1/2}}{\sqrt{\pi}\,\Gamma(m+\lambda-1/2)}\,\mathrm{d}_{r^2}^m(r^{2m}g)\int_0^u (u-\psi)^{m+\lambda-3/2}\,\mathrm{d}_\psi^\lambda(f)\,\mathrm{d}\psi, \qquad (6.77)$$

which also holds if $\lambda \geqslant 1/2$. For fixed values of ψ, r and v_r, the functions $F_{2m}(u,r)$ are the moments of the DF $F(E,L)$ with respect to v_T^2. In other words, we can apply the Hausdorff conditions to Eq. (6.67) with

$$x = v_T^2, \qquad (6.78)$$

$$F(x) = \pi M\, F(E,L), \qquad (6.79)$$

$$h = 2\psi - v_r^2 = 2u. \qquad (6.80)$$

Thus, if and only if

$$(-1)^k \Delta^k \widetilde{F}_{2m}(u,r) \geqslant 0, \qquad \forall\, m,k \geqslant 0, \qquad (6.81)$$

then the DF is nonnegative everywhere. This leads to the following necessary and sufficient conditions for the existence of a nonnegative DF, for spherical systems with separable augmented densities

$$\sum_{j=0}^{k}(-1)^j \binom{k}{j} \frac{2^{m+k-1/2}\,u^{k-j}}{\Gamma(m+j+\lambda-1/2)}\,\mathrm{d}_{r^2}^{m+j}\left(r^{2(m+j)}g(r)\right) \times \int_0^u (u-\psi)^{m+j+\lambda-3/2}\,\mathrm{d}_\psi^\lambda f(\psi)\,\mathrm{d}\psi \geqslant 0, \qquad (6.82)$$

for all k, m, and a fixed $\lambda \geqslant 3/2 - \beta_0$.

6.4.3 Sufficient conditions

Evidently, the general equations (6.82) are too complicated for practical purposes. We will therefore look for more stringent yet simpler conditions for a nonnegative DF. We propose the sufficient conditions

$$\sum_{j=0}^{k}(-1)^j \binom{k}{j} \frac{1}{\Gamma(m+j+\lambda-1/2)}\,\mathrm{d}_{r^2}^{m+j}\left(r^{2(m+j)}g(r)\right) \geqslant 0. \qquad (6.83)$$

Indeed, together with the constraints (6.62) - (6.63) on $f(\psi)$, this implies Eq. (6.82), as can be seen in the following way: we can write (6.83) in the form

$$\sum_{j=0}^{k}(-1)^j \binom{k}{j} \mu_{m+j}^r \geqslant 0, \qquad (6.84)$$

with

$$\mu^r_{m+j} = \frac{1}{\Gamma(m+j+\lambda-1/2)}\,\mathrm{d}^{m+j}_{r^2}\left(r^{2(m+j)}g(r)\right). \tag{6.85}$$

This means that the set $\{\mu^r_m\}$ defines a moment sequence of some probability distribution in the unit interval $[0,1]$:

$$\mu^r_m = \int_0^1 X^m F^r(X)\,\mathrm{d}X. \tag{6.86}$$

Now consider the conditions

$$\sum_{j=0}^{k}(-1)^j\binom{k}{j}\left(1-\frac{\psi}{u}\right)^{j-k}\mu^r_{m+j} \geqslant 0, \tag{6.87}$$

with $\psi \leqslant u$. This is the same moment sequence (up to a constant factor), but now for a probability distribution in the interval $[0,h]$, with

$$h = \frac{u}{u-\psi} \geqslant 1. \tag{6.88}$$

The corresponding probability distribution is simply the same $F^r(X)$, extended to the larger interval $[0,h]$ with a Heaviside step function:

$$\mu^r_m = \int_0^h X^m F^r(X)\,H(1-X)\,\mathrm{d}X. \tag{6.89}$$

In other words, Eq. (6.84) immediately implies Eq. (6.87). With additional factors and an integration, we have

$$\int_0^u \sum_{j=0}^{k}(-1)^j\binom{k}{j}\mu^r_{m+j}2^{k+m-1/2}\,u^{k-j}(u-\psi)^{m+j+\lambda-3/2}\,\mathrm{d}^{\lambda}_{\psi}f(\psi)\,\mathrm{d}\psi \geqslant 0, \tag{6.90}$$

which is nothing else than Eq. (6.82).

The sufficient conditions (6.83) can also be written into a more compact form. To this aim, we list the following auxiliary formulae (An 2011):

$$x^{n+1}\frac{\mathrm{d}^n}{\mathrm{d}x^n}\left(x^n f(x)\right) = \left(x^2\frac{\mathrm{d}}{\mathrm{d}x}\right)^n\left(xf(x)\right), \tag{6.91}$$

$$\frac{\mathrm{d}^n}{\mathrm{d}x^n}f(x) = \left(-\omega^2\frac{\mathrm{d}}{\mathrm{d}\omega}\right)^n f(\omega^{-1}) \quad \text{with } \omega = x^{-1}, \tag{6.92}$$

$$\frac{\mathrm{d}^i x^\alpha}{\mathrm{d}x^i} = \frac{\Gamma(\alpha+1)}{\Gamma(\alpha+1-i)}x^{\alpha-i}, \tag{6.93}$$

where we used the operator

$$\left(x^2\frac{\mathrm{d}}{\mathrm{d}x}\right)^n f(x) = \underbrace{\left(x^2\frac{\mathrm{d}}{\mathrm{d}x}\left(x^2\frac{\mathrm{d}}{\mathrm{d}x}\cdots\left(x^2\frac{\mathrm{d}f}{\mathrm{d}x}(x)\right)\right)\right)}_{n \text{ derivatives}}. \tag{6.94}$$

With $x = r^2$ and $\omega = r^{-1}$, we find

$$\sum_{j=0}^{k}(-1)^j\binom{k}{j}\frac{x^{-m-j-1}}{\Gamma(m+j+\lambda-1/2)}\left(x^2\frac{\mathrm{d}}{\mathrm{d}x}\right)^{m+j}\big(x\,g(x)\big) \geqslant 0, \tag{6.95}$$

and

$$\sum_{j=0}^{k}(-1)^m\binom{k}{j}\frac{\omega^{m+j+1}}{\Gamma(m+j+\lambda-1/2)}\,\mathrm{d}_\omega^{m+j}\left(\frac{g(\omega^{-1})}{\omega}\right) \geqslant 0. \tag{6.96}$$

Multiplying by $\Gamma(m+k+\lambda-1/2)\,\omega^{\lambda-5/2}$ gives

$$(-1)^m\sum_{j=0}^{k}\binom{k}{j}\frac{\Gamma(m+k+\lambda-1/2)}{\Gamma(m+j+\lambda-1/2)}\omega^{m+j+\lambda-3/2}\,\mathrm{d}_\omega^{m+j}\left(\frac{g(\omega^{-1})}{\omega}\right) \geqslant 0, \tag{6.97}$$

and now we recognize Eq. (6.93), with $i = k-j$ and $\alpha = m+k+\lambda-3/2$. In other words,

$$(-1)^m\sum_{j=0}^{k}\binom{k}{j}\,\mathrm{d}_\omega^{k-j}\left(\omega^{m+k+\lambda-3/2}\right)\mathrm{d}_\omega^{m+j}\left(\frac{g(\omega^{-1})}{\omega}\right) \geqslant 0, \tag{6.98}$$

which is nothing more than the Leibniz derivation rule:

$$(-1)^m\,\mathrm{d}_\omega^k\left[\omega^{m+k+\lambda-3/2}\,\mathrm{d}_\omega^m\left(\frac{g(\omega^{-1})}{\omega}\right)\right] \geqslant 0, \tag{6.99}$$

which is also equivalent to

$$(-1)^k\left(x^2\frac{\mathrm{d}}{\mathrm{d}x}\right)^k\left[x^{-m-k-\lambda+3/2}\left(x^2\frac{\mathrm{d}}{\mathrm{d}x}\right)^m\big(x\,g(x)\big)\right] \geqslant 0, \tag{6.100}$$

and finally, using Eq. (6.91) twice, we get the compact formula

$$(-1)^k\,\mathrm{d}_x^k\left[x^{3/2-\lambda}\,\mathrm{d}_x^m\left(x^m\,g(x)\right)\right] \geqslant 0, \tag{6.101}$$

for all k, m (where we omitted the factor x^{k+1}). This means that for each m, the functions $x^{3/2-\lambda}\,\mathrm{d}_x^m\left(x^m\,g(x)\right)$ are completely monotonic. According to the Haussdorff-Bernstein-Widder theorem (Bernstein 1928), this implies that each of these functions can be written as the Laplace transform of a nonnegative function. This property was further explored in An et al. (2012).

6.5 Explicit formulae

To summarize, we found a set of sufficient consistency requirements

$$\frac{\mathrm{d}^l f}{\mathrm{d}\psi^l}(\psi) \geqslant 0, \qquad 0 \leqslant \psi \leqslant \psi_0, \quad 0 \leqslant l \leqslant \lfloor \lambda \rfloor, \tag{6.102}$$

$$\frac{\mathrm{d}^\lambda f}{\mathrm{d}\psi^\lambda}(\psi) \geqslant 0, \tag{6.103}$$

$$(-1)^k \, \mathrm{d}_x^k \left[x^{3/2-\lambda} \, \mathrm{d}_x^m \left(x^m \, g(x) \right) \right] \geqslant 0, \tag{6.104}$$

for all k, m, and with $\lambda \geqslant 3/2 - \beta_0$. Note that the constraints on f and g are coupled. Also, we recover the necessary constraints (6.55) discussed in An (2011) as the $k = 0$ case.

The conditions (6.83) or (6.101) put rather complicated constraints on $g(r)$. To gain more insight into them, we will look at some examples. First, let us consider models with a constant anisotropy, so that $g(r) = r^{-2\beta_0}$. Then we require

$$\sum_{j=0}^{k} (-1)^j \binom{k}{j} \frac{1}{\Gamma(m+j+\lambda-1/2)} \mathrm{d}_{r^2}^{m+j} \left(r^{2(m+j-\beta_0)} \right) \geqslant 0, \tag{6.105}$$

so that

$$r^{-2\beta_0} \sum_{j=0}^{k} (-1)^j \binom{k}{j} \frac{(1-\beta_0)_{m+j}}{\Gamma(m+j+\lambda-1/2)} \geqslant 0, \tag{6.106}$$

which leads to

$$\frac{r^{-2\beta_0}(1-\beta_0)_m}{\Gamma(m+\lambda-1/2)} \, {}_2F_1(-k, 1-\beta_0+m, m+\lambda-1/2; 1) = \frac{r^{-2\beta_0}(1-\beta_0)_m \, \Gamma(k+\lambda+\beta_0-3/2)}{\Gamma(k+m+\lambda-1/2)\Gamma(\lambda+\beta_0-3/2)} \geqslant 0. \tag{6.107}$$

Since $\lambda \geqslant 3/2 - \beta_0$, the inequality indeed holds, as expected. Now, let us examine the low-order conditions for general $\beta(r)$. As stated above, the case $k = 0$ leads to the necessary conditions (6.55). Furthermore, we find:

$$k = 1, m = 0: \qquad \beta(r) + \lambda - 3/2 \geqslant 0, \tag{6.108}$$

$$k = 1, m = 1: \qquad \frac{r}{2}\frac{\mathrm{d}\beta}{\mathrm{d}r} + (1-\beta)(\beta+\lambda-3/2) \geqslant 0, \tag{6.109}$$

$$k = 2, m = 0: \qquad -\frac{r}{2}\frac{\mathrm{d}\beta}{\mathrm{d}r} + (\beta+\lambda-1/2)(\beta+\lambda-3/2) \geqslant 0. \tag{6.110}$$

Evidently, the first inequality can fail for anisotropy profiles where $\beta_0 > \beta_\infty$. However, every inequality will contain a positive term in λ^k. So, the conditions do hold if we put more

restrictions on $f(\psi)$, i.e. by further increasing the value of λ for which the derivatives of $f(\psi)$ are nonnegative. This is a general rule: the conditions with $k = 0$ put real restrictions on $\beta(r)$, but the conditions with $k > 0$ hold if the first λ derivatives of $f(\psi)$ are nonnegative, for a sufficiently high value of $\lambda \geqslant \lfloor 3/2 - \beta_0 \rfloor$.

Chapter 7

Ram-pressure stripping of late-type dwarf galaxies in Fornax

In this chapter, we apply our quadratic programming algorithm to observational data; in concreto, we will seek dynamical models for a population of dwarf galaxies in the Fornax cluster. Thus, we demonstrate that the early-type galaxies trace very radial orbits, consistent with the hypothesis that they originated from late-type galaxies that underwent ram-pressure stripping when they passed through the intracluster gas in the central region of Fornax. The results here presented are published in De Rijcke et al. (2010). The scientific rationale and data preparation were worked out by S. De Rijcke; the modelling and analysis was carried out by the author.

7.1 Introduction

So far, we have used our techniques to model the structure of theoretical systems. In this chapter, we will turn our attention to observational data. More specifically, we will examine whether dynamical modelling is able to provide an explanation for the origin of the early-type dwarf galaxy population in the Fornax cluster.

In concreto, we put to the test the hypothesis that the Fornax cluster dwarf galaxies are mostly a relatively recently acquired population, of which the star-forming, late-type members are converted into quiescent, early-type ones by ram-pressure stripping. This conversion would take place when a galaxy traces a sufficiently radial orbit, such that it plunges inside the inner few hundred kiloparsecs of the cluster and interacts with the hot intracluster gas. In other words, we will try to find anisotropic spherical models that are consistent with the available morphological, positional and kinematical data, especially with the radially increasing late-to-early-type ratio. As it turns out, we are indeed able to construct such models, although they necessarily consist of extremely radially anisotropic orbital distributions. In principle, this corroborates the idea that the Fornax cluster dwarfs are an infall population and that environmental factors, in this case ram-pressure stripping,

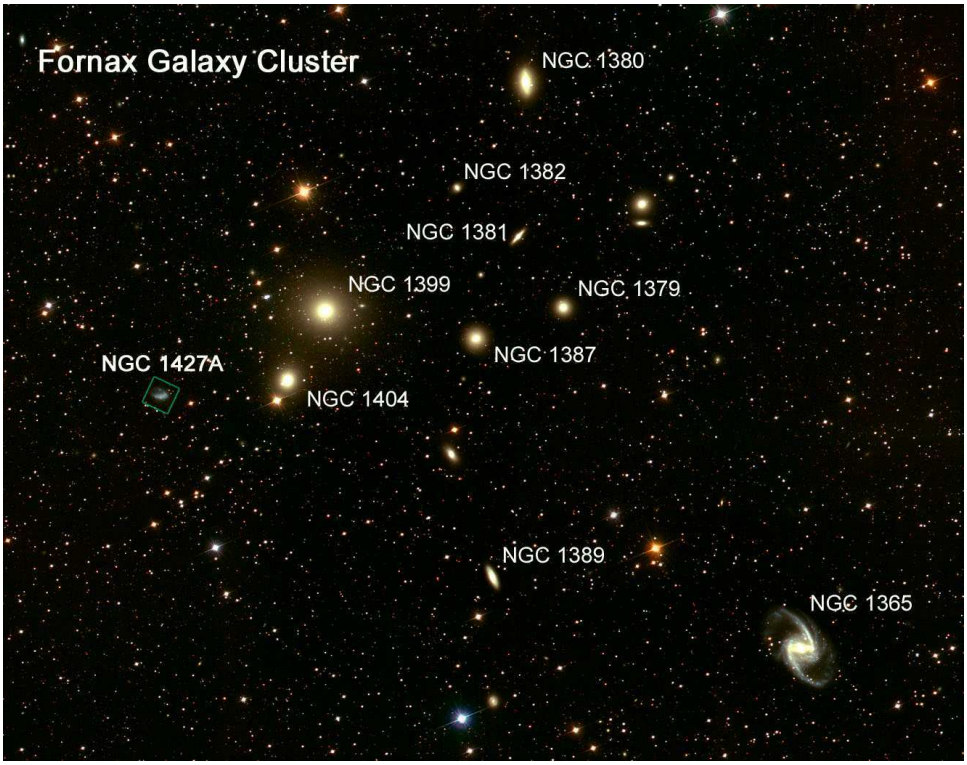

Figure 7.1 The Fornax cluster. *Illustration Credit*: NASA, ESA, Z. Levay and L. Frattare (STScI). *Image Credit*: A. Karick and M. Gregg (LLNL/UC,D) using the Michigan Curtis Schmidt Telescope at CTIO: digital colour composite/mosaic in B, V and I bands.

play a prominent role in converting late-type dwarfs into early-type ones.

The fraction of passively evolving, i.e. red and dead, galaxies is a steeply rising function of local galaxy density. This is all the more true for dwarf galaxies ($M_B \gtrsim -18$ mag) (Haines et al. 2007; Barazza et al. 2009). Using optical imaging of galaxies in 127 rich clusters, Lu et al. (2009) conclude that the red-sequence dwarf-to-giant ratio has increased by a factor of ~ 3 between redshifts $z \sim 0.2$ and 0, with little evolution before that. Comparing the luminosity functions of X-ray clusters at redshifts $z \sim 0.5$ and $z \sim 0.1$, Stott et al. (2007), on the other hand, find an increase of the red-sequence dwarf-to-giant ratio by a factor of ~ 2 over this 4 Gyr interval. Despite large cluster-to-cluster variations, this is strong evidence for a significant increase of the number of quenched dwarf galaxies in clusters over the last half of the Hubble time.

This is plausibly related to the accretion of galaxies onto clusters along filaments. Before entering the clusters, mutual interactions between filament galaxies enhance their star-formation rates, especially in faint galaxies (Fadda et al. 2008; Porter et al. 2008). This oc-

curs independent of the filament galaxies being group members or not (although it increases the vigour of the enhancement if they are not), indicating that gas-rich dwarfs accrete onto clusters despite possible pre-processing in smaller galaxy groups. Other tentative evidence for the recent accretion and quenching of dwarf galaxies comes from stellar populations studies of Coma cluster systems by Smith et al. (2009). These authors find the dwarfs in the south-west region of the Coma cluster to have significantly younger mean ages than their central counterparts, with the dwarf red sequence having been established between redshifts $z \sim 0.2$ and ~ 0.1.

Several mechanisms responsible for this conversion from late- to early-type dwarfs in a cluster environment have been put forward in the literature. Using simulations, tidal stirring or "harassment" has been shown to be quite effective in converting disky dwarf irregulars into rounder dwarf spheroidals in a Local Group environment (Mayer et al. 2001 ; Moore et al. 1996). However, in a cluster environment, tidal heating is probably of less importance. The tidal radius imposed by a cluster's tidal forces only becomes smaller than a dwarf galaxy's physical size (typically of the order of a few kiloparsecs) for orbital radii smaller than a few tens of kiloparsecs. Thus, cluster potential tidal heating is expected to affect only those few dwarfs that come exceedingly close to the cluster centre. A Monte Carlo simulation of harassment of infalling dwarf galaxies by a harasser population typical for the Virgo cluster has shown that strong tidal encounters are very rare, involving less than 15 per cent of the infalling dwarfs (Smith et al. 2010).

As a dwarf galaxy orbits through the hot intracluster medium (ICM), its gas experiences a ram pressure, which depends on the galaxy's orbital velocity and the ICM density, and can be stripped away (Mori & Burkert 2000). We show below that, in the Fornax cluster environment, ram-pressure stripping can remove the gas from dwarf galaxies entering inside the inner few hundred kiloparsecs, making this the dominant mechanism that converts late-type into early-type dwarfs (with tidal heating additionally responsible for the removal of angular momentum).

We will investigate quantitatively if the idea that the Fornax cluster dwarf galaxies have mostly been accreted in the not too distant past and subsequently transformed from late-type to early-type by ram-pressure stripping is compatible with the available morphological and kinematical data. We therefore assume that dwarf galaxies are born as late-type systems, containing gas and hosting ongoing star formation, albeit at a fluctuating star-formation rate (Cole et al. 2007). Given the inefficiency of supernova feedback, they are expected to retain at least part of their gas and, without external intervention, to remain late-types until entering the cluster (Valcke et al. 2008). There, they are stripped of their gas and join the red sequence. In the introductory chapter, we defined the two-body relaxation time for a galaxy moving in a cluster through a background of N galaxies as

$$t_{\rm relax} \approx \frac{0.1\,N}{\ln N} t_{\rm cross}, \tag{7.1}$$

with $N \gtrsim \mathcal{O}\left(10^2\right)$ and $t_{\rm cross}$ the crossing time. Clearly, the relaxation time for a dwarf galaxy orbiting in the Fornax cluster, perturbed mainly by the few tens of brightest cluster members, is longer than the crossing time. This implies that the dwarfs are not a relaxed

population: if they are an infall population and entered the cluster a few crossing times ago, they must still have a highly radial orbital distribution. We want to exploit this fact to test the infall scenario.

In the next section, we give a description of how we model the effects of ram-pressure stripping, followed by an overview of the available morphological and kinematical data. The details of the dynamical modelling of the Fornax cluster dwarf population are given in Section 7.4. We end with a presentation and discussion of the results in Sections 7.5 and 7.6.

7.2 Ram-pressure stripping in the Fornax cluster

The Fornax Cluster mass profile estimates of Paolillo et al. (2002) and Drinkwater et al. (2001) can be well approximated by the sum of two NFW profiles, one for NGC1399, the central bright elliptical dominating the Fornax Cluster, and one for the cluster (see the left panel of Fig. 7.2 and Table 7.4). From this, we immediately obtain the total mass density $\rho_{\rm tot}(r)$ and the gravitational potential $\psi(r)$:

$$\rho_{\rm tot}(r) = \frac{\rho_{\rm bcg}}{x_{\rm bcg}\,(1+x_{\rm bcg})^2} + \frac{\rho_{\rm clus}}{x_{\rm clus}\,(1+x_{\rm clus})^2}, \tag{7.2}$$

$$\psi(r) = \frac{\psi_{\rm bcg}}{x_{\rm bcg}}\left(\ln(1+x_{\rm bcg}) - \frac{x_{\rm bcg}}{1+b_{\rm bcg}}\right) + \frac{\psi_{\rm clus}}{x_{\rm clus}}\left(\ln(1+x_{\rm clus}) - \frac{x_{\rm clus}}{1+b_{\rm clus}}\right), \tag{7.3}$$

with

$$x_{\rm bcg} = r/r_{\rm bcg}, \qquad x_{\rm clus} = r/r_{\rm clus}, \tag{7.4}$$

$$b_{\rm bcg} = b/r_{\rm bcg}, \qquad b_{\rm clus} = b/r_{\rm clus}, \tag{7.5}$$

$$\rho_{\rm bcg} = \frac{M_{\rm bcg}}{4\pi\, c_{\rm bcg}\, r_{\rm bcg}^3}, \qquad \rho_{\rm clus} = \frac{M_{\rm clus}}{4\pi\, c_{\rm clus}\, r_{\rm clus}^3}, \tag{7.6}$$

$$\psi_{\rm bcg} = \frac{GM_{\rm bcg}}{c_{\rm bcg}\, r_{\rm bcg}}, \qquad \psi_{\rm clus} = \frac{GM_{\rm clus}}{c_{\rm clus}\, r_{\rm clus}}, \tag{7.7}$$

$$c_{\rm bcg} = \left(\ln(1+b_{\rm bcg}) - \frac{b_{\rm bcg}}{1+b_{\rm bcg}}\right), \qquad c_{\rm clus} = \left(\ln(1+b_{\rm clus}) - \frac{b_{\rm clus}}{1+b_{\rm clus}}\right). \tag{7.8}$$

The masses $M_{\rm bcg}$, $M_{\rm clus}$ and the scale-lengths $r_{\rm bcg}$, $r_{\rm clus}$ are given in Table 7.4, and $b = 50$ Mpc is an arbitrary cut-off boundary such that the total mass accumulates to $M_{\rm tot} = M_{\rm bcg} + M_{\rm clus}$ at b. The parameters of these NFW profiles were chosen because they provided the best fit to the data points.

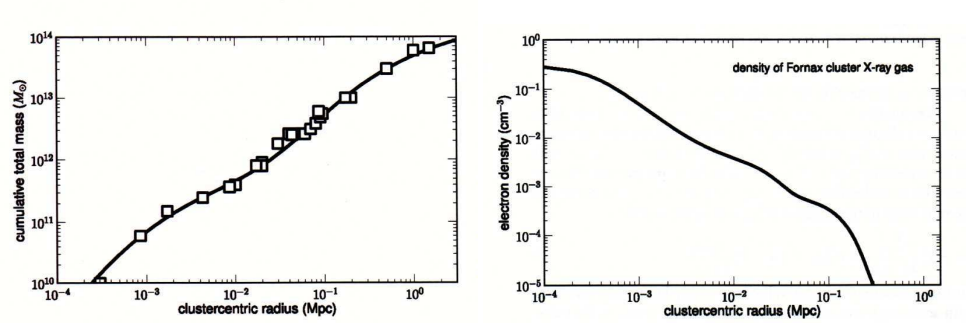

Figure 7.2 Left panel: the cumulative total mass function of the Fornax cluster. The mass profile is parametrized as the sum of two NFW-models; the data points (squares) are taken from Paolillo et al. (2002) and Drinkwater et al. (2001). Right panel: The ICM density, parametrized using three profiles (see text).

Based on ROSAT HRI observations, Paolillo et al. (2002) also derived the structure of the X-ray halo of the Fornax cluster. They showed that the density distribution of this intracluster medium (ICM), which is the medium stripping gas from the dwarf galaxies orbiting through it, can be well approximated by the sum of three spherically symmetric profiles,

$$\rho_{\rm icm}(r) = \sum_{k=1}^{3} \rho_{{\rm icm},1} \left[1 + \left(\frac{r}{r_{{\rm icm},k}} \right)^2 \right]^{-\frac{3}{2} B_{{\rm icm},k}} , \tag{7.9}$$

with the central densities $\rho_{{\rm icm},k}$, the scale-radii $r_{{\rm icm},k}$ and the exponents $B_{{\rm icm},k}$ again listed in Table 7.4. Using these parameter values, we reconstruct the spatial density profile of the hot gas (see the right panel of Fig. 7.2).

Mori & Burkert (2000) calculated the minimum core mass $M_{\rm crit}(r, v_{\rm gal})$ a dwarf galaxy must have to retain its gas when subjected to a given ram pressure: their equations (13),

$$M_{\rm crit}(r, v_{\rm gal}) \approx 2.52 \times 10^9 \left(\frac{\rho_{\rm icm}}{10^{-4}\ {\rm cm}^{-3}} \right)^{5/2} \left(\frac{v_{\rm gal}}{1000\ {\rm km\,s}^{-1}} \right)^5 M_\odot , \tag{7.10}$$

based on analytical arguments, and (32), based on numerical simulations. These authors modelled dwarf galaxies as gaseous haloes embedded in a Burkert dark matter potential and the core mass M_0 is the dark matter mass inside one core radius r_0 of the Burkert potential (Burkert 1995). Both critical mass estimates are presented in the left panel of Fig. 7.3, using (7.9) for the gas density. We show the critical mass curves for three galaxy velocities: 400 km s^{-1}, 800 km s^{-1}, and the local escape velocity $v_{\rm esc}(r) = \sqrt{2\psi(r)}$. Clearly, both critical mass estimates give similar results: dwarf galaxies on orbits that are radial enough to bring them inside the inner few hundred kiloparsec of the Fornax cluster can be stripped of their gas. In the subsequent analysis, we will use Eq. (7.10).

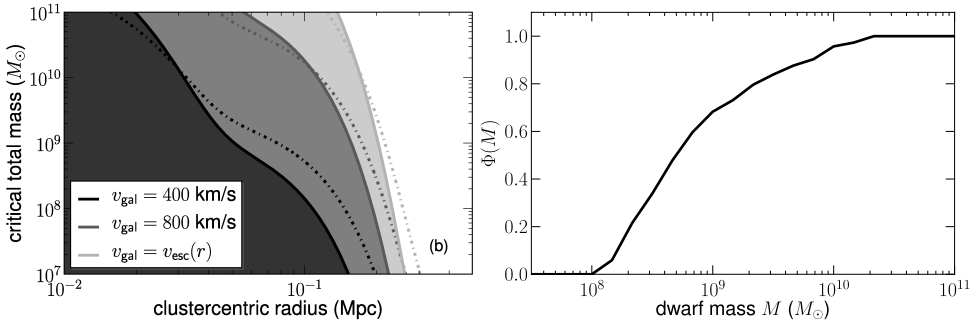

Figure 7.3 Left panel: The critical mass $M_{\rm crit}$ for ram-pressure stripping as a function of clustercentric radius for the ICM density profile derived by Paolillo et al. (2002) and for three choices for the velocity of the galaxy with respect to the ICM: $v_{\rm gal} = 400$km s^{-1} (black), $v_{\rm gal} = 800$km s^{-1} (dark grey), and $v_{\rm gal}(r) = v_{\rm esc}(r)$, the escape velocity (light grey). The full lines trace the critical mass as calculated by Mori & Burkert (2000) using analytical arguments; the dash-dotted lines trace the numerical estimate for $M_{\rm crit}$. Right panel: The cumulative core mass function $\Phi(M)$ of the Fornax cluster dwarfs in the luminosity interval $-14 > {\rm M}_B > -18$ mag. We used the FCC to construct the luminosity distribution and converted this into a core mass distribution using a constant $M/L_B = 5 M_\odot / L_{B,\odot}$.

We have selected dwarf galaxies in the luminosity range $-14 > M_B > -18$ mag from the Fornax Cluster Catalog (FCC) of Ferguson (1989) and the Fornax Cluster Spectroscopic Survey of Drinkwater et al. (2000). FCC Galaxies classified as "dE" and "dS0" are assumed to be "early-types" systems, the others end up in the "late-type" bin. Thus, this is an optical classification, which discriminates between star-forming late-type dwarfs and quiescent early-type ones based on the presence or absence of star-forming knots, HII regions, and optical emission lines.

For late-type dwarf galaxies in the luminosity range that we are considering, between $\log(L_B) = 8$ and 9.5 in solar units, the circular velocities vary between roughly 30 and 85 km s^{-1} (De Rijcke et al. 2007). Using the scaling relations provided by Burkert (1995), this corresponds to core masses roughly in the range $4 \times 10^8 - 1.5 \times 10^{10}$ $M_\odot$ and core radii of the order $r_0 \approx 1 - 10$ kpc. Consequently, this means that the mass-to-light ratio is almost constant, $M_0/L_B \approx 5 M_\odot / L_{B,\odot}$. We will simply use this constant value further on to convert between observed luminosities and core masses. This allows us to derive the cumulative function $\Phi(M_0)$ of the core masses of the dwarfs in the chosen luminosity interval, shown in the right panel of Fig. 7.3.

The relation between the orbital distribution of the Fornax cluster dwarfs and the observed late-to-early-type ratio now becomes apparent. On an orbit with pericentric distance r_-, only dwarfs with a core mass M_0 higher than the critical mass at pericentre

$M_{\rm crit}\left(r_-, v_{\rm gal}(r_-)\right)$ retain their gas, the others are stripped and quenched. For a given orbit with binding energy E, angular momentum L, this implies that a fraction

$$f_{\rm late}(E,L) = 1 - \Phi\left(M_{\rm crit}\left(r_-, v_{\rm gal}(r_-)\right)\right) \tag{7.11}$$

of the dwarfs on it are late-types, the others are early-types; here, the corresponding peri-centre r_- is derived from (2.30) - (2.31) and $v_{\rm gal}(r_-) = L/r_-$. In other words, if we are able to find a suitable DF $F(E,L)$ that describes the orbital distribution of the dwarf galaxies, then the corresponding subsample of late-type dwarf galaxies is given by

$$\bar{F}(E,L) = F(E,L) f_{\rm late}(E,L). \tag{7.12}$$

For a very radially anisotropic orbital distribution, many dwarfs are on plunging orbits that bring them deep into the centre of the Fornax cluster. In that case, the overall late-to-early-type ratio will be small (even at large radii because of the back-splash effect). If, on the other hand, the orbital distribution is more tangentially anisotropic, with many dwarfs on near-circular orbits, the overall late-to-early-type ratio will be large (except in the inner few hundred kiloparsecs where dwarfs get stripped and quenched anyhow). In the next section, we describe how we construct dynamical models for the Fornax cluster dwarf population which reproduce the observed dwarf density profile and which have a prescribed anisotropy profile.

7.3 The observed properties of the dwarf galaxies

As we stated in the previous section, we have selected dwarf galaxies in the luminosity range $-14 > M_B > -18$ mag from the Fornax Cluster Catalog (FCC) of Ferguson (1989) and the Fornax Cluster Spectroscopic Survey of Drinkwater et al. (2000), and classified them as early-type or late-type. We have rejected the dwarfs from the sample that belong to the Fornax-SW subcluster. Three dwarfs are clearly connected to NGC 1350, both in position and velocity, and are removed as well. As a final check, we compare the dwarfs' projected velocities with the escape velocity (see Section 7.2 for our derivation of the escape velocity) at their projected radii and remove three more galaxies with velocities close to the escape velocity. This leaves us with a final kinematics sample of 113 dwarf galaxies, shown in the top left panel of Fig. 7.4.

We use the radial velocity data of Thomas et al. (2008) to construct the velocity dispersion profile of the dwarf population. The yellow region in the top right panel of Fig. 7.4 traces the velocity dispersion profile of the dwarfs, calculated within a 10-galaxy running box, and the 1σ uncertainty around the profile.

The bottom panels of Fig. 7.4 show the projected densities of the total sample (yellow dots, left panel) and the late-type subsample (yellow triangles, right panel). The late-to-early-type ratio is an increasing function of radius. Near the centre, the late-types make out

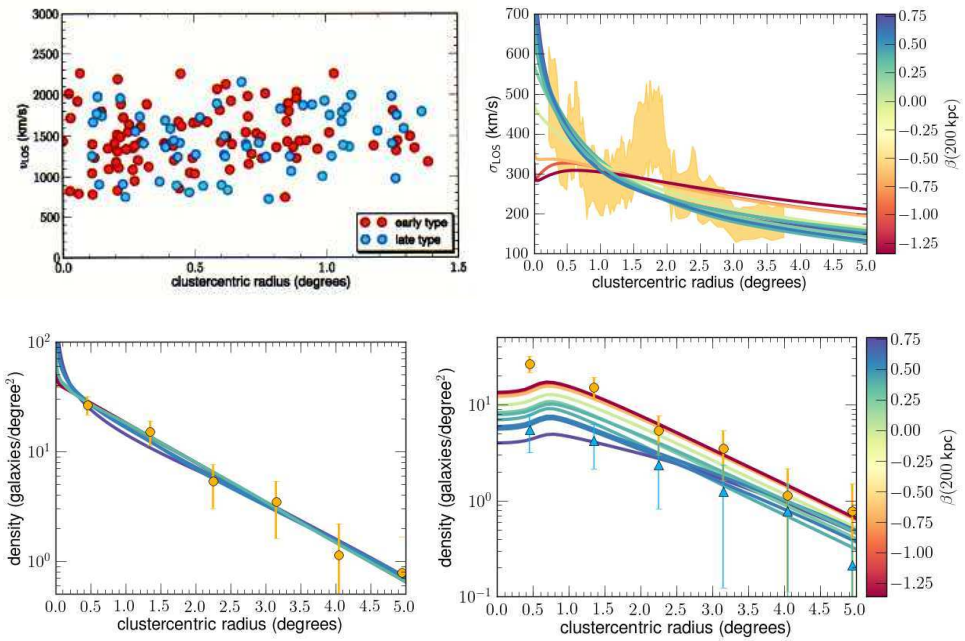

Figure 7.4 Top left: our final sample of 113 early- and late-type dwarf galaxies. Top right: the line-of-sight velocity dispersion profile of all dwarfs, $\sigma_{\rm los}$. The yellow area is derived from the data, while the curves show the corresponding profiles of our dynamical models. The curves are colour-coded according to the models' anisotropy $\beta(r)$ at a radius of 200 kpc, as indicated by the legend. Bottom left: the projected density of the entire sample of Fornax dwarf galaxies (dots), with the fitted model profiles. Bottom right: the projected density of the late-type dwarf galaxies (triangles), with the models calculated from Eq. (7.19).

~ 20 % of the total population (in projection). This increases to ~ 60 % beyond a radius of 3°. The total dwarf sample density will serve as the input data for our dynamical models.

7.4 The dynamics of the Fornax cluster dwarfs

The question is then which velocity anisotropy profile gives the best approximation of the observed late- and early-type density profiles. Given the sparse dwarf sample, we do not attempt to find the most likely DF. Instead, we construct a set of models with anisotropy profiles of the form (7.14) for a range of values of β_0, β_∞, $r_{\rm a}$, and δ (see Tables 7.1-7.3). These models explore the relevant parameter space going from tangentially

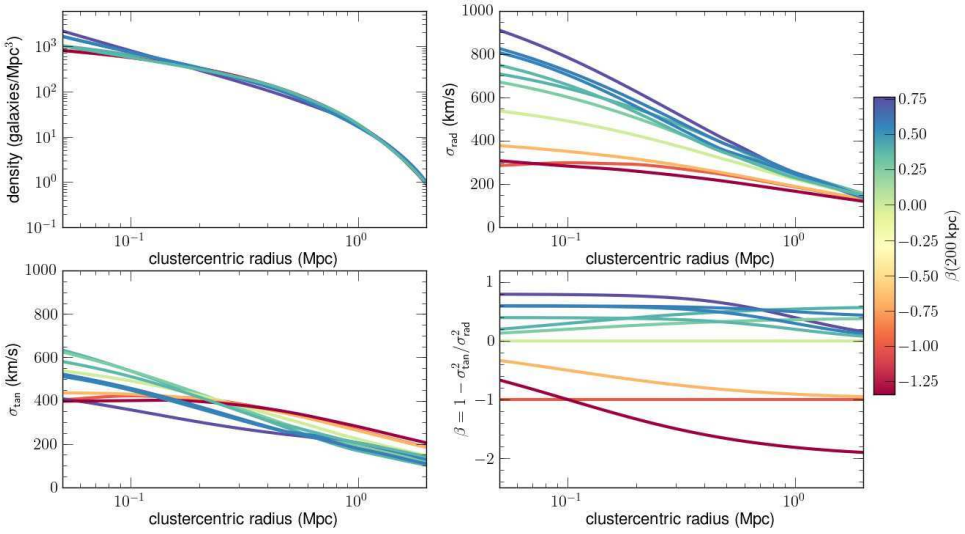

Figure 7.5 The spatial moments of our models: $\rho(r)$, $\sigma_r(r)$, $\sigma_\theta(r)$ and $\beta(r)$.

anisotropic, with anisotropies as low as $\beta = -2.0$, over isotropic to radially anisotropic, with anisotropies as high as $\beta = 0.8$.

As can be seen, the projected density profile $\Sigma^{(\rm all)}$ of the entire sample of Fornax cluster dwarfs can be well approximated by an exponential with a scale-length of 1.1° (with an adopted distance to the Fornax cluster of 18 Mpc, 1° corresponds to 0.31 Mpc). We use this exponential to extract 100 data values $\Sigma^{(\rm all)}(\Omega_m)$ at angular radii between 0.1° and 10°.

As in the previous chapters, we construct a library of augmented densities of the form (4.11),

$$\tilde{\rho}_i(\psi, r) = \rho_{0,i} \left(\frac{\psi - E_{0,i}}{\psi_0 - E_{0,i}}\right)^{p_i} \left[1 - \left(\frac{\psi - E_{0,i}}{\psi_0 - E_{0,i}}\right)^{s_i}\right]^{q_i} \left(\frac{r}{r_{\rm a}}\right)^{-2\beta_0} \left(1 + \frac{r^{2\delta}}{r_{\rm a}^{2\delta}}\right)^{\beta_\delta}, \quad (7.13)$$

and corresponding DFs $F_i(E, L)$ given by Eq. (4.57). The $\rho_{0,i}$ are normalizing constants as in (5.20). Each of these components generates a given four-parameter velocity anisotropy profile

$$\beta(r) = \frac{\beta_0 + \beta_\infty (r/r_{\rm a})^{2\delta}}{1 + (r/r_{\rm a})^{2\delta}}, \quad (7.14)$$

with fixed values $\beta_0, \beta_\infty, \delta$ and $r_{\rm a}$. Our library consists of components for which p_i takes the values 1.6, 1.8, 2.0, 2.2, 2.5, 3.0, 3.5, 4.0, 4.5, and 5.0. The parameters q_i and s_i are set to 0 and 1, respectively. Finally, the components have a finite extent, with maximum radii $r_{{\rm max},i} = \psi^{-1}(E_{0,i})$ taking the values 5, 10, 20, 50, 100, 250, 500, 1000, and 2000 kpc. For

each of these library components, the projected densities in the data points are

$$\Sigma_i(\mathbf{\Omega}_m) = 2\int_{R_m}^{+\infty} \frac{\tilde{\rho}_i\left(\psi(r), r\right) r}{\sqrt{r^2 - R^2}}\,\mathrm{d}r, \qquad m = 1, \ldots, N_{\text{data}}, \tag{7.15}$$

where the angular positions on the sky $\mathbf{\Omega}_m$ are converted to physical units $_{R_m}$ using the cluster distance. The QP-algorithm then builds each DF iteratively as a sum of N components,

$$F(E, L) = \sum_{i=1}^{N} a_i\, F_i(E, L), \tag{7.16}$$

extracted from the library, such that the quantity

$$\chi^2_N = \frac{1}{N_{\text{data}}} \sum_{m=1}^{N_{\text{data}}} \frac{1}{\left(\Sigma^{(\text{all})}(\mathbf{\Omega}_m)\right)^2} \left(\Sigma^{(\text{all})}(\mathbf{\Omega}_m) - \sum_{i=1}^{N} a_i\, \Sigma_i(r_m) \right)^2, \tag{7.17}$$

is minimized, with the conditions that $F(E_j, L_k) \geqslant 0$ over a grid $\{E_j, L_k\}$ in integral space. We find that for each model, $N = 10$ components are sufficient to provide satisfactory fits.

In total, we created 10 models with different $\beta(r)$-profiles. Their parameters and the QP results are listed in Tables 7.1-7.3 (with the $r_{\text{max},i}$ in Mpc).

Once we have a model's DF, we can calculate all observational quantities both for the whole dwarf population, and, using the late-type fraction f_{late} given by Eq. (7.11), for the early- and late-type subpopulations. The velocity moments of each model are

$$\mu^{(\text{all})}_{2n,2m}(r) = 2\pi \iint F(E, L)\, v_r^{2n}\, v_T^{2m+1}\, \mathrm{d}v_r\, \mathrm{d}v_T, \tag{7.18}$$

for the total dwarf population, and

$$\mu^{(\text{late})}_{2n,2m}(r) = 2\pi \iint \bar{F}(E, L)\, v_r^{2n}\, v_T^{2m+1}\, \mathrm{d}v_r\, \mathrm{d}v_T, \tag{7.19}$$

for the late-type dwarfs, with $\bar{F}(E, L)$ defined in Eq. (7.12). The line-of-sight velocity distributions (or LOSVDs) are given by

$$F^{(\text{all})}_{\text{los}}(\mathbf{\Omega}, v_z) = \iiint F(E, L)\, \mathrm{d}z\, \mathrm{d}v_x\, \mathrm{d}v_y, \tag{7.20}$$

$$F^{(\text{late})}_{\text{los}}(\mathbf{\Omega}, v_z) = \iiint \bar{F}(E, L)\, \mathrm{d}z\, \mathrm{d}v_x\, \mathrm{d}v_y, \tag{7.21}$$

$$F^{(\text{early})}_{\text{los}}(\mathbf{\Omega}, v_z) = F^{(\text{all})}_{\text{los}}(\mathbf{\Omega}, v_z) - F^{(\text{late})}_{\text{los}}(\mathbf{\Omega}, v_z). \tag{7.22}$$

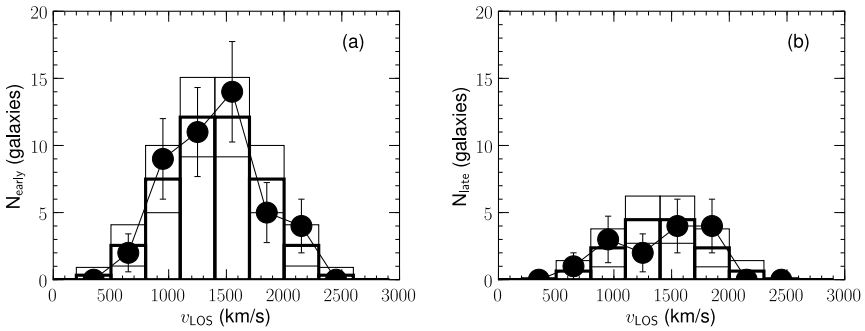

Figure 7.6 The line-of-sight velocity distributions (LOSVDs) of the early-type (left panel) and late-type (right panel) dwarf populations inside the inner 350 kpc of the Fornax cluster. The thick-line histograms are the LOSVDs of the $(\beta_0 = 0.8, \beta_\infty = 0.0)$-model. The thin-line histograms indicate the 1σ uncertainty level. The data points are the observed LOSVDs.

7.5 Results and discussion

In Fig. 7.4, we show the projected density profiles (bottom panels) and the line-of-sight velocity dispersion profiles (top right panel) of the models, derived from Eqs. (7.18) and (7.19), and compare them with the observed quantities. The model curves are colour-coded according to the anisotropy at a radius of 200 kpc. We also derived the spatial densities and dispersions of the whole population, displayed in Fig. 7.5.

By construction, all models reproduce the projected density profile of the whole dwarf population. Because of the unavoidable superposition of radial orbits passing very closely to the cluster centre, the most radially anisotropic models have a central density peak inside the inner data point (recall the central density slope - anisotropy inequality (An & Evans 2006); see the previous chapter).

All models that are more radially anisotropic than $\beta(200\,\mathrm{kpc}) \sim 0$ reproduce the steep line-of-sight velocity dispersion profile. Thus, tangentially anisotropic dynamical models can be ruled out by the kinematical data alone. However, only the most radially anisotropic models succeed in sufficiently depleting the number of late-type dwarfs. $\beta(200\,\mathrm{kpc})$ needs be as high as $\sim 0.6 - 0.8$ to reproduce, within the error bars, the late-type projected density profile. Only for these extreme radial anisotropies, the late-type density is low enough.

According to our assumptions, early-type dwarfs are selected to be on orbits that pass close enough to the cluster centre for ram-pressure stripping to be effective. Therefore, we expect them to have the peaked, broad-winged LOSVD of a radially anisotropic population. Late-types, on the other hand, are expected to be moving on orbits avoiding the cluster centre so they should have the flat-topped LOSVD typical for a tangentially anisotropic population. In order to test this corollary of our basic assumptions, we compare the observed

with the model LOSVDs, given by Eqs. (7.21) - (7.22). In Fig. 7.6, we show the integrated LOSVDs of the early-type (left panel) and late-type (right panel) dwarf populations inside the inner 350 kpc ($\approx 1^\circ$) of the Fornax cluster. This is the region least influenced by substructure and with a symmetric sampling around the cluster centre. The thick-line histograms are the LOSVDs of the $(\beta_0 = 0.8, \beta_\infty = 0.0)$-model. We first calculated the model's full LOSVD of the early-type dwarf galaxies within a 350 kpc aperture. Since there are 45 early-type dwarf galaxies in our sample inside this aperture, we sampled 45 velocities from this theoretical LOSVD and, as for the observed dwarfs, made a histogram of 10 velocity bins. This was repeated 10.000 times to create an ensemble of 45-galaxy LOSVDs. The symmetrized ensemble mean, together with the 1σ uncertainty about this mean, is the quantity presented in the left panel of Fig. 7.6. Given the presence of 45 early-type dwarfs, the model predicts there should be 13 late-type systems inside the inner 350 kpc (the observed number is 14). The predicted and observed late-type dwarf LOSVDs are shown in the right panel. The agreement between the model and observed LOSVDs is clearly very satisfactory.

7.6 Conclusions

We have tested the hypothesis that the Fornax cluster dwarf galaxies are a relatively recent infall population in which late-type systems are converted into early-type ones, predominantly by the action of ram-pressure stripping. We have assumed that the dwarf galaxies are born as late-type systems and are converted into early-types if they venture close enough to the cluster centre for the ICM ram pressure to remove their gas. With these assumptions, we have shown that dynamical models for the dwarf population can reproduce *(i)* the steeply declining line-of-sight velocity dispersion profile, *(ii)* the exponential projected density profile of all dwarfs, *(iii)* the radially increasing late-to-early-type dwarf ratio, and *(iv)* the central line-of-sight velocity distribution *only* if the dwarf orbital distribution is extremely radially anisotropic. Only models with $\beta(200\,\mathrm{kpc}) \gtrsim 0.6$ meet the observational constraints.

This corroborates the idea that the Fornax cluster dwarfs are predominantly an infall population and that the observed morphology-density relation is a result of environmental influences (predominantly ram-pressure stripping) on the star-formation histories of dwarf galaxies.

This chapter concludes our main body of work. We have developed a dynamical modelling technique to create DFs with a given four-parameter velocity anisotropy profile that fit a set of data points. The flexibility of our anisotropies made it possible to apply our method to dark matter haloes, the GDSAI, and the dwarf galaxy population of the Fornax cluster. In a final chapter, we will describe our work in a side-project in which the stability of certain Hernquist models with and without a supermassive black hole was investigated by means of N-body simulations.

Table 7.1. Components of the 10 QP-models (part 1)

$\beta_0 = -1$	$\beta_\infty = -1$	$\delta = 0.5$	$r_\mathrm{a} = 0.01$ Mpc		$\chi^2_{10} = 0.003$
$a_{10,i}$	72.50	7.98	1.24	−9.23	−0.35
	−0.36	0.77	1.87	6.73	0.23
p_i	6.00	7.00	8.00	5.00	4.00
	3.00	3.00	3.50	4.50	6.00
$r_{\mathrm{max},i}$	0.50	1.00	0.05	0.25	0.02
	0.10	0.05	0.50	0.25	0.10
$\beta_0 = 0.0$	$\beta_\infty = -2$	$\delta = 0.5$	$r_\mathrm{a} = 0.01$ Mpc		$\chi^2_{10} = 0.010$
$a_{10,i}$	74.10	18.84	−13.29	0.21	−1.64
	0.21	0.16	2.51	−0.13	0.56
p_i	10.00	7.00	10.00	4.50	5.00
	4.00	4.00	5.00	4.50	4.00
$r_{\mathrm{max},i}$	1.00	0.50	0.50	0.25	0.10
	0.02	2.00	0.25	0.02	0.25
$\beta_0 = 0.0$	$\beta_\infty = -1$	$\delta = 0.5$	$r_\mathrm{a} = 0.01$ Mpc		$\chi^2_{10} = 0.016$
$a_{10,i}$	27.68	9.92	43.29	3.18	−0.01
	−1.22	−1.33	−0.37	0.61	−0.18
p_i	5.00	4.50	6.00	3.00	3.00
	4.00	3.00	3.00	3.00	3.50
$r_{\mathrm{max},i}$	0.50	0.25	0.50	0.25	2.00
	0.10	0.10	0.05	1.00	0.50
$\beta_0 = 0.0$	$\beta_\infty = 0.0$	$\delta = 0.5$	$r_\mathrm{a} = 0.01$ Mpc		$\chi^2_{10} = 0.045$
$a_{10,i}$	85.62	−53.93	−1.47	64.53	−0.83
	−14.87	1.41	−10.65	3.59	8.41
p_i	3.50	2.00	3.00	2.20	1.60
	2.20	3.00	2.50	1.60	1.00
$r_{\mathrm{max},i}$	0.50	0.25	0.05	0.25	0.05
	0.50	2.00	0.10	0.50	0.25

Table 7.2. Components of the 10 QP-models (part 2)

$\beta_0 = 0.0$	$\beta_\infty = 0.4$	$\delta = 0.5$	$r_a = 0.01$ Mpc		$\chi^2_{10} = 0.45$
$a_{10,i}$	100.00	−2.23	7.48	−13.08	−9.95
	−39.53	−2.27	−8.33	43.98	5.37
p_i	3.00	1.80	1.60	2.50	2.20
	3.00	1.60	1.60	2.50	4.00
$r_{\max,i}$	0.50	0.05	0.25	0.10	0.50
	0.25	0.50	0.10	0.25	2.00
$\beta_0 = 0.0$	$\beta_\infty = 0.6$	$\delta = 0.5$	$r_a = 0.01$ Mpc		$\chi^2_{10} = 108.3$
$a_{10,i}$	17.13	68.74	−15.74	11.31	−1.62
	1.41	0.04	0.01	0.01	0.01
p_i	2.50	1.60	2.00	1.80	1.60
	2.20	2.20	2.50	2.20	1.60
$r_{\max,i}$	0.50	0.25	0.10	0.50	0.50
	0.50	0.02	1.00	2.00	2.00
$\beta_0 = 0.4$	$\beta_\infty = 0.0$	$\delta = 1.0$	$r_a = 0.10$ Mpc		$\chi^2_{10} = 1.39$
$a_{10,i}$	100.00	2.31	−6.99	68.72	1.00
	−33.26	31.64	−0.14	18.03	−100.00
p_i	3.00	1.60	2.00	2.50	1.80
	2.20	2.50	3.00	1.60	2.20
$r_{\max,i}$	0.50	0.25	0.05	0.50	0.25
	0.10	0.25	0.02	0.50	0.50
$\beta_0 = 0.6$	$\beta_\infty = 0.0$	$\delta = 1.0$	$r_a = 0.10$ Mpc		$\chi^2_{10} = 135.6$
$a_{10,i}$	19.95	18.60	−10.19	7.88	−4.57
	52.36	−7.79	0.01	1.09	0.11
p_i	2.50	1.60	1.60	2.20	1.60
	1.80	1.80	1.60	2.00	3.00
$r_{\max,i}$	0.50	0.25	0.05	0.50	0.50
	0.25	0.10	2.00	1.00	0.02

Table 7.3. Components of the 10 QP-models (part 3)

$\beta_0 = 0.6$	$\beta_\infty = 0.4$	$\delta = 1.0$		$r_a = 0.10$ Mpc	$\chi^2_{10} = 189.7$
$a_{10,i}$	9.60	0.01	87.89	−18.48	0.01
	−7.25	6.20	0.01	0.37	0.90
p_i	2.20	3.00	1.60	1.60	2.50
	1.60	1.60	1.60	2.50	3.00
$r_{\max,i}$	0.50	2.00	0.25	0.10	1.00
	0.05	0.50	1.00	0.50	0.05
$\beta_0 = 0.8$	$\beta_\infty = 0.0$	$\delta = 1.0$		$r_a = 0.10$ Mpc	$\chi^2_{10} = 111.4$
$a_{10,i}$	3.02	7.21	13.75	−43.47	−5.30
	57.99	−9.10	−0.32	42.29	$_2$.22
p_i	2.20	3.00	1.60	1.60	1.60
	1.80	1.60	2.20	2.50	1.60
$r_{\max,i}$	0.50	2.00	0.25	1.00	0.50
	0.25	0.05	0.01	0.50	1.00

NFW profiles

components	scale-length (kpc)	total mass at 50 Mpc ($M_\odot$)
NGC 1399	0.6	2×10^{12}
Cluster	150	2×10^{14}

ICM densities

central density (cm^{-3})	scale-length (kpc)	B
0.3	0.34	0.54
0.0025	183	41
0.00055	778	24

Table 7.4 Parameters used in the NFW profile (7.2)-(7.3) and the ICM densities (7.9).

Part IV

OTHER WORK

Chapter 8

Stability of Hernquist models with a supermassive black hole

Instead of fitting models to given data, we will now attempt the converse: given a set of Hernquist models, we will extract data sets of particles, by means of a Monte Carlo code. We will investigate the radial-orbit stability of these systems using N-body simulations; in particular, we discuss the influence of a central supermassive black hole on the stability of these systems. The results of this chapter are found in Buyle et al. (2007). The N-body simulations were carried out by P. Buyle, the Monte Carlo simulations and stability analysis were done by the author.

8.1 Introduction

Nowadays it is accepted that almost every galaxy hosts a central supermassive black hole (SBH) at its core. Since the kinematical discovery of the first SBH with the Hubble Space Telescope (HST), extensive studies have been carried out by many groups that investigate the demography of SBHs and the effect of the SBHs on their environment. The most popular discoveries are the correlations between the mass of the SBH ($M_{\rm BH}$) and respectively the total blue magnitude L_B of the hot stellar component in which it resides (Kormendy & Richstone 1995), the central velocity dispersion of the hot stellar component (Ferrarese & Merritt 2000; Gebhardt et al. 2000), the central light concentration $C(\alpha)$ or equivalent the Sérsic index n (Graham et al. 2001) and the maximum rotational velocity of the galaxy (Ferrarese 2002; Baes et al. 2003; Pizzella et al. 2005; Buyle et al. 2006). These relations have been calibrated with the known masses of the SBHs of the nearest galaxies, that mostly have been derived by means of either stellar or gas kinematics.

Sophisticated axisymmetric 3-integral dynamical models that allow a variation in mass-to-light ratio and anisotropy as a function of radius have been obtained by fits to the line-of-sight velocity distributions (LOSVDs) in the galaxies, which were derived primarily from

high-resolution spectra taken with the HST

$$F_{\rm los}(\mathbf{\Omega}, v_z) = \iiint F(E, L)\, \mathrm{d}z\, \mathrm{d}v_x\, \mathrm{d}v_y. \tag{8.1}$$

The accuracy of the applied dynamical models to the observed stellar kinematics is still improving steadily and is reflected on the complexity of the DFs. Despite this positive progress on the dynamical front, very few anisotropic dynamical models of a galactic nucleus have been tested for dynamical stability (Ferrarese & Ford 2005). One of the reasons for this is the complexity of the distribution functions, which are mostly numerically derived. Hence, to simulate these numerical DFs one normally approximates numerically the solution of the Jeans equation to derive the velocity dispersion profile and then uses Gaussians to provide local velocity distributions. However, it is known from simulations of galactic systems that this method causes serious numerical artifacts (Kazantzidis et al. 2004).

Among the few theoretical analytical systems that contain a SBH are the ones derived by Ciotti (1996), Baes et al. (2003) and Baes et al. (2005), where the attention is drawn primarily to the Hernquist model since this is the best-known approximation to the Sérsic profiles that are observed in bulges and elliptical galaxies, and by Stiavelli (1998) where the distribution function of a stellar system around an SBH is derived from statistical mechanic considerations. Ciotti (1996) initially starts with a 2-component system containing the luminous and dark matter and creates both isotropic and anisotropic (based on the Osipkov-Merritt strategy, see Eq. (2.168)) systems. The dark matter halo (also represented by a Hernquist model) can be transformed into a central SBH by setting the core radius to zero.

In this chapter we present the results of a dynamical stability investigation of spherical systems containing an SBH, as a function of the mass of the SBH and the anisotropy radius of the system. In Section 8.2 we describe a Monte Carlo algorithm that we developed to generate the initial conditions for the models, together with our N-body code and technique for investigating the stability. We present in Section 8.3 the results of a stability investigation of a family of anisotropic Hernquist models without an SBH, with different anisotropy behaviours (Baes & Dejonghe 2002). In Section 8.4 we describe the Osipkov-Merritt Hernquist models with a central SBH, introduced by Ciotti (1996). We investigate the stability of these systems in detail in Section 8.5, comparing them with the corresponding models without an SBH. We perform this in a 2-parameter space as a function of the anisotropy radius $r_{\rm a}$ and the mass of the central SBH μ. In Section 8.6 we present our final results and conclusions.

8.2 Computational method

8.2.1 Definition of the Hernquist models

First we introduce some general characteristics of the models in our dynamical study. All systems are based on the spherical Hernquist potential-density pair (Hernquist 1990), including a supermassive black hole in the centre. Given this mass profile, we shall investigate several distribution functions (DFs) consistent with the density outside the centre, and which we will refer to as the stellar component. If we denote the total stellar mass by $M_{\rm s}$, we can write the total mass as $M_{\rm tot} = M_{\rm s}(1+\mu)$, where the fractional quantity μ determines the SBH mass $\mu M_{\rm s}$. In our subsequent analysis we will work in dimensionless units $G = M_{\rm s} = 1$, so that the gravitating binding potential and the density are given by

$$\psi(r) = \frac{1}{1+r} + \frac{\mu}{r}, \tag{8.2}$$

$$\rho(r) = \frac{1}{2\pi}\frac{1}{r(1+r)^3} \quad (r > 0). \tag{8.3}$$

We will also express the time-steps in our N-body code (the time between two successive calculations) in dimensionless units of half-mass dynamical time, which is defined as the dynamical time (Section 2.2 in Binney & Tremaine 2008) at the stellar half-mass radius:

$$T_h = \sqrt{\frac{3\pi}{16G\bar{\rho}}}, \tag{8.4}$$

where

$$\bar{\rho} = \frac{3M(r_{1/2})}{4\pi r_{1/2}^3}. \tag{8.5}$$

For a Hernquist model with $\mu = 0$ the half-mass dynamical time and the half-mass radius are

$$T_h = \frac{\sqrt{2}}{2}\pi\left(1+\sqrt{2}\right)^{3/2}, \tag{8.6}$$

$$r_{1/2} = 1+\sqrt{2}. \tag{8.7}$$

We will also use these units for models with an SBH.

A conversion to observational units can be obtained through the close similarity between the Hernquist and De Vaucouleurs profiles (Hernquist 1990), with $r_{1/2} \approx 1.33 r_{\rm e}$, where $r_{\rm e}$ is the effective radius. Then a physical length, time and velocity are found by the

scaling relations

$$\tilde{r} = \tilde{r}_u r, \tag{8.8}$$

$$\tilde{T}_h = \sqrt{\frac{\tilde{r}_u^3}{G\tilde{M}_\mathrm{s}}} T_h, \tag{8.9}$$

$$\tilde{v} = \sqrt{\frac{G\tilde{M}_\mathrm{tot}}{\tilde{r}_u}} v, \tag{8.10}$$

with $\tilde{M}_\mathrm{s}$ the stellar mass, $\tilde{M}_\mathrm{tot}$ the total mass and $\tilde{r}_u = (1.33 r_\mathrm{e})/(1+\sqrt{2})$, expressed in physical units.

Every model was simulated by means of 10^5 equal-mass particles that all follow the distribution function of the system and are contained within a sphere of radius $r_\mathrm{b} = 2000$ which encloses about 99.9% of the stellar mass of the system. We performed the simulations for 50 dynamical times, and used the values of the axis ratios c/a and b/a during this time as (in)stability indicators (see Section 8.2.4).

8.2.2 Constructing the data sets

Since we will investigate our models by means of N-body simulations, the first objective is to obtain representative discrete data sets from the considered distribution functions $F(E, L)$. In order to extract discrete data samples from the models, we need to simulate random particles uniformly in the phase-space enclosed by the DFs. To this aim we used a Monte Carlo simulator, developed by the author.

The procedure works as follows: we write each DF as $F(r, v_r, v_T)$ and we consider a 4-dimensional grid space with (r, v_r, v_T) as abscissae and the function values on the ordinate axis. We start with a single cell in this space, extending from the origin to a boundary $(r_\mathrm{b}, v_{r,\mathrm{b}}, v_{T,\mathrm{b}})$, where r_b is chosen to be sufficiently large, and $v_{r,\mathrm{b}} = v_{T,\mathrm{b}} = \sqrt{2\psi(0)}$, and with the ordinate set at the (known or estimated) DF maximum f_b. These boundaries (for infinite values a sufficiently large value is taken, see further) enclose a 7-dimensional phase-space volume

$$V_1 = \left(\frac{4\pi}{3} r_\mathrm{b}^3\right)\left(2 v_{r,\mathrm{b}}\right)\left(\pi v_{T,\mathrm{b}}^2\right) f_\mathrm{b}. \tag{8.11}$$

In the second step we attempt to split the cell into 8 sub-cells with different ordinates (i.e. the up to that point known function maxima in each cell). Therefore a co-ordinate $(r_s, v_{r,s}, v_{T,s})$ is sought to serve as the common corner point in the abscissae for these sub-cells: starting in the cell centre, the total phase-space volume of the originating sub-cells is calculated, and through a number of iterations the cell is scanned for a better splitting point, i.e. which minimizes this volume. In this manner, the original cell is being split as

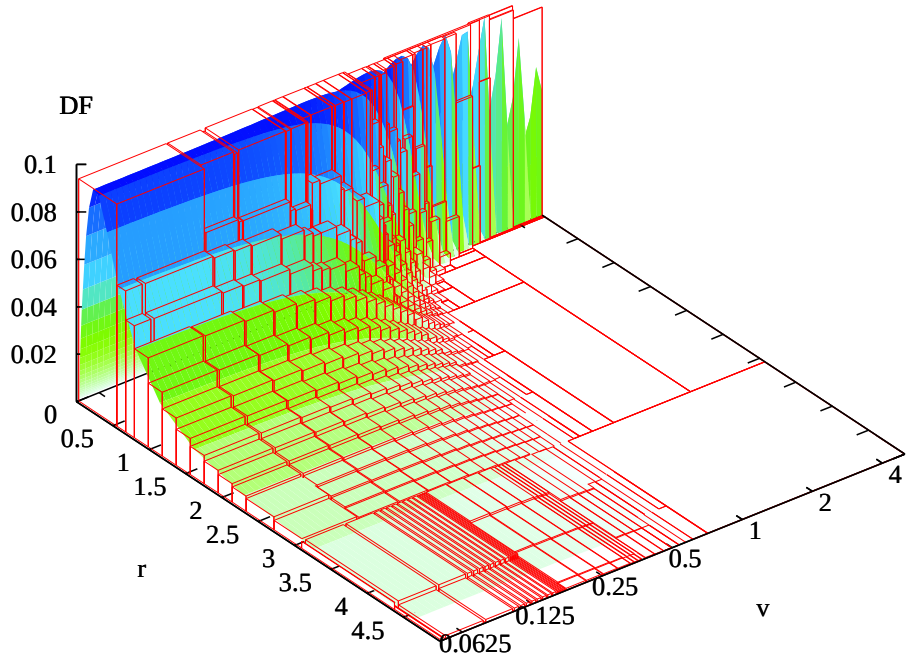

Figure 8.1 Visualization of an isotropic Hernquist system with $\mu = 0.1$ and our approximation with cells. After 8 subdivisions 991 cells were constructed, with a total phase-space volume of $V_8 = 1.533$, while the real total stellar DF volume is 1. Thus, the ratio of rejected to accepted particles is 0.533 and on average $\sim 35\%$ of all randomly chosen test particles in the cell volume will be rejected, resulting in a highly efficient Monte Carlo simulation.

efficiently as possible into 8 new cells, adding up to a new total volume

$$V_2 = \sum_{i=1}^{8} V_{2;i} = \sum_{i=1}^{8} \frac{8\pi^2}{3}(r_{\mathrm{b};i}^3 - r_{\mathrm{a};i}^3)(v_{r,\mathrm{b};i} - v_{r,\mathrm{a};i})(v_{T,\mathrm{b};i}^2 - v_{T,\mathrm{a};i}^2) f_{\mathrm{b};i}, \tag{8.12}$$

which is a better approximation to the real DF volume. Here, for a cell i we denoted $V_{2;i}$ its volume, $(r_{\mathrm{a};i}, v_{r,\mathrm{a};i}, v_{T,\mathrm{a};i})$ and $(r_{\mathrm{b};i}, v_{r,\mathrm{b};i}, v_{T,\mathrm{b};i})$ its lower and upper bounds in the abscissae, and $f_{\mathrm{b};i}$ its maximum DF value.

Next, each cell in our grid is examined according to the procedure above and split if it leads to a significant decrease in the total volume. Thus, after the examination of every cell, a new volume V_3 is obtained. This loop is repeated until after M steps the phase-space volume V_M has converged sufficiently close to the real volume. Typically, in our simulations, the cells cover a volume that is a factor 1.5 to 5 larger than the model's

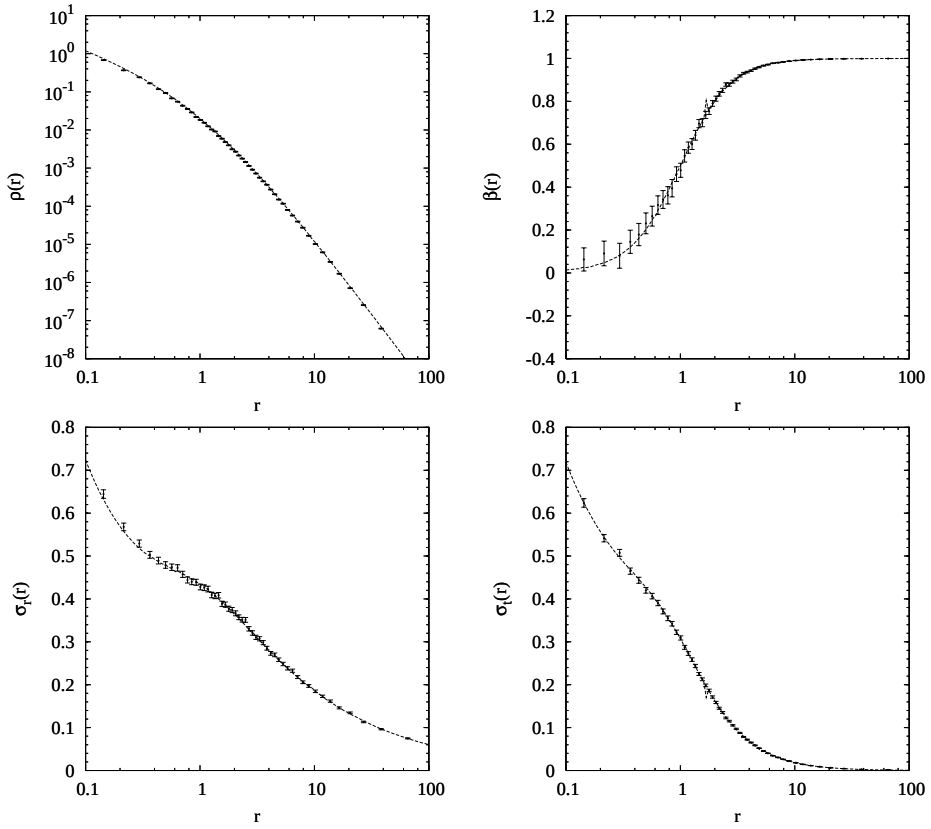

Figure 8.2 The relevant profiles $\rho(r)$, $\sigma_r(r)$, $\sigma_T(r)$ and $\beta(r)$ of the outcome of a simulation of a Hernquist system with $\mu = 0.1$ and $r_{\rm a} = 1$. The continuous lines denote the theoretical model, the discrete data represent 10^5 simulated particles, binned and with error bars.

actual phase-space volume; a further refinement is unnecessary, since constructing more cells would be more time-consuming than actually generating our desired number (10^5) of particles (see below). If the grid is successfully constructed, $F(r, v_r, v_T)$ is entirely enveloped by a set of 4-dimensional grid cells.

Now we can proceed to a classical acceptance-rejection Monte Carlo (MC) simulation (in the remainder, we refer to setting up the initial conditions of a DF as a "MC simulation"). To generate a data point n, first a value V_n is randomly chosen between 0 and V_M. We can associate this value with a unique cell j and an ordinate f_n for which

$$\sum_{i=1}^{j-1} V_{M;i} < V_n \leqslant \sum_{i=1}^{j} V_{M;i}, \tag{8.13}$$

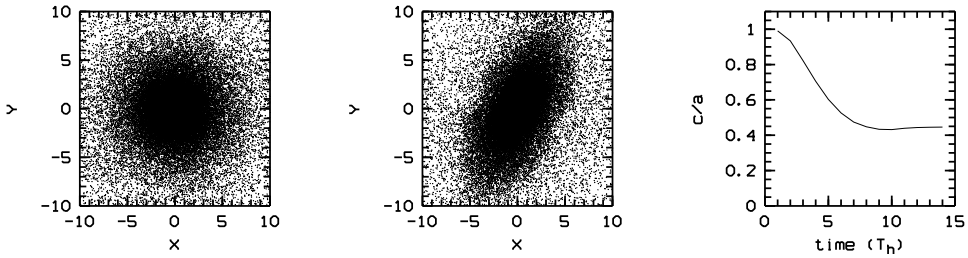

Figure 8.3 (a) The initial particle positions of a Hernquist model with an increasing anisotropy with $\beta = 0.5$ and $\lambda = 5$. 80% of the total mass is shown in the figure. (b) The density distribution after 10 half-mass dynamical times. A bar is clearly visible. (c) The axis ratio c/a plotted as a function of time. As can be seen from both the density distributions and the axis ratio, an elliptical bar is created indicating that the system is unstable.

and

$$V_n = \sum_{i=1}^{j-1} V_{M;i} + \frac{8\pi^2}{3}(r_{\mathrm{b};j}^3 - r_{\mathrm{a};j}^3)(v_{r,\mathrm{b};j} - v_{r,\mathrm{a};j})(v_{T,\mathrm{b};j}^2 - v_{T,\mathrm{a};j}^2) f_n. \tag{8.14}$$

Then, in cell j the coordinates $r_{\mathrm{a};j}^3 \leqslant r_n^3 \leqslant r_{\mathrm{b};j}^3$, $v_{r,\mathrm{a};j} \leqslant v_{r,n} \leqslant v_{r,\mathrm{b};j}$ and $v_{T,\mathrm{a};j}^2 \leqslant v_{t,n}^2 \leqslant v_{T,\mathrm{b};j}^2$ are randomly generated. Thus, a point $(r_n, v_{r,n}, v_{T,n}, f_n)$ is uniformly chosen in the 7-dimensional phase-space volume V_M. Now, if $f_n \leqslant F(r_n, v_{r,n}, v_{T,n})$, the coordinate $(r_n, v_{r,n}, v_{T,n})$ is accepted as a valid data point, otherwise it is rejected. Furthermore, if $f_{\mathrm{b};j} < F(r_n, v_{r,n}, v_{T,n})$, the cell volume is accordingly increased to the new maximum, so the grid keeps being improved.

In this manner we construct a data set of N accepted coordinates inside the chosen radius r_{b} which follow the distribution. The MC simulation is regarded successful if the cell volumes have changed negligibly (if the relative change of the total volume is smaller than 10^{-3}) during the MC simulation. If not, a new MC simulation with the final grid (with volume V_{M+N}) is necessary. Also, if the ratio between rejected and accepted points is very large, causing the MC simulation to be slow, the grid might have to be refined further (as aforementioned, we stop refining the grid once the cells cover a volume that is a factor 1.5 to 5 larger than the model's actual phase-space volume).

Finally, every coordinate $(r_n, v_{r,n}, v_{T,n})$ has to be converted into a phase-space point $(x_n, y_n, z_n, v_{x,n}, v_{y,n}, v_{z,n})$. This is done by uniformly simulating the surface of a sphere with radius r_n (creating (x_n, y_n, z_n)), a circle with radius $v_{T,n}$ (creating $(v_{\theta,n}, v_{\varphi,n})$) and the sign of $v_{r,n}$. The velocities can then be transformed into the appropriate Cartesian coordinates. For isotropic functions $F(E)$ the grid abscissae simplify to the 2-dimensional (r, v) space, and the entire procedure is analogous.

Our method has several advantages: the construction of a grid and the subsequent MC simulation of points is straightforward, fast, accurate and generally applicable. This con-

trasts with algorithms that require integrations and inversions of DFs, which can experience numerical problems when applied to intricate functions. Also, no intermediate steps are required (e.g. simulating the density first before assigning velocities to each particle) and once a grid is made for a model, it can be re-used to generate an arbitrary number of particles. Moreover, since a peak can be adequately isolated by a cell, infinite ranges in the coordinate space or the DF values can be approximated by choosing appropriate large boundary values.

As an example, we show in Fig. 8.1 the constructed cells for an isotropic Hernquist system with a central SBH of $\mu = 0.1$ (see Section 8.4). A simulated data sample (10^5 accepted particles) for an anisotropic Hernquist system with a central SBH of $\mu = 0.1$ and an anisotropy radius of $r_a = 1$ is shown in Fig. 8.2. In all our MC simulations, we truncate the infinite boundary radius at $r_{\rm b} = 2000$. For the DFs with an infinite maximum, we set $f_{\rm b} = 10^{15}$, and for the SBH-models we set the maximum velocity at the arbitrarily large value $v_{\rm b} = 10^{15}$ (these values are in fact much larger than needed. In reality, no particle is ever assigned such a high DF value or initial velocity and never reaches such high velocities during the subsequent N-body simulations). For another application of our code, see Cloet-Osselaer et al. (2012).

8.2.3 N-body code

We studied the stability of our models by using an N-body code that is based on the "self-consistent field" method (Hernquist & Ostriker 1992). This method relies on the series expansion in a bi-orthogonal spherical basis set for both the density and gravitational potential

$$\rho(r,\theta,\phi) = \sum_{nlm} A_{nlm}\ \rho_{nlm}(r,\theta,\phi) = \sum_{nlm} A_{nlm}\ \tilde{\rho}_{nl}(r)\ Y_{lm}(\theta,\phi), \tag{8.15}$$

$$\mathbf{\Phi}(r,\theta,\phi) = \sum_{nlm} A_{nlm}\ \mathbf{\Phi}_{nlm}(r,\theta,\phi) = \sum_{nlm} A_{nlm}\ \tilde{\mathbf{\Phi}}_{nl}(r)\ Y_{lm}(\theta,\phi), \tag{8.16}$$

where $Y_{lm}(\theta,\phi)$ are the spherical harmonics. Some freedom is considered for this expansion since ($\tilde{\rho}_{nl}(r)$,$\tilde{\mathbf{\Phi}}_{nl}(r)$) can have different forms (e.g. Plummer model, Bessel functions, spherical harmonic functions), however here we will use a form similar to the Hernquist model due to its trivial connection with our anisotropic systems that we wish to examine:

$$\tilde{\rho}_{nl}(r) = \frac{K_{nl}}{\sqrt{\pi}} \frac{r^l}{r(1+r)^{2l+3}} C_n^{(2l+3/2)}(\xi), \tag{8.17}$$

$$\tilde{\mathbf{\Phi}}_{nl}(r) = -2\sqrt{\pi} \frac{r^l}{(1+r)^{2l+1}} C_n^{(2l+3/2)}(\xi), \tag{8.18}$$

where K_{nl} is a normalization constant, $\xi = (r-1)/(r+1)$ and $C_n^{(2l+3/2)}(\xi)$ are Gegenbauer polynomials (e.g. Szegö 1939, Sommerfeld 1964). The coefficients A_{nlm}, can be calculated by means of all the particles that describe the DF of our system (see Hernquist

& Ostriker 1992 for more details). The spherical accelerations for each particle are found by taking the gradient of the potential (Eq. 8.16). Finally new positions and velocities are derived with the use of an integrator which is equivalent to the standard time-centred leapfrog (Allen & Tildesley 1992; Hut et al. 1995),

$$x_{i+1} = x_i + \Delta t v_i + \frac{1}{2}\Delta t^2 a_i, \tag{8.19}$$

$$v_{i+1} = v_i + \frac{1}{2}\Delta t(a_i + a_{i+1}). \tag{8.20}$$

The indices n, (l, $m = -l..l$) are indirectly an indication for the accuracy of the simulation for respectively radial and tangential motion, since they determine the number of terms in the expansion (see Section 5.2 in Hernquist & Ostriker 1992 for a statistical analysis). For the systems without the SBH we find that $n_{\rm max} = 4$ and $l_{\rm max} = 2$ assures a total energy conservation of better than $\sim 10^{-6}$ over 50 half-mass dynamical times T_h and still allows a low CPU time per N-body time-step (the time between two successive calculations) of $\Delta t = T_h/416 \approx 0.02$. For the systems with an SBH, we used $n_{\rm max} = 6$, $l_{\rm max} = 2$ when $\mu \leqslant 0.05$, and $n_{\rm max} = 8$, $l_{\rm max} = 4$ for larger values of μ. The gravitational effect of the SBH is added analytically by an extra radial acceleration proportional to the mass of the SBH. To avoid numerical divergences when particles pass close to the SBH, we included a softening length $\varepsilon = 0.05$. At this radius the dynamical crossing time of a particle is $T_h = 0.37$, and in consequence the chosen time-step of 0.02 assured a energy conservation better than 1% over 50 half-mass dynamical times.

In order to check the robustness of our results, we performed two kinds of tests. We *(i)* re-ran a number of simulations with different, smaller time-steps, and *(ii)* we performed simulations with higher $n_{\rm max}$ and $l_{\rm max}$ values. A detailed comparison of these extra runs with the original simulations shows that our results and conclusions do not change: the variation of the global instability indicators, such as axis ratios or $2K_r/K_T$, as a function of time are essentially the same. In a later follow-up study, we also re-ran the simulations with a multi-step version of the N-body code and more particles. Again, the results were similar, although we required more than 50 half-mass dynamical times to obtain the same outcome.

8.2.4 Quantifying the instabilities

When a system is unstable, it tends to create a bar feature at its centre (see Fig. 8.3) which roughly has an ellipsoidal shape. As noted by other authors (Merritt 1987; Palmer & Papaloizou 1987), the physical cause of instability is similar to that of the formation of a bar in a disc (Lynden-Bell 1979), where a small perturbation changes the orbits with a lower angular momentum (initially precessing ellipses) into boxes which are aligned along the initiated bar. A particle in a box orbit is unable to precess all the way round and will fall each time back to the bar. This effect will cause the bar to increase in both size and strength. To measure the radial stability of the systems we fitted the shape of an ellipsoidal mass distribution by means of an iterative procedure (Dubinski & Carlberg 1991; Katz

1991; Meza & Zamorano 1997; Meza 2002) at every half-mass dynamical time. This detected any bar feature that is located within a certain radius. The initial condition of this method is

$$\rho = \rho(a) \text{ with } a = \left(x^2 + \frac{y^2}{q^2} + \frac{z^2}{s^2} \right)^{1/2}, \tag{8.21}$$

and with $M_{ij} = \sum \frac{x_i x_j}{a^2}$, the principal components of the inertia tensor $M_{zz} \leq M_{yy} \leq M_{xx}$ and the axis ratios q and s equal to 1, assuming a spherical mass distribution within a certain sphere with a given radius for which we chose $r_{\rm a} = 5$. For all considered models this radius encloses approximately 70% of the total mass. To achieve these conditions a transition to the centre of mass has to be made followed by swapping the coordinate axes into the correct order. In the next step the eigenvalues and eigenvectors of the inertia tensor I_{ij} are calculated, transforming it into a diagonal matrix. At this point the new axis ratios can be calculated

$$q = \left(\frac{M_{yy}}{M_{xx}} \right)^{1/2} = \frac{b}{a} \text{ and } s = \left(\frac{M_{zz}}{M_{xx}} \right)^{1/2} = \frac{c}{a}, \tag{8.22}$$

which in turn are used as the conditions for the next iteration step. The iteration was stopped as soon as both axis ratios converged to a value within a pre-established tolerance of 10^{-3}. Thus at each half-mass dynamical time the values of these axis ratios serve as measures of the strength of the bar instability, if present. In particular we will focus our attention on two values of c/a, namely at the moment when these ratios reach a minimum (i.e. when the instability is strongest) and at the final time $t = 50 T_h$.

8.3 Hernquist models without a black hole

In this section we investigate the stability of two different families of anisotropic Hernquist models without a central supermassive black hole. For the analytical construction of these models we refer to Baes & Dejonghe (2002), however we will recapitulate the characteristics of each family.

8.3.1 Family I: Decreasing anisotropy

We find Hernquist models with a decreasing anisotropy by assuming an augmented density of the form

$$\tilde{\rho}(\psi, r) = \frac{1}{2\pi} \frac{\psi^{4-2\beta_n}}{(1-\psi)^{1-2\beta_0}} \frac{(1+r)^{2(\beta_0-\beta_n)}}{r^{2\beta_0}}, \tag{8.23}$$

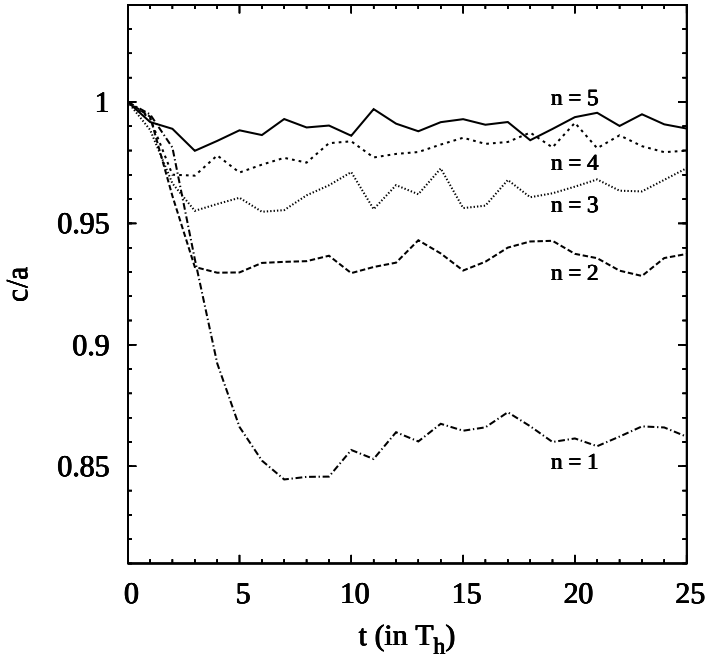

Figure 8.4 Axis ratios as a function of time of the anisotropic systems with a decreasing anisotropy.

with $\beta_n = \beta_0 - \frac{n}{2}$ and n a natural number. After some algebra we find the distribution function

$$\begin{aligned} F(E,L) = & \frac{2^{\beta_0}}{(2\pi)^{5/2}}\Gamma(5-2\beta_n)L^{-2\beta_0}E^{5/2-2\beta_n+\beta_0} \\ & \times \sum_{k=0}^{n}\binom{n}{k}\frac{1}{\Gamma(\frac{2+k}{2}-\beta_0)\Gamma(\frac{7-k}{2}-2\beta_n+\beta_0)}\left(\frac{L}{\sqrt{2E}}\right)^k \\ & \times {}_2F_1\left(5-2\beta_n, 1-2\beta_0; \frac{7-k}{2}-2\beta_n+\beta_0; E\right), \end{aligned} \tag{8.24}$$

with ${}_2F_1$ a hypergeometric function, and the anisotropy

$$\beta(r) = 1 - \frac{\sigma_\theta^2(r)}{\sigma_r^2(r)} = \frac{\beta_0 + \beta_n r}{1+r}, \tag{8.25}$$

which decreases as a function of radius. Since for $\beta_0 \leqslant 0$ we only find tangentially dominated systems which are free of radial instabilities, we limit ourselves to the investigation of

the case $\beta_0 = 0.5$. For this value, $n = 0$ corresponds to a system with constant anisotropy. We plotted the axis ratios c/a for a number of different models with different n in Fig. 8.4. Here and in the remainder of the chapter, we define those models that keep the axis ratio $c/a \gtrsim 0.95$ over 50 dynamical times as being stable. The only model that does not satisfy this criterion is that with $n = 1$, which is everywhere radially anisotropic. For $n \geq 2$, the models become tangentially anisotropic at larger radii and as a consequence are much more stable. This is evident from Fig. 8.4. It is clear that the minimum of c/a is reached rapidly, whereafter the systems are in an equilibrium state, but are slightly non-spherical.

8.3.2 Family II: Increasing anisotropy

The models of our second family are Cuddeford (1991) models (see Eq. (2.168)) with an augmented density and DF of the general form

$$\tilde{\rho}(\psi, r) = r^{-2\beta_0} f(\psi) \left(1 + \lambda r^2\right)^{-1+\beta_0} \quad \text{with} \quad \lambda = \frac{1}{r_a^2}, \tag{8.26}$$

$$F(E, L) = F_0(Q) L^{-2\beta_0} \quad \text{with} \quad 0 \leqslant Q = E - \frac{L^2}{2r_a^2} \leqslant 1, \tag{8.27}$$

and E denotes the energy, L the angular momentum and r_a the anisotropy radius. The explicit form of $f(\psi)$ for the Hernquist potential-density pair can be found in Baes & Dejonghe (2002). As mentioned by them, the DFs can be written analytically for the half-integer values $\beta_0 = 0.5, 0, -0.5, -1$, so we will limit ourselves to these cases. For every value of β_0, we also computed numerically the maximum anisotropy value $\lambda_{\max}(\beta_0)$, outside which the DFs become negative for some values of Q and L. The area of physical systems is indicated in Fig. 8.5. Our models have the following functional form:

- $\beta_0 = 0.5$:

$$F(E, L) = \frac{Q}{4\pi^3 L} \frac{3Q^2 + \lambda(3Q^2 - 5Q + 2)}{\sqrt{Q^2 + \lambda(1-Q)^2}}. \tag{8.28}$$

- $\beta_0 = 0$:

$$F(E, L) = \frac{1}{8\sqrt{2}\pi^3} \left[\frac{3 \arcsin\sqrt{Q}}{(1-Q)^{5/2}} + \sqrt{Q}(1-2Q) \left(\frac{8Q^2 - 8Q - 3}{(1-Q)^2} + 8\lambda \right) \right]. \tag{8.29}$$

- $\beta_0 = -0.5$:

$$F(E, L) = \frac{L f(Q)}{2\pi^3 (1-Q)^4 \sqrt{Q^2 + \lambda(1-Q)^2}}, \tag{8.30}$$

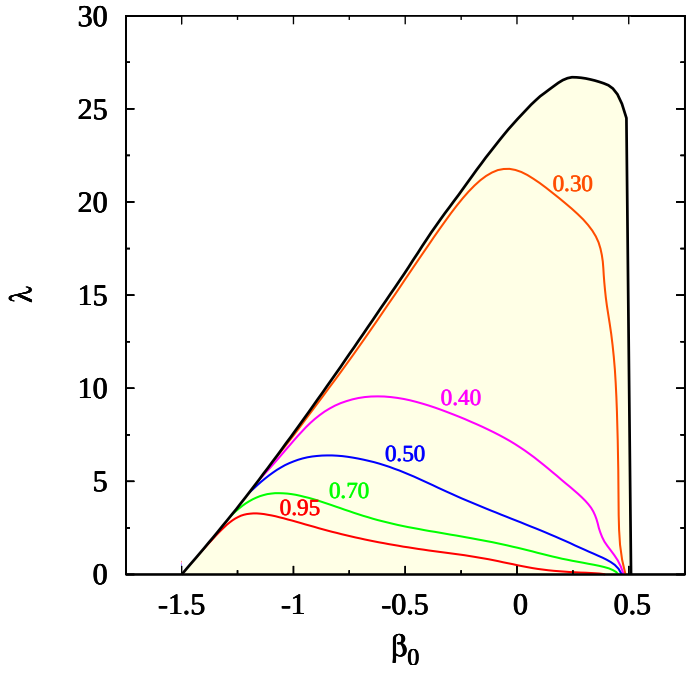

Figure 8.5 The stability of the Hernquist models without a black hole and with increasing anisotropy (see Section 8.3.2), expressed as the minima of the axis ratios c/a during the simulations. The shaded area indicates the region of physical systems, i.e. with a non-negative distribution function.

with

$$\begin{aligned} f(Q) = {} & 6(1+\lambda)^2Q^6 - 2(16\lambda^2+26\lambda+10)Q^5 \\ & + (70\lambda^2+87\lambda+20)Q^4 - 2\lambda(40\lambda+33)Q^3 \\ & + \lambda(50\lambda+19)Q^2 - 16\lambda^2Q + 2\lambda^2. \end{aligned} \tag{8.31}$$

- $\beta_0 = -1$:

$$F(E,L) = \frac{L^2}{256\sqrt{2}\pi^3(1-Q)^5}\times \tag{8.32}$$

$$\left[\frac{f_1(Q)}{\sqrt{1-Q}}\arctan\left(\frac{\sqrt{Q}}{\sqrt{1-Q}}\right) + \frac{f_2(Q)}{\sqrt{Q}}\right], \tag{8.33}$$

with

$$f_1(Q) = 15\left[(16\lambda+120)Q^2-(72+32\lambda)Q+15+16\lambda\right], \tag{8.34}$$

$$\begin{aligned} f_2(Q) = {} & 384(1+\lambda)^2Q^6 \\ & -(1984\lambda^2+3712\lambda+1728)Q^5 \\ & +(4160\lambda^2+7008\lambda+2784)Q^4 \\ & -(4480\lambda^2+6192\lambda+1200)Q^3 \\ & +(2560\lambda^2+2368\lambda+930)Q^2 \\ & -(704\lambda^2+240\lambda+225)Q+64\lambda^2. \end{aligned} \tag{8.35}$$

For all models the anisotropy is given by the simple formula

$$\beta(r) = \frac{\beta_0 r_\mathrm{a}^2 + r^2}{r_\mathrm{a}^2 + r^2}, \tag{8.36}$$

showing an increase in anisotropy as a function of radius. The results of the N-body investigation for all β_0 and λ are summarized in Fig. 8.5, where we plotted the minimal axis ratios c/a for the DFs in this parameter space. To derive this plot, we simulated systems with $\beta_0 = 0.5, 0, -0.5, -1$ and $\lambda = 1, 2, 4, 6, 10, 16, 24$, all of which are physical. The case where $\beta_0 = 0$ corresponds to the traditional anisotropic Osipkov-Merritt Hernquist model that has been previously investigated in a similar way by Meza & Zamorano (1997). These authors state the system with $r_\mathrm{a} \approx 1.1$ (or $\lambda \approx 0.82$) as stable. To compare our study with theirs, we simulated this model in addition to the other systems. For this model we find an axis ratio $c/a \approx 0.95$ after 50 dynamical times, and $2K_r/K_T \approx 2.24$ during the entire run. These values are in agreement with their results, therefore we will define $c/a = 0.95$ as our stability criterion.

As is to be expected, the anisotropy radius λ strongly affects the formation of radial-orbit instabilities, so that only models with a low value of λ remain stable. Furthermore, we note that all models remain in their new equilibrium state after $t \approx 10T_h$, as in case of the DFs of Family I. As an example, the c/a ratio evolution for one of the systems is given in Fig. 8.3.

8.4 Hernquist models with a supermassive black hole

The now established presence of diverse components in a great variety of galaxies calls for more advanced dynamical models. In this respect a dark matter halo and a central

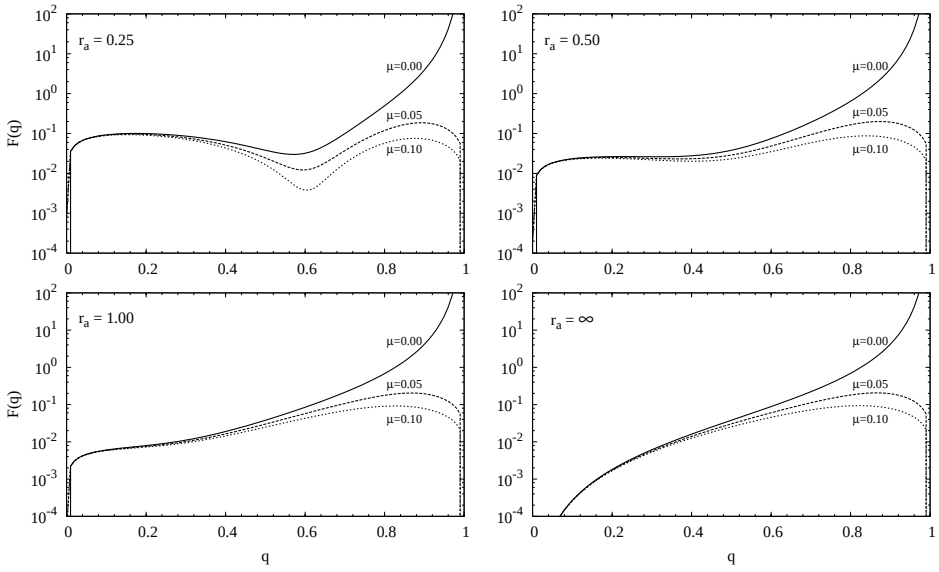

Figure 8.6 The distribution functions defined by Ciotti (1996), with different anisotropy radii r_a and SBH mass μ. The value $r_\mathrm{a} = \infty$ corresponds with the isotropic case; for $\mu = 0$ the DFs reduce to Eq. (8.29).

supermassive black hole are important and can change the galaxy's properties dramatically. However, up to now there are few known analytical systems that include e.g. a supermassive black hole. The only models known so far are presented in Ciotti (1996), Baes & Dejonghe (2004) and Baes et al. (2005), which are all based on the γ-models with special attention to the Hernquist model and in Stiavelli (1998) where the distribution function of a stellar system around an SBH is derived from statistical mechanic considerations.

In this section we investigate the radial stability of both isotropic and anisotropic Hernquist models containing a supermassive black hole, as these represent the closest analytical approach to the observations. For the following sections we will use the representation of Ciotti (1996); again, we are not going into great detail in the derivation of the analytical distribution function.

In essence the DFs are obtained from an analytical Osipkov-Merritt inversion of the systems governed by Eq. (8.2) and (8.3). As a consequence, these models can be viewed as a extension of Eq. (8.29). Subsequently, we will refer to these combined systems as Osipkov-Merritt models. The DFs can be written as

$$F(Q) = F_i(Q) + \frac{F_a(Q)}{r_\mathrm{a}^2}, \tag{8.37}$$

where Q has the same definition as in Eq. (8.27). A more natural parameter q is defined

through

$$Q = q\left(1+\frac{\mu}{1-q}\right), \quad 0 \leqslant q \leqslant 1. \tag{8.38}$$

8.4.1 Family I: Isotropic

We find an isotropic system by letting r_a diverge to ∞. Then Eq. (8.37) simplifies to

$$F(E) = F_i(E) = \frac{1}{2\sqrt{8}\pi^3}\left(\frac{dE}{dl}\right)^{-1}\frac{d}{dl}\left[\tilde{F}_i^{\pm}(l)\right], \tag{8.39}$$

with the argument l defined as $l^2 = 1-q$. For $\tilde{F}_i^{\pm}(l)$ we refer to Ciotti (1996) as this involves combinations of elliptic and Jacobian functions. These models only differ from those of Baes et al. (2005) in the definition of the parameter μ.

Although the systems are isotropic, their DFs have a local maximum when $\mu > 0$ (as shown in Fig. 8.6). Hence, the sufficient criteria of Antonov (1962) and Doremus et al. (1973) for isotropic systems cannot be applied. However, in our subsequent analysis of the systems with and without an SBH in Section 8.5, it will be shown that all models with $r_\mathrm{a} > 1$ are stable. In other words, it becomes evident that the addition of a central SBH, although it changes the dynamics dramatically, does not influence the stability of an isotropic system.

8.4.2 Family II: Anisotropic

In a similar way as the isotropic case the distribution function can be written as

$$F(Q) = F_i(Q) + \frac{F_a(Q)}{r_\mathrm{a}^2}, \tag{8.40}$$

$$= \frac{1}{2\sqrt{8}\pi^3}\left(\frac{dQ}{dl}\right)^{-1}\frac{d}{dl}\left[\tilde{F}_i^{\pm}(l) + \frac{\tilde{F}_a^{\pm}(l)}{r_\mathrm{a}^2}\right], \tag{8.41}$$

where again $\tilde{F}_a^{\pm}(l)$ is defined in Ciotti (1996). In Fig. 8.6 we display systems with several values of μ and r_a. Notice that for small values of r_a the DFs have a local minimum. As a consequence, for every μ there exists a smallest possible r_a, where this minimum becomes zero; smaller values of this boundary r_a result in negative DFs, thus creating unphysical systems. For $\mu = 0$, the minimal anisotropy radius is $r_\mathrm{a} \approx 0.202$; for $\mu = 0.1$ the boundary becomes $r_\mathrm{a} \approx 0.240$. From the viewpoint of a stability analysis these systems are the most interesting. In the following section we will discuss their evolution in detail, comparing them with the models without an SBH (Eq. (8.29)).

8.5 Stability analysis of the Osipkov-Merritt models

To investigate any trend about the radial stability of these systems, we investigate the 2-parameter space ($r_{\rm a}$,μ). In total, we performed 25 simulations, with $r_a = 0.25$, 0.50, 0.70, 0.85, 1.00 and $\mu = 0.01$, 0.03, 0.05, 0.07, 0.10. In this way we derived a grid of values of the c/a axis ratios, shown in Fig. 8.7. As stated before, the $\mu = 0$-axis corresponds to the systems in (Eq. 8.29). The solid lines indicate the minimal values reached during the simulation (i.e. when the instability is strongest). The rate at which these minima are reached strongly depends on $r_{\rm a}$, ranging from a few half-mass dynamical times for highly radial models to $t \approx 50T_h$ for systems with $r_{\rm a} = 1.00$. After the point of time upon which a system obtains its minimal c/a the influence of the SBH causes a diminution of the bar instability, resulting in the c/a axis ratios at $t = 50T_h$ shown by the dashed lines. Thus, in each system the particles are affected by two counteracting forces: the (relatively fast) bar formation and the (more gradually) scattering near the centre due to the spherically symmetric gravitational potential of the black hole. The contour line $c/a = 0.95$ is highlighted as our stability criterion.

Clearly, an SBH mass of a few percent can prevent or reduce the bar instabilities in anisotropic systems. This result agrees well with similar studies in disk galaxies (Norman et al. 1996 ; Shen & Sellwood 2004 ; Athanassoula et al. 2005 ; Hozumi & Hernquist 2005). The effect is most clearly visible for models with strong radial anisotropies, where the decrease of the bar strength is proportional to the SBH mass. In other words, while more radially anisotropic systems develop stronger bars than more isotropic models, the bars of the former are more easily affected by a supermassive black hole. This is to be expected, since radial systems host more eccentric orbits, therefore more particles from the outer regions pass near the centre where their orbits can be altered by the Kepler force of the SBH.

A full dynamical analysis would require a detailed study of the orbital distribution of the stellar mass. However, we can gain important insights into the evolution of the models by visualizing their density and velocity dispersions in the principal planes of the bars. In order to retain a notion of 'radial' and 'tangential' motion in an evolved system (resembling a triaxial model) at a certain time t, we use the method described in Section 8.2.4 to approximate the mass distribution inside the radius r_i of each particle by an ellipsoid. Then, the velocity of a particle can be written into two components perpendicular resp. parallel to its surface $v_i = v_{i,\perp} + v_{i,\parallel}$. Subsequently, the perpendicular and parallel velocity dispersion

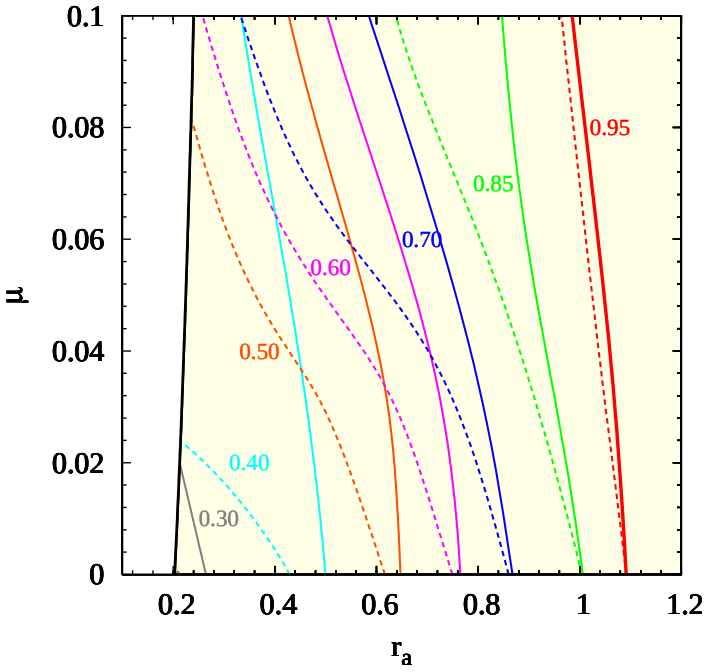

Figure 8.7 Contour plot of the axis ratio c/a for the Osipkov-Merritt models as a function of anisotropy radius and mass of the SBH. The shaded area indicates the region of physical systems, i.e. with a non-negative distribution function. The solid lines indicate the minimal values during the simulation, the dashed lines show the axis ratios at the end of the simulation (at $t = 50T_h$).

of the m nearest neighbours around a position $\boldsymbol{r}$ are

$$\sigma_\perp^2(\boldsymbol{r}) = \frac{1}{m-1}\sum_{i=1}^{m}\left(v_{i,\perp} - \bar{v}_\perp\right)^2, \tag{8.42}$$

$$\sigma_\parallel^2(\boldsymbol{r}) = \frac{1}{2(m-1)}\sum_{i=1}^{m}\left(v_{i,\parallel} - \bar{v}_\parallel\right)^2. \tag{8.43}$$

In a similar manner we define

$$K_\perp = \frac{1}{N}\sum_{i=1}^{N} v_{i,\perp}^2, \tag{8.44}$$

$$K_\parallel = \frac{1}{N}\sum_{i=1}^{N} v_{i,\parallel}^2, \tag{8.45}$$

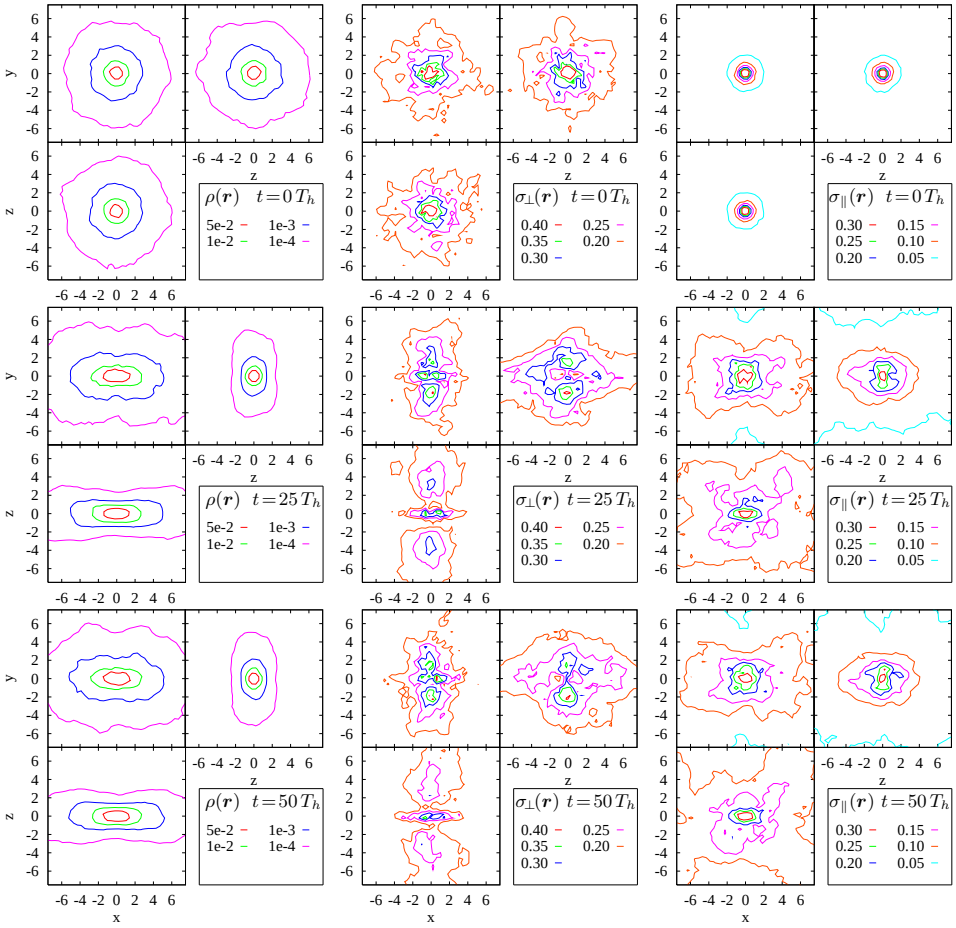

Figure 8.8 The spatial density ρ and the velocity dispersions $\sigma_\perp$ and $\sigma_\parallel$, in the three principal planes, of an Osipkov-Merritt Hernquist system without an SBH, and with $r_\mathrm{a} = 0.25$. Dynamical times $t = 0$, $t = 25T_h$ and $t = 50T_h$ are displayed.

so that $2K_\perp/K_\parallel$ can serve as a non-spherical extension of $2K_r/K_T$.

In Figs. 8.8-8.11 we show the evolution of 4 systems by means of the density $\rho(\boldsymbol{r})$ and velocity dispersions $\sigma_\perp(\boldsymbol{r})$ and $\sigma_\parallel(\boldsymbol{r})$, in at dynamical times $t = 0,\ t = 25T_h$ and $t = 50T_h$. In each principal plane the moments are calculated on a grid of 2500 points, with 50 nearest neighbours around every grid position.

Fig. 8.8 displays an Osipkov-Merritt system without an SBH and anisotropy radius $r_\mathrm{a} = 0.25$. This model has a strong bar formation, resulting into a new equilibrium state after $t = 10T_h$ which it retains during the rest of the run (as can be seen at $t = 25T_h$ and

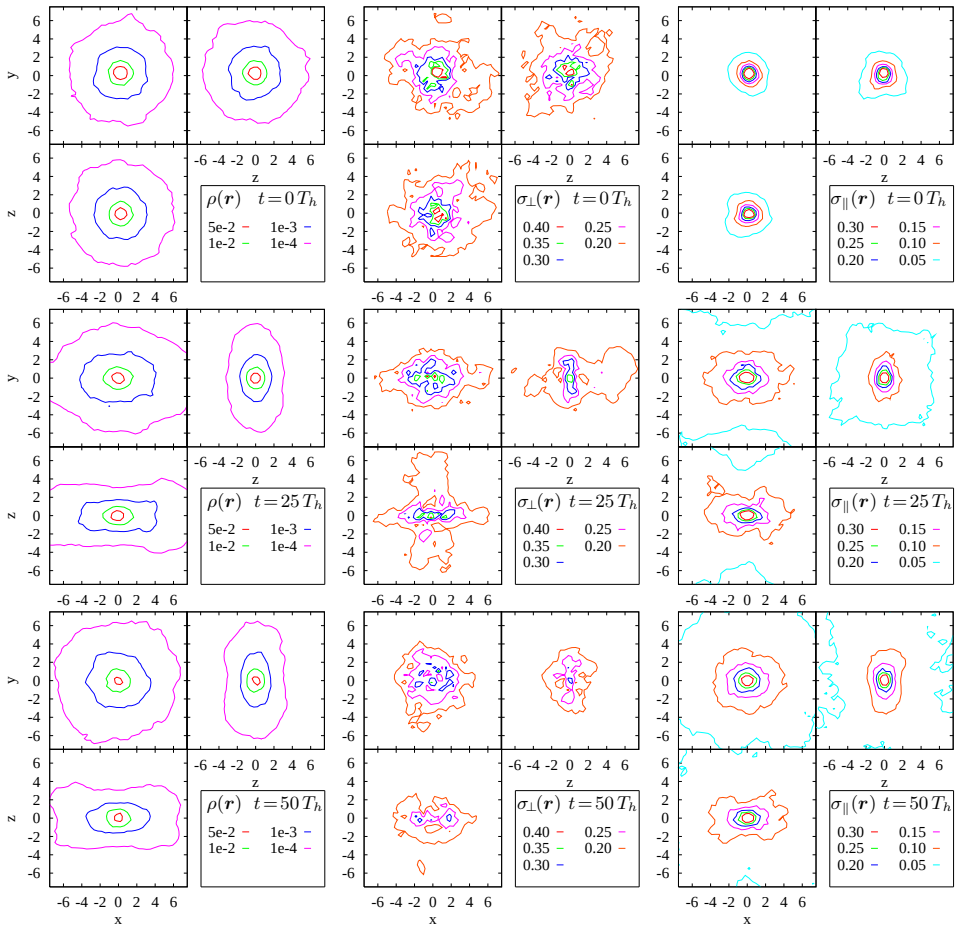

Figure 8.9 The spatial density ρ and the velocity dispersions $\sigma_\perp$ and $\sigma_\parallel$, in the three principal planes, of an Osipkov-Merritt Hernquist system with an SBH of $\mu = 0.05$, and with $r_\mathrm{a} = 0.25$. Dynamical times $t = 0$, $t = 25T_h$ and $t = 50T_h$ are displayed.

$t = 50T_h$). This bar alters the density distribution into a roughly triaxial symmetry, even peanut-shaped in the XZ-plane where the radial instability is the most prominent. The tangential dispersion $\sigma_\parallel$ increases significantly. This occurs especially at the edges, where in contrast the radial dispersion vanishes. This can be explained by the mechanism of the bar formation: particles that pass through the bar are pulled towards it, and eventually align their orbit with the bar. Only the orbits along the principal axes remain largely unaffected by the bar due to the symmetric forces on these particles, hence their motion remains radial.

In Fig. 8.9 a model with $r_\mathrm{a} = 0.25$ and $\mu = 0.05$ is shown. Again a bar is formed, but

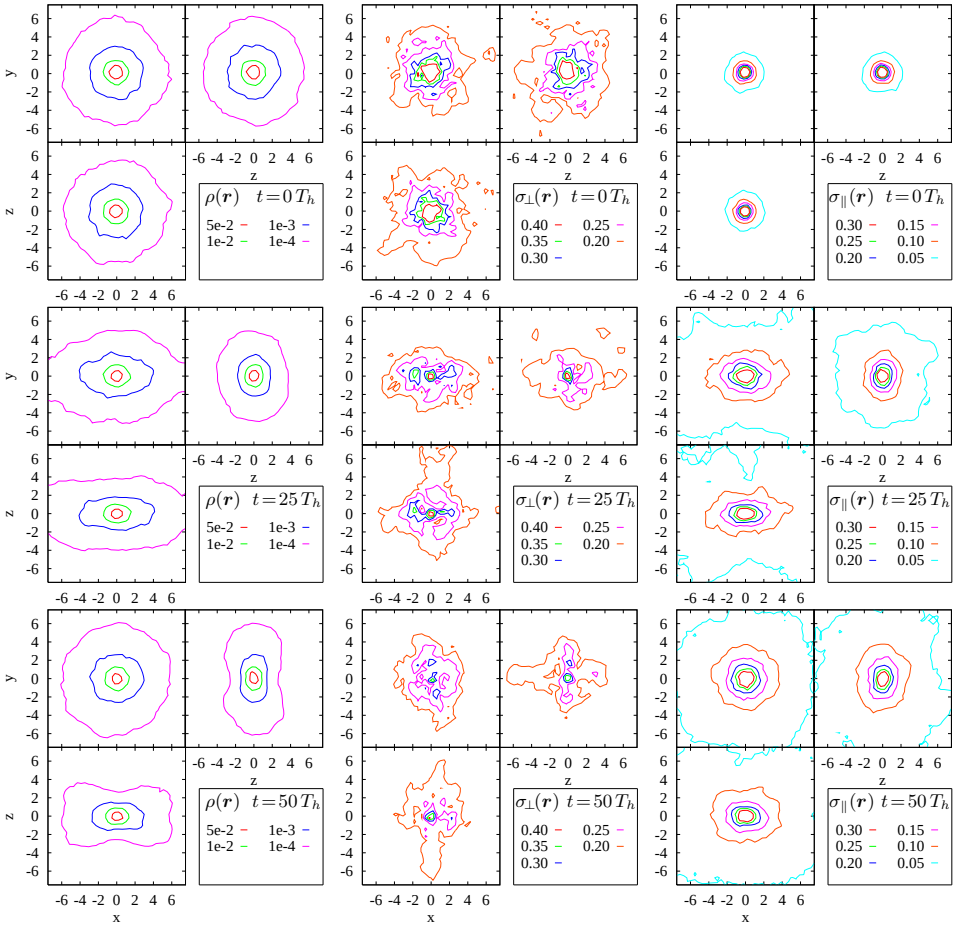

Figure 8.10 The spatial density ρ and the velocity dispersions $\sigma_\perp$ and $\sigma_\parallel$, in the three principal planes, of an Osipkov-Merritt Hernquist system with an SBH of $\mu = 0.1$, and with $r_\mathrm{a} = 0.25$. Dynamical times $t = 0$, $t = 25T_h$ and $t = 50T_h$ are displayed.

less pronounced than in the absence of an SBH. Clearly, during the run the bar is reduced by the SBH, causing a gradual increase in the c/a axis ratio (XZ-plane). More striking however is the evolution in the XY-plane, where the ellipticity has disappeared. Thus, the model has become an oblate axisymmetric system. This is also reflected in the dispersions: $\sigma_\parallel$ again follows the bar structure, but the cross-form $\sigma_\perp$ vanishes as particles pass near the SBH. Since most particles reside in the XY-plane, on eccentric orbits (since r_a is small), the scattering in this plane is strongest. After $t = 50T_h$, we expect a further small increase in the c/a axis ratio, but as the velocity dispersion becomes more isotropic fewer particles

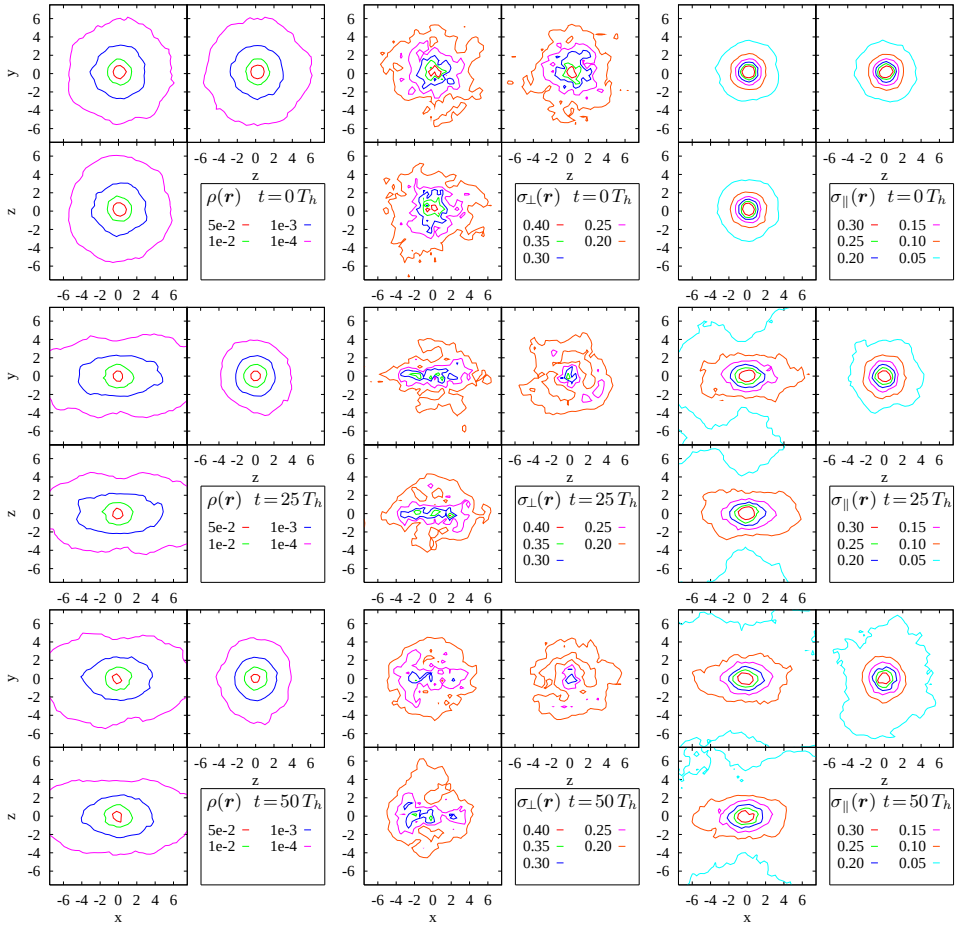

Figure 8.11 The spatial density ρ and the velocity dispersions $\sigma_\perp$ and $\sigma_\parallel$, in the three principal planes, of an Osipkov-Merritt Hernquist system with an SBH of $\mu = 0.05$, and with $r_\mathrm{a} = 0.50$. Dynamical times $t = 0$, $t = 25T_h$ and $t = 50T_h$ are displayed.

from the outer regions will pass near the centre (i.e. be affected by the SBH), hence the model will not change much further.

This can also be seen by comparing the system with $\mu = 0.05$ to a model with $\mu = 0.1$ (Fig. 8.10). This model has essentially the same properties as the former. The larger SBH mass has above all influence on its efficiency, resulting in a faster bar reduction.

Finally, we consider the effect of the anisotropy radius by analysing a system with $\mu = 0.05$ and $r_\mathrm{a} = 0.5$ (Fig. 8.11). Compared to Fig. 8.9, the initial bar is less strong, as expected. However, its structure and evolution is different from the system with $r_\mathrm{a} =$

0.25. First, $\sigma_\perp$ remains spherically distributed during the run, thus less scattering occurs. This implies less reduction of the bar instability. Moreover, the density does not become symmetric around the Z-axis. In contrast, the X-axis is now the symmetry axis during the entire run, resulting in a prolate axisymmetric system. It thus seems that models with an SBH become oblate or prolate, depending on their velocity anisotropy. It would indeed be very interesting to compare the orbital structure of both these systems in full detail.

As a final remark we note that inside a radius $r_K = \sqrt{\mu}/(1-\sqrt{\mu})$ the force of the SBH is stronger than the stellar component, so that all models remain spherical inside this radius. In conclusion, systems with an SBH become axisymmetric systems with a spherically symmetric core.

8.6 Conclusions and summary

Most mass estimates of SBHs result from dynamical models of either stellar or gas kinematics. The inclusion of strong radial anisotropy is considered in these models (Binney & Mamon 1982), yet they have never been tested for radial stability. Our goal was to test the stability of systems with a central SBH and to look for any trend as a function of the mass of the SBH. We used the same method that was previously introduced by Meza & Zamorano (1997) and extended it to systems with a central SBH. We first tested the procedure on Hernquist systems (Baes & Dejonghe 2002) without an SBH and with different anisotropic behaviour. Our method appeared to be efficient in discriminating the stable from the unstable systems.

Instead of focusing on complicated numerically derived dynamical models, we opted for analytical distribution functions that take the effect of a central SBH into account, in order to be able to look for any trend. Since the isotropic Hernquist models with an SBH do not have distribution functions that are monotonically increasing functions of the binding energy (Ciotti 1996; Baes & Dejonghe 2004) and hence the sufficient criteria of Antonov (1962) and Doremus et al. (1973) for isotropic systems cannot be applied, we first investigated the radial stability of these systems. No effect was found by letting the mass of the SBH vary, giving only stable systems. However, in the case of the anisotropic systems with an SBH we did find a dependence of the stability of the system on the mass of the SBH. The more massive the SBH, the more stable a system becomes, but especially the more the instability is reduced. A trend which is most obvious in very anisotropic systems (thus with very small anisotropy radius r_a). An SBH with a mass of a few percent of the entire galaxy mass, is able to weaken the strength of the bar, which is in correspondence with similar studies in disk galaxies (Norman et al. 1996; Shen & Sellwood 2004; Athanassoula et al. 2005; Hozumi & Hernquist 2005). Judging from Fig. 8.7, the stability boundary of $c/a \gtrsim 0.95$ over 50 dynamical times, shifts from $r_\mathrm{a} \approx 1.1$ for $\mu = 0$ to $r_a \approx 1.0$ for $\mu = 0.1$. This corresponds to $2K_r/K_T = 2.2$ for $\mu = 0$ and to $2K_r/K_T = 2.0$ for $\mu = 0.1$. These values are in very good agreement with previous authors.

Remarkably, systems with an SBH but with different anisotropy radii r_a evolve differ-

ently: highly radial systems first become triaxial whereafter the SBH makes them more oblate, while less radial models tend to form first into axisymmetric prolate structures, that then become less elongated due to the influence of the SBH.

It is also interesting to note that the central density distribution of systems with an SBH remains spherically symmetric during the entire simulation out to a radius of half the effective radius. This is not the case for systems without an SBH, which become axisymmetric or triaxial, depending on $r_{\rm a}$. Interestingly, this includes the region that is considered for the $M_{\rm BH} - \sigma$ relation, which predicts such an evolutionary link between the central SBH and the spheroid where it resides. Similarly, the central anisotropy parameter decreases as a function of time at a rate proportional to the mass of the SBH, due to more tangential orbits at the centre.

Our analysis of the influence of a central SBH on the stability of a dynamical system supplements previous research that shows that both central density cusps (Sellwood & Evans 2001; Holley-Bockelmann et al. 2001) and isotropic cores (Trenti & Bertin 2006) also act as dynamical stabilizers.

BIBLIOGRAPHY AND PUBLICATIONS

Bibliography

Bibliography

[1] **H. Aceves, H. Velázquez, and F. Cruz**. *Sérsic properties of disc galaxy mergers*. MNRAS, 373: 632–642, 2006.

[2] **C. Alard**. *Dark matter haloes and self-similarity*. MNRAS, 428: 340–348, 2013.

[3] **M. P. Allen and D. J. Tildesley**. *Computer Simulation of Liquids*. Oxford Univ. Press, 408 p., 1992.

[4] **P. D. Allen, S. P. Driver, A. W. Graham, E. Cameron, J. Liske, and R. de Propris**. *The Millennium Galaxy Catalogue: bulge-disc decomposition of 10095 nearby galaxies*. MNRAS, 371: 2–18, 2006.

[5] **J. An and H. Zhao**. *Fitting functions for dark matter density profiles*. MNRAS, 428: 2805–2811, 2013.

[6] **J. An, E. Van Hese, and M. Baes**. *Phase-space consistency of stellar dynamical models determined by separable augmented densities*. MNRAS, 422: 652–664, 2012.

[7] **J. H. An**. *Constraints on Velocity Anisotropy of Spherical Systems with Separable Augmented Densities*. ApJ, 736: 151, 2011.

[8] **J. H. An and N. W. Evans**. *A Cusp Slope-Central Anisotropy Theorem*. ApJ, 642: 752–758, 2006.

[9] **Y. C. Andredakis, R. F. Peletier, and M. Balcells**. *The Shape of the Luminosity Profiles of Bulges of Spiral Galaxies*. MNRAS, 275: 874–+, 1995.

[10] **V. A. Antonov**. *Solution of the problem of stability of stellar system Emden's density law and the spherical distribution of velocities*. Vestnik Leningradskogo Universiteta, Leningrad: University, 1962.

[11] **Y. Ascasibar, G. Yepes, S. Gottlöber, and V. Müller**. *On the physical origin of dark matter density profiles*. MNRAS, 352: 1109–1120, 2004.

[12] **E. Athanassoula, J. C. Lambert, and W. Dehnen**. *Can bars be destroyed by a central mass concentration?- I. Simulations*. MNRAS, 363: 496–508, 2005.

[13] **M. Baes and H. Dejonghe**. *The Hernquist model revisited: Completely analytical anisotropic dynamical models*. A&A, 393: 485–497, 2002.

[14] **M. Baes and H. Dejonghe**. *A completely analytical family of dynamical models for spherical galaxies and bulges with a central black hole*. MNRAS, 351: 18–30, 2004.

[15] **M. Baes and G. Gentile**. *Analytical expressions for the deprojected Sérsic model*. A&A, 525: A136+, 2011.

[16] **M. Baes and E. van Hese**. *Dynamical models with a general anisotropy profile*. A&A, 471: 419–432, 2007.

[17] **M. Baes and E. van Hese**. *Analytical expressions for the deprojected Sérsic model. II. General expressions in terms of the Fox H function*. A&A, 534: A69, 2011.

[18] **M. Baes, H. Dejonghe, and S. De Rijcke**. *Kinematics of elliptical galaxies with a diffuse dust component - II. Dust effects on kinematic modelling*. MNRAS, 318: 798–808, 2000.

[19] **M. Baes, P. Buyle, G. K. T. Hau, and H. Dejonghe**. *Observational evidence for a connection between supermassive black holes and dark matter haloes*. MNRAS, 341: L44–L48, 2003.

[20] **M. Baes, H. Dejonghe, and P. Buyle**. *The dynamical structure of isotropic spherical galaxies with a central black hole*. A&A, 432: 411–422, 2005.

[21] **F. D. Barazza, C. Wolf, M. E. Gray, S. Jogee, M. Balogh, D. H. McIntosh, D. Bacon, M. Barden, E. F. Bell, A. Böhm, J. A. R. Caldwell, B. Häussler, A. Heiderman, C. Heymans, K. Jahnke, E. van Kampen, K. Lane, I. Marinova, K. Meisenheimer, C. Y. Peng, S. F. Sanchez, A. Taylor, L. Wisotzki, and X. Zheng**. *Relating basic properties of bright early-type dwarf galaxies to their location in Abell 901/902*. A&A, 508: 665–675, 2009.

[22] **J. A. Barber and H. Zhao**. *Violating the General Density-Slope Anisotropy Inequality*. ArXiv e-prints, 2014.

[23] **E. W. Barnes**. *A New Development of the Theory of the Hypergeometric Functions*. In *Proc. London Math. Soc.*, volume s2, page 141, 1908.

[24] **J. Barnes, P. Hut, and J. Goodman**. *Dynamical instabilities in spherical stellar systems*. ApJ, 300: 112–131, 1986.

[25] **O. Bendinelli, L. Ciotti, and G. Parmeggiani**. *Series inversion of Abel equation for very peaked profiles: The $R^{1/4}$-law*. A&A, 279: 668–673, 1993.

[26] **S. N. Bernstein**. *Sur les fonctions absolument monotones*. Acta Mathematica, 52: 1–66, 1928.

[27] **J. Binney**. *The phase space structure of R to the 1/4th galaxies - Are these galaxies 'isothermal' after all*. MNRAS, 200: 951–964, 1982.

[28] **J. Binney and G. A. Mamon**. *M/L and velocity anisotropy from observations of spherical galaxies, or must M87 have a massive black hole*. MNRAS, 200: 361–375, 1982.

[29] **J. Binney and S. Tremaine**. *Galactic Dynamics: Second Edition*. Princeton University Press, 2008.

[30] **M. Boylan-Kolchin, V. Springel, S. D. M. White, A. Jenkins, and G. Lemson**. *Resolving cosmic structure formation with the Millennium-II Simulation*. MNRAS, 398: 1150–1164, 2009.

[31] **J. S. Bullock, A. Dekel, T. S. Kolatt, A. V. Kravtsov, A. A. Klypin, C. Porciani, and J. R. Primack**. *A Universal Angular Momentum Profile for Galactic Halos*. ApJ, 555: 240–257, 2001.

[32] **A. Burkert**. *The Structure of Dark Matter Halos in Dwarf Galaxies*. ApJ, 447: L25+, 1995.

[33] **P. Buyle, L. Ferrarese, G. Gentile, H. Dejonghe, M. Baes, and U. Klein**. *The $v_c - \sigma_c$ relation in low-mass and low surface brightness galaxies*. MNRAS, 373: 700–704, 2006.

[34] **P. Buyle, C. Hunter, and H. Dejonghe**. *Completely analytical families of anisotropic γ-models*. MNRAS, 375: 773–792, 2007.

[35] **P. Buyle, E. Van Hese, S. De Rijcke, and H. Dejonghe**. *Radial-orbit instability of a family of anisotropic Hernquist models with and without a supermassive black hole*. MNRAS, 375: 1157–1170, 2007.

[36] **N. Caon, M. Capaccioli, and M. D'Onofrio**. *On the Shape of the Light Profiles of Early Type Galaxies*. MNRAS, 265: 1013–+, 1993.

[37] **M. Cappellari, R. C. E. van den Bosch, E. K. Verolme, R. Bacon, M. Bureau, Y. Copin, R. L. Davies, E. Emsellem, D. Krajnovic, H. Kuntschner, R. McDermid, B. W. Miller, R. F. Peletier, and P. T. de Zeeuw**. *Dynamical Modeling of SAURON Galaxies*. Coevolution of Black Holes and Galaxies, 2004.

[38] **M. Cappellari, R. Bacon, M. Bureau, M. C. Damen, R. L. Davies, P. T. de Zeeuw, E. Emsellem, J. Falcón-Barroso, D. Krajnović, H. Kuntschner, R. M. McDermid, R. F. Peletier, M. Sarzi, R. C. E. van den Bosch, and G. van de Ven**. *The SAURON project - IV. The mass-to-light ratio, the virial mass estimator and the*

Fundamental Plane of elliptical and lenticular galaxies. MNRAS, 366: 1126–1150, 2006.

[39] **V. F. Cardone**. *The lensing properties of the Sersic model*. A&A, 415: 839–848, 2004.

[40] **V. F. Cardone, E. Piedipalumbo, and C. Tortora**. *Spherical galaxy models with power-law logarithmic slope*. MNRAS, 358: 1325–1336, 2005.

[41] **R. G. Carlberg, H. K. C. Yee, E. Ellingson, S. L. Morris, R. Abraham, P. Gravel, C. J. Pritchet, T. Smecker-Hane, F. D. A. Hartwick, J. E. Hesser, J. B. Hutchings, and J. B. Oke**. *The Average Mass Profile of Galaxy Clusters.* ApJ, 485: L13–L16, 1997.

[42] **S. A. Cellone, J. C. Forte, and D. Geisler**. *A morphological and color study of Fornax low surface brightness galaxies in the Washington system.* ApJS, 93: 397–424, 1994.

[43] **J. Chanamé, J. Kleyna, and R. van der Marel**. *Constraining the Mass Profiles of Stellar Systems: Schwarzschild Modeling of Discrete Velocity Data Sets.* ApJ, 682: 841–860, 2008.

[44] **L. Ciotti**. *Stellar systems following the R exp 1/m luminosity law*. A&A, 249: 99–106, 1991.

[45] **L. Ciotti**. *The Analytical Distribution Function of Anisotropic Two-Component Hernquist Models*. ApJ, 471: 68–+, 1996.

[46] **L. Ciotti and G. Bertin**. *Analytical properties of the $R^{1/m}$ law*. A&A, 352: 447–451, 1999.

[47] **L. Ciotti and B. Lanzoni**. *Stellar systems following the R^1/m^ luminosity law. II. Anisotropy, velocity profiles, and the fundamental plane of elliptical galaxies.* A&A, 321: 724–732, 1997.

[48] **L. Ciotti and L. Morganti**. *Two-component galaxy models: the effect of density profile at large radii on the phase-space consistency*. MNRAS, 393: 179–191, 2009.

[49] **L. Ciotti and L. Morganti**. *Consistency criteria for generalized Cuddeford systems*. MNRAS, 401: 1091–1098, 2010a.

[50] **L. Ciotti and L. Morganti**. *How general is the global density slope-anisotropy inequality?* MNRAS, 408: 1070–1074, 2010b.

[51] **L. Ciotti and S. Pellegrini**. *Self-consistent two-component models of elliptical galaxies.* MNRAS, 255: 561–571, 1992.

[52] **A. Cloet-Osselaer, S. De Rijcke, J. Schroyen, and V. Dury**. *The degeneracy between star formation parameters in dwarf galaxy simulations and the M_{star}-M_{halo} relation*. MNRAS, 423: 735–745, 2012.

[53] **A. A. Cole, E. D. Skillman, E. Tolstoy, J. S. Gallagher, III, A. Aparicio, A. E. Dolphin, C. Gallart, S. L. Hidalgo, A. Saha, P. B. Stetson, and D. R. Weisz**. *Leo A: A Late-blooming Survivor of the Epoch of Reionization in the Local Group*. ApJ, 659: L17–L20, 2007.

[54] **S. Cole and C. Lacey**. *The structure of dark matter haloes in hierarchical clustering models*. MNRAS, 281: 716–736, 1996.

[55] **P. Colín, A. A. Klypin, and A. V. Kravtsov**. *Velocity Bias in a Λ Cold Dark Matter Model*. ApJ, 539: 561–569, 2000.

[56] **M. M. Crone, A. E. Evrard, and D. O. Richstone**. *The cosmological dependence of cluster density profiles*. ApJ, 434: 402–416, 1994.

[57] **P. Cuddeford**. *An analytic inversion for anisotropic spherical galaxies*. MNRAS, 253: 414–426, 1991.

[58] **P. Cuddeford and P. Louis**. *Spherical galaxian distribution functions with adjustable anisotropy*. MNRAS, 275: 1017–1027, 1995.

[59] **N. Dalal, Y. Lithwick, and M. Kuhlen**. *The Origin of Dark Matter Halo Profiles*. ArXiv e-prints, 2010.

[60] **L. Danese, G. de Zotti, and G. di Tullio**. *On velocity dispersions of galaxies in rich clusters*. A&A, 82: 322–327, 1980.

[61] **J. I. Davies, S. Phillipps, M. G. M. Cawson, M. J. Disney, and E. J. Kibblewhite**. *Low surface brightness galaxies in the Fornax Cluster - Automated galaxy surface photometry. III*. MNRAS, 232: 239–258, 1988.

[62] **W. J. G. de Blok**. *The Core-Cusp Problem*. Advances in Astronomy, 2010: 789293, 2010.

[63] **V. De Bruyne, H. Dejonghe, A. Pizzella, M. Bernardi, and W. W. Zeilinger**. *Toward an Alternative Way of Looking at Elliptical Galaxies: Case Studies for NGC 4649 and NGC 7097*. ApJ, 546: 903–915, 2001.

[64] **V. De Bruyne, S. De Rijcke, H. Dejonghe, and W. W. Zeilinger**. *Modelling galactic spectra - I. A dynamical model for NGC 3258*. MNRAS, 349: 440–460, 2004.

[65] **S. De Rijcke**. *Determination of the dynamical structure of elliptical galaxies by direct fits to spectra*. PhD thesis, Faculteit Wetenschappen, Universiteit Gent, 2000.

[66] **S. De Rijcke and H. Dejonghe**. *Determination of the dynamical structure of galaxies using optical spectra*. MNRAS, 298: 677–691, 1998.

[67] **S. De Rijcke, P. Prugniel, F. Simien, and H. Dejonghe**. *The internal dynamics of the Local Group dwarf elliptical galaxies NGC 147, 185 and 205*. MNRAS, 369: 1321–1333, 2006.

[68] **S. De Rijcke, W. W. Zeilinger, G. K. T. Hau, P. Prugniel, and H. Dejonghe**. *Generalizations of the Tully-Fisher Relation for Early- and Late-Type Galaxies*. ApJ, 659: 1172–1175, 2007.

[69] **S. De Rijcke, E. Van Hese, and P. Buyle**. *The Conversion of Late-type Into Early-type Dwarf Galaxies by Ram-pressure Stripping in the Fornax Cluster*. ApJ, 724: L171–L175, 2010.

[70] **G. de Vaucouleurs**. *Recherches sur les Nebuleuses Extragalactiques.* Annales d'Astrophysique, 11: 247–287, 1948.

[71] **W. Dehnen**. *A Family of Potential-Density Pairs for Spherical Galaxies and Bulges*. MNRAS, 265: 250–256, 1993.

[72] **W. Dehnen and D. E. McLaughlin**. *Dynamical insight into dark matter haloes*. MNRAS, 363: 1057–1068, 2005.

[73] **H. Dejonghe**. *Stellar dynamics and the description of stellar systems*. Phys. Rep., 133: 217–313, 1986.

[74] **H. Dejonghe**. *A completely analytical family of anisotropic Plummer models*. MNRAS, 224: 13–39, 1987.

[75] **H. Dejonghe**. *A quadratic programming technique for modeling gravitating systems.* ApJ, 343: 113–124, 1989.

[76] **H. Dejonghe and T. de Zeeuw**. *Analytic axisymmetric galaxy models with three integrals of motion*. ApJ, 333: 90–129, 1988.

[77] **H. Dejonghe and D. Merritt**. *Inferring the mass of spherical stellar systems from velocity moments*. ApJ, 391: 531–549, 1992.

[78] **H. Dejonghe, M. Baes, V. De Bruyne, S. De Rijcke, K. Van Caelenberg, and E. Van Hese**. *Dynamical Structure of Gravitating Systems Using Quadratic Programming*. In L. P. Ossipkov & I. I. Nikiforov, editor, *Stellar Dynamics: from Classic to Modern*, pages 292–+, 2001.

[79] **A. Del Popolo**. *On the universality of density profiles*. MNRAS, 408: 1808–1817, 2010.

[80] **A. Del Popolo**. *On the density-profile slope of clusters of galaxies*. MNRAS, 424: 38–51, 2012.

[81] **B. K. Dhar and L. L. R. Williams**. *Surface mass density of the Einasto family of dark matter haloes: are they Sersic-like?* MNRAS, 405: 340–346, 2010.

[82] **J. Diemand, M. Zemp, B. Moore, J. Stadel, and C. M. Carollo**. *Cusps in cold dark matter haloes*. MNRAS, 364: 665–673, 2005.

[83] **M. D'Onofrio, M. Capaccioli, and N. Caon**. *On the Shape of the Light Profiles of Early Type Galaxies - Part Two - the - Diagram*. MNRAS, 271: 523–+, 1994.

[84] **J. P. Doremus, G. Baumann, and M. R. Feix**. *Stability of a Self Gravitating System with Phase Space Density Function of Energy and Angular Momentum*. A&A, 29: 401–+, 1973.

[85] **M. J. Drinkwater, S. Phillipps, J. B. Jones, M. D. Gregg, J. H. Deady, J. I. Davies, Q. A. Parker, E. M. Sadler, and R. M. Smith**. *The Fornax spectroscopic survey. I. Survey strategy and preliminary results on the redshift distribution of a complete sample of stars and galaxies*. A&A, 355: 900–914, 2000.

[86] **M. J. Drinkwater, M. D. Gregg, and M. Colless**. *Substructure and Dynamics of the Fornax Cluster*. ApJ, 548: L139–L142, 2001.

[87] **J. Dubinski and R. G. Carlberg**. *The structure of cold dark matter halos*. ApJ, 378: 496–503, 1991.

[88] **A. R. Duffy, J. Schaye, S. T. Kay, and C. Dalla Vecchia**. *Dark matter halo concentrations in the Wilkinson Microwave Anisotropy Probe year 5 cosmology*. MNRAS, 390: L64–L68, 2008.

[89] **J. Einasto and U. Haud**. *Galactic models with massive corona. I - Method. II - Galaxy*. A&A, 223: 89–106, 1989.

[90] **Á. Elíasdóttir and O. Möller**. *A comparison of the strong lensing properties of the Sérsic and the Navarro, Frenk and White profiles*. J. Cosmology Astropart. Phys., 7: 6–+, 2007.

[91] **N. W. Evans and J. An**. *Hypervirial models of stellar systems*. MNRAS, 360: 492–498, 2005.

[92] **N. W. Evans, P. T. de Zeeuw, and D. Lynden-Bell**. *The flattened isochrone*. MNRAS, 244: 111–129, 1990.

[93] **D. Fadda, A. Biviano, F. R. Marleau, L. J. Storrie-Lombardi, and F. Durret**. *Starburst Galaxies in Cluster-feeding Filaments Unveiled by Spitzer*. ApJ, 672: L9–L12, 2008.

[94] **B. Famaey, K. Van Caelenberg, and H. Dejonghe**. *Three-integral models for axisymmetric galactic discs.* MNRAS, 335: 201–215, 2002.

[95] **H. C. Ferguson**. *Population studies in groups and clusters of galaxies. II - A catalog of galaxies in the central 3.5 deg of the Fornax Cluster*. AJ, 98: 367–418, 1989.

[96] **L. Ferrarese**. *Beyond the Bulge: A Fundamental Relation between Supermassive Black Holes and Dark Matter Halos*. ApJ, 578: 90–97, 2002.

[97] **L. Ferrarese and H. Ford**. *Supermassive Black Holes in Galactic Nuclei: Past, Present and Future Research*. Space Science Reviews, 116: 523–624, 2005.

[98] **L. Ferrarese and D. Merritt**. *A Fundamental Relation between Supermassive Black Holes and Their Host Galaxies*. ApJ, 539: L9–L12, 2000.

[99] **C. Fox**. *The G and H-Functions as Symmetrical Fourier Kernels*. Trans. Amer. Math. Soc, 98: 395–429, 1961.

[100] **W. Fricke**. *Dynamische Begründung der Geschwindigkeitsverteilung im Sternsystem*. Astronomische Nachrichten, 280: 193–216, 1952.

[101] **T. Fukushige and J. Makino**. *On the Origin of Cusps in Dark Matter Halos.* ApJ, 477: L9–L12, 1997.

[102] **D. A. Gadotti**. *Structural properties of pseudo-bulges, classical bulges and elliptical galaxies: a Sloan Digital Sky Survey perspective*. MNRAS, 393: 1531–1552, 2009.

[103] **L. Gao, J. F. Navarro, S. Cole, C. S. Frenk, S. D. M. White, V. Springel, A. Jenkins, and A. F. Neto**. *The redshift dependence of the structure of massive Λ cold dark matter haloes.* MNRAS, 387: 536–544, 2008.

[104] **K. Gebhardt, R. Bender, G. Bower, A. Dressler, S. M. Faber, A. V. Filippenko, R. Green, C. Grillmair, L. C. Ho, J. Kormendy, T. R. Lauer, J. Magorrian, J. Pinkney, D. Richstone, and S. Tremaine**. *A Relationship between Nuclear Black Hole Mass and Galaxy Velocity Dispersion*. ApJ, 539: L13–L16, 2000.

[105] **K. Gebhardt, D. Richstone, S. Tremaine, T. R. Lauer, R. Bender, G. Bower, A. Dressler, S. M. Faber, A. V. Filippenko, R. Green, C. Grillmair, L. C. Ho, J. Kormendy, J. Magorrian, and J. Pinkney**. *Axisymmetric Dynamical Models of the Central Regions of Galaxies*. ApJ, 583: 92–115, 2003.

[106] **O. Gerhard, G. Jeske, R. P. Saglia, and R. Bender**. *Breaking the degeneracy between anisotropy and mass - The dark halo of the E0 galaxy NGC 6703*. MNRAS, 295: 197–+, 1998.

[107] **O. E. Gerhard**. *Line-of-sight velocity profiles in spherical galaxies: breaking the degeneracy between anisotropy and mass.* MNRAS, 265: 213, 1993.

[108] **I. S. Gradshteyn and I. M. Ryzhik**. *Table of integrals, series and products*. New York: Academic Press, 4th ed., edited by Geronimus, Yu.V. (4th ed.); Tseytlin, M.Yu. (4th ed.), 1965.

[109] **A. W. Graham and S. P. Driver**. *A Concise Reference to (Projected) Sérsic $R^{1/n}$ Quantities, Including Concentration, Profile Slopes, Petrosian Indices, and Kron Magnitudes*. PASA, 22: 118–127, 2005.

[110] **A. W. Graham and R. Guzmán**. *HST Photometry of Dwarf Elliptical Galaxies in Coma, and an Explanation for the Alleged Structural Dichotomy between Dwarf and Bright Elliptical Galaxies*. AJ, 125: 2936–2950, 2003.

[111] **A. W. Graham, P. Erwin, N. Caon, and I. Trujillo**. *A Correlation between Galaxy Light Concentration and Supermassive Black Hole Mass*. ApJ, 563: L11–L14, 2001.

[112] **A. W. Graham, D. Merritt, B. Moore, J. Diemand, and B. Terzić**. *Empirical Models for Dark Matter Halos. II. Inner Profile Slopes, Dynamical Profiles, and ρ/σ^3*. AJ, 132: 2701–2710, 2006.

[113] **C. P. Haines, A. Gargiulo, F. La Barbera, A. Mercurio, P. Merluzzi, and G. Busarello**. *The different physical mechanisms that drive the star formation histories of giant and dwarf galaxies*. MNRAS, 381: 7–32, 2007.

[114] **S. H. Hansen and B. Moore**. *A universal density slope–velocity anisotropy relation for relaxed structures*. New Astronomy, 11: 333–338, 2006.

[115] **S. H. Hansen and M. Sparre**. *A Derivation of (Half) the Dark Matter Distribution Function*. ApJ, 756: 100, 2012.

[116] **S. H. Hansen and J. Stadel**. *The velocity anisotropy - density slope relation*. Journal of Cosmology and Astro-Particle Physics, 5: 14–27, 2006.

[117] **S. H. Hansen, B. Moore, M. Zemp, and J. Stadel**. *A universal velocity distribution of relaxed collisionless structures*. Journal of Cosmology and Astro-Particle Physics, 1: 14–25, 2006.

[118] **S. H. Hansen, D. Juncher, and M. Sparre**. *An Attractor for Dark Matter Structures*. ApJ, 718: L68–L72, 2010.

[119] **F. Hausdorff**. *Summationsmethoden und Momentfolgen. I*. Mathematische Zeitschrift, 9: 74–109, 1921.

[120] **F. Hausdorff**. *Summationsmethoden und Momentfolgen. II*. Mathematische Zeitschrift, 9: 280–299, 1921.

[121] **P. He**. *Equilibrium statistical mechanics for self-gravitating systems: local ergodicity and extended Boltzmann-Gibbs/White-Narayan statistics*. MNRAS, 419: 1667–1681, 2012.

[122] **M. Hénon**. *L'amas isochrone. - III. Fonction de distribution*. Annales d'Astrophysique, 23: 474–477, 1960.

[123] **M. Hénon**. *Numerical Experiments on the Stability of Spherical Stellar Systems*. A&A, 24: 229–238, 1973.

[124] **R. N. Henriksen**. *Central Relaxation of Dark Matter Halos*. ApJ, 671: 1147–1159, 2007.

[125] **R. N. Henriksen**. *Nature and Nurture in Dark Matter Halos*. ApJ, 690: 102–110, 2009.

[126] **L. Hernquist**. *An analytical model for spherical galaxies and bulges*. ApJ, 356: 359–364, 1990.

[127] **L. Hernquist**. *N-body realizations of compound galaxies*. ApJS, 86: 389–400, 1993.

[128] **L. Hernquist and J. P. Ostriker**. *A self-consistent field method for galactic dynamics*. ApJ, 386: 375–397, 1992.

[129] **J. Hjorth and L. L. R. Williams**. *Statistical Mechanics of Collisionless Orbits. I. Origin of Central Cusps in Dark-matter Halos*. ApJ, 722: 851–855, 2010.

[130] **K. Holley-Bockelmann, J. C. Mihos, S. Sigurdsson, and L. Hernquist**. *Models of Cuspy Triaxial Galaxies*. ApJ, 549: 862–870, 2001.

[131] **S. Hozumi and L. Hernquist**. *Secular Evolution of Barred Galaxies with Massive Central Black Holes*. PASJ, 57: 719–731, 2005.

[132] **C. Hunter**. *Determination of the distribution function of an elliptical galaxy*. AJ, 80: 783, 1975.

[133] **C. Hunter and E. Qian**. *Two-integral distribution functions for axisymmetric galaxies*. MNRAS, 262: 401–428, 1993.

[134] **P. Hut, J. Makino, and S. McMillan**. *Building a better leapfrog*. ApJ, 443: L93–L96, 1995.

[135] **O. Iguchi, Y. Sota, A. Nakamichi, and M. Morikawa**. *Local virial relation for self-gravitating system*. Phys. Rev. E, 73 (4): 046112–+, 2006.

[136] **W. Jaffe**. *A simple model for the distribution of light in spherical galaxies*. MNRAS, 202: 995–999, 1983.

[137] **Y. P. Jing and Y. Suto**. *The Density Profiles of the Dark Matter Halo Are Not Universal*. ApJ, 529: L69–L72, 2000.

[138] **H. E. Kandrup, I. M. Vass, and I. V. Sideris**. *Transient chaos and resonant phase mixing in violent relaxation*. MNRAS, 341: 927–936, 2003.

[139] **N. Katz**. *Dissipationless collapse in an expanding universe*. ApJ, 368: 325–336, 1991.

[140] **S. Kazantzidis, J. Magorrian, and B. Moore**. *Generating Equilibrium Dark Matter Halos: Inadequacies of the Local Maxwellian Approximation*. ApJ, 601: 37–46, 2004.

[141] **A. A. Kilbas and M. Saigo**. *On the H-function*. J. Appl. Math. Stochast. Anal., 12: 191, 1999.

[142] **J. Kormendy and D. Richstone**. *Inward Bound—The Search For Supermassive Black Holes In Galactic Nuclei*. ARA&A, 33: 581–+, 1995.

[143] **A. Kronawitter, R. P. Saglia, O. Gerhard, and R. Bender**. *Orbital structure and mass distribution in elliptical galaxies*. A&AS, 144: 53–84, 2000.

[144] **G. Lake**. *Dynamical modeling of elliptical galaxies. I - Analytical prolate models. II - Numerical prolate models*. ApJ, 243: 111–126, 1981.

[145] **A. Lapi and A. Cavaliere**. *Self-similar Dynamical Relaxation of Dark Matter Halos in an Expanding Universe*. ApJ, 743: 127, 2011.

[146] **M. Lingam and P. H. Nguyen**. *The double-power approach to spherically symmetric astrophysical systems*. MNRAS, 440: 2636–2664, 2014.

[147] **T. Lu, D. G. Gilbank, M. L. Balogh, and A. Bognat**. *Recent arrival of faint cluster galaxies on the red sequence: luminosity functions from 119deg^2 of CFHTLS*. MNRAS, 399: 1858–1876, 2009.

[148] **A. D. Ludlow, J. F. Navarro, V. Springel, M. Vogelsberger, J. Wang, S. D. M. White, A. Jenkins, and C. S. Frenk**. *Secondary infall and the pseudo-phase-space density profiles of cold dark matter haloes*. MNRAS, 406: 137–146, 2010.

[149] **A. D. Ludlow, J. F. Navarro, S. D. M. White, M. Boylan-Kolchin, V. Springel, A. Jenkins, and C. S. Frenk**. *The density and pseudo-phase-space density profiles of cold dark matter haloes*. MNRAS, 415: 3895–3902, 2011.

[150] **D. Lynden-Bell**. *Stellar dynamics: Exact solution of the self-gravitation equation*. MNRAS, 123: 447–+, 1962.

[151] **D. Lynden-Bell**. *Statistical mechanics of violent relaxation in stellar systems*. MNRAS, 136: 101, 1967.

[152] **D. Lynden-Bell**. *On a mechanism that structures galaxies*. MNRAS, 187: 101–107, 1979.

[153] **G. A. Mamon and E. L. Łokas**. *Dark matter in elliptical galaxies - I. Is the total mass density profile of the NFW form or even steeper?* MNRAS, 362: 95–109, 2005.

[154] **G. A. Mamon and E. L. Łokas**. *Dark matter in elliptical galaxies - II. Estimating the mass within the virial radius.* MNRAS, 363: 705–722, 2005.

[155] **A. M. Mathai**. *A Handbook of Generalized Special Functions for Statistical and Physical Sciences*. Oxford University Press, Oxford, 235 p., 1993.

[156] **A. M. Mathai, R. K. Saxena, and H. J. Haubold**. *The H-Function: Theory and Applications*. Springer-Verlag New York, 268 p., 2009.

[157] **L. Mayer, F. Governato, M. Colpi, B. Moore, T. Quinn, J. Wadsley, J. Stadel, and G. Lake**. *Tidal Stirring and the Origin of Dwarf Spheroidals in the Local Group*. ApJ, 547: L123–L127, 2001.

[158] **A. Mazure and H. V. Capelato**. *Exact solutions for the spatial de Vaucouleurs and Sérsic laws and related quantities.* A&A, 383: 384–389, 2002.

[159] **C. S. Meijer**. *On the G-Function. I-VIII*. In *Proc. Nederl. Akad. Wetensch.*, volume 49, pages 227–+, 1946.

[160] **D. Merritt**. *Spherical stellar systems with spheroidal velocity distributions*. AJ, 90: 1027–1037, 1985.

[161] **D. Merritt**. *Stability of elliptical galaxies - Numerical experiments*. In P. T. de Zeeuw, editor, *Structure and Dynamics of Elliptical Galaxies*, volume 127 of *IAU Symposium*, pages 315–327, 1987.

[162] **D. Merritt**. *Elliptical Galaxy Dynamics*. PASP, 111: 129–168, 1999.

[163] **D. Merritt and P. Saha**. *Mapping spherical potentials with discrete radial velocities*. ApJ, 409: 75–90, 1993.

[164] **D. Merritt, J. F. Navarro, A. Ludlow, and A. Jenkins**. *A Universal Density Profile for Dark and Luminous Matter?* ApJ, 624: L85–L88, 2005.

[165] **D. Merritt, A. W. Graham, B. Moore, J. Diemand, and B. Terzić**. *Empirical Models for Dark Matter Halos. I. Nonparametric Construction of Density Profiles and Comparison with Parametric Models.* AJ, 132: 2685–2700, 2006.

[166] **A. Meza**. *Stability of rotating spherical stellar systems*. A&A, 395: 25–30, 2002.

[167] **A. Meza and N. Zamorano**. *Numerical Stability of a Family of Osipkov-Merritt Models*. ApJ, 490: 136–142, 1997.

[168] **C. Möllenhoff and J. Heidt**. *Surface photometry of spiral galaxies in NIR: Structural parameters of disks and bulges*. A&A, 368: 16–37, 2001.

[169] **B. Moore, N. Katz, G. Lake, A. Dressler, and A. Oemler**. *Galaxy harassment and the evolution of clusters of galaxies*. Nature, 379: 613–616, 1996.

[170] **B. Moore, F. Governato, T. Quinn, J. Stadel, and G. Lake**. *Resolving the Structure of Cold Dark Matter Halos*. ApJ, 499: L5–L8, 1998.

[171] **B. Moore, T. Quinn, F. Governato, J. Stadel, and G. Lake**. *Cold collapse and the core catastrophe*. MNRAS, 310: 1147–1152, 1999.

[172] **M. Mori and A. Burkert**. *Gas Stripping of Dwarf Galaxies in Clusters of Galaxies*. ApJ, 538: 559–568, 2000.

[173] **R. Nagai and M. Miyamoto**. *A family of self-gravitating stellar systems with axial symmetry*. PASJ, 28: 1–17, 1976.

[174] **J. F. Navarro, C. S. Frenk, and S. D. M. White**. *The Structure of Cold Dark Matter Halos*. ApJ, 462: 563–575, 1996.

[175] **J. F. Navarro, C. S. Frenk, and S. D. M. White**. *A Universal Density Profile from Hierarchical Clustering*. ApJ, 490: 493–508, 1997.

[176] **J. F. Navarro, E. Hayashi, C. Power, A. R. Jenkins, C. S. Frenk, S. D. M. White, V. Springel, J. Stadel, and T. R. Quinn**. *The inner structure of ΛCDM haloes - III. Universality and asymptotic slopes*. MNRAS, 349: 1039–1051, 2004.

[177] **J. F. Navarro, A. Ludlow, V. Springel, J. Wang, M. Vogelsberger, S. D. M. White, A. Jenkins, C. S. Frenk, and A. Helmi**. *The diversity and similarity of simulated cold dark matter haloes*. MNRAS, 402: 21–34, 2010.

[178] **P. H. Nguyen and M. Lingam**. *Analytical families of two-component anisotropic polytropes and their relativistic extensions*. MNRAS, 436: 2014–2028, 2013.

[179] **C. A. Norman, J. A. Sellwood, and H. Hasan**. *Bar Dissolution and Bulge Formation: an Example of Secular Dynamical Evolution in Galaxies*. ApJ, 462: 114–+, 1996.

[180] **J. Oñorbe, R. Domínguez-Tenreiro, A. Sáiz, and A. Serna**. *Bright and dark matter in elliptical galaxies: mass and velocity distributions from self-consistent hydrodynamical simulations*. MNRAS, 376: 39–60, 2007.

[181] **L. P. Osipkov**. *Spherical systems of gravitating bodies with an ellipsoidal velocity distribution*. Pis ma Astronomicheskii Zhurnal, 5: 77–80, 1979.

[182] **P. L. Palmer and J. Papaloizou**. *Instability in spherical stellar systems*. MNRAS, 224: 1043–1053, 1987.

[183] **M. Paolillo, G. Fabbiano, G. Peres, and D.-W. Kim**. *Deep ROSAT HRI Observations of the NGC 1399/NGC 1404 Region: Morphology and Structure of the X-Ray Halo*. ApJ, 565: 883–907, 2002.

[184] **A. Pizzella, E. M. Corsini, E. Dalla Bontà, M. Sarzi, L. Coccato, and F. Bertola**. *On the Relation between Circular Velocity and Central Velocity Dispersion in High and Low Surface Brightness Galaxies*. ApJ, 631: 785–791, 2005.

[185] **H. C. Plummer**. *On the problem of distribution in globular star clusters*. MNRAS, 71: 460–470, 1911.

[186] **S. C. Porter, S. Raychaudhury, K. A. Pimbblet, and M. J. Drinkwater**. *Star formation in galaxies falling into clusters along supercluster-scale filaments*. MNRAS, 388: 1152–1160, 2008.

[187] **P. Prugniel and F. Simien**. *The fundamental plane of early-type galaxies: non-homology of the spatial structure.* A&A, 321: 111–122, 1997.

[188] **G. D. Quinlan and L. Hernquist**. *The dynamical evolution of massive black hole binaries - II. Self-consistent N-body integrations*. New Astronomy, 2: 533–554, 1997.

[189] **G. D. Quinlan, L. Hernquist, and S. Sigurdsson**. *Models of Galaxies with Central Black Holes: Adiabatic Growth in Spherical Galaxies*. ApJ, 440: 554–+, 1995.

[190] **E. Rasia, G. Tormen, and L. Moscardini**. *A dynamical model for the distribution of dark matter and gas in galaxy clusters*. MNRAS, 351: 237–252, 2004.

[191] **E. Retana-Montenegro, E. van Hese, G. Gentile, M. Baes, and F. Frutos-Alfaro**. *Analytical properties of Einasto dark matter haloes*. A&A, 540: A70, 2012.

[192] **T. Richardson and M. Fairbairn**. *Analytical solutions to the mass-anisotropy degeneracy with higher order Jeans analysis: a general method*. MNRAS, 432: 3361–3380, 2013.

[193] **T. Rindler-Daller, H. Dejonghe, and W. W. Zeilinger**. *Spherical models for early-type galaxies with cuspy mass densities*. MNRAS, 356: 1403–1408, 2005.

[194] **Stefan G. Samko, Anatoly A. Kilbas, and Oleg I. Marichev**. *Fractional Integrals and Derivatives: Theory and Applications*. CRC, 1993.

[195] **K. B. Schmidt, S. H. Hansen, and A. V. Macciò**. *Alas, the Dark Matter Structures Were Not That Trivial*. ApJ, 689: L33–L36, 2008.

[196] **P. Schneider, J. Ehlers, and E. E. Falco**. *Gravitational Lenses*. Springer-Verlag Berlin Heidelberg New York, 1992.

[197] **M. Schwarzschild**. *A numerical model for a triaxial stellar system in dynamical equilibrium*. ApJ, 232: 236–247, 1979.

[198] **J. A. Sellwood and N. W. Evans**. *The Stability of Disks in Cusped Potentials*. ApJ, 546: 176–188, 2001.

[199] **J. L. Sersic**. *Atlas de galaxias australes*. Cordoba, Argentina: Observatorio Astronomico, 1968, 1968.

[200] **S. Sharma and M. Steinmetz**. *The Angular Momentum Distribution of Gas and Dark Matter in Galactic Halos*. ApJ, 628: 21–44, 2005.

[201] **J. Shen and J. A. Sellwood**. *The Destruction of Bars by Central Mass Concentrations*. ApJ, 604: 614–631, 2004.

[202] **R. Smith, J. I. Davies, and A. H. Nelson**. *How effective is harassment on infalling late-type dwarfs?* MNRAS, 405: 1723–1735, 2010.

[203] **R. J. Smith, J. R. Lucey, M. J. Hudson, S. P. Allanson, T. J. Bridges, A. E. Hornschemeier, R. O. Marzke, and N. A. Miller**. *A spectroscopic survey of dwarf galaxies in the Coma cluster: stellar populations, environment and downsizing*. MNRAS, 392: 1265–1294, 2009.

[204] **A. Sommerfeld**. *Differential Equations in Physics*. New York: Academic Press, 335 p., 1964.

[205] **Y. Sota, O. Iguchi, M. Morikawa, and A. Nakamichi**. *Local Virial Relation and Velocity Anisotropy for Collisionless Self-Gravitating Systems*. Progress of Theoretical Physics Supplement, 162: 62–69, 2006.

[206] **V. Springel**. *The cosmological simulation code GADGET-2*. MNRAS, 364: 1105–1134, 2005.

[207] **J. Stadel, D. Potter, B. Moore, J. Diemand, P. Madau, M. Zemp, M. Kuhlen, and V. Quilis**. *Quantifying the heart of darkness with GHALO - a multibillion particle simulation of a galactic halo*. MNRAS, 398: L21–L25, 2009.

[208] **M. Stiavelli**. *Violent Relaxation Around a Massive Black Hole*. ApJ, 495: L91+, 1998.

[209] **J. P. Stott, I. Smail, A. C. Edge, H. Ebeling, G. P. Smith, J.-P. Kneib, and K. A. Pimbblet**. *An Increase in the Faint Red Galaxy Population in Massive Clusters since z ˜ 0.5*. ApJ, 661: 95–101, 2007.

[210] **G. Szegö**. *Orthogonal Polynomials*. New York: American Mathematical Society, 432 p., 1939.

[211] **J. E. Taylor and J. F. Navarro**. *The Phase-Space Density Profiles of Cold Dark Matter Halos*. ApJ, 563: 483–488, 2001.

[212] **P. A. Thomas, M. J. Drinkwater, and E. Evstigneeva**. *Formation of ultra-compact dwarf galaxies: tests of the galaxy threshing scenario in Fornax*. MNRAS, 389: 102–112, 2008.

[213] **M. Trenti and G. Bertin**. *Partial Suppression of the Radial Orbit Instability in Stellar Systems*. ApJ, 637: 717–726, 2006.

[214] **I. Trujillo, A. W. Graham, and N. Caon**. *On the estimation of galaxy structural parameters: the Sérsic model*. MNRAS, 326: 869–876, 2001.

[215] **S. Valcke, S. de Rijcke, and H. Dejonghe**. *Simulations of the formation and evolution of isolated dwarf galaxies*. MNRAS, 389: 1111–1126, 2008.

[216] **G. van de Ven, R. C. E. van den Bosch, E. K. Verolme, and P. T. de Zeeuw**. *The dynamical distance and intrinsic structure of the globular cluster ω Centauri*. A&A, 445: 513–543, 2006.

[217] **R. P. van der Marel, J. Magorrian, R. G. Carlberg, H. K. C. Yee, and E. Ellingson**. *The Velocity and Mass Distribution of Clusters of Galaxies from the CNOC1 Cluster Redshift Survey*. AJ, 119: 2038–2052, 2000.

[218] **E. Van Hese and H. Dejonghe**. *A Dynamical Modeling Technique for Clusters of Galaxies*. In S. Borgani, M. Mezzetti, & R. Valdarnini, editor, *Tracing Cosmic Evolution with Galaxy Clusters*, volume 268 of *Astronomical Society of the Pacific Conference Series*, pages 453–+, 2002.

[219] **E. Van Hese, M. Baes, and H. Dejonghe**. *The Dynamical Structure of Dark Matter Halos with Universal Properties*. ApJ, 690: 1280–1291, 2009.

[220] **E. Van Hese, M. Baes, and H. Dejonghe**. *On the Universality of the Global Density Slope-Anisotropy Inequality*. ApJ, 726: 80–+, 2011.

[221] **E. Vasiliev**. *A new code for orbit analysis and Schwarzschild modelling of triaxial stellar systems*. MNRAS, 434: 3174–3195, 2013.

[222] **U. I. K. Veltmann**. *Distribution of brightness and density in globular clusters and two-parameter generalized isochronic models*. AZh, 56: 976–982, 1979.

[223] **R. Wojtak, E. L. Łokas, S. Gottlöber, and G. A. Mamon**. *Radial velocity moments of dark matter haloes*. MNRAS, 361: L1–L5, 2005.

[224] **R. Wojtak, E. L. Łokas, G. A. Mamon, S. Gottlöber, A. Klypin, and Y. Hoffman**. *The distribution function of dark matter in massive haloes*. MNRAS, 388: 815–828, 2008.

[225] **A. Zait, Y. Hoffman, and I. Shlosman**. *Dark Matter Halos: Velocity Anisotropy-Density Slope Relation*. ApJ, 682: 835–840, 2008.

[226] **M. Zemp, J. Diemand, M. Kuhlen, P. Madau, B. Moore, D. Potter, J. Stadel, and L. Widrow**. *The graininess of dark matter haloes*. MNRAS, 394: 641–659, 2009.

[227] **H. Zhao**. *Analytical models for galactic nuclei*. MNRAS, 278: 488–496, 1996.

List of publications

List of Publications

[1] **H. Dejonghe, M. Baes, V. De Bruyne, S. De Rijcke, K. Van Caelenberg, and E. Van Hese**. *Dynamical Structure of Gravitating Systems Using Quadratic Programming*. In L. P. Ossipkov & I. I. Nikiforov, editor, *Stellar Dynamics: from Classic to Modern*, pages 292–+, 2001.

[2] **E. Van Hese and H. Dejonghe**. *A Dynamical Modeling Technique for Clusters of Galaxies*. In S. Borgani, M. Mezzetti, & R. Valdarnini, editor, *Tracing Cosmic Evolution with Galaxy Clusters*, volume 268 of *Astronomical Society of the Pacific Conference Series*, pages 453–+, 2002.

[3] **P. Buyle, E. Van Hese, S. De Rijcke, and H. Dejonghe**. *Radial-orbit instability of a family of anisotropic Hernquist models with and without a supermassive black hole*. *MNRAS*, 375: 1157–1170, 2007.

[4] **M. Baes and E. van Hese**. *Dynamical models with a general anisotropy profile*. *A&A*, 471: 419–432, 2007.

[5] **E. Van Hese, M. Baes, and H. Dejonghe**. *The Dynamical Structure of Dark Matter Halos with Universal Properties*. *ApJ*, 690: 1280–1291, 2009.

[6] **S. De Rijcke, E. Van Hese, and P. Buyle**. *The Conversion of Late-type Into Early-type Dwarf Galaxies by Ram-pressure Stripping in the Fornax Cluster*. *ApJ*, 724: L171–L175, 2010.

[7] **E. Van Hese, M. Baes, and H. Dejonghe**. *On the Universality of the Global Density Slope-Anisotropy Inequality*. *ApJ*, 726: 80–+, 2011.

[8] **M. Baes and E. van Hese**. *Analytical expressions for the deprojected Sérsic model. II. General expressions in terms of the Fox H function*. *A&A*, 534: A69, 2011.

[9] **E. Retana-Montenegro, E. van Hese, G. Gentile, M. Baes, and F. Frutos-Alfaro**. *Analytical properties of Einasto dark matter haloes*. *A&A*, 540: A70, 2012.

[10] **J. An, E. Van Hese, and M. Baes**. *Phase-space consistency of stellar dynamical models determined by separable augmented densities*. *MNRAS*, 422: 652–664, 2012.